Second harmonic generation and control in dielectric metasurfaces

Carlo Gigli

Université de Paris

MPQ

Thèse de doctorat en Physique

Second harmonic generation and control in dielectric metasurfaces

Carlo Gigli

Présentée et soutenue publiquement le
12 Mars 2021

École Doctorale
ED564 Physique en Île de France

Laboratoire
Matériaux et Phénomènes Quantiques

Groupe de recherche
Dispositifs Optiques Nonlinéaires

Université
Université de Paris

Jury composé de

Giuseppe LEO Univeristé de Paris	Directeur de thèse
Christelle MONAT École Centrale de Lyon	Rapporteur
Thomas ZENTGRAF University of Paderborn	Rapporteur
Jacqueline BLOCH C2N	Président du jury
Philippe LALANNE Institut d'Optique d'Aquitaine	Examinateur
Angela VASANELLI Université de Paris	Examinateur
Patrice GENEVET CHREA	Examinateur
Costantino DE ANGELIS Università di Brescia	Invité
Jean-Michel GÉRARD CEA Grenoble	Invité

Second harmonic generation and control in dielectric metasurfaces

PhD thesis

Carlo Gigli

Disclaimer

Ph.D. Thesis, Université de Paris, Second harmonic generation and control in AlGaAs nanoresonators and metasurfaces.

Carlo Gigli

The work described in this thesis was performed at Matériaux et Phénomènes Quantiques, Université de Paris, 10 Rue A. Domon et L. Duquet - 75013 Paris. This thesis was funded by the Ecole Doctorale de Physique en Ile de France (EDPIF).

The author declares no conflict of interest.

Colophon

This document was typeset with the help of KOMA-Script and LaTeX using the kaobook class.

Preface

The scientific community celebrates this year the 60th anniversary of the first observation of second-harmonic generation (SHG) in a quartz crystal by Franken and coworkers in 1961, which marked the birth of nonlinear optics. Since then, this field has drawn a great interest, ranging from fundamental studies to the development of cutting-edge applications. Some of them rely on conversion processes to generate coherent radiation in frequency windows where different sources are not available; some others are attractive for the development of all-optical signal processing systems at the core of integrated photonic circuitry. In the 1980s optical bistability in nonlinear materials was particularly appealing for all-optical modulation. However, such control was achievable only at large scales and high operating powers, which prevented the spreading of commercial systems. Later on, at the end of the 1990s, the onset of photonic crystals envisaged the possibility to scale down electromagnetic confinement, and in turn optical control, to dimensions smaller than the wavelength of light. However, the size of periodic structures hindered the design of compact devices operating independently at the nanoscale, as it is the case for electronic circuitry. Finally, the recent progress of both nanofabrication techniques and numerical tools triggered the emergence of all-dielectric nanoresonators, which provide a valuable alternative to tailor the properties of electromagnetic fields at the subwavelength scale.

This thesis deals with nonlinear optical generation from aluminum-gallium-arsenide (AlGaAs) nanoresonators, either isolated or arrayed, tackling the problem in all its different aspects, from modeling of nonlinear optics in open cavities to fabrication development of metasurfaces and their experimental characterization. The work reported in this manuscript was mostly carried out in the research group Dispositifs Optique Nonlinéaires (DON), within the laboratory Matériaux et Phénomènes Quantiques (MPQ) at Université de Paris, under the supervision of professor Giuseppe Leo. The DON group, which I had the pleasure to join in these three years of PhD, combines activities in optomechanics, metamaterials and nonlinear optics. Its competences and the facilities of the laboratory gave me the opportunity to develop all the three aspects required by this challenging field: theory, technology and optical measurement. I had the chance to personally fabricate the samples illustrated in this work, which originate from a well-established know-how acquired by the group during previous PhD theses, at the MPQ cleanroom with the precious support of Stephan Suffit and Pascal Filloux. Epitaxial growths were provided either by the C2N in Paris or the CEA in Grenoble. The experimental measurements were completely carried out in MPQ, on the optical setup that I built and improved in collaboration with Giuseppe Marino, postdoc of the group, who accompanied my work for all the three years and performed some of the measurement reported in the manuscript. The numerical models were developed either

within the group, by myself and G. Marino, or by external co-workers. Importantly, all the discussed results would not have been possible without the invaluable collaboration of external research groups, in particular LP2N in Bordeaux, University of Brescia, CEA in Grenoble, C2N in Paris, Stanford University and Politecnico di Milano. The knowledge acquired during the visits in Bordeaux, Brescia and Milan, together with the frequent fruitful discussions and exchanges have been of key importance in all the steps of this work.

The manuscript is organized as follows:

Chapter 1 provides a general introduction to the topic of optical nanoantennas, metamaterials and metasurfaces. It constitutes a brief review of recent advancements both in linear and nonlinear optics in order to provide a general context to this PhD work.

Chapter 2 introduces the theoretical framework of light-matter interaction at sub-λ scale and nonlinear generation in nano-objects. Starting from Maxwell equations, I will define the main concepts of extinction, scattering and absorption in the linear and nonlinear regimes. Then, I will introduce multipolar analysis for nanoparticles suspended in uniform media and its key features for efficient SHG in nanodisks.

In **Chapter 3** the same problem is revised with the formalism of quasi normal modes (QNM) in non-Hermitian systems. After a brief introduction of QNM framework, the study of nonlinear generation in leaky resonators is discussed in detail. The extension of QNM formalism to the nonlinear domain enables to identify and quantify the key figures of merit to achieve efficient nonlinear generation. This allows to evaluate the role of phase mismatch in nanocavities and the nonlinear modes overlap.

Chapter 4 provides the motivations for the material choice and technical details for the fabrication of nanodisks and metasurfaces. Furthermore, the experimental setup is presented together with nonlinear characterization of isolated nanodisks and uniform arrays. These results are discussed and compared to literature, in order to evaluate the role of optical coupling and far-field interference in nanoresonators arrays. Specifically, we demonstrate how homogeneous metasurfaces can be optimized to partially redirect SH emission into the zero-diffracted order and control SH polarization state.

Chapter 5 is devoted to nonlinear phase engineering. The topic is introduced discussing the differences between resonant and non-resonant approaches for beam shaping in linear metasurfaces. The pros and cons of both techniques are analyzed through numerical calculations, then I will propose a design protocol for SH phase engineering in AlGaAs nanostructures. Firstly, I face the problem of normal SH emission for on-axis applications. Then, based on an optimized asymmetric AlGaAs resonator, I will discuss the numerical modeling to extract a set building blocks sampling the SH harmonic phase in $[0, 2\pi]$. Finally

I will experimentally validate these predictions with three new devices: a $\chi^{(2)}$ meta-grating, a $\chi^{(2)}$ meta-lens and a $\chi^{(2)}$ hologram.

Chapter 6 reports the conclusion and provides some future perspectives.

For the sake of readability, I decided to divide the references and report them at the end of each chapter. The list of my publications and the list of abbreviations are reported after the appendices.

Abstract

In analogy with their RF counterparts, optical nanoantennas aim at transferring energy from free propagating radiation to localized sources and vice versa. In particular, strong light matter interaction at the nanoscale can boost nonlinear generation processes with efficiencies comparable to optically guided systems while revealing new phenomena with respect to bulk components. In this case the localized source is constituted by the intrinsic optical nonlinearity of matter as well as nanoantennas provide local field enhancement and control radiation properties at harmonic frequencies. During last decade, all-dielectric Mie resonators were proposed as an ideal candidate for harmonic generation due to high material refractive index, strong bulk nonlinearities and negligible ohmic losses.

This thesis work concentrates on the numerical modelling and experimental demonstration of second harmonic generation (SHG) from isolated or arrayed AlGaAs nanoresonators. The first part is devoted to the analysis of nonlinear generation processes in open-boundaries cavities through quasi normal modes formalism in non-Hermitian systems pointing out the analogies and differences with closed-cavities counterparts (e.g. micro-disks, micro-rings, etc. . .). Successively SHG is experimentally investigated in isolated AlGaAs Mie-resonators and in arrays of nanocylinders for the control of polarization, radiation pattern and power funneling into different diffraction orders. Finally, SH phase engineering with all-dielectric metasurfaces is discussed in detail. Design guidelines, numerical models and technological implementations are proposed for the case of AlGaAs metasurfaces on sapphire. These tools are experimentally validated for nonlinear beam steerers, meta-lenses and meta holograms offering new routes to the development of ultrathin photonic devices for nonlinear imaging.

Keywords

Nonlinear nanophotonics, nonlinear open-cavities, quasi normal modes, Mie-resonators, nonlinear metasurfaces, nonlinear phase engineering.

Résumé

Par analogie avec leurs homologues dans les RF, les nanoantennes optiques visent à transférer l'énergie de la propagation libre vers des sources localisées et vice-versa. En particulier, l'interaction forte de la lumière avec la matière à la nano-échelle peut stimuler les processus de génération non-linéaire avec des rendements comparables à ceux des systèmes guidés, tout en révélant des nouveaux phénomènes par rapport aux composants massifs. Dans ce cas, la source localisée est constituée par la non-linéarité optique intrinsèque de la matière et les nanoantennes fournissent une augmentation du champ local et contrôlent les propriétés de rayonnement aux fréquences harmoniques. Dans les dernières années, les résonateurs de Mie diélectriques ont été proposés comme un candidat idéal pour la génération d'harmoniques en raison de l'élevé indice de réfraction des matériaux, de fortes non-linéarités et de négligeables pertes ohmiques. Ce travail de thèse se concentre sur la modélisation numérique et la démonstration expérimentale de la génération de second harmonique (GSH) dans des nanorésonateurs en AlGaAs, isolés ou en réseau. La première partie est consacrée à l'analyse des processus de génération non linéaires dans les cavités ouvertes à travers le formalisme de modes quasi normaux dans les systèmes non hermitiens en soulignant les analogies et les différences avec les cavités fermées (ex: micro-disques, micro-anneaux, etc.). Successivement, la GSH est étudié expérimentalement dans des résonateurs de Mie en AlGaAs à la fois isolés et dans des réseaux pour le contrôle de la polarisation, du diagramme de rayonnement et de la canalisation de puissance dans différents ordres de diffraction. Dans la dernière partie on discute en détail l'ingénierie de phase du SH avec des métasurfaces diélectriques. Des directives de conception, des modèles numériques et des implémentations technologiques sont proposés pour le cas des métasurfaces de AlGaAs sur saphir. Ces outils sont validés expérimentalement pour les déflecteurs de faisceau non linéaires, les méta-lentilles et les méta-hologrammes en représentant de nouvelles solutions pour le développement de dispositifs photoniques ultra-fins pour l'imagerie non linéaire.

Mot-clés

Nanophotonique non-linéaire, Cavités non-hermitiennes, modes quasi normaux, metasurfaces, génération de seconde harmonique, nanoresonateurs de Mie, ingénierie de phase

Contents

Introduction 1

Contents

1.1 Elements of nanophotonics and metamaterials

One of the main objectives of optics is the control of light propagation and confinement. Progress in optics historically started with the development of bulky lenses and mirrors, then prisms and gratings, and so on. The improvement of these devices slew down as Abbe's diffraction limit was approached. Nanophotonics aims at manipulating electromagnetic (EM) waves at subwavelength scale to go beyond this limit. The recent evolution of fabrication technologies, numerical tools and theoretical models opened the way to novel devices with unprecedented performances.

Before getting to the main topic of this PhD thesis, we will briefly introduce some key concepts and review the latest advancements which enabled to shrink light at the nanoscale and improve current optical components. This will help to fix the historical framework and provide the motivations for this work.

Optical antennas

Any radio frequency (RF) communication can be summarized in the following way: an electric signal created by a transmitter is transferred to free radiation through an antenna; far from this source, another antenna optimizes the energy transfer to a receiver, which detects and processes the original signal. In that region of the spectrum, controlling and guiding EM waves is critical for a successful communication and it is almost exclusively achieved by engineering antennas geometry and properties.

This control plays a central role also in the optical regime ($\lambda \in [400-700]$ nm) for example for the development of telescopes, microscopes and spectrometers whose functions are usually implemented with mirrors, lenses and other diffraction elements. The reason that limited the development of optical antennas has mainly a technological origin. From the radiowave domain it is well-known that, in order to effectively transfer a localized signal to free radiation, an antenna should have sub-wavelength dimensions. In the optical regime this requires fabrication technologies with a resolution of tens on nm, which explains why their extensive development has only occurred in the last decades. As for their RF counterparts, optical antennas are defined as transducers which convert a freely propagating optical radiation into localized energy and vice-versa [1, 2].

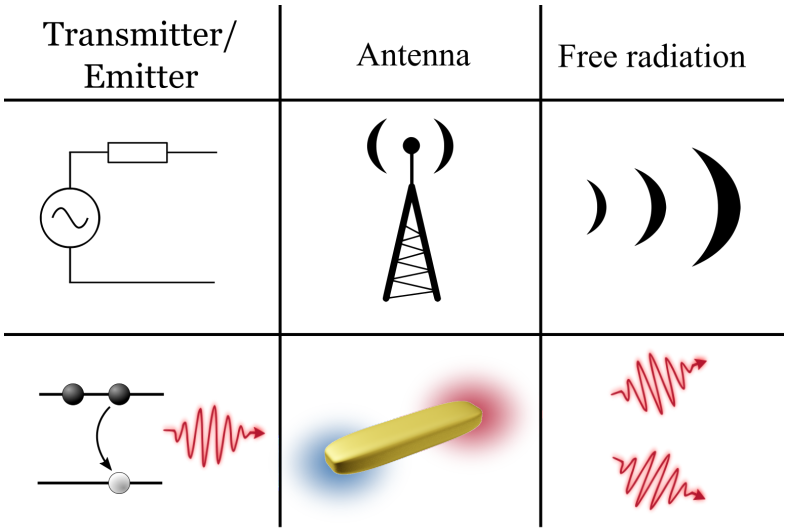

Figure 1.1: Role of antennas in different regions of the EM spectrum. Top: the RF signal created by a transmitter is coupled to free space through an antenna and vice-versa. Bottom: at optical frequency the radiative decay of a localized source (quantum dots, organic molecules, etc...) is enhanced by the presence of a nanoantenna.

Historically, the first optical antennas have been metallic nanoparticles (NPs). Pioneering theoretical investigations of light scattering by small particles were carried out by Lord Rayleigh at the end of 19th century [3]. When the size a of a NP is much smaller than wavelength λ, a quasi-static approximation can be adopted. Within this limit, the scattering by a NP has a purely electric-dipole character, which led among others to the explanation of the blue sky or the redness of sunset [4]. Following these studies, in 1908 Mie derived an analytical solution to Maxwell equations describing light interaction with spherical particles [5]. When $a \sim \lambda$, a complete multipolar nature of the scattering has to be considered. NPs can exhibit strong electric and magnetic response, revealing optical properties well beyond those of common materials.

In metals, a large amount of free (or conduction) electrons can be collectively excited by an external wave, resulting e.g. in light propagation at a metal-dielectric interface, called surface plasmon polaritons (SPP). The EM wave is confined in a sub-λ region close to the surface, overcoming the constraints imposed by diffraction limit. When a NP is excited by a low-frequency external field, conduction electrons are displaced with a negligible phase delay. As the frequency increases, such delay gets more and more pronounced, and when it reaches 90° the oscillation amplitude is maximum, as it happens for a spring-mass

system [6]. For many metals these resonances, usually termed as localized surface plasmon resonances (LSPRs), occur at optical frequencies, giving rise to peculiar effects as sub-λ EM field confinement or directional scattering [7, 8].

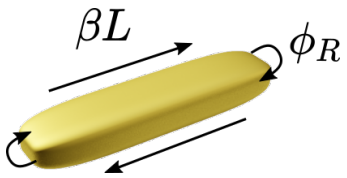

Figure 1.2: Fabry-Perot representation of a plasmonic nanoantenna. L is the nanoantennas physical length, β the propagation constant and ϕ_R the additional phase due to reflection at antenna edges.

In RF domain antennas' resonances are studied as Fabry-Perot oscillations which occur whenever the metallic wire length corresponds to a multiple of $\lambda/2$. When we scale down to the optical regime, reflection coefficients at the edges of the Fabry-Perot cavity become complex due to the polaritonic nature of the excitation. Since this additional phase term ϕ_R acts as an increase of antennas effective length, the relation between multiples of half resonance wavelength and geometrical length is no longer satisfied. LSPR can be therefore understood as SPP standing-wave phenomena [6, 9]. Taking a nanorod with length L (see Fig. 1.2), Fabry-Perot resonance condition can be recast in

$$\beta L + \phi_R = n\pi \tag{1.1}$$

with β the propagation constant of the oscillating mode inside the nanorod. One can get exactly to the same conclusion saying that when one of the antenna dimensions is comparable with the metal skin depth (i.e. the nanorod section), the incident radiation is no more perfectly reflected from the metal surface. Approaching the plasma frequency of the metal $f_p = c/\lambda_p$, free-electron gas oscillations are excited and the antenna perceives a shorter effective wavelength λ_{eff} than free space one λ. An empirical linear scaling law can be derived [10]

$$\lambda_{\text{eff}} = n_1 + n_2 \frac{\lambda}{\lambda_p} \tag{1.2}$$

where n_1 and n_2 are coefficients related to antenna geometry and material properties. Fig. 1.3a-c shows some typical nanoantenna geometries.

Rigorously speaking, NPs play the same role as RF antennas just when they are coupled with emitting molecules or quantum dots with strong effects on their radiative and nonradiative properties. In that case, EM confinement in small volumes (see Fig. 1.3a) increases the photonic local densisty of states (LDOS) which is responsible for the critical modification of emitters properties, as for example Purcell enhancement [14]. Usually the size of quantum emitters (QE) is much smaller than free-space wavelength, which leads in turn to a strong mismatch between the electronic confinement length and radiation wavelength. Then the impedance matching favored by plasmonic antennas boosts light coupling between free space and localized modes, increasing quantum yield, reducing lifetimes and consequently non-radiative losses. A typical example of organic dyes interacting

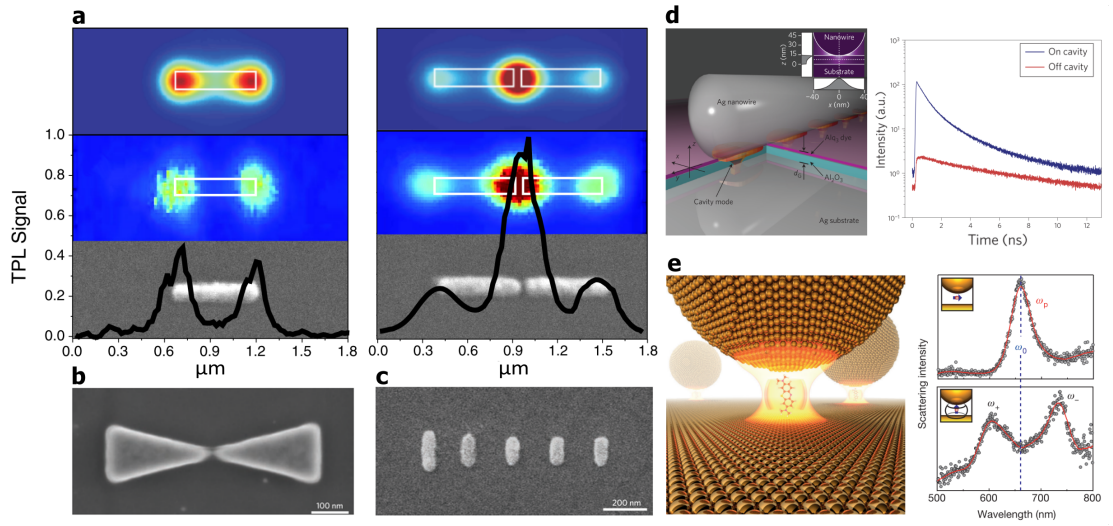

Figure 1.3: Some examples of plasmonic antennas. a) Two-photon luminescence from single (left) or coupled (right) nanorods. From top to bottom: theoretical prediction, experimental measurement and SEM image [11]. b,c) Examples of bow-tie (b) and Yagi-Uda (c) antennas [1]. d) Spontaneous-emission enhancement from a fluorescent organic dye (pink slab) weakly coupled to an Ag nanowire (grey rod). The rightmost figure shows the intensity time decay with (blue) or without (red) the plasmonic cavity [12]. e) Strong coupling between methylene-blue molecule and a metallic nanoparticle on mirror [13].

with a plasmonic nanoantenna is shown in Fig. 1.3d, which highlights the fluorescence enhancements of cavity-coupled emitters. The related coupling strength is described by the so-called Rabi frequency Ω_R. When Ω_R exceeds the damping losses of the NP, which are usually the leading term due to the strong dissipation of metals [15], the energy is periodically transferred between the emitter and the photonic cavity before being lost by radiation or thermalization. The two oscillators are said to be strongly coupled, leading to the emergence of mixed resonant states at different frequencies compared to those of the unperturbed nanoantenna and emitter, see Fig. 1.3e [13]. All these effects triggered many investigations in several fields [8, 16], ranging from efficiency and directional control in light-emitting diode technology to light trapping in solar cells and molecular sensing. In the latter case, optical hotspots enhance Raman scattering signals, promoting the development of surface-plasmon enhanced Raman spectroscopy (SERS).

Metamaterials

In optics the manipulation of electromagnetic fields is usually achieved through the modulation of permittivity ε. The refractive index $n = \sqrt{\varepsilon}$ for most bulk dielectrics ranges between 1 and 4 in the visible/near IR. An option to extend the control possibilities is the fabrication of compact arrays of resonant elements with engineered properties. In this sense the strong electric and magnetic response of NPs are attractive to create new materials with effective optical properties out of the common intuition. Indeed, when NPs are arranged in a lattice with periodicity a much lower than their resonating wavelength λ_0, or equivalently when the resonance frequency ω_0 of the particles is much lower than the first Bragg resonance of the lattice $\omega_B = \pi c/a$, spatial dispersion can be neglected and the array can be treated as an homogeneous material with effective permittivity ε_{eff} and permeability μ_{eff}. The homogenization problem is largely discussed in literature, and the

reader is referred to review [17] for a detailed treatment.

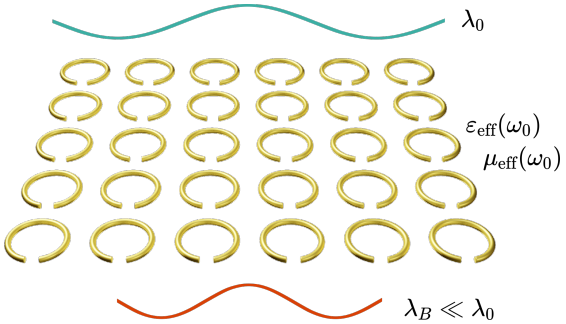

Figure 1.4: Schematic of a two.dimensional (2D) metamaterial composed by SRRs, whose resonance wavelength λ_0 is much larger than Bragg wavelength λ_B.

Non-magnetic conducting sheets can for example exhibit an effective permeability $\mu_{\text{eff}} \neq 0$, with values not available in natural materials [18]. For this ability to extend the range of natural bulk material properties, these artificial structures are referred to as metamaterials. Striking electrodynamics effects offered by negative permittivity and permeability, as negative refraction, reversed Doppler and Cherenkov effects, were already pointed out in 1968 by Veselago [19]. In 2000, Pendry proposed a lens with a focusing resolution not limited by the light wavelength [20]. One of the most studied metallic systems with strong magnetic response is the split-ring resonator (SRR), see Fig. 1.4, which experimentally proved to be an ideal candidate as building block for periodic arrays with both $\varepsilon_{\text{eff}} < 0$ and $\mu_{\text{eff}} < 0$, usually referred to as Negative Index Materials (NIM), at microwaves [21, 22]. These artificial materials paved the way to the field of transformation optics [23] and led for example to the demonstration of gradient index metamaterials [24] and electromagnetic cloaking [25]. Scaling down these structures to optical frequencies is quite challenging both from the fabrication point of view and for the closer distance to plasma frequencies of the materials. Different strategies have been proposed, which often rely on metal-insulator-metal (MIM) structures like waveguides [26–29] or fishnet metamaterials [30].

From metals to dielectrics

As seen above, inducing a magnetic response in plasmonic nanostructures at optical frequencies can be extremely challenging. Furthermore, it is true that plasmonics can enhance the EM field at the nanoscale, overcoming the diffraction limit and increasing the LDOS to boost Purcell effect. However, all these opportunities come at a price: rather than being periodically transferred between electric and magnetic fields as in photonic cavities, energy is stored in the motion of free electrons (kinetic energy) and thus mostly lost due to absorption. Differently from mid-IR, where metallic losses are manageable, for operations at optical frequencies in which efficiency matters, as light emission, harvesting and nonlinear generation, these losses constitute a big problem [31].

A valuable alternative for some applications is represented by high-index dielectric resonators. Indeed when the characteristic size d of a dielectric nanoparticle is comparable with the wavelength λ in the medium ($d \sim \lambda/n$ with n the refractive index) the magnetic and electric responses have comparable contributions to the scattering. Technological

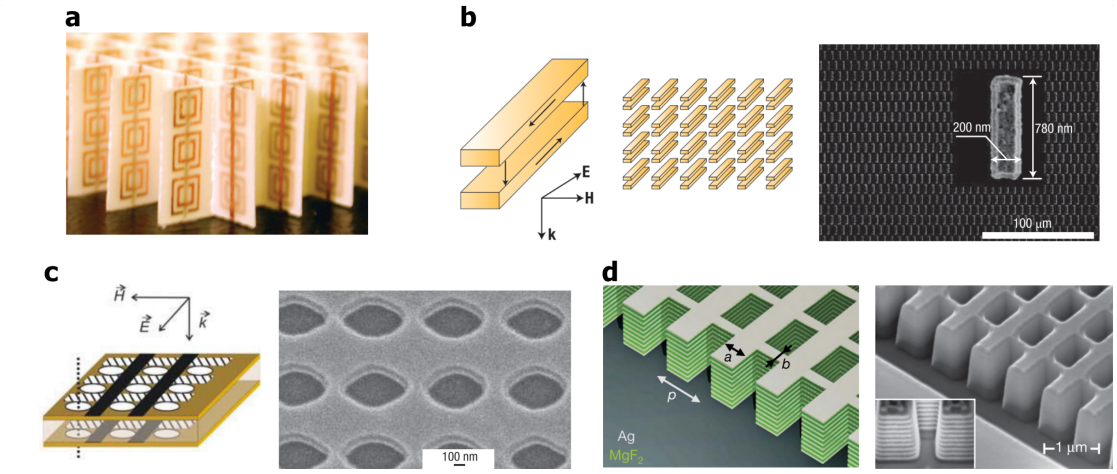

Figure 1.5: Some examples of metamaterials. a) Left-handed metamaterial made of square copper SRR, used to demonstrate negative refractive index in the microwaves [22]. (b) Double periodic arrays of parallel gold nanorods exhibiting negative refractive index at optical frequencies [27]. (c) First demonstration of negative refractive index in the near-IR with a dielectric-metal multilayer made of two nanostructured gold films separated by a thin sapphire layer. (d) Fishnet metamaterial exhibiting negative refractive index at telecom wavelengths. The SEM image reports 21-layer fishnet structure alternating layers of 30 nm silver and 50 nm magnesium fluoride [30].

progress during the last decade enabled the fabrication of sub-λ high-index dielectric resonators that overcome the dissipative limitations of their plasmonic counterparts and also offer new opportunities associated to near-field enhancement, longer exciton lifetimes and semiconductor doping control for active devices.

At variance with metallic NPs, the origin of these resonances in dielectrics is related to oscillating displacement currents rather than free electrons, and the first appearing resonance when size parameter $x = dn/\lambda \approx 1$ is a magnetic dipole. A schematic comparison between the generation of a magnetic dipole in a metallic SRR and in a dielectric nanoparticle is sketched in Fig. 1.6a [32]. In the latter, the local field enhancement is lower than in the former; however, the larger mode volume and negligible losses make dielectric NPs attractive for several applications, as will be shown below. The predictions on magnetic dipole driven scattering at optical frequencies from silicon particles [36] were almost simultaneously demonstrated by two groups in 2012 [32, 37]. Increasing the NP refractive index, the spectral position of different resonances remains set by the size parameter x but the scattering efficiency increases, see Fig. 1.6b [38]. This basically means that the effective interaction surface (cross-section) between an external plane wave and the NP increases with n and the resonator is more efficient in localizing free-radiation in the near field.

Local field enhancement combined with low thermal losses was exploited to generate electric and magnetic hot spots in nanodimers [39], enhance Raman signal with low heat conversion [40, 41] and demonstrate non-plasmonic nanolasers [33], see Fig. 1.6c. The different peaks in Fig. 1.6b give a visual intuition on the highly multimodal nature of scattering in dielectric NPs. Nonresonant interference of Mie modes motivated several studies on directional control and non-radiative states. The former is based on the notion that whenever two resonances with opposite parities are excited with the same amplitude but opposite phase, backward scattering is suppressed. This effect was already predicted by Kerker in 1983 [42]. Zero backward scattering condition was demonstrated at optical

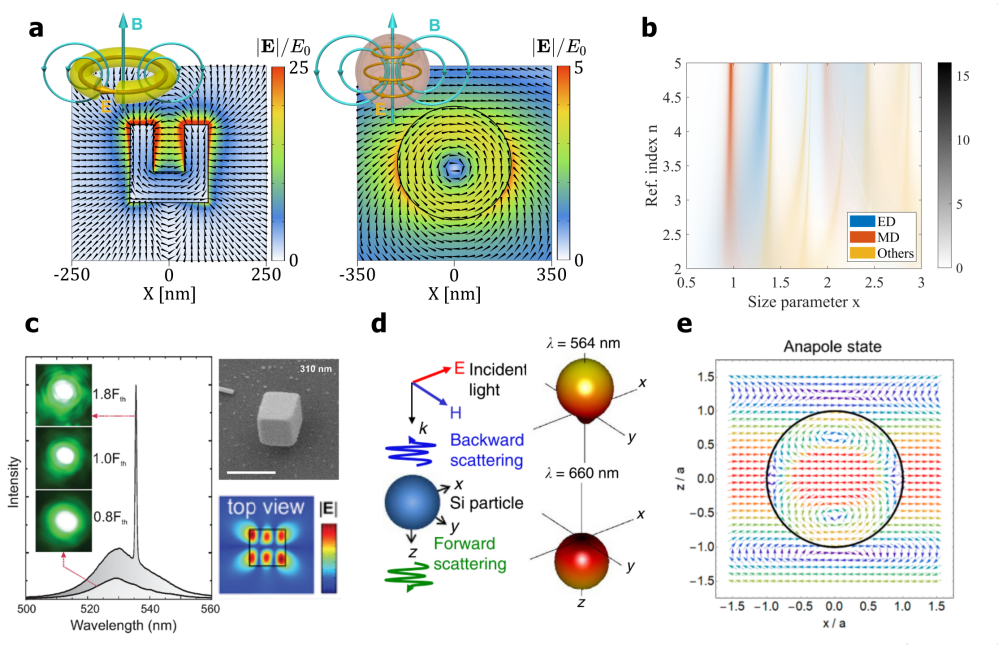

Figure 1.6: Mie scattering by dielectric nanoparticles. (a) Electric near-field enhancement at telecom wavelength in a gold SRR (left) and silicon nanosphere (right), exhibiting a magnetic dipole response. Inset: sketch of electric and magnetic fields close to a magnetic dipole resonance [32]. (b) Scattering efficiency vs dielectric nanosphere size parameter $x = 2rn/\lambda$ and refractive index n: blue (red) shaded areas correspond to electric (magnetic) dipole resonances; the yellow region sums up all the contributions with higher orders. (c) $CsPbBr_3$ halide perovskite nanocubes supporting Mie resonances, used to demonstrate lasing at visible frequencies [33]. (d) Directional scattering by a Si nanosphere. On the right, the far-field diagrams at 564 nm (top) and 660 nm (bottom) demonstrate backward to forward switched emission [34]. (e) Electric near-field distribution in a dielectric sphere supporting an anapole state: the internal anapolar field cannot satisfy the condition of continuous tangential field on the sphere surface if external field is removed [35].

frequencies with Si [34] and GaAs [43] spherical NPs combining magnetic- and electric-dipole resonances. The almost symmetric condition, minimization of forward scattering (as complete canceling would violate optical theorem), can be also achieved, see Fig. 1.6d.

Similarly, nonresonant interference can result in nonzero internal field with a null far-field scattering. Fig. 1.6e shows a plane wave whose propagation is not perturbed by the presence of a dielectric nanosphere, even though the object is polarized: this situation is an anapole state, which can lead to a strong field confinement without radiation losses [35, 44]. Lorentz reciprocity is not violated as the anapole is not an eigenmode of the system, conversely its existence strictly relies on the presence of an external excitation, and as soon as this is removed the anapole state is lost [35].

Differently from nonresonant approaches, strong field enhancement can be achieved through coupling of modes with similar far-field patterns. Tuning the geometrical parameters of the nanocavity, two Mie resonances radiating in the same direction can destructively interfere producing a mode with suppressed radiation losses, called bound state in the continuum (BIC) [45]. This situation can appear as an anticrossing in the dispersion curves of two modes. Mathematically, a perfect BIC mode cannot be excited via free radiation, as this would violate Lorentz reciprocity, and in a scattering experiment it can be considered as a resonance with zero linewidth. Instead, it can be excited by local emitters or through nonlinear effects. Physically, it is interesting to study the case of weak losses, referring to it

as a quasi-BIC with a high quality factor. Again, Lorentz reciprocity imposes that coupling free radiation with this mode is very inefficient, nonetheless the possibility to excite high-Q modes in leaky subwavelength cavities remains interesting for several applications, e.g. for nonlinear optics as it will be addressed in the following [46].

1.2 Motivations

After the first demonstration of second harmonic generation (SHG) by Franken et al. in 1961 [47] and the theoretical investigations on wave mixing by Bloembergen et al. in 1962 [48], the possibility to induce a nonlinear optical response in materials held promises to reproduce logic operations with photons as in electronic transistors, i.e. to *control light with light* via ultrafast all-optical switching [49, 50], as well as for many other applications ranging from harmonic and supercontinuum generation, Raman scattering, generation of ultra-short pulses [51] to quantum optics [52] and nonlinear imaging[53].

For several years the quest for integrated optics motivated the development of waveguide-based photonic circuits [54], as ring resonators [55], slot waveguides [56] and photonic crystals [57, 58]. In parallel to the progress in these fields, recent advancements in nanophotonics opened up to nanoantennas, as a valuable alternative to scale down nonlinear optical devices. In the following, we will review some of the most significant works that have drawn the attention of the scientific community on this field and motivated this PhD thesis. We provide here below just the general context and possibilities offered by nonlinear nanophotonics, deferring the detailed description of nonlinear generation to Section 2.3 of Chapter 2.

Nonlinear nanophotonics

As the integration of modern electronic devices started to experience a saturation due to fundamental limitations in speed and bandwidth, the perspective of replacing them with their photonic counterparts appeared as very promising. Nevertheless, the diffraction limit of light represented a huge constraint for the miniaturization and integration of photonic circuits. The development of plasmonic nanostructures promoted by nanofabrication progress represented a first favorable way to overcome this limitation [1, 59]. Besides, the strong field enhancement achieved with metallic nanoresonators in a small mode volume triggered a plethora of solutions to reveal nonlinear optical phenomena that require high intensity fields [60]. LSPRs can be tuned adjusting NP geometrical parameters in order to enhance third-order nonlinear effects, which are always present in all materials.

Fig. 1.7a shows how four-wave mixing (FWM, see Section 2.3) [61] can be enhanced by tuning the distance between two gold nanospheres. Similar results were reported in literature for third harmonic generation (THG) [62, 63], and Fig. 1.7b displays the variation of THG signal with geometrical parameters of a linear gold antenna.

The third-order susceptibility of metals was also exploited to study the modulation of ultrafast optical response of a NP. Fig. 1.7c reports the extinction cross section variation of a

gold nanorod in a pump-and-probe experiment. When a pump beam excites electrons by intra- or interband absorption, the stimulated Kerr-type nonlinearity modifies both real and imaginary parts of the permittivity. When the probe wavelength is tuned with the LSPR, the detected decay time of extinction signal is significantly reduced. In a similar way, plasmonic nanoantennas can be used for ultrafast all-optical control. Fig. 1.7d reports the modulation of the extinction signal from a linear antenna embedded in indium tin oxide (ITO) under picosecond pump beam excitation. Hot-electron injection from gold nanoantenna enhance the large free-carrier nonlinearity of ITO, which in turn modifies the plasmonic resonance. This double mechanism produces a large modulation of the antenna dipole resonance at a picosecond timescale.

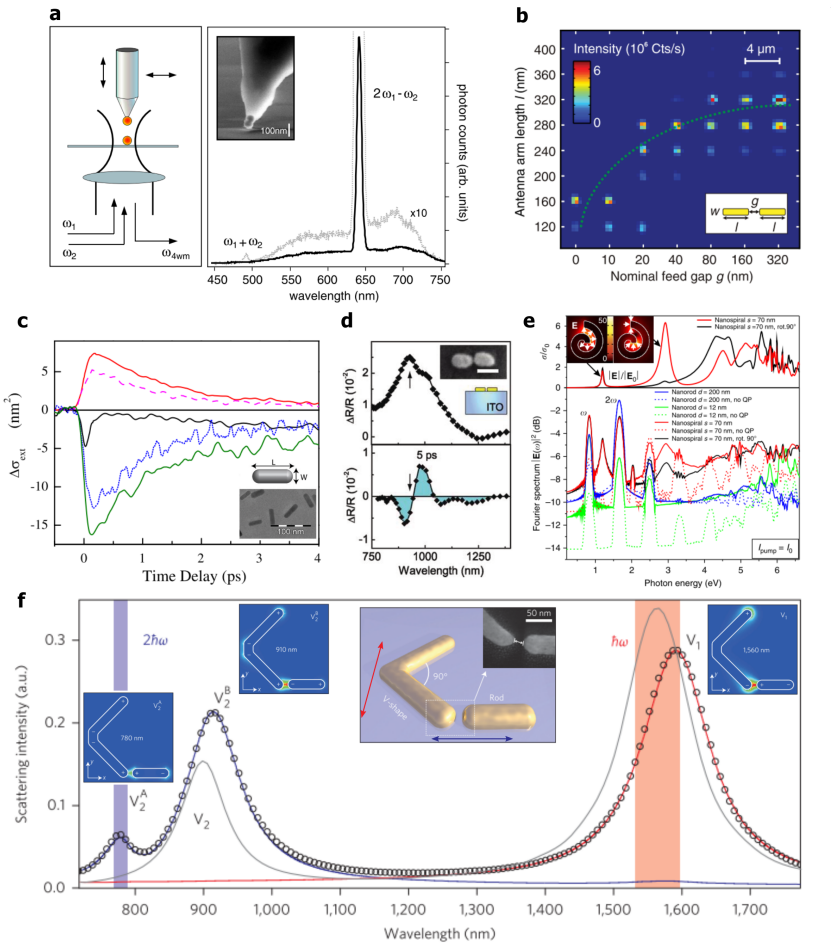

Figure 1.7: Nonlinear generation in plasmonic nanoparticles. (a) FWM from two coupled gold nanoparticles. One of the two NPs is attached to an optical fiber which enables to tune their relative position. On the right, FWM spectrum [61]. (b) THG from two gold nanorods (see inset) vs. their relative position and length. [63]. (c) Ultrafast all-optical modulation of extinction cross section of plasmonic nanorods. A pump beam excites electrons by interband absorption and a probe monitors the change of sample transmission. The five curves report the result for different probe wavelengths [64]. (d) All-optical control in plasmonic nanodimers on ITO. Extinction (top) and fast nonlinear response (bottom) probed 5 ps after the pump modulation [65]. (e) Supercontinuum generation in metallic nanospirals. Top: extinction cross section of two spirals with different orientations. The inset reports the near field distribution in correspondence of two main resonances at low frequencies. Bottom: nonlinear spectra for different geometrical parameters [66]. (f) Nonlinear mode matching in plasmonic resonators. Total linear scattering spectra of a V-shaped antenna, either isolated (gray line) or coupled to a nanorod (black circles). Red (blue) area highlights resonances at pump (SH) frequency. The red and blue lines report the linear scattering for two different input polarizations [67].

A different framework has to be set for quadratic nonlinearity. As it will be shown in Section 2.3, second order nonlinear processes are possible only in non-centrosymmetric materials within electric-dipole approximation of light-matter interaction. As most metals are organized in face-centered cubic lattices, SHG should be inhibited by symmetry. However in nanoplasmonics this constraint is relaxed for two reasons: 1) treating conduction electrons as a free gas in a hydrodynamic model [68] makes a quadratic bulk contribution appear, which arises from higher-order nonlocal magnetic-dipole and electric-quadrupole interactions; and 2) the symmetry condition is broken at interfaces. Based on a hydrodynamic description, higher harmonics and supercontinuum generation from metallic nanospiral was demonstrated, see Fig. 1.7e. For SHG, symmetry breaking was proved both with metamaterials [69] and isolated particles [67]. In the former case [70] the spatial ordering of meta-atoms results in a modification of plasmonic resonances by long-range coupling. Arranging the same meta-atoms in different configurations, the nonlinear response can be enhanced up to a factor 50. In the latter case, gold nanostructures with no axial symmetry were designed to maximize mode spatial overlap at pump and second-harmonic (SH) frequencies [67]. In Fig1.7f, the linear spectral response of the nanoparticle exhibits two peaks around 1550 nm and 775 nm for two different input polarizations (red and blue curves). This resonant behavior boosts SH conversion efficiency up to 5×10^{-10} W^{-1}. Better performances were reported by tuning the interference of gold nanoparticles so as to obtain resonances at pump and SH frequencies, which led to a measured conversion efficiency of 4×10^{-7} W^{-1} [71].

Nevertheless, ohmic losses, heating and low damage thresholds, which were announced to be possible limitations of plasmonic NPs in the linear regime, are even more dramatic for nonlinear optics, where high intensity fields are required. This limitation, combined with a substantial advancement in semiconductor fabrication technologies, pushed the interest of scientific community towards all-dielectric alternatives [72]. Indeed high-refractive index semiconductors as Si, Ge, AlGaAs and GaP combine very low, or even zero, absorption losses in the near-IR range with strong optical nonlinearities. Furthermore, differently from plasmonic nanostructures that generate hot spots close to the interfaces with very small mode volumes, in dielectrics the electromagnetic field is concentrated inside the nanoparticle volume. This condition is particularly favorable for nonlinear optics, as it enables to exploit the strong bulk nonlinearities of the material.

Silicon nanoantennas were the first to be investigated, partly thanks to a more mature technology and a third-order nonlinearity $\chi^{(3)}_{Si} \sim 2.45 \times 10^{-19}$ m^2/V^2 [73] of the same order of gold ($\chi^{(3)}_{Au} \sim 2 \times 10^{-19}$ m^2/V^2 [74]). The excitation of a magnetic resonance in periodic arrays of Si nanodisks in the near-IR enabled to enhance THG by two orders of magnitude with respect to bulk silicon slab [75]. The higher near-field enhancement achieved with a magnetic- rather than an electric-dipole response is displayed in the inset of Fig. 1.8a. The same figure shows that resonances at pump frequency boost nonlinear generation as it appears when one compares the linear scattering in the near-IR with the corresponding THG spectrum in the visible. A conversion efficiency of 10^{-7} was demonstrated with Si disks arrays. Better performances were obtained with germanium, whose larger $\chi^{(3)}$ resulted in a conversion efficiency in the near-IR more than 10 times higher than Si [76], with a pump intensity of 15 GW/cm^2. In this spectral range, Ge absorbs both at pump and TH. Nevertheless, combining the high internal energy storage of an anapole state (Fig. 1.8b) with

very low aspect ratio geometry, a conversion efficiency of 10^{-6} was demonstrated. In analogy with plasmonic NP, Kerr-type nonlinearity can also be used for ultrafast modulation. A 65 fs all-optical switching was demonstrated with magnetic dipole excitation in Si nanodisks, see Fig. 1.8c, which offers another all-dielectric alternative together with photonic crystals [77] for all-optical control. Increasing the quality factor of resonances through collective Fano effects in Si nanoparticles arrays [78] proved to enhance THG by one order of magnitude (1.2×10^{-6}) with a slower switching time (490 fs). Fast TPA contribution in nonlinear response is attractive for optical self-action effects, but it also constitutes a limitation of SOI platform when working at high intensities. Ref. [79] reports a maximum pump intensity of 5 GW/cm$^{(2)}$ before the onset of saturation due to free-carrier absorption.

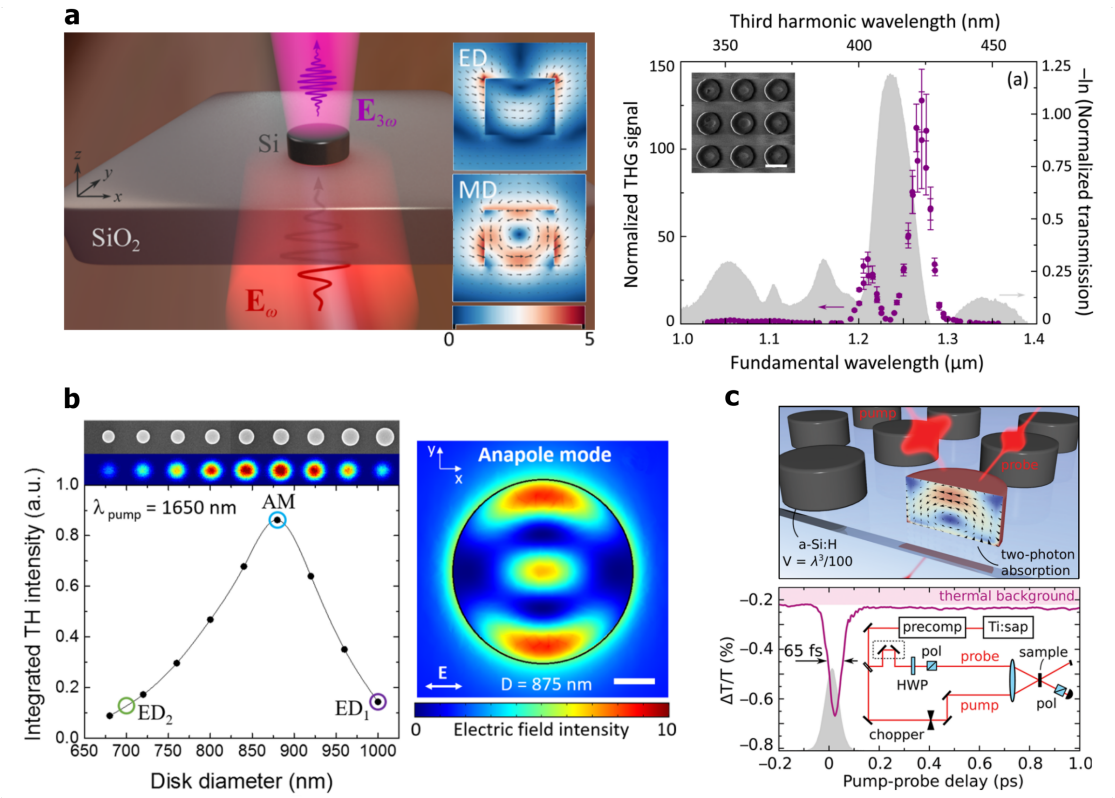

Figure 1.8: THG from dielectric NPs. (a) Left: Sketch of THG from an isolated Si nanodisk. Inset: electric near-field in correspondence of a electric- or magnetic-dipole resonance. Right: THG spectrum from Si nanodisks arrays. The gray area shows the linear extinction, purple dots the measured TH signal [75]. (b) THG from germanium nanodiks in the presence of an anapole state excitation. Left: TH signal for different disks diameters. Inset: SEM images and TH intensity maps. Right: near-field distribution at anapole condition. [76]. (c) Ultrafast modulation in Si nanodisks, with refractive index modulated through TPA with a Ti:sapphire pulsed laser [79].

In this respect, III-V semiconductor alloys as GaAs [80], AlGaAs [81, 82] and GaP [83], as well as lithium niobate [84] and transition-metal dichalcogenides [85, 86] combine the advantages of a high-refractive index with no TPA in the near-IR with non-centrosymmetry, which enables second-order nonlinearity (see Section 2.3).

My PhD thesis focused mainly on AlGaAs nanoresonators for SHG. The seminal paper by Carletti et al. in 2015 [87] predicted that the strong electromagnetic field enhancement induced by a magnetic-dipole resonance in an air-suspended AlGaAs nanodisk could boost SHG efficiency up to 10^{-3} in the near-IR with a pump intensity of 1 GW/cm^2. (100)-epitaxially growth AlGaAs was identified as a first promising candidate thanks to the

strong GaAs quadratic nonlinearity ($\chi^{(2)}_{GaAs} \sim 2 \times 10^{-10}$ m/V), the possibility to tune the material bandgap with Al concentration, and the robust (100)-GaAs technology compatible with optoelectronic devices. $Al_{0.18}Ga_{0.82}As$ was proposed as a good compromise to work in TPA-free regime with a pump at telecom wavelength, while preserving a $\chi^{(2)}$ almost as strong as for GaAs [88]. The presence of two resonances in the linear extinction spectrum of the nanodisk, at pump and SH frequencies, is a keypoint to maximize SHG (see Fig. 1.9a). Those predictions were confirmed by theoretical investigations on Mie modes selection rules for the ideal case of air-suspended nanospheres [89]. In 2016 three independent experimental works [80–82] validated this model demonstrating SHG efficiency as high as 8.5×10^{-5} with a pump intensity of 7 GW/cm^2 [82], see Fig. 1.9b-d. The fulfillment of magnetic-dipole excitation is detected as a peak in SH signal, shown in Fig. 1.9b, when varying the nanodisk radius. The discrepancy of about 2 orders of magnitude with the first theoretical expectations are partly due to the presence of a substrate, which reduces the modes quality factor, and the reduced collection angle of microscope objectives. As displayed in back-focal plane characterization in Fig. 1.9c, the SH harmonic radiation pattern of a nanodisk reveals a zero at normal emission and two lobes at large angles, due to the selection rules imposed by the system symmetry [89].

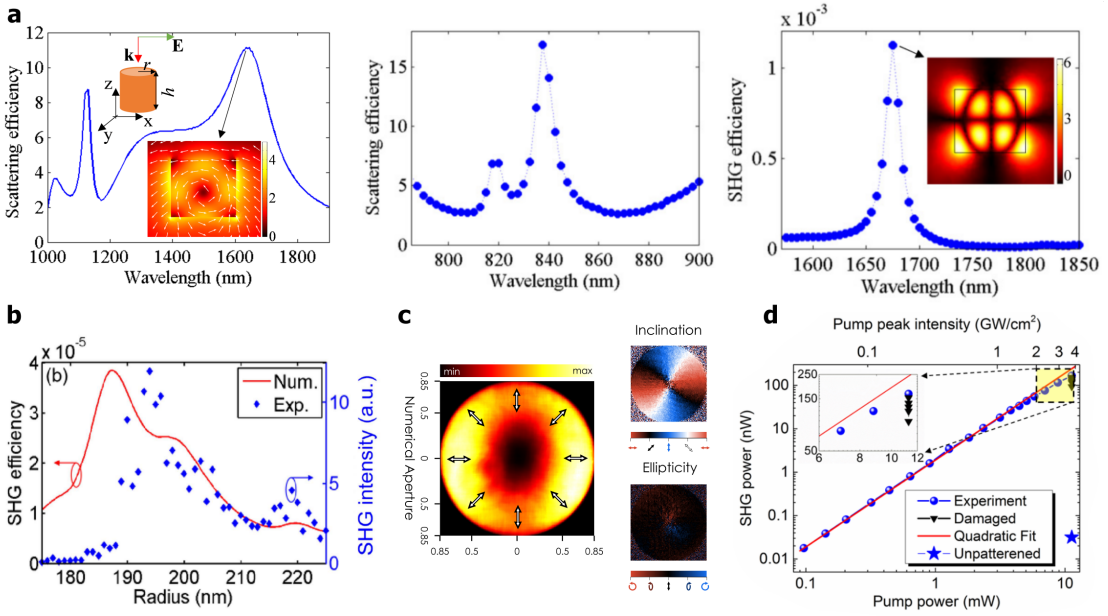

Figure 1.9: SHG in all-dielectric nanodisks. (a) Theoretical prediction of SHG in an AlGaAs nanodisk with 400-nm height. From left to right: linear scattering spectrum around pump wavelength, linear scattering around SH wavelength and SHG efficiency. Insets: electric field distributions in correspondence of main resonances [87]. (b) Numerically computed (red line) and experimentally measured (blue dots) SHG in AlGaAs nanodisks with different radii [90]. (c) Back focal plane SH intensity (left) and Stokes parameters (right) from an AlGaAs nanodisk in forward direction [82]. (d) Relation between SHG and pump power in GaAs nanodisks [80].

These pioneering results inspired a multitude of following works, which we can divide in two categories: some aimed at maximizing the conversion efficiency inside the nanocavity and others at controlling the emission properties in terms of SH polarization and radiation pattern.

SHG enhancement. SHG optimization in dielectric nanocavities motivated the development of different strategies and technological platforms. The excitation of a magnetic dipole in

nanodisks was primarily interesting for the strong field confinement inside the resonator volume. The same concept was developed by maximizing the internal energy through the interference of nanocavity modes with suppressed radiation losses. This anapole-state condition was achieved in single nanodisks [91], symmetric [92] and asymmetric [93] dimers as well as in hybrid plasmonic-dielectric nanoparticles [94]. In the best case, the anapole excitation at pump frequency resulted in a SHG efficiency of 1.9×10^{-5} for an incident intensity of $1\,\mathrm{GW/cm^2}$ [91] which is comparable with the results obtained with magnetic dipole excitation. This relatively modest outcome is explained by the small efficiency in exciting the interference of two modes leading to the anapole state through external free radiation.

Compared to microcavities, Mie resonances in all-dielectric spheres with small size parameter $x = nd/\lambda$ exhibit significantly lower quality factors ($Q \sim 10$), which limit SHG efficiency. As anticipated in Section 1.1, it seems more intriguing to look for a resonant mode with negligible radiation losses (i.e. with a high quality factor), as quasi-BIC mode. These optical bound states within the continuum of radiation modes were predicted in dielectric nanocavities, stemming from the coupling of two modes that are approximately orthogonal inside the resonator and destructively interfering outside [95, 96]. Theoretical investigations of supercavity modes for nonlinear generation anticipated a two-order-of-magnitude SHG enhancement from AlGaAs nanodisks with respect to magnetic-dipole configuration[97]. Very recently a quasi-BIC resonance with quality factor ~ 188 has been experimentally demonstrated, with SHG efficiency of $1.3 \times 10^{-6}\ \mathrm{W^{-1}}$[98], of the same order of the record value for magnetic-dipole-driven SHG ($6 \times 10^{-6}\ \mathrm{W^{-1}}$ [82]). This somehow disappointing outcome can be explained by the difficulty in coupling free-space excitation to an optical bound mode with very low radiation losses. Nevertheless, high Q-factor modes, in analogy with nonlinear generation in microcavities, remain the most promising solution to boost SHG efficiency in dielectric nanoparticles. These considerations will be pushed forward in Chapter 3, by developing a modal theory for nonlinear generation in non-Hermitian systems. Finally we acknowledge the possibility to enhance nonlinear generation through topologically protected states. This approach is gaining a growing interest in the scientific community, but it goes beyond the scope of the present work. We refer the interested reader to thematic reviews [99].

SHG control. Fig. 1.9 highlights two key features of SHG in (100)-AlGaAs nanodisks: 1) the possibility to create different SH polarization states, and 2) null on-axis emission for normal incidence.

The first feature is evidenced by Stokes parameters in Fig. 1.9b. The excitation of a main magnetic or electric response at SH by rotating input polarization was shown as an efficient control mechanism on SH polarization state [100–102]. SH polarization control in isolated and consequently arrayed nanoparticles will be discussed in Chapter 4.

The second feature constitutes a severe limitation when working with small numerical apertures or when an on-axis response is required. Breaking this constrain with a tilted excitation [103] was proven to enhance SH collected power by over one order of magnitude [104]. More recent works suggested the possibility to overcome this limitation by using either a different AlGaAs epitaxial growth as (110) or (111)-oriented AlGaAs [105], or asymmetryc AlGaAs nanoresonators [106], or different crystalline structures as Wurzite

instead of commonly developped zincblende epitaxial structure [107]. This topic will be treated more in detail in Chapter 5.

Nonlinear metasurfaces

As mentioned above, 2D arrays of nanoparticles can be used to break symmetry constraints for nonlinear generation [70] and excite collective modes. When the latter results in peaked scattering features like Fano [108–110] or BIC resonances [96, 111], nonlinear effects at the nanoscale can be enhanced. Such feature can scale down and improve the performances of bulk devices, with the aim of optical integration and ultra-fast response.

Alternatively, the same building blocks can be used to locally engineer amplitude and phase of nonlinear generation with features that are unavailable with bulk optics due to phase matching constraints. In the following we will refer to these devices as nonlinear metasurfaces.

Linear metasurfaces offered attractive solutions to scale down optical devices as lenses, spatial light modulators, blazed gratings and so on. In the late 60s it was already demonstrated how, adjusting the position of inclusions in aperiodic gratings, light could be deflected into desired directions [112]. This idea, called detour phase, was at the origin of first computer generated holograms (CGHs). A different approach derived from the investigations in the 50s by Pancharatnam [113] on the propagation of elliptically polarized waves in absorbing biaxial crystals, and later generalized by Berry in the 80s [114]. The Pancharatnam-Berry, or geometrical, phase difference between two positions relies on metasurface elements orientation. Finally, in the late 90s, the acquisition of different phase delays in single-mode waveguides at subwavelength scale was demonstrated [115]. All these methods can be implemented through non-resonant elements. During the last decade, the resonating approach for phase engineering gained a growing interest, due to the development of fabrication technologies enabling to pattern sub-λ structures. In this case, either the geometric-phase approach was extended to resonating elements, or the phase acquired by scattered light from resonating nano-objects was exploited. I will compare resonant and non-resonant approaches in Chapter 5.

Nonlinear beam shaping in an embedded device requires strong field enhancement, and consequently resonances, for an efficient generation. The development of nonlinear metasurfaces followed the same technological evolution of isolated nanoantennas. In 2015, Li et al. extended the concept of geometrical phase to harmonic generation in plasmonic metasurfaces [116], see Fig. 1.10a. The phase of circularly polarized THG beam depends on the orientation of plasmonic nanorods. Successively in 2016, Almeida et al. demonstrated TH holography with plasmonic metasurfaces (Fig. 1.10b) based on the idea that a change of nanostructures size impacts the resonances at pump frequency and, consequently, the phase of TH signal.

In dielectrics, the presence of a large number of modes at harmonic frequencies makes the design more complex, due to the interplay of several resonances when the nanoresonators size is changed. Wang et al. proposed in 2018 a set of silicon nanocyliders which balances multipoles with opposite parities to achieve unidirectional scattering, as predicted by

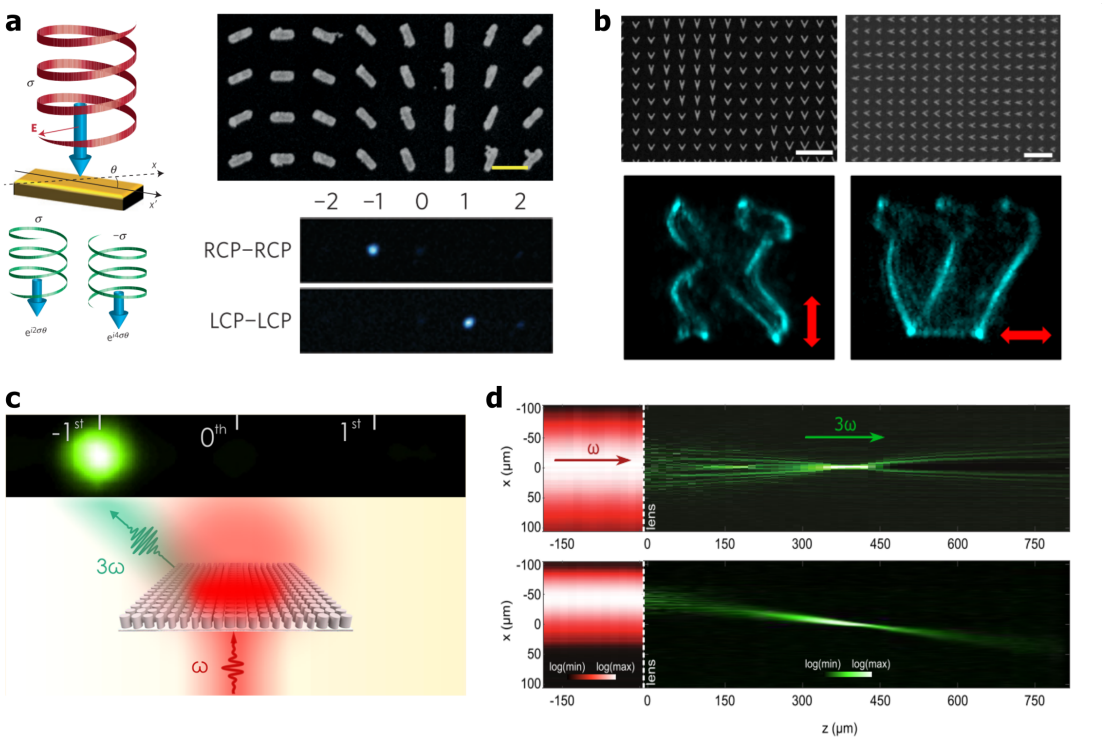

Figure 1.10: Beam shaping with nonlinear metasurfaces. (a) TH geometrical phase control with gold nanorods. The SEM image shows a metasurface for beam steering. On the bottom-right experimental measurements for a right circularly polarized (RCP) deflecting RCP TH beam to the 1-diffraction order, and a left circularly polarized (LCP) beam deflecting LCP TH beam to the -1-diffraction order [116]. (b) TH holography with gold double-layered metasurfaces. Switching from vertical to horizontal input polarization the Hebrew letters Alef and Shin are reproduced [117]. (c) All-dielectric silicon metasurface steering the TH beam into the first diffraction order [118]. (d) $\chi^{(3)}$ Fresnel lens allowing to study lens equation in the nonlinear regime [119].

first Kerker condition [120]. The extension of Huygens' condition to THG was adopted to demonstrate nonlinear beam steering in all-dielectric metasurfaces, see Fig. 1.10c. Finally, nonlinear metasurfaces enabled to generalize the classical study of object imaging to the nonlinear regime, which is hardly achievable with bulk optics [119], see Fig. 1.10d. These works hold promises for the development of nonlinear imaging devices, yet a clear solution for SH phase encoding seems missing to date. In Chapter 5, I will show that SH phase encoding in AlGaAs-on-sapphire nanostructures offers high conversion efficiency, demonstrating for the first time dielectric $\chi^{(2)}$ metasurfaces for beam shaping.

References

[1] L. Novotny and N. Van Hulst, 'Antennas for light,' *Nature Photonics*, vol. 5, pp. 83–90, 2011. DOI: 10.1038/nphoton.2010.237.

[2] D. Pohl, 'Near-field optics seen as an antenna problem,' in *Near-field Optics, Principles and Applications*, 2000, pp. 9–21.

[3] L. Rayleigh, 'On the electromagnetic theory of light,' *The London, Edinburgh, and Dublin Philosophical Magazine and Journal of Science*, vol. 12, pp. 81–101, 1881. DOI: 10.1080/14786448108627074.

[4] L. Rayleigh, 'On the transmission of light through an atmosphere containing small particles in suspension, and on the origin of the blue of the sky,' *The London, Edinburgh, and Dublin Philosophical Magazine and Journal of Science*, vol. 47, pp. 375–384, 1899.

[5] G. Mie, 'Beiträge zur Optik trüber Medien, speziel kolloidaler Metallösungen. Ann. Phys,' vol. 25, pp. 377–445, 1908.

[6] P. Biagioni, J. S. Huang, and B. Hecht, 'Nanoantennas for visible and infrared radiation,' *Reports on Progress in Physics*, vol. 75, 2012. DOI: 10.1088/0034-4885/75/2/024402.

[7] V. Giannini, A. I. Fernández-Domínguez, S. C. Heck, and S. A. Maier, 'Plasmonic nanoantennas: Fundamentals and their use in controlling the radiative properties of nanoemitters,' *Chemical Reviews*, vol. 111, pp. 3888–3912, 2011. DOI: 10.1021/cr1002672.

[8] A. F. Koenderink and A. Polman, 'Nanophotonics: Shrinking light-based technology,' *Science*, vol. 348, pp. 516–521, 2015.

[9] S. B. Hasan, R. Filter, A. Ahmed, R. Vogelgesang, R. Gordon, C. Rockstuhl, and F. Lederer, 'Relating localized nanoparticle resonances to an associated antenna problem,' *Physical Review B - Condensed Matter and Materials Physics*, vol. 84, pp. 1–5, 2011. DOI: 10.1103/PhysRevB.84.195405.

[10] L. Novotny, 'Effective wavelength scaling for optical antennas,' *Physical Review Letters*, vol. 98, pp. 1–4, 2007. DOI: 10.1103/PhysRevLett.98.266802.

[11] P. Ghenuche, S. Cherukulappurath, T. H. Taminiau, N. F. Van Hulst, and R. Quidant, 'Spectroscopic mode mapping of resonant plasmon nanoantennas,' *Physical Review Letters*, vol. 101, pp. 1–4, 2008. DOI: 10.1103/PhysRevLett.101.116805.

[12] K. J. Russell, T. L. Liu, S. Cui, and E. L. Hu, 'Large spontaneous emission enhancement in plasmonic nanocavities,' *Nature Photonics*, vol. 6, pp. 459–462, 2012. DOI: 10.1038/nphoton.2012.112.

[13] R. Chikkaraddy, B. De Nijs, F. Benz, S. J. Barrow, O. A. Scherman, E. Rosta, A. Demetriadou, P. Fox, O. Hess, and J. J. Baumberg, 'Single-molecule strong coupling at room temperature in plasmonic nanocavities,' *Nature*, vol. 535, pp. 127–130, 2016. DOI: 10.1038/nature17974.

[14] M. Pelton, 'Modified spontaneous emission in nanophotonic structures,' *Nature Photonics*, vol. 9, pp. 427–435, 2015. DOI: 10.1038/nphoton.2015.103.

[15] S. I. Bozhevolnyi and J. B. Khurgin, 'The case for quantum plasmonics,' *Nature Photonics*, vol. 11, pp. 398–400, 2017. DOI: 10.1038/nphoton.2017.103.

[16] J. J. Baumberg, J. Aizpurua, M. H. Mikkelsen, and D. R. Smith, 'Extreme nanophotonics from ultrathin metallic gaps,' *Nature Materials*, vol. 18, pp. 668–678, 2019. DOI: 10.1038/s41563-019-0290-y.

[17] C. R. Simovski, 'Material parameters of metamaterials (a Review),' *Optics and Spectroscopy (English translation of Optika i Spektroskopiya)*, vol. 107, pp. 726–753, 2009. DOI: 10.1134/S0030400X09110101.

[18] J. B. Pendry, A. J. Holden, D. J. Robbins, and W. J. Stewar, 'Magnetism from Conductors and Enhanced Nonlinear Phenomena,' *IEEE TRANSACTIONS ON MICROWAVE THEORY AND TECHNIQUES*, vol. 47, pp. 2075–2084, 1999. DOI: 10.1109/22.798002.

[19] V. G. Veselago, 'The electrodynamics of substances with simultaneously negative values of ϵ and μ,' *Sov. Phys. Usp*, vol. 10, pp. 509–514, 1968.

[20] J. B. Pendry, 'Negative Refraction Makes a Perfect Lens,' vol. 85, pp. 3966–3969, 2000.

[21] D. R. Smith, W. J. Padilla, D. C. Vier, S. C. Nemat-Nasser, and S. Schultz, 'Composite Medium with Simultaneously Negative Permeability and Permittivity D.,' *Zeitschrift fur die Gesamte Innere Medizin und Ihre Grenzgebiete*, vol. 84, p. 4184, 2000. DOI: 10.1103/PhysRevLett.84.4184.

[22] R. A. Shelby, D. R. Smith, and S. Schultz, 'Experimental verification of a negative index of refraction,' *Science*, vol. 292, pp. 77–79, 2001. DOI: 10.1126/science.1058847.

[23] J. B. Pendry, D. Schurig, and D. R. Smith, 'Controlling electromagnetic fields,' *Science*, vol. 312, pp. 1780–1782, 2006. DOI: 10.1126/science.1125907.

[24] D. R. Smith, J. J. Mock, A. F. Starr, and D. Schurig, 'Gradient index metamaterials,' *Physical Review E - Statistical, Nonlinear, and Soft Matter Physics*, vol. 71, pp. 1–6, 2005. DOI: 10.1103/PhysRevE.71.036609.

[25] D. Schurig, J. J. Mock, B. J. Justice, S. A. Cummer, J. B. Pendry, A. F. Starr, and D. R. Smith, 'Metamaterial electromagnetic cloak at microwave frequencies,' *Science*, vol. 314, pp. 977–980, 2006. DOI: 10.1126/science.1133628.

[26] S. Zhang, W. Fan, N. C. Panoiu, K. J. Malloy, R. M. Osgood, and S. R. J. Brueck, 'Experimental demonstration of near-infrared negative-index metamaterials.,' *Physical review letters*, vol. 95, pp. 1–4, 2005. DOI: 10.1103/PhysRevLett.95.137404.

[27] V. M. Shalaev, W. Cai, U. K. Chettiar, H.-k. Yuan, A. K. Sarychev, V. P. Drachev, and A. V. Kildishev, 'Negative index of refraction in optical metamaterials,' vol. 30, pp. 3356–3358, 2005.

[28] H. J. Lezec, J. A. Dionne, and H. A. Atwater, 'Negative refraction at visible frequencies,' *Science*, vol. 316, pp. 430–432, 2007. DOI: 10.1126/science.1139266.

[29] S. P. Burgos, R. De Waele, A. Polman, and H. A. Atwater, 'A single-layer wide-angle negative-index metamaterial at visible frequencies,' *Nature Materials*, vol. 9, pp. 407–412, 2010. DOI: 10.1038/nmat2747.

[30] J. Valentine, S. Zhang, T. Zentgraf, E. Ulin-Avila, D. A. Genov, G. Bartal, and X. Zhang, 'Three-dimensional optical metamaterial with a negative refractive index,' *Nature*, vol. 455, pp. 376–379, 2008. DOI: 10.1038/nature07247.

[31] J. B. Khurgin, 'How to deal with the loss in plasmonics and metamaterials,' *Nature Nanotechnology*, vol. 10, pp. 2–6, 2015. DOI: 10.1038/nnano.2014.310.

[32] A. I. Kuznetsov, A. E. Miroshnichenko, Y. H. Fu, J. Zhang, and B. Lukyanchukl, 'Magnetic light,' *Scientific Reports*, vol. 2, pp. 1–6, 2012. DOI: 10.1038/srep00492.

[33] E. Tiguntseva, K. Koshelev, A. Furasova, P. Tonkaev, V. Mikhailovskii, E. V. Ushakova, D. G. Baranov, T. Shegai, A. A. Zakhidov, Y. Kivshar, and S. V. Makarov, 'Room-Temperature Lasing from Mie-Resonant Nonplasmonic Nanoparticles,' *ACS nano*, vol. 14, pp. 8149–8156, 2020. DOI: 10.1021/acsnano.0c01468.

[34] Y. H. Fu, A. I. Kuznetsov, A. E. Miroshnichenko, Y. F. Yu, and B. Luk'yanchuk, 'Directional visible light scattering by silicon nanoparticles,' *Nature Communications*, vol. 4, pp. 1–6, 2013. DOI: 10.1038/ncomms2538.

[35] F. Monticone, D. Sounas, A. Krasnok, and A. Alù, 'Can a Nonradiating Mode Be Externally Excited? Nonscattering States versus Embedded Eigenstates,' *ACS Photonics*, vol. 6, pp. 3108–3114, 2019. DOI: 10.1021/acsphotonics.9b01104.

[36] A. García-Etxarri, R. Gómez-Medina, L. S. Froufe-Pérez, C. López, L. Chantada, F. Scheffold, J. Aizpurua, M. Nieto-Vesperinas, and J. J. Sáenz, 'Strong magnetic response of submicron Silicon particles in the infrared,' *Optics Express*, vol. 19, pp. 4815–4826, 2011. DOI: 10.1364/oe.19.004815.

[37] A. B. Evlyukhin, S. M. Novikov, U. Zywietz, R. L. Eriksen, C. Reinhardt, S. I. Bozhevolnyi, and B. N. Chichkov, 'Demonstration of magnetic dipole resonances of dielectric nanospheres in the visible region,' *Nano Letters*, vol. 12, pp. 3749–3755, 2012. DOI: 10.1021/nl301594s.

[38] A. I. Kuznetsov, A. E. Miroshnichenko, M. L. Brongersma, Y. S. Kivshar, and B. Luk'yanchuk, 'Optically resonant dielectric nanostructures,' *Science*, vol. 354, pp. 1–8, 2016. DOI: 10.1126/science.aag2472.

[39] R. M. Bakker, D. Permyakov, Y. F. Yu, D. Markovich, R. Paniagua-Domínguez, L. Gonzaga, A. Samusev, Y. Kivshar, B. Lukyanchuk, and A. I. Kuznetsov, 'Magnetic and electric hotspots with silicon nanodimers,' *Nano Letters*, vol. 15, pp. 2137–2142, 2015. DOI: 10.1021/acs.nanolett.5b00128.

[40] P. Albella, R. A. De La Osa, F. Moreno, and S. A. Maier, 'Electric and Magnetic Field Enhancement with Ultralow Heat Radiation Dielectric Nanoantennas: Considerations for Surface-Enhanced Spectroscopies,' *ACS Photonics*, vol. 1, pp. 524–529, 2014. DOI: 10.1021/ph500060s.

[41] M. Caldarola, P. Albella, E. Cortés, M. Rahmani, T. Roschuk, G. Grinblat, R. F. Oulton, A. V. Bragas, and S. A. Maier, 'Non-plasmonic nanoantennas for surface enhanced spectroscopies with ultra-low heat conversion,' *Nature Communications*, vol. 6, pp. 1–8, 2015. DOI: 10.1038/ncomms8915.

[42] M. Kerker, D. S. Wang, and C. L. Giles, 'Electromagnetic Scattering By Magnetic Spheres.,' *Journal of the Optical Society of America*, vol. 73, pp. 765–767, 1983. DOI: 10.1364/JOSA.73.000765.

[43] S. Person, M. Jain, Z. Lapin, J. J. Sáenz, G. Wicks, and L. Novotny, 'Demonstration of zero optical backscattering from single nanoparticles,' *Nano Letters*, vol. 13, pp. 1806–1809, 2013. DOI: 10.1021/nl4005018.

[44] A. E. Miroshnichenko, A. B. Evlyukhin, Y. F. Yu, R. M. Bakker, A. Chipouline, A. I. Kuznetsov, B. Luk'yanchuk, B. N. Chichkov, and Y. S. Kivshar, 'Nonradiating anapole modes in dielectric nanoparticles,' *Nature Communications*, vol. 6, pp. 1–8, 2015. DOI: 10.1038/ncomms9069.

[45] C. W. Hsu, B. Zhen, A. D. Stone, J. D. Joannopoulos, and M. Soljacic, 'Bound states in the continuum,' *Nature Reviews Materials*, vol. 1, pp. 1–13, 2016. DOI: 10.1038/natrevmats.2016.48.

[46] K. Koshelev and Y. Kivshar, 'Dielectric Resonant Metaphotonics,' *ACS Photonics*, vol. 7, A–K, 2020. DOI: 10.1021/acsphotonics.0c01315.

[47] P. A. Franken, A. E. Hill, C. W. Peters, and G. Weinreich, 'Generation of optical harmonics,' *Physical Review Letters*, vol. 7, pp. 118–119, 1961. DOI: 10.1103/PhysRevLett.7.118.

[48] J. A. Armstrong, N. Bloembergen, J. Ducuing, and P. S. Pershan, 'Interactions between light waves in a nonlinear dielectric,' *Physical Review*, vol. 127, pp. 1918–1939, 1962. DOI: 10.1103/PhysRev.127.1918.

[49] D. A. Miller, 'Are optical transistors the logical next step?' *Nature Photonics*, vol. 4, pp. 3–5, 2010. DOI: 10.1038/nphoton.2009.240.

[50] S. Radic, D. J. Moss, and B. J. Eggleton, 'Nonlinear Optics in Communications: From Crippling Impairment to Ultrafast Tools,' in *Optical Fiber Telecommunications V1A*, Elsevier Inc., 2008, ch. 20, pp. 759–828. DOI: 10.1016/B978-0-12-374171-4.00020-4.

[51] G. Agrawal, *Nonlinear Fiber Optics*. Academic Press, 1989.

[52] A. Yariv, *Quantum Electronics*. Wiley, 1989.

[53] R. Boyd, *Nonlinear Optics*, 3rd. Academic Press, 2008.

[54] M. A. Foster, A. C. Turner, J. E. Sharping, B. S. Schmidt, M. Lipson, and A. L. Gaeta, 'Broad-band optical parametric gain on a silicon photonic chip,' *Nature*, vol. 441, pp. 960–963, 2006. DOI: 10.1038/nature04932.

[55] M. Ferrera, L. Razzari, D. Duchesne, R. Morandotti, Z. Yang, M. Liscidini, J. E. Sipe, S. Chu, B. E. Little, and D. J. Moss, 'Low-power continuous-wave nonlinear optics in doped silica glass integrated waveguide structures,' *Nature Photonics*, vol. 2, pp. 737–740, 2008. DOI: 10.1038/nphoton.2008.228.

[56] C. Koos, P. Vorreau, T. Vallaitis, P. Dumon, W. Bogaerts, R. Baets, B. Esembeson, I. Biaggio, T. Michinobu, F. Diederich, W. Freude, and J. Leuthold, 'All-optical high-speed signal processing with silicon-organic hybrid slot waveguides,' *Nature Photonics*, vol. 3, pp. 216–219, 2009. DOI: 10.1038/nphoton.2009.25.

[57] M. F. Yanik, S. Fan, M. Soljačić, and J. D. Joannopoulos, 'All-optical transistor action with bistable switching in a photonic crystal cross-waveguide geometry,' *Optics Letters*, vol. 28, pp. 2506–2508, 2003. DOI: 10.1364/ol.28.002506.

[58] C. Husko, A. De Rossi, S. Combrí, Q. V. Tran, F. Raineri, and C. W. Wong, 'Ultrafast all-optical modulation in GaAs photonic crystal cavities,' *Applied Physics Letters*, vol. 94, pp. 8–10, 2009. DOI: 10.1063/1.3068755.

[59] D. K. Gramotnev and S. I. Bozhevolnyi, 'Plasmonics beyond the diffraction limit,' *Nature Photonics*, vol. 4, pp. 83–91, 2010. DOI: 10.1038/nphoton.2009.282.

[60] M. Kauranen and A. V. Zayats, 'Nonlinear plasmonics,' *Nature Photonics*, vol. 6, pp. 737–748, 2012. DOI: 10.1038/NPHOTON.2012.244.

[61] M. Danckwerts and L. Novotny, 'Optical frequency mixing at coupled gold nanoparticles,' *Physical Review Letters*, vol. 98, pp. 1–4, 2007. DOI: 10.1103/PhysRevLett.98.026104.

[62] M. Lippitz, M. A. Van Dijk, and M. Orrit, 'Third-harmonic generation from single gold nanoparticles,' *Nano Letters*, vol. 5, pp. 799–802, 2005. DOI: 10.1021/nl0502571.

[63] T. Hanke, G. Krauss, D. Träutlein, B. Wild, R. Bratschitsch, and A. Leitenstorfer, 'Efficient nonlinear light emission of single gold optical antennas driven by few-cycle near-infrared pulses,' *Physical Review Letters*, vol. 103, pp. 1–4, 2009. DOI: 10.1103/PhysRevLett.103.257404.

[64] H. Baida, D. Mongin, D. Christofilos, G. Bachelier, A. Crut, P. Maioli, N. Del Fatti, and F. Vallée, 'Ultrafast nonlinear optical response of a single gold nanorod near its surface plasmon resonance,' *Physical Review Letters*, vol. 107, pp. 1–5, 2011. DOI: 10.1103/PhysRevLett.107.057402.

[65] M. Abb, P. Albella, J. Aizpurua, and O. L. Muskens, 'All-optical control of a single plasmonic nanoantenna - ITO hybrid,' *Nano Letters*, vol. 11, pp. 2457–2463, 2011. DOI: 10.1021/nl200901w.

[66] A. V. Krasavin, P. Ginzburg, G. A. Wurtz, and A. V. Zayats, 'Nonlocality-driven supercontinuum white light generation in plasmonic nanostructures,' *Nature Communications*, vol. 7, pp. 1–6, 2016. DOI: 10.1038/ncomms11497.

[67] M. Celebrano, X. Wu, M. Baselli, S. Großmann, P. Biagioni, A. Locatelli, C. De Angelis, G. Cerullo, R. Osellame, B. Hecht, L. Duò, F. Ciccacci, and M. Finazzi, 'Mode matching in multiresonant plasmonic nanoantennas for enhanced second harmonic generation,' *Nature Nanotechnology*, vol. 10, pp. 412–417, 2015. DOI: 10.1038/nnano.2015.69.

[68] J. E. Sipe, V. C. So, M. Fukui, and G. I. Stegeman, 'Analysis of second harmonic generation at metal surfaces,' *Physical Review B*, vol. 21, pp. 4389–4402, 1980. DOI: 10.1016/0038-1098(80)90142-8.

[69] M. W. Klein, C. Enkrich, M. Wegener, and S. Linden, 'Second-Harmonic Generation from Magnetic Metamaterials,' *Science*, vol. 313, pp. 502–504, 2006. DOI: 10.1126/science.1129198.

[70] H. Husu, R. Siikanen, J. Mäkitalo, J. Lehtolahti, J. Laukkanen, M. Kuittinen, and M. Kauranen, 'Metamaterials with tailored nonlinear optical response,' *Nano Letters*, vol. 12, pp. 673–677, 2012. DOI: 10.1021/nl203524k.

[71] S. D. Gennaro, M. Rahmani, V. Giannini, H. Aouani, T. P. Sidiropoulos, M. Navarro-Cía, S. A. Maier, and R. F. Oulton, 'The Interplay of Symmetry and Scattering Phase in Second Harmonic Generation from Gold Nanoantennas,' *Nano Letters*, vol. 16, pp. 5278–5285, 2016. DOI: 10.1021/acs.nanolett.6b02485.

[72] C. De Angelis, G. Leo, and D. N. Neshev, *Nonlinear meta-optics*, 1st. CRC Press, 2020.

[73] N. K. Hon, R. Soref, and B. Jalali, 'The third-order nonlinear optical coefficients of Si, Ge, and Si 1-xGex in the midwave and longwave infrared,' *Journal of Applied Physics*, vol. 110, pp. 1–8, 2011. DOI: 10.1063/1.3592270.

[74] J. Renger, R. Quidant, N. Van Hulst, and L. Novotny, 'Surface-enhanced nonlinear four-wave mixing,' *Physical Review Letters*, vol. 104, pp. 2–5, 2010. DOI: 10.1103/PhysRevLett.104.046803.

[75] M. R. Shcherbakov, D. N. Neshev, B. Hopkins, A. S. Shorokhov, I. Staude, E. V. Melik-Gaykazyan, M. Decker, A. A. Ezhov, A. E. Miroshnichenko, I. Brener, A. A. Fedyanin, and Y. S. Kivshar, 'Enhanced third-harmonic generation in silicon nanoparticles driven by magnetic response,' *Nano Letters*, vol. 14, pp. 6488–6492, 2014. DOI: 10.1021/nl503029j.

[76] G. Grinblat, Y. Li, M. P. Nielsen, R. F. Oulton, and S. A. Maier, 'Enhanced third harmonic generation in single germanium nanodisks excited at the anapole mode,' *Nano Letters*, vol. 16, pp. 4635–4640, 2016. DOI: 10.1021/acs.nanolett.6b01958.

[77] M. Notomi, 'Manipulating light with strongly modulated photonic crystals,' *Reports on Progress in Physics*, vol. 73, pp. 1–57, 2010. DOI: 10.1088/0034-4885/73/9/096501.

[78] J. Yang, H. Giessen, and P. Lalanne, 'Simple analytical expression for the peak-frequency shifts of plasmonic resonances for sensing,' *Nano Letters*, vol. 15, pp. 3439–3444, 2015. DOI: 10.1021/acs.nanolett.5b00771.

[79] M. R. Shcherbakov, P. P. Vabishchevich, A. S. Shorokhov, K. E. Chong, D. Y. Choi, I. Staude, A. E. Miroshnichenko, D. N. Neshev, A. A. Fedyanin, and Y. S. Kivshar, 'Ultrafast All-Optical Switching with Magnetic Resonances in Nonlinear Dielectric Nanostructures,' *Nano Letters*, vol. 15, pp. 6985–6990, 2015. DOI: 10.1021/acs.nanolett.5b02989.

[80] S. Liu, M. B. Sinclair, S. Saravi, G. A. Keeler, Y. Yang, J. Reno, G. M. Peake, F. Setzpfandt, I. Staude, T. Pertsch, and I. Brener, 'Resonantly Enhanced Second-Harmonic Generation Using III-V Semiconductor All-Dielectric Metasurfaces,' *Nano Letters*, vol. 16, pp. 5426–5432, 2016. DOI: 10.1021/acs.nanolett.6b01816.

[81] V. F. Gili, L. Carletti, A. Locatelli, D. Rocco, M. Finazzi, L. Ghirardini, I. Favero, C. Gomez, A. Lemaître, M. Celebrano, C. De Angelis, and G. Leo, 'Monolithic AlGaAs second-harmonic nanoantennas,' *Optics Express*, vol. 24, pp. 15 965–15 971, 2016. DOI: 10.1364/OE.24.015965.

[82] R. Camacho-Morales, M. Rahmani, S. Kruk, L. Wang, L. Xu, D. A. Smirnova, A. S. Solntsev, A. Miroshnichenko, H. H. Tan, F. Karouta, S. Naureen, K. Vora, L. Carletti, C. De Angelis, C. Jagadish, Y. S. Kivshar, and D. N. Neshev, 'Nonlinear Generation of Vector Beams from AlGaAs Nanoantennas,' *Nano Letters*, vol. 16, pp. 7191–7197, 2016. DOI: 10.1021/acs.nanolett.6b03525.

[83] J. Cambiasso, G. Grinblat, Y. Li, A. Rakovich, E. Cortés, and S. A. Maier, 'Bridging the Gap between Dielectric Nanophotonics and the Visible Regime with Effectively Lossless Gallium Phosphide Antennas,' *Nano Letters*, vol. 17, pp. 1219–1225, 2017. DOI: 10.1021/acs.nanolett.6b05026.

[84] L. Carletti, C. Li, J. Sautter, I. Staude, C. de Angelis, T. Li, and D. N. Neshev, 'Second-harmonic generation in monolithic lithium niobate metasurfaces,' *Optics express*, vol. 27, pp. 33 391–33 398, 2019. DOI: 10.1364/oe.27.033391.

[85] S. Busschaert, R. Reimann, M. Cavigelli, R. Khelifa, A. Jain, and L. Novotny, 'Transition Metal Dichalcogenide Resonators for Second Harmonic Signal Enhancement,' *ACS Photonics*, vol. 7, pp. 2482–2488, 2020. DOI: 10.1021/acsphotonics.0c00751.

[86] N. Bernhardt, K. Koshelev, S. J. White, K. W. C. Meng, J. E. Fröch, S. Kim, T. T. Tran, D. Y. Choi, Y. Kivshar, and A. S. Solntsev, 'Quasi-BIC Resonant Enhancement of Second-Harmonic Generation in WS2Monolayers,' *Nano Letters*, vol. 20, pp. 5309–5314, 2020. DOI: 10.1021/acs.nanolett.0c01603.

[87] L. Carletti, A. Locatelli, O. Stepanenko, G. Leo, and C. De Angelis, 'Enhanced second-harmonic generation from magnetic resonance in AlGaAs nanoantennas,' *Optics Express*, vol. 23, pp. 26 544–26 550, 2015. DOI: 10.1364/OE.23.026544.

[88] M. Ohashi, T. Kondo, R. Ito, S. Fukatsu, Y. Shiraki, K. Kumata, and S. S. Kano, 'Determination of quadratic nonlinear optical coefficient of AlxGa1-xAs system by the method of reflected second harmonics,' *Journal of Applied Physics*, vol. 74, pp. 596–601, 1993. DOI: 10.1063/1.355272.

[89] K. Frizyuk, I. Volkovskaya, D. Smirnova, A. Poddubny, and M. Petrov, 'Second-harmonic generation in Mie-resonant dielectric nanoparticles made of noncentrosymmetric materials,' *Physical Review B*, vol. 99, pp. 1–17, 2019. DOI: 10.1103/PhysRevB.99.075425.

[90] L. Carletti, D. Rocco, A. Locatelli, C. De Angelis, V. F. Gili, M. Ravaro, I. Favero, G. Leo, M. Finazzi, L. Ghirardini, M. Celebrano, G. Marino, and A. V. Zayats, 'Controlling second-harmonic generation at the nanoscale with monolithic AlGaAs-on-AlOx antennas,' *Nanotechnology*, vol. 28, pp. 1–10, 2017. DOI: 10.1088/1361-6528/aa5645.

[91] M. Timofeeva, L. Lang, F. Timpu, C. Renaut, A. Bouravleuv, I. Shtrom, G. Cirlin, and R. Grange, 'Anapoles in Free-Standing III-V Nanodisks Enhancing Second-Harmonic Generation,' *Nano Letters*, vol. 18, pp. 3695–3702, 2018. DOI: 10.1021/acs.nanolett.8b00830.

[92] D. Rocco, V. F. Gili, L. Ghirardini, L. Carletti, I. Favero, A. Locatelli, G. Marino, D. N. Neshev, M. Celebrano, M. Finazzi, G. Leo, and C. De Angelis, 'Tuning the second-harmonic generation in AlGaAs nanodimers via non-radiative state optimization [Invited],' *Photonics Research*, vol. 6, B6–B12, 2018. DOI: 10.1364/prj.6.0000b6.

[93] L. Xu, M. Rahmani, D. Smirnova, K. Z. Kamali, G. Zhang, D. Neshev, and A. E. Miroshnichenko, 'Highly-efficient longitudinal second-harmonic generation from doubly-resonant AlGaAs nanoantennas,' *Photonics*, vol. 5, pp. 1–11, 2018. DOI: 10.3390/photonics5030029.

[94] V. F. Gili, L. Ghirardini, D. Rocco, G. Marino, I. Favero, I. Roland, G. Pellegrini, L. Duò, M. Finazzi, L. Carletti, A. Locatelli, A. Lemaître, D. Neshev, C. De Angelis, G. Leo, and M. Celebrano, 'Metal-dielectric hybrid nanoantennas for efficient frequency conversion at the anapole mode,' *Beilstein Journal of Nanotechnology*, vol. 9, pp. 2306–2314, 2018. DOI: 10.3762/bjnano.9.215.

[95] M. V. Rybin, K. L. Koshelev, Z. F. Sadrieva, K. B. Samusev, A. A. Bogdanov, M. F. Limonov, and Y. S. Kivshar, 'High- Q Supercavity Modes in Subwavelength Dielectric Resonators,' *Physical Review Letters*, vol. 119, pp. 1–5, 2017. DOI: 10.1103/PhysRevLett.119.243901.

[96] A. A. Bogdanov, K. L. Koshelev, P. V. Kapitanova, M. V. Rybin, S. A. Gladyshev, Z. F. Sadrieva, K. B. Samusev, Y. S. Kivshar, and M. F. Limonov, 'Bound states in the continuum and Fano resonances in the strong mode coupling regime,' *Advanced Photonics*, vol. 1, pp. 1–12, 2019. DOI: 10.1117/1.ap.1.1.016001.

[97] L. Carletti, K. Koshelev, C. De Angelis, and Y. Kivshar, 'Giant Nonlinear Response at the Nanoscale Driven by Bound States in the Continuum,' *Physical Review Letters*, vol. 121, pp. 1–5, 2018. DOI: 10.1103/PhysRevLett.121.033903.

[98] K. Koshelev, S. Kruk, E. Melik-Gaykazyan, J.-H. Choi, A. Bogdanov, H.-G. Park, and Y. Kivshar, 'Subwavelength dielectric resonators for nonlinear nanophotonics.,' *Science (New York, N.Y.)*, vol. 367, pp. 288–292, 2020. DOI: 10.1126/science.aaz3985.

[99] D. Smirnova, D. Leykam, Y. Chong, and Y. Kivshar, 'Nonlinear topological photonics,' *Applied Physics Reviews*, vol. 7, pp. 1–26, 2020. DOI: 10.1063/1.5142397.

[100] S. S. Kruk, R. Camacho-Morales, L. Xu, M. Rahmani, D. A. Smirnova, L. Wang, H. H. Tan, C. Jagadish, D. N. Neshev, and Y. S. Kivshar, 'Nonlinear optical magnetism revealed by second-harmonic generation in nanoantennas,' *Nano Letters*, vol. 17, pp. 3914–3918, 2017. DOI: 10.1021/acs.nanolett.7b01488.

[101] L. Ghirardini, L. Carletti, V. Gili, G. Pellegrini, L. Duò, M. Finazzi, D. Rocco, A. Locatelli, C. De Angelis, I. Favero, M. Ravaro, G. Leo, A. Lemaître, and M. Celebrano, 'Polarization properties of second-harmonic generation in AlGaAs optical nanoantennas,' *Optics Letters*, vol. 42, pp. 559–562, 2017. DOI: 10.1364/OL.42.000559.

[102] F. J. Löchner, A. N. Fedotova, S. Liu, G. A. Keeler, G. M. Peake, S. Saravi, M. R. Shcherbakov, S. Burger, A. A. Fedyanin, I. Brener, T. Pertsch, F. Setzpfandt, and I. Staude, 'Polarization-Dependent Second Harmonic Diffraction from Resonant GaAs Metasurfaces,' *ACS Photonics*, vol. 5, pp. 1786–1793, 2018. DOI: 10.1021/acsphotonics.7b01533.

[103] L. Carletti, A. Locatelli, D. Neshev, and C. De Angelis, 'Shaping the Radiation Pattern of Second-Harmonic Generation from AlGaAs Dielectric Nanoantennas,' *ACS Photonics*, vol. 3, pp. 1500–1507, 2016. DOI: 10.1021/acsphotonics.6b00050.

[104] L. Carletti, G. Marino, L. Ghirardini, V. F. Gili, D. Rocco, I. Favero, A. Locatelli, A. V. Zayats, M. Celebrano, M. Finazzi, L. Giuseppe, C. de Angelis, and D. N. Neshev, 'Nonlinear goniometry by second harmonic generation in AlGaAs nanoantennas,' *ACS Photonics*, vol. 5, pp. 4386–4392, 2018. DOI: 10.1021/acsphotonics.8b00810.

[105] J. D. Sautter, L. Xu, A. E. Miroshnichenko, M. Lysevych, I. Volkovskaya, D. A. Smirnova, R. Camacho-Morales, K. Zangeneh Kamali, F. Karouta, K. Vora, H. H. Tan, M. Kauranen, I. Staude, C. Jagadish, D. N. Neshev, and M. Rahmani, 'Tailoring Second-Harmonic Emission from (111)-GaAs Nanoantennas,' *Nano Letters*, vol. 19, pp. 3905–3911, 2019. DOI: 10.1021/acs.nanolett.9b01112.

[106] D. Rocco, C. Gigli, L. Carletti, G. Marino, M. A. Vincenti, G. Leo, and C. D. Angelis, 'Vertical Second Harmonic Generation in asymmetric dielectric nanoantennas,' *IEEE Photonics Journal*, vol. 12, pp. 1–7, 2020. DOI: 10.1109/JPHOT.2020.2988502.

[107] G. Saerens, I. Tang, M. I. Petrov, K. Frizyuk, C. Renaut, F. Timpu, M. Reig Escalé, I. Shtrom, A. Bouravleuv, G. Cirlin, R. Grange, and M. Timofeeva, 'Engineering of the Second-Harmonic Emission Directionality with III–V Semiconductor Rod Nanoantennas,' *Laser and Photonics Reviews*, vol. 2000028, pp. 1–10, 2020. DOI: 10.1002/lpor.202000028.

[108] B. Luk'Yanchuk, N. I. Zheludev, S. A. Maier, N. J. Halas, P. Nordlander, H. Giessen, and C. T. Chong, 'The Fano resonance in plasmonic nanostructures and metamaterials,' *Nature Materials*, vol. 9, pp. 707–715, 2010. DOI: 10.1038/nmat2810.

[109] M. F. Limonov, M. V. Rybin, A. N. Poddubny, and Y. S. Kivshar, 'Fano resonances in photonics,' *Nature Photonics*, vol. 11, pp. 543–554, 2017. DOI: 10.1038/NPHOTON.2017.142.

[110] P. P. Vabishchevich, S. Liu, M. B. Sinclair, G. A. Keeler, G. M. Peake, and I. Brener, 'Enhanced Second-Harmonic Generation Using Broken Symmetry III-V Semiconductor Fano Metasurfaces,' *ACS Photonics*, vol. 5, pp. 1685–1690, 2018. DOI: 10.1021/acsphotonics.7b01478.

[111] L. Xu, K. Zangeneh Kamali, L. Huang, M. Rahmani, A. Smirnov, R. Camacho-Morales, Y. Ma, G. Zhang, M. Woolley, D. Neshev, and A. E. Miroshnichenko, 'Dynamic Nonlinear Image Tuning through Magnetic Dipole Quasi-BIC Ultrathin Resonators,' *Advanced Science*, vol. 1802119, pp. 1–7, 2019. DOI: 10.1002/advs.201802119.

[112] A. W. Lohmann and D. P. Paris, 'Binary Fraunhofer Holograms, Generated by Computer,' *Applied Optics*, vol. 6, pp. 1739–1748, 1967. DOI: 10.1364/ao.6.001739.

[113] S. Pancharatnam, 'Generalized theory of interference, and its applications,' *Proc. Indian Acad. Sci.*, vol. 44, pp. 247–262, 1956.

[114] M. Berry, 'Quantal phase factors accompanying adiabatic changes,' *Proc. R. Soc. Lond. A*, vol. 392, pp. 45–57, 1984. DOI: 10.1142/9789813221215_0006.

[115] P. Lalanne, S. Astilean, P. Chavel, E. Cambril, and H. Launois, 'Blazed binary subwavelength gratings with efficiencies larger than those of conventional échelette gratings,' *Optics Letters*, vol. 23, pp. 1081–1083, 1998. DOI: 10.1364/ol.23.001081.

[116] G. Li, S. Chen, N. Pholchai, B. Reineke, P. W. H. Wong, E. Y. B. Pun, K. W. Cheah, T. Zentgraf, and S. Zhang, 'Continuous control of the nonlinearity phase for harmonic generations,' *Nature Materials*, vol. 14, pp. 607–612, 2015. DOI: 10.1038/nmat4267.

[117] E. Almeida, O. Bitton, and Y. Prior, 'Nonlinear metamaterials for holography,' *Nature Communications*, vol. 7, pp. 1–7, 2016. DOI: 10.1038/ncomms12533.

[118] L. Wang, S. Kruk, K. Koshelev, I. Kravchenko, B. Luther-Davies, and Y. Kivshar, 'Nonlinear Wavefront Control with All-Dielectric Metasurfaces,' *Nano Letters*, vol. 18, pp. 3978–3984, 2018. DOI: 10.1021/acs.nanolett.8b01460.

[119] C. Schlickriede, S. S. Kruk, S. S. Kruk, L. Wang, B. Sain, Y. Kivshar, and T. Zentgraf, 'Nonlinear Imaging with All-Dielectric Metasurfaces,' *Nano Letters*, vol. 20, pp. 4370–4376, 2020. DOI: 10.1021/acs.nanolett.0c01105.

[120] K. Wang, J. G. Titchener, S. S. Kruk, L. Xu, H.-p. Chung, M. Parry, I. I. Kravchenko, Y.-h. Chen, A. S. Solntsev, Y. S. Kivshar, D. N. Neshev, and A. A. Sukhorukov, 'Quantum metasurface for multiphoton interference and state reconstruction,' *Science*, vol. 1108, pp. 1104–1108, 2018.

Theoretical framework 2

Contents

Absorption and scattering of light by small particles is an archetypal problem in electromagnetic theory and its treatment can be found in several reference textbooks [1, 2]. In order to uniform the mathematical formalism throughout the manuscript and provide the physical context, we introduce in this chapter the fundamental concepts to describe light interaction with nano-objects that exhibit strong nonlinear optical responses. Starting from the macroscopic formulation of Maxwell equations, we derive first the useful figures of merit to study linear scattering. Then, the main concepts of nonlinear optics will be recalled with particular focus on second harmonic generation in gallium arsenide, which constitutes the main subject of this thesis. Finally some numerical tools to solve the problem of nonlinear radiation by nano-objects will be presented.

2.1 Macroscopic electrodynamics

In macroscopic electrodynamics all the classical phenomena are described by Maxwell equations, which in SI units take on the form:

$$\nabla \times \boldsymbol{\mathcal{E}}(\boldsymbol{r}, t) = -\frac{\partial \boldsymbol{\mathcal{B}}(\boldsymbol{r}, t)}{\partial t} \tag{2.1}$$

$$\nabla \cdot \boldsymbol{\mathcal{B}}(\boldsymbol{r}, t) = 0 \tag{2.2}$$

$$\nabla \cdot \boldsymbol{\mathcal{D}}(\boldsymbol{r}, t) = \rho(\boldsymbol{r}, t) \tag{2.3}$$

$$\nabla \times \boldsymbol{\mathcal{H}}(\boldsymbol{r}, t) = \frac{\partial \boldsymbol{\mathcal{D}}(\boldsymbol{r}, t)}{\partial t} + \boldsymbol{\mathcal{J}}(\boldsymbol{r}, t) \tag{2.4}$$

$\boldsymbol{\mathcal{E}}(\boldsymbol{r}, t)$ and $\boldsymbol{\mathcal{H}}(\boldsymbol{r}, t)$ denote the electric and magnetic field distributions, $\boldsymbol{\mathcal{D}}(\boldsymbol{r}, t)$ the electric displacement, $\boldsymbol{\mathcal{B}}(\boldsymbol{r}, t)$ the magnetic induction, $\boldsymbol{\mathcal{J}}(\boldsymbol{r}, t)$ the current density (including driving sources and conduction currents) and ρ the charge density. Equations (2.3) and (2.4) relate electromagnetic fields with fixed or moving charges, constituting the core of light interaction with matter. The electromagnetic properties of matter are usually embedded in the polarization $\boldsymbol{\mathcal{P}}(\boldsymbol{r}, t)$ and magnetization $\boldsymbol{\mathcal{M}}(\boldsymbol{r}, t)$ vectors defined by the constitutive relations

$$\boldsymbol{\mathcal{D}}(\boldsymbol{r}, t) = \boldsymbol{\varepsilon}\boldsymbol{\mathcal{E}}(\boldsymbol{r}, t) = \varepsilon_0 \boldsymbol{\mathcal{E}}(\boldsymbol{r}, t) + \boldsymbol{\mathcal{P}}(\boldsymbol{r}, t) \tag{2.5}$$

$$\boldsymbol{\mathcal{B}}(\boldsymbol{r}, t) = \boldsymbol{\mu}\boldsymbol{\mathcal{H}}(\boldsymbol{r}, t) = \mu_0 \boldsymbol{\mathcal{H}}(\boldsymbol{r}, t) + \boldsymbol{\mathcal{M}}(\boldsymbol{r}, t) \tag{2.6}$$

where $\boldsymbol{\varepsilon}$ and $\boldsymbol{\mu}$ are the electric permittivity and magnetic permeability tensors of the material. For isotropic materials, these are scalar quantities defined as $\varepsilon = \varepsilon_0 \varepsilon_r$ with $\varepsilon_0 \approx 8,85{\times}10^{-12}\mathrm{F/m}$ the vacuum permittivity and ε_r the relative permittivity of the material, and similarily $\mu = \mu_0 \mu_r$ with $\mu_0 = 4\pi \times 10^{-7}\mathrm{H/m}$ the vacuum magnetic permeability and μ_r the relative permeability of the medium. Importantly, all the defined fields are spatial averages of microscopic fields associated with local charges, which constitutes the key feature of macroscopic formulation.

Maxwell equations are more easily handled in the frequency domain. In a linear medium an electromagnetic field can be written as a superposition of monochromatic waves:

$$\mathbf{E}(\boldsymbol{r}, \omega) = \sum_i a_i \mathbf{E}_0 e^{i(\boldsymbol{k}\cdot\boldsymbol{r} - \omega t)} \tag{2.7}$$

where $e^{-i\omega t}$ convention is used for propagating wave. The time-dependent filed $\boldsymbol{\mathcal{E}}(\boldsymbol{r}, t)$ is related to its spectral representation by the Fourier transform*:

$$\boldsymbol{\mathcal{E}}(\boldsymbol{r}, t) = \int_{-\infty}^{\infty} \mathbf{E}(\boldsymbol{r}, \omega) e^{-i\omega t} d\omega \tag{2.8}$$

* To provide a visual separation between temporal and spectral domains we represents fields in time domain with calligraphic font (e.g. $\boldsymbol{\mathcal{E}}$) and in frequency domain with normal font (e.g. $\mathbf{E}$)

Using the spectral representation, equations (2.1)-(2.4) become:

$$\nabla \times \mathbf{E}(\boldsymbol{r}, \omega) = i\omega \mathbf{B}(\boldsymbol{r}, \omega) \tag{2.9}$$

$$\nabla \cdot \mathbf{B}(\boldsymbol{r}, \omega) = 0 \tag{2.10}$$

$$\nabla \cdot \mathbf{D}(\boldsymbol{r}, \omega) = \rho(\boldsymbol{r}, \omega) \tag{2.11}$$

$$\nabla \times \mathbf{H}(\boldsymbol{r}, \omega) = -i\omega \mathbf{D}(\boldsymbol{r}, \omega) + \mathbf{J}(\boldsymbol{r}, \omega) \tag{2.12}$$

On the right-hand side of (2.12) one finds the polarization current inside the term $-i\omega\mathbf{D}$, and the conduction and source currents in $\mathbf{J}$. Constitutive equations (2.5)-(2.6) should actually include also the description of conduction (or free carriers) currents $\mathbf{J}_c = \sigma\mathbf{E}$, with σ being the conductivity of the material. In the present context polarization and conduction currents are merged together introducing a complex dielectric constant $\boldsymbol{\varepsilon}$. Consequently, applying Fourier transform to constitutive equations (2.5)-(2.6), and (2.9)-(2.12) become:

$$\begin{bmatrix} 0 & i\boldsymbol{\varepsilon}^{-1}(\boldsymbol{r}, \omega)\nabla\times \\ -i\boldsymbol{\mu}^{-1}(\boldsymbol{r}, \omega)\nabla\times & 0 \end{bmatrix} \begin{bmatrix} \mathbf{E}(\boldsymbol{r}, \omega) \\ \mathbf{H}(\boldsymbol{r}, \omega) \end{bmatrix} = \omega \begin{bmatrix} \mathbf{E}(\boldsymbol{r}, \omega) \\ \mathbf{H}(\boldsymbol{r}, \omega) \end{bmatrix} + \begin{bmatrix} i\boldsymbol{\varepsilon}^{-1}(\boldsymbol{r}, \omega)\mathbf{J}_0(\boldsymbol{r}, \omega) \\ 0 \end{bmatrix} \tag{2.13}$$

or equivalently:

$$\nabla \times \boldsymbol{\mu}^{-1} \nabla \times \mathbf{E} - \omega^2 \boldsymbol{\varepsilon} \mathbf{E} = i\omega \mathbf{J}_0 \tag{2.14}$$

$$\nabla \times \boldsymbol{\varepsilon}^{-1} \nabla \times \mathbf{H} - \omega^2 \boldsymbol{\mu} \mathbf{H} = -\nabla \times \boldsymbol{\varepsilon}^{-1} \mathbf{J}_0 \tag{2.15}$$

where $\mathbf{J}_0$ are the sole source currents and $\boldsymbol{\varepsilon}$ and $\boldsymbol{\mu}$ are generally spatially variant, dispersive and anisotropic. For the sake of simplicity in the following we will consider isotropic and non-magnetic materials for which $\boldsymbol{\varepsilon} = \varepsilon_0\varepsilon_r$ and $\boldsymbol{\mu} = \mu_0$ are scalar quantities. In absence of external sources ($\mathbf{J}_0 = 0$) equations (2.14)-(2.15) lead to the homogeneous Helmoltz wave equations:

$$\Delta \mathbf{E}(\boldsymbol{r}, \omega) + \omega^2 \varepsilon \mu \mathbf{E}(\boldsymbol{r}, \omega) = 0 \tag{2.16}$$

$$\Delta \mathbf{H}(\boldsymbol{r}, \omega) + \omega^2 \varepsilon \mu \mathbf{H}(\boldsymbol{r}, \omega) = 0 \tag{2.17}$$

where Δ is the Laplacian operator and the identity $\nabla \times \nabla\times = -\Delta + \nabla\nabla\cdot$ was used. Helmoltz equation brings out also the dispersion relation inside the propagation medium:

$$k^2(\omega) = \omega^2 \varepsilon(\omega)\mu(\omega) = \frac{\omega^2}{c^2}\varepsilon_r \tag{2.18}$$

2.2 Light interaction at the nanoscale

Light scattering by nanoobjects

A typical scattering experiment can be sketched as in Fig. 2.1: an external excitation described by $[\mathbf{E}_{inc}, \mathbf{H}_{inc}]$ (e.g. a plane wave generated by a current distribution at infinity) is incident on a nano-object transferring part of its energy to it. A portion of the exchanged energy is stocked by the object, another part is dissipated (e.g. through thermal losses) and the rest is scattered away. The total electromagnetic field is the sum of background field $[\mathbf{E}_b, \mathbf{H}_b]$ and scattered field $[\mathbf{E}_S, \mathbf{H}_S]$. $[\mathbf{E}_b, \mathbf{H}_b]$ denotes the interaction result of incident field with the environment if the nano-object were removed, which corresponds to $[\mathbf{E}_{inc}, \mathbf{H}_{inc}]$ just in the particular case of a nanoobject suspended in a uniform medium.

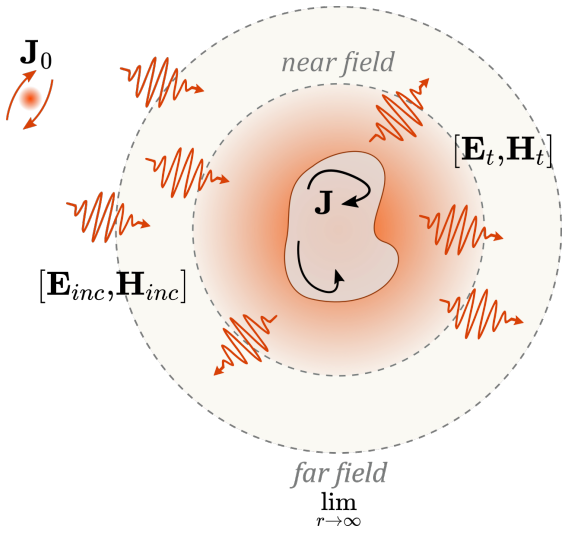

Figure 2.1: Light scattering by a nano-object. An external plane wave $[\mathbf{E}_{inc}, \mathbf{H}_{inc}]$ impinges on the nanostructure inducing a current distribution $\mathbf{J}$ in its volume. The resulting radiated fields satisfies outgoing boundary conditions.

Poynting theorem and cross sections

The energy balance of the system can be better interpreted in the time domain. From curl equations (2.1)-(2.4) one can derive:

$$\boldsymbol{\mathcal{H}} \cdot (\nabla \times \boldsymbol{\mathcal{E}}) - \boldsymbol{\mathcal{E}} \cdot (\nabla \times \boldsymbol{\mathcal{H}}) = -\boldsymbol{\mathcal{H}} \cdot \frac{\partial \boldsymbol{\mathcal{B}}}{\partial t} - \boldsymbol{\mathcal{E}} \cdot \frac{\partial \boldsymbol{\mathcal{D}}}{\partial t} - \boldsymbol{\mathcal{J}} \cdot \boldsymbol{\mathcal{E}} \tag{2.19}$$

Applying the divergence theorem on an arbitrary closed surface Σ (see Fig. 2.2) surrounding a finite volume Ω, the Poynting theorem for a linear material is derived:

$$-\frac{1}{2}\frac{\partial}{\partial t}\int_{\Omega} (\boldsymbol{\mathcal{D}} \cdot \boldsymbol{\mathcal{E}} + \boldsymbol{\mathcal{B}} \cdot \boldsymbol{\mathcal{H}}) d\boldsymbol{r} = \oint_{\Sigma} (\boldsymbol{\mathcal{E}} \times \boldsymbol{\mathcal{H}}) \cdot \mathbf{n} d\sigma + \int_{\Omega} \boldsymbol{\mathcal{J}} \cdot \boldsymbol{\mathcal{E}} d\boldsymbol{r}. \tag{2.20}$$

The left-hand term denotes the derivative of total electromagnetic energy stored inside the volume Ω, $W(\Omega, t)$ at a finite time while the right-hand side describes the two loss mechanisms: scattering and absorption respectively. This concept is schematically explained in Fig. 2.2: at time $t < t_0$ an external plane wave excites the system in a steady-state and all the energy contributions are balanced. At $t = t_0$ the external source is switched off, and the system enter a transient state in which all the stored energy is lost in time by radiation or transformed into heat. Thus, from (2.20) the total stored eneregy inside the volume Ω at time t_0 can be expressed as:

$$W(\Omega, t) = \int_{t_0}^{\infty} \oint_{\Sigma} (\boldsymbol{\mathcal{E}} \times \boldsymbol{\mathcal{H}}) \cdot \mathbf{n} d\sigma dt + \int_{t_0}^{\infty} \int_{\Omega} \boldsymbol{\mathcal{J}} \cdot \boldsymbol{\mathcal{E}} d\boldsymbol{r} dt. \tag{2.21}$$

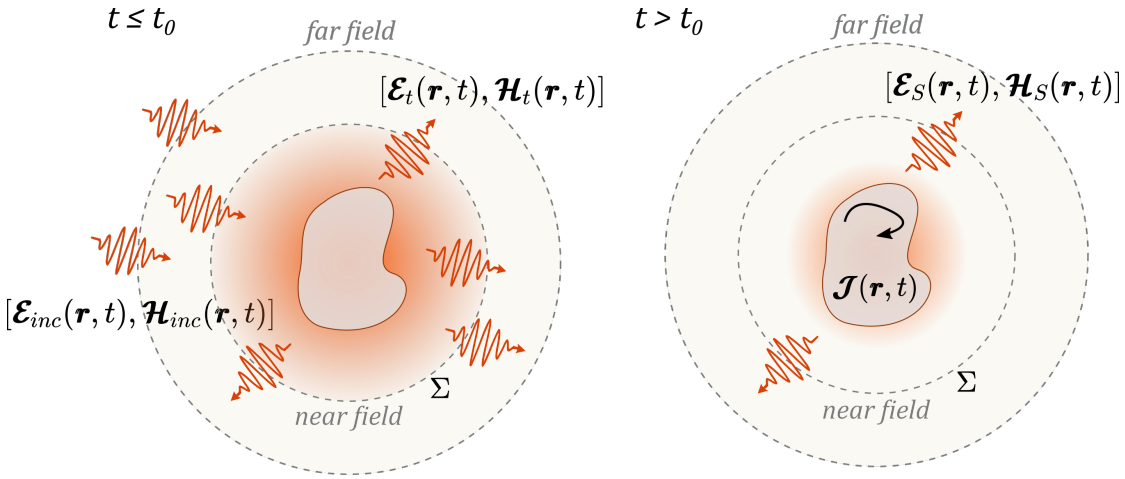

Figure 2.2: Schematic representation of Poynting theorem. At time $t < t_0$, a plane wave $[\boldsymbol{\mathcal{E}}_{inc}, \boldsymbol{\mathcal{H}}_{inc}]$ interacts with a nanoobject transferring part of its energy to it. At time $t = t_0$ the external excitation is removed, the current distribution $\boldsymbol{\mathcal{J}}$ established in the nanostructure is the source of radiated field $[\boldsymbol{\mathcal{E}}_S, \boldsymbol{\mathcal{H}}_S]$ until all the energy has leaked away or has been absorbed by the material.

Moving to time-harmonic domain, the complex Poynting theorem in the presence of an external excitation becomes:

$$-\frac{1}{2} \int_{\Omega} \mathbf{J}^* \cdot \mathbf{E} d\boldsymbol{r} = 2i\omega \int_{\Omega} W d\boldsymbol{r} + \oint_{\Sigma} \mathbf{S} \cdot \mathbf{n} d\sigma \tag{2.22}$$

where W and $\mathbf{S}$ are the electromagnetic energy density and the total Poynting vector respectively:

$$W = \frac{1}{4}(\mathbf{E} \cdot \mathbf{D}^* + \mathbf{B} \cdot \mathbf{H}^*) \tag{2.23}$$

$$\mathbf{S} = \frac{1}{2}\mathbf{E} \times \mathbf{H}^* \tag{2.24}$$

Decomposing the electric and magnetic contributions of incident and scattered field, the

total Poynting vector can be rewritten as [2]:

$$\mathbf{S} = \mathbf{S}_{inc} + \mathbf{S}_{sca} + \mathbf{S}_{ext} \tag{2.25}$$

where:

$$\mathbf{S}_{inc} = \frac{1}{2}\mathbf{E}_b \times \mathbf{H}_b^* \tag{2.26}$$

$$\mathbf{S}_{sca} = \frac{1}{2}\mathbf{E}_S \times \mathbf{H}_S^* \tag{2.27}$$

$$\mathbf{S}_{ext} = \frac{1}{2}(\mathbf{E}_b \times \mathbf{H}_S^* + \mathbf{E}_S \times \mathbf{H}_b^*) \tag{2.28}$$

The time-average of equation (2.22) leads therefore to the power balance:

$$W_{abs} + W_{sca} = W_{inc} + W_{ext} \tag{2.29}$$

with:

$$W_{abs} = -\frac{1}{2}\int_\Omega \mathrm{Re}(\mathbf{J}^* \cdot \mathbf{E})d\boldsymbol{r} \tag{2.30}$$

$$W_{sca} = \oint_\Sigma < \mathbf{S}_{sca} > \cdot\mathbf{n}d\sigma = \frac{1}{2}\oint_\Sigma \mathrm{Re}(\mathbf{E}_S \times \mathbf{H}_S^*) \cdot \mathbf{n}d\sigma \tag{2.31}$$

$$W_{inc} = \oint_\Sigma < \mathbf{S}_{inc} > \cdot\mathbf{n}d\sigma = \frac{1}{2}\oint_\Sigma \mathrm{Re}(\mathbf{E}_b \times \mathbf{H}_b^*) \cdot \mathbf{n}d\sigma \tag{2.32}$$

$$W_{ext} = \oint_\Sigma < \mathbf{S}_{ext} > \cdot\mathbf{n}d\sigma = \frac{1}{2}\oint_\Sigma \mathrm{Re}(\mathbf{E}_b \times \mathbf{H}_S^* + \mathbf{E}_S \times \mathbf{H}_b^*) \cdot \mathbf{n}d\sigma \tag{2.33}$$

W_{abs} corresponds to the average power transformed into heat while W_{sca} is the scattered power. W_{inc}, the total incident power, is null when the integral is performed over a closed surface and the surrounding medium is not absorbing. Therefore, $W_{ext} = W_{abs} + W_{sca}$, called extinction power, denotes the total amount of power subtracted from the external excitation. In case of a plane wave excitation, these contributions can be normalized by the wave intensity $S_0 = 1/2\sqrt{\varepsilon_0/\mu_0}|\mathbf{E}_0|$, introducing the concept of cross-sections:

$$\sigma_{ext} = \sigma_{sca} + \sigma_{abs} \tag{2.34}$$

The extinction cross section denotes the effective nanoparticle area that the electromagnetic field perceives in the interaction. Independently on nano-object properties, it can be shown that extinction cross section is strictly related to scattering amplitude in forward direction

$$\sigma_{ext} = \frac{4\pi}{k|\mathbf{E}_0|^2}\mathrm{Im}[\mathbf{E}_0^* \cdot \mathbf{E}_S(\boldsymbol{k} = \boldsymbol{k}_0)] \tag{2.35}$$

where k is the wavevector in surrounding medium and $\boldsymbol{k}_0$ denotes the propagation direction of incident plane wave. This powerful relationship, called *Optical Theorem* [1], states that the

total power transferred to the nano-object only depends on the scattered field in the same direction of incoming plane wave.

Multipole expansion in spherical coordinates

One of the most significant exactly soluble problems of nano-optics is the scattering by a spherical particle suspended in a uniform medium. The natural modes of this system, called vector spherical wave functions (VSWF), can be computed analytically as solutions of source-free Maxwell equations in spherical coordinates and they provide a valuable tool to approximate the response of nonspherical particles. Indeed multipolar expansion of electromagnetic fields consists in replacing the nanoscatterer under study with a set of point multipoles which generate an equivalent field. Practically this is implemented by projecting the total field inside the resonator on VSWFs. Since the electromagnetic properties of those point multipoles are well-known, they can offer a useful tool to design on-demand scattering properties. In many cases this series can be truncated to low order elements which describes with accurate approximation the original fields. For small objects compared to wavelength, electromagnetic fields can often be approximated with the sole electric dipole contribution while all higher multipole orders can be neglected. At variance, as the size is increased, an optical magnetic response can be evidenced [3]. The interaction of few multipoles can lead to more complex and appealing optical functionalities, as unidirectional scattering [4, 5] or nonradiating anapoles [6].

Being solutions of the source-free Maxwell equation, in time-harmonic domain VSWF are analytically derived as the solution of vector helmoltz equation in spherical coordinates [1]. To introduce the problem, let us first consider the scalar version of Helmoltz equation introduced in (2.16)-(2.17):

$$\Delta\Psi(\boldsymbol{r},\omega) + k^2\Psi(\boldsymbol{r},\omega) = 0 \tag{2.36}$$

In spherical coordinates, the solution can be found separating the radial and angular variables:

$$\Psi(\boldsymbol{r},\omega) = \sum_{lm} \psi_l(r) Y_{lm}(\theta,\varphi) \tag{2.37}$$

where r is the radial coordinate while θ and φ the polar and azimuthal angles respectively.

The radial functions $\psi_l(r)$ are solutions of:

$$\left[\frac{d^2}{dr^2} + \frac{2}{r}\frac{d}{dr} + k^2 - \frac{l(l+1)}{r^2}\right]\psi_l(r) = 0 \tag{2.38}$$

which can be reconducted to Bessel equation and whose mathematical solutions are given

by the spherical Bessel, Neumann and Hankel functions:

$$\begin{aligned} j_l(kr) &= \left(\frac{\pi}{2kr}\right)^{1/2} J_{l+1/2}(kr) \\ n_l(kr) &= \left(\frac{\pi}{2kr}\right)^{1/2} N_{l+1/2}(kr) \\ h_l^{(1,2)}(kr) &= \left(\frac{\pi}{2kr}\right)^{1/2} [J_{l+1/2}(kr) \pm iN_{l+1/2}(kr)] \end{aligned} \tag{2.39}$$

The boundary conditions (Sommerfeld radiation condition) and regularity of electromagnetic field determine which of these function will be retained.

The angular dependece is given by the equation

$$-\left[\frac{1}{\sin\theta}\frac{\partial}{\partial\theta}\left(\sin\theta\frac{\partial}{\partial\theta}\right)+\frac{1}{\sin^2\theta}\frac{\partial^2}{\partial\theta^2}\right]Y_{lm} = l(l+1)Y_{lm} \tag{2.40}$$

whose general solution is well-known and applied in several domains from quantum mechanics to fluid dynamics:

$$Y_{lm}(\theta,\varphi) = \sqrt{\frac{2l+1}{4\pi}\frac{(l-m)!}{(l+m)!}}P_l^m(\cos\theta)e^{im\varphi} \tag{2.41}$$

where $P_l^m(\cos\theta)$ are the associated Legendre polynomials:

$$P_l^m(\cos\theta) = (-1)^m(\sin\theta)^m\frac{d^m P_l\cos\theta}{d(\cos\theta)^m} \tag{2.42}$$

We can now introduce the vector spherical wave functions:

$$\mathbf{X}_{lm}(\theta,\phi) = \frac{-i}{\sqrt{l(l+1)}}(\boldsymbol{r}\times\boldsymbol{\nabla})Y_{lm}(\theta,\varphi) \tag{2.43}$$

which are solutions of source-free vector Helmoltz equations. Therefore a general solution of Maxwell equations can be expanded in a combination of these functions [1]. To provide an easier visual interpretation, the spatial distribution in absolute value for the first scalar and vector spherical harmonics with $l < 3$ is reported in Fig. 2.3

The scattered electromagnetic field from an isolated particle in an homogeneous surrounding upon a plane wave excitation with amplitude E_0, angular frequency ω and

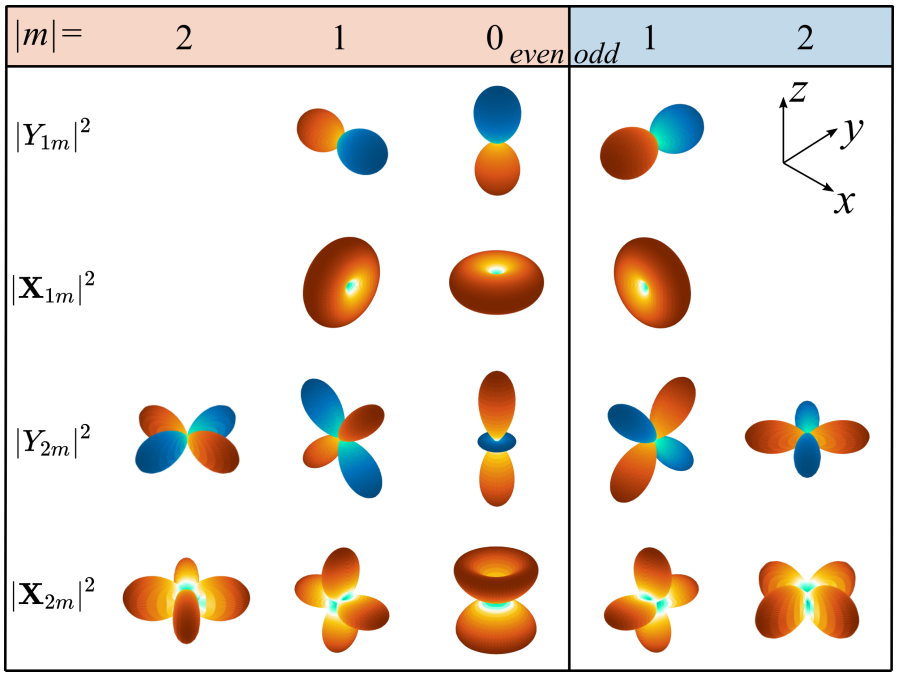

Figure 2.3: Spatial distribution in square modulus of the first spherical harmonics with $l < 3$. The whole set is divided in two, depending on the choice of real (even) or imaginary (odd) part of $\exp(im\varphi)$ in (2.41). Colors of the scalar harmonics denote the positive (red) or negative (blue) values.

wavevector $\boldsymbol{k}$ can be expanded in spherical coordinates as

$$\mathbf{E}_S(r,\theta,\varphi) = E_0 \sum_{l=1}^{\infty}\sum_{l=-m}^{m} i^l[\pi(2l+1)]^{1/2}\left\{\frac{1}{k}a_E(l,m)\nabla\times\left[h_l^{(1)}(kr)\mathbf{X}_{lm}(\theta,\varphi)\right] + a_M(l,m)h_l^{(1)}(kr)\mathbf{X}_{lm}(\theta,\varphi)\right\} \tag{2.44}$$

$$\mathbf{H}_S(r,\theta,\varphi) = \frac{E_0}{\eta}\sum_{l=1}^{\infty}\sum_{l=-m}^{m} i^{l-1}[\pi(2l+1)]^{1/2}\left\{\frac{1}{k}a_M(l,m)\nabla\times\left[h_l^{(1)}(kr)\mathbf{X}_{lm}(\theta,\varphi)\right] + a_E(l,m)h_l^{(1)}(kr)\mathbf{X}_{lm}(\theta,\varphi)\right\} \tag{2.45}$$

with η the impedence of the host medium. The VSWFs form a complete basis to describe the electromagnetic field radiated by the isolated particle. a_E and a_M define the electric and magnetic multipole coefficients, whose analytical expression was demonstrated for a spherical particle by Gustav Mie in 1908 [7]. From their knowledge, the scattering (σ_{sca}) cross section introduced in equations (2.31)-(2.34) can be written as [2]:

$$\sigma_{sca} = \frac{\pi}{k^2}\sum_{l=1}^{\infty}\sum_{m=-l}^{l}(2l+1)\left[|a_E(l,m)|^2 + |a_M(l,m)|^2\right] \tag{2.46}$$

The square moduli in the sum allow to determine the contribution of each multipole to the total scattering efficiency. In Fig. 2.4a the analytical result for a dielectric nanosphere with radius $r = 200$ nm and refractive index $n = 4$ has been reported. When the wavelength in the material (λ/n) is comparable with the nano-object size (r), its response cannot be approximated with the sole electric dipole and many multipolar contributions arise. Tuning the nanosphere size and refractive index is therefore possible to optimize a specific response (e.g. conceiving a nanostructure with a main electric or magnetic dipolar character as depicted in Fig. 2.4b).

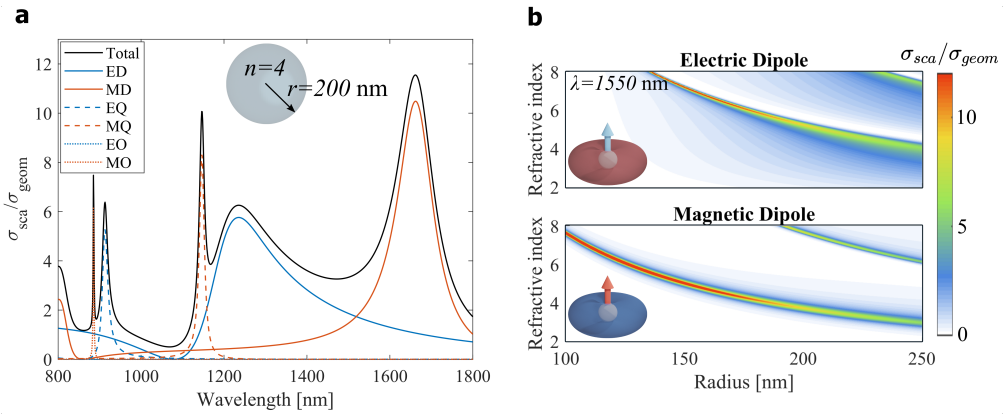

Figure 2.4: Mie scattering by a sphere in a uniform medium. (a) Scattering cross section of a sphere with radius $r = 200$ nm and refractive index $n = 4$. The total scattering (black) has been decomposed in electric (blue) and magnetic (red) multipolar contributions according to Mie theory. (b) Electric (top) and magnetic (bottom) contributions to the scattering cross section vs the radius and refractive index of the sphere. Excitation wavelength has been fixed at $\lambda = 1550$ nm. The reported scattering spectra are normalized with respect to geometrical cross sections $\sigma_{geom} = \pi r^2$

In most of the cases the electromagnetic problem cannot be solved analytically, but the scattered field can be computed numerically. The orthogonality properties of VSWF can be applied to invert equations (2.44)-(2.45) and extract the multipole coefficients [8]:

$$a_E(l,m) = -\frac{\eta}{E_0 i^{l+1}\sqrt{\pi(2l+1)}h_l^{(1)}(kr)}\int_0^{2\pi}\int_0^{\pi}\mathbf{X}^*_{lm}(\theta,\varphi)\cdot\mathbf{H}_S(r,\theta,\varphi)\sin(\theta)d\theta d\varphi \quad (2.47)$$

$$a_M(l,m) = \frac{1}{E_0 i^{l}\sqrt{\pi(2l+1)}h_l^{(1)}(kr)}\int_0^{2\pi}\int_0^{\pi}\mathbf{X}^*_{lm}(\theta,\varphi)\cdot\mathbf{E}_S(r,\theta,\varphi)\sin(\theta)d\theta d\varphi \quad (2.48)$$

The two integrals represent the projection of the scattered field on the VSWF. As it was previously shown in Fig. 2.20 in the time domain, the origin of the scattered field are the source currents induced inside the nano-object volume V, which are given by:

$$\mathbf{J}_S(\boldsymbol{r}) = -i\omega\varepsilon_0(\varepsilon-\varepsilon_b)\mathbf{E}_t(\boldsymbol{r}) \quad (2.49)$$

with ε_b the permittivity of the background and $\mathbf{E}_t(\boldsymbol{r})$ the total electric field. Within this

formalism, one can explicit the multipole coefficients in terms of the source current [8]:

$$a_E(l,m) = \frac{(-i)^{l-1}k^2\eta O_{lm}}{E_0\sqrt{\pi(2l+1)}}\int_V \exp(-im\varphi)\Big\{\left[\Psi_l(kr)+\Psi_l''(kr)\right]P_l^m(\cos\theta)\hat{\boldsymbol{r}}\cdot\mathbf{J}_S(\boldsymbol{r}) + \frac{\Psi_l'(kr)}{kr}\left[\tau_{lm}(\theta)\hat{\boldsymbol{\theta}}\cdot\mathbf{J}_S(\boldsymbol{r}) - i\pi_{lm}(\theta)\hat{\boldsymbol{\varphi}}\cdot\mathbf{J}_S(\boldsymbol{r})\right]\Big\}d^3r \tag{2.50}$$

$$a_M(l,m) = \frac{(-i)^{l+1}k^2\eta O_{lm}}{E_0\sqrt{\pi(2l+1)}}\int_V \exp(-im\varphi)j_l(kr)\left[i\pi_{lm}(\theta)\hat{\boldsymbol{\theta}}\cdot\mathbf{J}_S(\boldsymbol{r}) + \tau_{lm}(\theta)\hat{\boldsymbol{\varphi}}\cdot\mathbf{J}_S(\boldsymbol{r})\right]d^3r \tag{2.51}$$

where $\Psi(kr) = krj_l(kr)$ are the Riccati-Bessel functions, and:

$$O_{lm} = \frac{1}{\sqrt{l(l+1)}}\left[\frac{(2l+1)(l-m)!}{4\pi(l+m)!}\right]^{1/2},$$

$$\tau_{lm}(\theta) = \frac{d}{d\theta}P_l^m(\cos\theta),$$

$$\pi_{lm}(\theta) = \frac{m}{\sin\theta}P_l^m(\cos\theta).$$

Equations (2.50)-(2.51) are more convenient for numerical implementation with respect to (2.47)-(2.48) as they just require the knowledge of the source currents inside the resonator to compute electric and magnetic multipole coefficients.

2.3 Nonlinear frequency generation in sub-λ resonators

The accurate control of scattering properties and electromagnetic field confinement in nano-objects is of paramount interest for tailoring the nonlinear optical response of different materials. In the broad spectrum of applications, it offers attractive solutions ranging from ultra-fast switching and reconfigurable nonlinear metasurfaces to the generation of entangled photons with controlled polarization and phase. In the following sections, we will briefly introduce some general concepts of nonlinear frequency generation in bulk materials and then we will present in detail the problem of nonlinear scattering by subwavelength objects.

Generation processes in nonlinear materials

In constitutive equations (2.5)-(2.6) it was shown that for non-magnetic materials the electromagnetic properties of matter are all included in the polarization vector $\boldsymbol{\mathcal{P}}(\boldsymbol{r},t)$. In most of the cases, the induced collective displacement of electrons originates a scattered

field synchronously oscillating with the external electric field and the material response has a linear dependence. For the sake of notation simplicity, let us introduce the problem considering a dispersion-less material, for which we can write:

$$\boldsymbol{\mathcal{P}}(t) = \varepsilon_0 \chi^{(1)} \boldsymbol{\mathcal{E}}(t) \tag{2.52}$$

where $\chi^{(1)}$ is known as the linear susceptibility and ε_0 is the permittivity of free space. In this regime the scattered power is linearly proportional to the incident one, and light-matter interaction result in common phenomena as refraction and reflection. For some materials, the interaction with a sufficiently intense field distorts electronic orbits and modifies their optical properties. The electromagnetic response is no more linear and equation (2.52) can be generalized allowing a nonlinear dependence [9]:

$$\boldsymbol{\mathcal{P}}(t) = \varepsilon_0 \left[\chi^{(1)} \boldsymbol{\mathcal{E}}(t) + \chi^{(2)} \boldsymbol{\mathcal{E}}^2(t) + \chi^{(3)} \boldsymbol{\mathcal{E}}^3(t) + ... \right] \tag{2.53}$$

with $\chi^{(2)}$ and $\chi^{(3)}$ the second- and third-order nonlinear susceptibilities, respectively. One intuitively expects that nonlinear phenomena are no more negligible when the amplitude of external field becomes comparable with the atomic electric field $E_a = e/(4\pi\varepsilon_0 a_0^2) \sim 5 \times 10^{11}$ V/m with e the electron charge and a_0 the Bohr radius of hydrogen atom. For bulk materials, $\chi^{(1)}$ is of the order of unity, thus we expect $\chi^{(2)} \sim 1$ pm/V and $\chi^{(3)} \sim 1$ (pm/V)^2.

In a more accurate picture, the susceptibilities of non-isotropic materials are tensors with rank higher than one. In this case the i-th component of polarization vector is written as:

$$\mathcal{P}_i = \varepsilon_0 \left(\sum_j \chi^{(1)}_{ij} \mathcal{E}_j + \sum_{jk} \chi^{(2)}_{ijk} \mathcal{E}_j \mathcal{E}_k + \sum_{jkl} \chi^{(3)}_{ijkl} \mathcal{E}_j \mathcal{E}_k \mathcal{E}_l + ... \right) \tag{2.54}$$

Replacing equation (2.53) or (2.54) in the electric displacement in (2.5) one has:

$$\boldsymbol{\mathcal{D}}(\boldsymbol{r}, t) = \varepsilon_0 \boldsymbol{\mathcal{E}}(\boldsymbol{r}, t) + \boldsymbol{\mathcal{P}}^{(1)}(\boldsymbol{r}, t) + \boldsymbol{\mathcal{P}}^{NL}(\boldsymbol{r}, t) = \boldsymbol{\mathcal{D}}(\boldsymbol{r}, t)^{(1)} + \boldsymbol{\mathcal{P}}^{NL}(\boldsymbol{r}, t) \tag{2.55}$$

Using (2.55) in (2.4), one can retrieve the wave propagation equation in the presence of a nonlinear medium. Assuming no free charges ($\rho = 0$) and source currents ($\boldsymbol{\mathcal{J}} = 0$) are present and the material to be non-magnetic ($\boldsymbol{\mathcal{M}} = 0$), it is possible to derive:

$$\nabla^2 \boldsymbol{\mathcal{E}} - \frac{\varepsilon_r}{c^2} \frac{\partial^2 \boldsymbol{\mathcal{E}}}{\partial t^2} = \frac{1}{\varepsilon_0 c^2} \frac{\partial \boldsymbol{\mathcal{P}}^{NL}}{\partial t^2} \tag{2.56}$$

Second-order processes

Among all possible nonlinear processes, this thesis is mainly devoted to the analysis of second-order phenomena, nonlinear processes which only occur in non-centrosymmetryc materials. Indeed, since an inversion symmetry of the crystal imposes that the sign of the polarization vector must change upon a change in the electric field sign, we have:

$$-\boldsymbol{\mathcal{P}}^{(2)} = \varepsilon_0 \chi^{(2)} [-\boldsymbol{\mathcal{E}}]^2 = \varepsilon_0 \chi^{(2)} [\boldsymbol{\mathcal{E}}]^2 = \boldsymbol{\mathcal{P}}^{(2)} \implies \chi^{(2)} = 0 \tag{2.57}$$

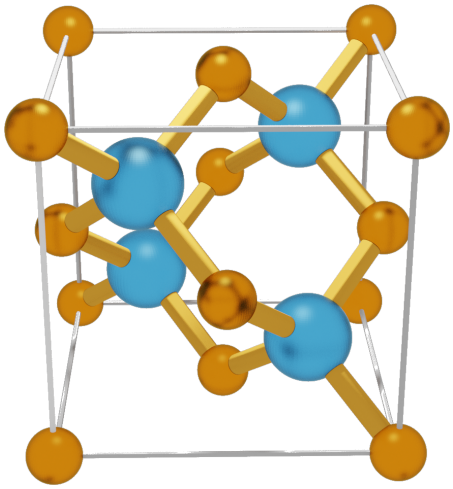

Figure 2.5: Schematic representation of a zincblende ($\bar{4}3m$ symmetry) crystalline structure.

In particular, let us consider aluminum gallium arsenide (AlGaAs), a III-V alloy with zincblende crystalline structure ($\bar{4}3m$ or T_d symmetry) as sketched in Fig. 2.5. In contracted form the quadratic polarizability for this material can be written as

$$\begin{bmatrix} \mathcal{P}_x^{(2)} \\ \mathcal{P}_y^{(2)} \\ \mathcal{P}_z^{(2)} \end{bmatrix} = 2\varepsilon_0 \begin{bmatrix} 0 & 0 & 0 & d_{14} & 0 & 0 \\ 0 & 0 & 0 & 0 & d_{25} & 0 \\ 0 & 0 & 0 & 0 & 0 & d_{36} \end{bmatrix} \begin{bmatrix} \mathcal{E}_x^2 \\ \mathcal{E}_y^2 \\ \mathcal{E}_z^2 \\ \mathcal{E}_y \mathcal{E}_z \\ \mathcal{E}_x \mathcal{E}_z \\ \mathcal{E}_x \mathcal{E}_y \end{bmatrix} \tag{2.58}$$

with $d_{14} = d_{25} = d_{36} = \chi^{(2)}_{xyz}/2$, or equivalently we can write

$$\mathcal{P}_i^{(2)} = \varepsilon_0 \sum_{jk} \chi^{(2)}_{ijk} \mathcal{E}_j \mathcal{E}_k \text{ with } \chi^{(2)}_{ijk} \neq 0 \text{ for } i \neq j \neq k \tag{2.59}$$

To simplify the notation let us consider at first a scalar field made by two time-harmonic

components in the form

$$\mathcal{E}(t) = E_1 e^{-i\omega_1 t} + E_2 e^{-i\omega_2 t} + \text{c.c.}$$

the second-order contribution to the nonlinear polarization is given by:

$$\begin{aligned}\mathcal{P}^{(2)}(t) =& \varepsilon_0 \chi^{(2)} \left[E_1^2 e^{-2i\omega_1 t} + E_2^2 e^{-2i\omega_2 t} + 2E_1 E_2 e^{-i(\omega_1+\omega_2)t} \right. \\ &\left. + 2E_1 E_2^* e^{-i(\omega_1-\omega_2)t} + \text{c.c} \right] + 2\varepsilon_0 \chi^{(2)} \left[E_1 E_1^* + E_2 E_2^* \right]\end{aligned} \tag{2.60}$$

To provide a clearer insight of equation (2.60), it is more convenient to move to the frequency domain and separate all its different contributions:

$$P(2\omega_1) = \varepsilon_0 \chi^{(2)} E_1^2 \quad \text{and} \quad P(2\omega_2) = \varepsilon_0 \chi^{(2)} E_2^2 \quad \text{(SHG)} \tag{2.61}$$

$$P(\omega_1 + \omega_2) = 2\varepsilon_0 \chi^{(2)} E_1 E_2 \quad \text{(SFG)} \tag{2.62}$$

$$P(\omega_1 - \omega_2) = 2\varepsilon_0 \chi^{(2)} E_1 E_2^* \quad \text{(DFG)} \tag{2.63}$$

$$P(0) = 2\varepsilon_0 \chi^{(2)} (E_1 E_1^* + E_2 E_2^*) \quad \text{(OR)} \tag{2.64}$$

They describe four different nonlinear phenomena which are schematically shown in Fig. 2.6: second-harmonic generation (SHG), sum-frequency generation (SFG), difference-frequency generation (DFG) and optical rectification (OR). Please note that energy must be conserved in any process. If for SHG and SFG this condition is trivially satisfied, in case of DFG the creation of a photon at $\omega_3 = \omega_1 - \omega_2$ must be accompanied by a second photon at ω_2, thus the lower frequency input is amplified.

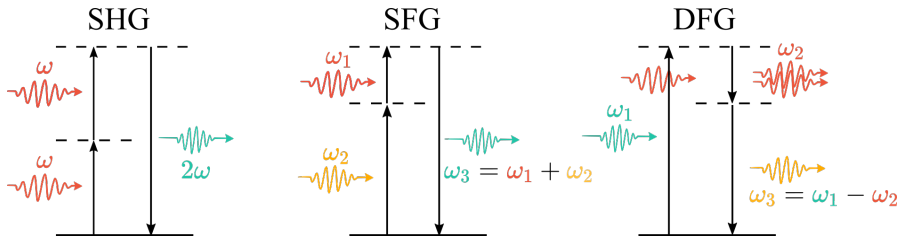

Figure 2.6: Second-order nonlinear generation processes. From left to right: second harmonic generation (SHG), sum frequency generation (SFG), difference frequency generation (DFG).

In this framework, equation (2.56) results in a set of coupled equations of the type:

$$\nabla^2 \mathbf{E}_n + \frac{\omega_n^2}{c^2} \varepsilon_r(\omega_n) \mathbf{E}_n = -\frac{\omega_n^2}{\varepsilon_0 c^2} \mathbf{P}_n^{NL} \tag{2.65}$$

where the index n denotes the different spectral components. Two waves at frequencies ω_1 and ω_2 can get nonlinearly coupled and constitute the source term of the Helmoltz equation at frequency ω_3. The solution of this system of coupled equations leads to complete description of the nonlinear interactions.

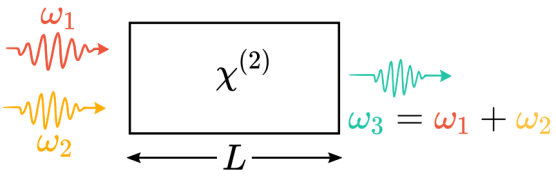

Figure 2.7: Sum frequency generation (SFG) of two signal ω_1 and ω_2 in a $\chi^{(2)}$ crystal

More specifically, as an example, let us suppose that these three waves propagate in a nonlinear bulk medium as sketched in Fig. 2.7, so that their electric field can be written as:

$$\mathcal{E}_j = A_j e^{i(k_j z - \omega_j t)} + \text{c.c} \quad (j = 1, 2, 3) \tag{2.66}$$

with z the linear propagation direction and A_j the slowly varying amplitude along z. It can be shown [9] that (2.65) leads to three coupled equations:

$$\frac{dA_3}{dz} = \frac{i\chi^{(2)}\omega_3^2}{k_3 c^2} A_1 A_2 e^{i\Delta k z}, \tag{2.67}$$

$$\frac{dA_1}{dz} = \frac{i\chi^{(2)}\omega_1^2}{k_1 c^2} A_3 A_2^* e^{-i\Delta k z} \tag{2.68}$$

$$\frac{dA_2}{dz} = \frac{i\chi^{(2)}\omega_2^2}{k_2 c^2} A_3 A_1^* e^{-i\Delta k z} \tag{2.69}$$

where $\Delta k = k_3 - k_2 - k_1$. We note that when $\Delta k = 0$ the amplitude A_3 increases linearly with z, meaning that when the three waves propagate in phase, energy is continously transferred from the fields at ω_1 and ω_2 to the field at $\omega_3 = \omega_1 + \omega_2$. This requirement is known as phase matching condition. Out of this condition, energy is periodically exchanged between the input fields and the output field with a characteristic length $L_c = \pi/\Delta k$ called coherence length. The sum-frequency intensity I_3 originated from the nonlinear interaction of the two pumps with intensities I_1 and I_2 after a distance L is given by:

$$I_3 = \frac{2\chi^{(2)^2}\omega_3^2 I_1 I_2}{n_1 n_2 n_3 \varepsilon_0 c^2} L^2 \,\text{sinc}^2\left(\frac{\Delta k L}{2}\right) \tag{2.70}$$

Third-order processes

At variance with the $\chi^{(2)}$ case, third-order nonlinear terms in (2.54) are not subjected to symmetry restrictions. In analogy with equation 2.60, we can analyze the third-order polarization vector

$$\mathcal{P}^{(3)}(t) = \varepsilon_0 \chi^{(3)} \mathcal{E}(t)^3 \tag{2.71}$$

induced by an electric field composed by the superposition of three monochromatic waves

$$\mathcal{E}(t) = E_1 e^{-i\omega_1 t} + E_2 e^{-i\omega_2 t} + E_3 e^{-i\omega_3 t} + \text{c.c.} \tag{2.72}$$

After some algebra one finds 44 frequency components, considering separately positive and negative frequencies, which highlights the multitude of $\chi^{(3)}$ effects such as four-wave mixing (FWM), self- and cross-phase modulation, self-focusing and optical Kerr effect [9]. In the particular case of a monochromatic driving field, we get

$$\mathcal{P}^{(3)}(t) = \varepsilon_0 \chi^{(3)} \left[E_0^3 e^{-i3\omega t} + \text{c.c.} \right] + 3\varepsilon_0 \chi^{(3)} \left[E_0^2 E_0^* e^{-i\omega t} + \text{c.c.} \right]. \tag{2.73}$$

The first term describes third-harmonic generation (THG), in which three photons at ω are annihilated to create one photon at 3ω. THG with some non-degenerate FWM processes are sketched in Fig. 2.8.

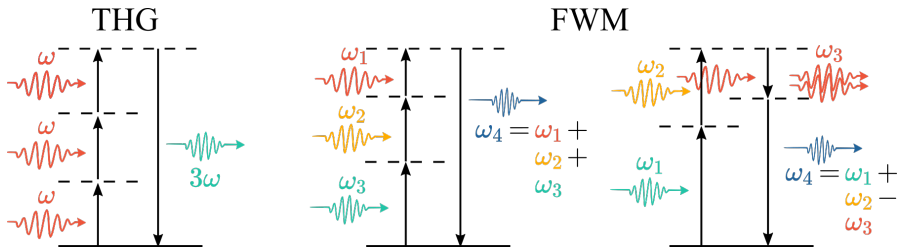

Figure 2.8: Third-order nonlinear generation processes. Left: third-harmonic generation (THG). Right: non-degenerate four-wave mixing (FWM).

The second term in (2.73) describes the propagation of a signal at ω which constitutes an additional contribution to the linear polarization vector. In the presence of this effect, the refractive index of the material can be written as

$$n = n_0 + n_2 I \tag{2.74}$$

where n_0 is the linear refractive index, I is the field intensity and

$$n_2 = \frac{3}{2n_0^2 \varepsilon_0 c} \chi^{(3)}. \tag{2.75}$$

Material refractive index, and consequently wave propagation, is modulated by the intensity of the incident wave, which can result for example in self-focusing [9].

Radiation by a localized nonlinear source

From a phenomenological point of view, equation (2.70) states that nonlinear generation with detectable intensity requires strong driving fields which overlap in phase for a large interaction length. In this perspective, optically resonant systems as Fabry-Perot cavities offer a valuable solution to confine the field, boost the nonlinear interaction and consequently the generation efficiency. Similarly, nanoresonators are excellent candidates for their ability to tightly trap the electromagnetic field at the sub-wavelength scale. Differently from the case of equations (2.67)-(2.69), in a nano-object the picture of interacting fields that propagate along a preferred direction, as in bulk media or optical waveguides, is no longer valid and the concept of phase matching has to be recast.

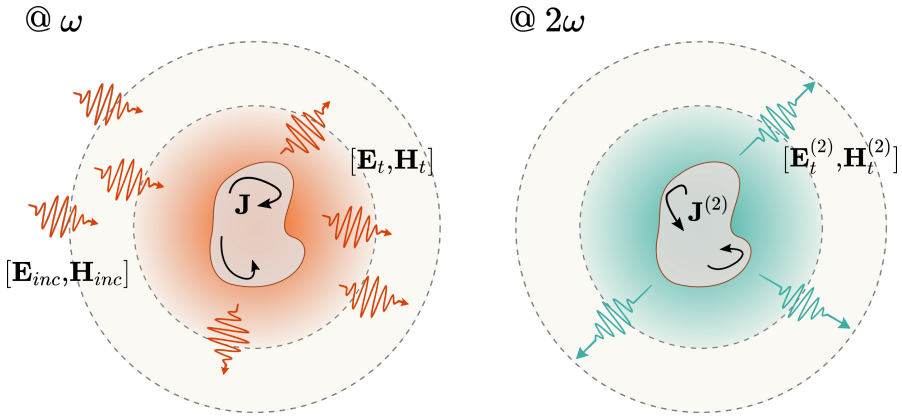

Figure 2.9: SHG process in a nanostructure. A plane wave $[\mathbf{E}_{inc}, \mathbf{H}_{inc}]$ interacts with the nano-object creating a current distribution $\mathbf{J}$ in its volume. The quadratic susceptibility of the material and the strong field confinement induce a second harmonic current distribution $\mathbf{J}^{(2)} = i\varepsilon_0\chi^{(2)}2\omega\mathbf{E}_t\mathbf{E}_t$ which is the driving term of the radiated field $[\mathbf{E}_t^{(2)}, \mathbf{H}_t^{(2)}]$ at 2ω.

Let us consider the specific case of SHG. The scattering problem presented in Fig. 2.1 can be generalized as a two-step process sketched in Fig. 2.9:

- An external wave $[\mathbf{E}_{inc}, \mathbf{H}_{inc}]$ excites the nanoresonator, leading to a total electromagnetic field $[\mathbf{E}_t, \mathbf{H}_t]$ at ω confined inside its volume;

- a nonlinear polarization vector bulids up in the nonlinear medium according to equation (2.61) leading to a localized current term

$$J_l^{(2)}(2\omega) = -2i\omega\varepsilon_0 \sum_{mn} \chi_{lmn}^{(2)} E_{t,m}(\omega) E_{t,n}(\omega). \tag{2.76}$$

  $\mathbf{J}^{(2)}$ is the driving source of a second wave equation at 2ω, whose solution determines the electromagnetic field $[\mathbf{E}_t^{(2)}, \mathbf{H}_t^{(2)}]$.

This simplified picture relies on two approximations:

- undepleted pump, i.e. the nonlinear interaction is weak and pump losses are just due to the material absorption;

- negligible cascading phenomena originated by photons at 2ω coupling back with photons at ω (DFG,SFG,...).

Once $[\mathbf{E}_t^{(2)}, \mathbf{H}_t^{(2)}]$ are known, it is possible to define the nonlinear absorption and scattering cross sections:

$$\sigma_{abs}^{(2)} = \frac{W_{abs}^{(2)}}{S_0} = -\frac{1}{2S_0}\int_\Omega \mathrm{Re}(\mathbf{J}_t^{(2)*}\cdot\mathbf{E}_t^{(2)})d\boldsymbol{r} \tag{2.77}$$

$$\sigma_{sca}^{(2)} = \frac{W_{sca}^{(2)}}{S_0} = \frac{1}{2S_0}\oint_\Sigma \mathrm{Re}(\mathbf{E}_t^{(2)}\times\mathbf{H}_t^{(2)*})\cdot\mathbf{n}d\sigma \tag{2.78}$$

As it is clear from (2.61) and (2.76), the power radiated at SH, $W_{sca}^{(2)}$, scales with the square of incident intensity S_0. Thus, at variance with linear scattering, cross sections (2.77)-(2.78) scale linearly with the impinging power. Consequently, we define the SHG efficiency, η_{SHG}, as the ratio between radiated power at 2ω and the square of the power impinging on the nanostructure

$$\eta_{SHG} = \frac{W_{sca}^{(2)}}{(\sigma_{geom}S_0)^2} \quad [\mathrm{W}^{-1}] \tag{2.79}$$

which is independent of the pump power. A closed-form solution for the problem in Fig. 2.9 can be found just for very specific cases, i.e. a nanosphere suspended in a uniform medium [10]. For more complex geometries it is necessary to rely on numerical calculations.

2.4 Numerical calculation of SHG in nanostructures

Since the birth of nano-optics, several numerical tools have been proposed to study the interaction of electromagnetic fields with nanostructured matter. Among others, let us mention the transition matrix null field method ($\mathcal{T}$-Matrix), the discrete dipole approximation (DDA), the finite difference time domain (FDTD) and the finite element method (FEM). A detailed comparisons can be found in [11, 12]. All along this work we adopt the FEM for its good accuracy in computing near-field distributions in complex 3D geometries and the possibility to handle complex empirical dispersion relations, which are sometimes hard to accurately fit with analytical models (e.g. Lorentz-Drude). In this section we provide technical details on the numerical solution of the problem of Fig. 2.9 with COMSOL Multiphysics.

Linear scattering

The general idea of FEM is to discretize the 3D geometry under study into a finite number of elements with a desired shape. For result accuracy and convergence speed, the most convenient choice in our case is to use tetrahedral elements. This mesh allows to discretize Maxwell equations (2.1)-(2.4) and iteratively search for approximate solutions under appropriate boundary conditions. In the RF module of COMSOL Multiphysics, wave equations are solved in the frequency domain. The analysis of light scattering by a nano-object, as in Fig. 2.9, requires to solve an unbounded problem. In COMSOL Multiphysics the infinite space can be modeled by surrounding the geometry under study with an ideal layer, called perfectly matched layer (PML), which absorbs all the outgoing waves preventing any reflection at the edges. An illustration of the typical mesh used to study the scattering of a nanocylinder on a substrate is reported in Fig. 2.10. The general guideline followed to design the mesh is to set the maximum element size equal to $\lambda/(5n)$, where λ is the wavelength in vacuum and n the refractive index of the material, with a further refinement close to critical points to avoid unphysical solutions and boost convergence.

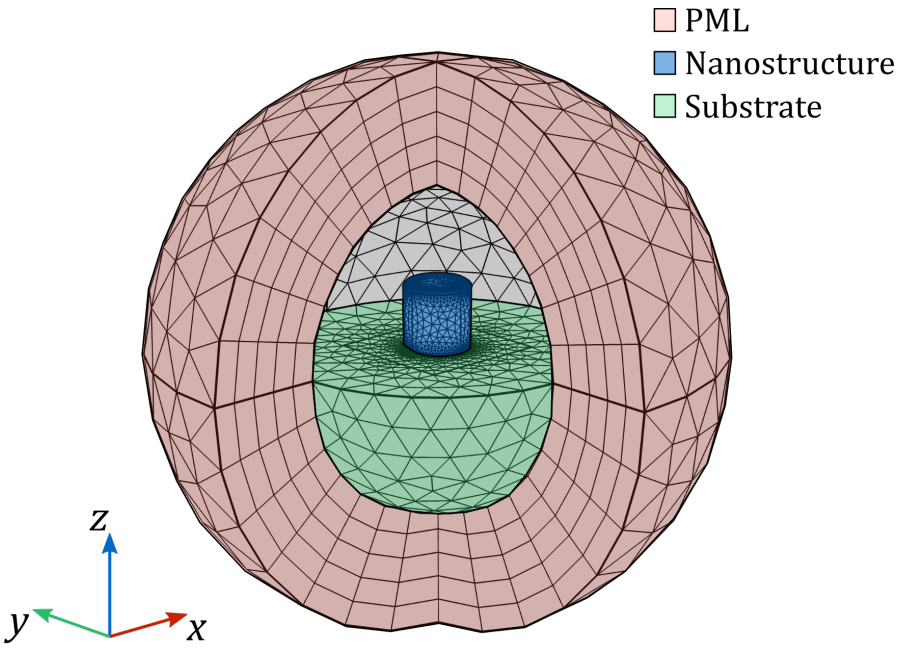

Figure 2.10: Mesh definition in COMSOL Multiphysics of a PML-mapped space for the analysis of light scattering by an isolated nanocylinder on substrate

The optical response is computed in scattered-field formulation of RF module. The background field $[\mathbf{E}_b, \mathbf{H}_b]$ is set analytically as the solution of the wave equation when the nanostructure is removed. It corresponds to the field refracted at the interface (set at $z = z_0$) between the hosting medium (n_h) and the substrate (n_s). For an impinging plane wave with k vector along $-z$

$$\begin{aligned} \mathbf{E}_b(x, y, z > z_0) &= \mathbf{E}_0 \left[e^{in_h kz} + r_s e^{-in_h kz} \right] \\ \mathbf{E}_b(x, y, z < z_0) &= \mathbf{E}_0 t_s e^{in_s kz} \end{aligned} \tag{2.80}$$

with r_s and t_s the reflection and transmission Fresnel coefficients.

To provide a numerical example, let us consider an AlGaAs nanocylinder suspended in air ($n_h = n_s = 1$) and excited by a linearly polarized plane wave along x ($\mathbf{E}_0 = E_0\hat{\mathbf{x}}$). We set the radius $r = 220$ nm and height $h = 400$ nm. The numerical computation of scattered near-field $[\mathbf{E}_S, \mathbf{H}_S]$ enables to derive the scattering cross section σ_{sca} according to (2.31). Besides, as the nanocylinder is surrounded by a uniform medium, (2.50)-(2.51) can be applied once the source current $\mathbf{J}_S$ has been computed, and the multipolar contribution to σ_{sca} can be retrieved via (2.46). The spectral response in the near infrared (see Fig. 2.11) exhibits several resonant peaks with different multipolar contributions.

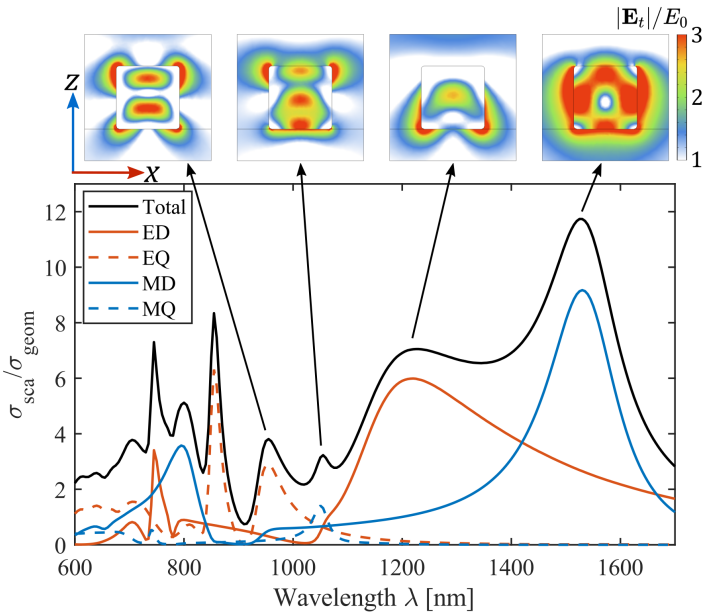

Figure 2.11: Linear scattering of a plane wave impinging on an air-suspended AlGaAs nanocylinder with radius $r = 220$ nm and height $h = 400$ nm. The k-vector of the external excitation is aligned with the axis of the cylinder. The numerically computed scattering cross section σ_{sca} is normalized by the geometrical one $\sigma_{geom} = \pi r^2$. The electric (red) and magnetic (blue) multipolar contribution to the scattering have been computed according to (2.50)-(2.51) for $l < 3$, and the azimuthal orders m have been summed up. Insets: field enhancement (electric field module normalized to the incident field amplitude) for the four peaks at lowest frequencies.

The resulting field enhancement in the structure volume, shown in the near-field distribution in Fig. 2.11, is one of the key features to maximize the nonlinear generation efficiency.

Second harmonic generation

Once the total field $[\mathbf{E}_t(\boldsymbol{r}, \omega), \mathbf{H}_t(\boldsymbol{r}, \omega)]$ is known, the radiation problem at 2ω in Fig. 2.9 can be solved independently in COMSOL Multyphysics. It suffices to undertake in its RF module a second study at 2ω, with the same geometry and PML, and impose an external current source as in (2.76) [13].

Let us consider the broad magnetic dipole resonance in Fig. 2.11 and compute the SH radiation, as described in (2.78) for a fundamental frequency (FF) in the range $\lambda_{FF} \in$

[1400 – 1700] nm. The result is shown in Fig. 2.12a, while Fig. 2.12b reports the near-field map at 2ω corresponding to the SHG maximum. The knowledge of total current near-field distribution enables in turn to extract the nonlinear radiation properties of the nanostructure, as the field outside the antenna can be written as:

$$\mathbf{E}_t^{(2)}(\boldsymbol{r}, 2\omega) = 2i\omega\mu \int_V \overleftrightarrow{\mathbf{G}}(\boldsymbol{r}, \boldsymbol{r}')\mathbf{J}(\boldsymbol{r}', 2\omega)d^3r \tag{2.81}$$

where $\overleftrightarrow{\mathbf{G}}(\boldsymbol{r}, \boldsymbol{r}')$ is the dyadic Green function of the system [14]. This can be performed numerically either in COMSOL, through Stratton-Chu formula, or with external near-to-far field transformation packages for a broader validity [15] (e.g. antennas on substrates, metals, thin layers,...). Fig. 2.12c reports an exemplary far-field calculation corresponding to the near field distribution in Fig. 2.12b. This provides an efficient tool to predict the collected power in a typical nonlinear microscopy characterization and optimize the nanostructure geometry. The resonant behavior highlighted by Fig. 2.12 and the comparison with nonlinear generation in microcavities make already possible some general considerations for the optimization process:

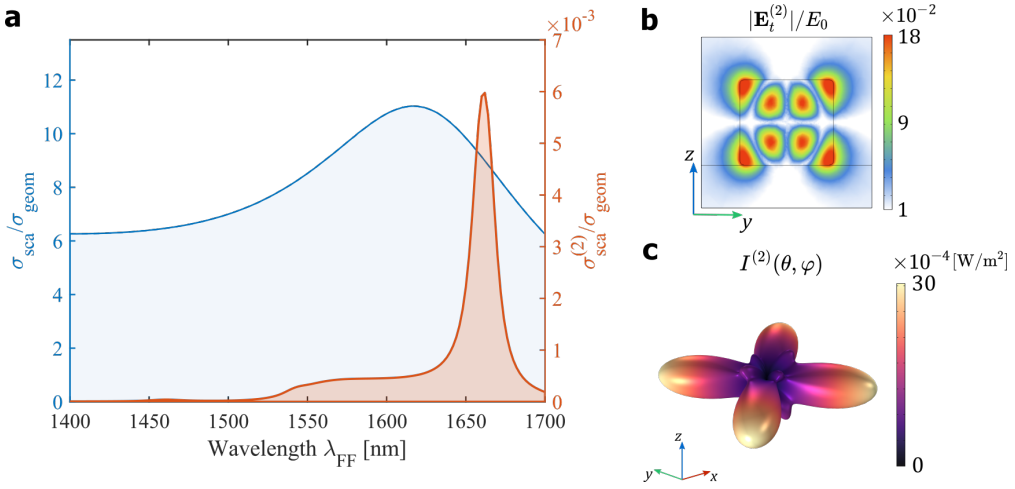

Figure 2.12: Numerical calculation of SHG in an air-suspended AlGaAs nanocylinder. (a) Linear (blue line) and SH (red line) scattering cross section computed as in (2.78) in the pump wavelength range $\lambda_{FF} \in$ [1400 nm – 1700 nm]. (b) Near-field module of SH electric field normalized to incident field SHG maximum, corresponding to $\lambda_{FF} = 1662$ nm. (c) Far-field transformation of the distribution in (b).

- an efficient generation is achieved when a doubly resonant condition (at FF and SH) is fulfilled, a well known outcome of nonlinear generation in closed cavities [16, 17];
- the longer light is trapped inside the cavity, the larger the interaction between FF and SH fields. Conversion efficiency is therefore expected to scale with the quality factors of resonances at FF and SH;
- field enhancement inside the nanostructure depends in some way on the overlap between the incident field and the resonant mode of the cavity. Thus, the SHG coefficient should quadratically scale with a term describing how well energy is transferred from the external plane wave to the nanoresonator;
- there should be a coefficient describing how efficiently energy is transferred between

the resonances at ω and 2ω (in optical waveguides, which often provide a useful analogy, this term depends on the spatial overlap of guided modes at FF and SH);

- finally, SH power needs to be efficiently extracted from the cavity. The far-field properties of the resonance must be taken into account to evaluate the fraction of total generated power that is effectively collected.

2.5 Conclusion

In this chapter we provided the theoretical context for studying nonlinear optical phenomena in nanostructures. After expliciting the fundamental physical quantities to describe a nonlinear scattering problem, numerical methods to solve Maxwell equations at harmonic frequencies have been proposed. Focusing the attention on the specific case of second harmonic generation in AlGaAs nanoresonators, it was possible to trace a clear parallelism between microcavities and nanoantennas. However, even if the proposed numerical tools can reveal the resonant behavior of harmonic generation, full vectorial calculations and multipolar analysis may not suffice to quantitatively define all the figures of merit that grant an efficient generation. During this thesis, it appeared clear that moving to the framework of modal analysis would offer a better description in terms of physical understanding and design guidelines. This theoretical development is the core of next chapter.

References

[1] J. D. Jackson, *Classical Electrodynamics*, Third Edit. John Wiley & Sons, 1998.

[2] C. F. Bohren and D. R. Huffman, *Absorption and Scattering of Light by Small Particles*. 1983.

[3] A. I. Kuznetsov, A. E. Miroshnichenko, Y. H. Fu, J. Zhang, and B. Lukyanchukl, 'Magnetic light,' *Scientific Reports*, vol. 2, pp. 1–6, 2012. DOI: 10.1038/srep00492.

[4] M. Kerker, D. S. Wang, and C. L. Giles, 'Electromagnetic Scattering By Magnetic Spheres.,' *Journal of the Optical Society of America*, vol. 73, pp. 765–767, 1983. DOI: 10.1364/JOSA.73.000765.

[5] S. Person, M. Jain, Z. Lapin, J. J. Sáenz, G. Wicks, and L. Novotny, 'Demonstration of zero optical backscattering from single nanoparticles,' *Nano Letters*, vol. 13, pp. 1806–1809, 2013. DOI: 10.1021/nl4005018.

[6] A. E. Miroshnichenko, A. B. Evlyukhin, Y. F. Yu, R. M. Bakker, A. Chipouline, A. I. Kuznetsov, B. Luk'yanchuk, B. N. Chichkov, and Y. S. Kivshar, 'Nonradiating anapole modes in dielectric nanoparticles,' *Nature Communications*, vol. 6, pp. 1–8, 2015. DOI: 10.1038/ncomms9069.

[7] G. Mie, 'Beiträge zur Optik trüber Medien, speziel kolloidaler Metallösungen. Ann. Phys,' vol. 25, pp. 377–445, 1908.

[8] P. Grahn, A. Shevchenko, and M. Kaivola, 'Electromagnetic multipole theory for optical nanomaterials,' *New Journal of Physics*, vol. 14, pp. 1–11, 2012. DOI: 10.1088/1367-2630/14/9/093033.

[9] R. Boyd, *Nonlinear Optics*, 3rd. Academic Press, 2008.

[10] K. Frizyuk, I. Volkovskaya, D. Smirnova, A. Poddubny, and M. Petrov, 'Second-harmonic generation in Mie-resonant dielectric nanoparticles made of noncentrosymmetric materials,' *Physical Review B*, vol. 99, pp. 1–17, 2019. DOI: 10.1103/PhysRevB.99.075425.

[11] M. Karamehmedović, R. Schuh, V. Schmidt, T. Wriedt, C. Matyssek, W. Hergert, A. Stalmashonak, G. Seifert, and O. Stranik, 'Comparison of numerical methods in near-field computation for metallic nanoparticles,' *Optics Express*, vol. 19, pp. 8939–8953, 2011. DOI: 10.1364/oe.19.008939.

[12] T. Grosges, A. Vial, and D. Barchiesi, 'Models of near-field spectroscopic studies : comparison between Finite-Element and Finite-Difference methods,' *Optics express*, vol. 13, pp. 8483–8497, 2005.

[13] L. Carletti, A. Locatelli, O. Stepanenko, G. Leo, and C. De Angelis, 'Enhanced second-harmonic generation from magnetic resonance in AlGaAs nanoantennas,' *Optics Express*, vol. 23, pp. 26 544–26 550, 2015. DOI: 10.1364/OE.23.026544.

[14] L. Novotny and B. Hecht, *Principles of nano-optics*. 2006, vol. 66.

[15] J. Yang, J. P. Hugonin, and P. Lalanne, 'Near-to-Far Field Transformations for Radiative and Guided Waves,' *ACS Photonics*, vol. 3, pp. 395–402, 2016. DOI: 10.1021/acsphotonics.5b00559.

[16] V. Berger, 'Second-harmonic generation in monolithic cavities,' *JOSA B*, vol. 14, pp. 1351–1360, 1997.

[17] M. Liscidini and L. C. Andreani, 'Second-harmonic generation in doubly resonant microcavities with periodic dielectric mirrors,' *Physical Review E - Statistical, Nonlinear, and Soft Matter Physics*, vol. 73, pp. 1–11, 2006. DOI: 10.1103/PhysRevE.73.016613.

QNM expansion in nonlinear nano-optics

3

Contents

Chapter 2 emphasized that linear and nonlinear responses of subwavelength structures to an external excitation commonly involve a large amount of resonances. Even if multipolar expansion provides an intuitive physical description of the system, it underlines that the interaction of light with nanoantennas relies on the natural modes of the structure which, except for the exemplary case of a sphere suspended in a uniform medium, do not correspond to vector spherical wave functions. Therefore, it appears natural to root back on a modal formalism to describe the nonlinear response of subwavelength resonators, as it is usually done in waveguides and closed cavities.

Let us introduce this framework with the pedagogic example of a one dimensional vibrating string. From undergraduate textbooks we know that when the string is fixed at both ends, i.e. $x = 0$ and $x = L$, its natural modes are standing waves with a transverse amplitude profile described by:

$$y_n(x,t) = a_n \sin\left(\frac{n\pi}{L}x\right)\cos(2\pi f_n t) \tag{3.1}$$

where L is the string length, n an integer number and $f_n = nv/2L$ the natural frequency of n-th mode (v being the speed of mechanical waves in the medium). When the system is excited with an external perturbation, energy is transferred to these modes, which are the sole vibrations allowed in the string. The response of the system can be decomposed as a sum of standing waves:

$$y(x,t) = \sum_n a_n \sin\left(\frac{n\pi}{L}x\right)\cos\left(\frac{n\pi v}{L}t\right) \tag{3.2}$$

The spectrum of this signal is a series of Dirac deltas with different amplitudes a_n, and mathematically we expect that this oscillation will last indefinitely in the system. In real world, when we excite an acoustic (e.g. vibrating string, Helmoltz resonator) as well as an optical resonator (e.g. Fabry-Perot cavity), we always experience a finite oscillation with a caracteristic exponential decay in time. Usually we cope with this problem introducing small perturbations to describe the energy leakage, and the efficiency of the resonator in storing energy defines its quality factor, Q.

In the following, we will describe optical nanoresonators in the broad context of open cavity systems. From the guided-optics perspective, nanoantennas can be seen as low-Q cavities with large radiation losses, and the scattering problem can be described schematically as a two step process [1]: 1) at time $t = 0$ an external field transfers energy to those resonator modes that it is able to excite; 2) these leaky modes exponentially decay in time, radiating away the stored energy. Total energy is therefore not conserved during the process in this open cavity, whose physics is described by non-Hermitian operators. The eigenstates of the wave equation obey to outgoing-wave boundary conditions (Sommerfeld radiation condition) at infinity, and consistently with literature of open-systems we will refer to them as Quasinormal Modes (QNM)[2].

3.1 Quasinormal Modes of electromagnetic resonators

In electrodynamics, quasinormal modes are the time-harmonic solutions of the source-free Maxwell equations (2.13) [1, 3–5]:

$$\begin{bmatrix} 0 & i\boldsymbol{\varepsilon}^{-1}(\boldsymbol{r},\widetilde{\omega}_m)\nabla\times \\ -i\boldsymbol{\mu}^{-1}(\boldsymbol{r},\widetilde{\omega}_m)\nabla\times & 0 \end{bmatrix}\begin{bmatrix}\widetilde{\mathbf{E}}_m(\boldsymbol{r})\\ \widetilde{\mathbf{H}}_m(\boldsymbol{r})\end{bmatrix} = \widetilde{\omega}_m\begin{bmatrix}\widetilde{\mathbf{E}}_m(\boldsymbol{r})\\ \widetilde{\mathbf{H}}_m(\boldsymbol{r})\end{bmatrix} \tag{3.3}$$

where $\boldsymbol{\varepsilon}$ and $\boldsymbol{\mu}$ are the permittivity and permeability tensors of the whole system (resonator plus its background), while $\widetilde{\omega}_m$ and $[\widetilde{\mathbf{E}}_m(\boldsymbol{r}), \widetilde{\mathbf{H}}_m(\boldsymbol{r})]$ are the eigenfrequencies and eigenvectors respectively. In closed systems, cavity eigenfrequencies ω_m are real quantities and losses are introduced as perturbations. Their main outcome is to transform a series of Dirac delta in the spectral response into Lorentzian features with finite bandwidth. Conversely, leaky systems exhibit QNMs with complex-valued eigenfrequencies $\widetilde{\omega}_m = \Omega_m - i\Gamma_m/2$ where Ω_m is the central resonant frequency and Γ_m is the damping rate directly related to the mode lifetime $\tau_m = 1/\Gamma_m$.

Let us write compactly the eigenproblem (3.3) [6]

$$\hat{\mathbf{H}}\widetilde{\boldsymbol{\psi}}_m(\boldsymbol{r}) = \widetilde{\omega}_m\widetilde{\boldsymbol{\psi}}_m(\boldsymbol{r}) \tag{3.4}$$

where $\widetilde{\boldsymbol{\psi}}_m = [\widetilde{\mathbf{E}}_m, \widetilde{\mathbf{H}}_m]$. The solution of any light scattering problem

$$\hat{\mathbf{H}}\boldsymbol{\Psi}(\omega, \boldsymbol{r}) = \omega\boldsymbol{\Psi}(\omega, \boldsymbol{r}) + \mathbf{S}(\omega, \boldsymbol{r}) \tag{3.5}$$

where $\boldsymbol{\Psi} = [\mathbf{E}, \mathbf{H}]$ and $\mathbf{S} = [i\varepsilon^{-1}\mathbf{J}_0, 0]$ is an external driving source, can be expanded on the QNM basis

$$\boldsymbol{\Psi}(\omega, \boldsymbol{r}) = \sum_m \alpha_m(\omega)\widetilde{\boldsymbol{\psi}}_m(\boldsymbol{r}) \tag{3.6}$$

which is exactly correct if the orthonormal basis is complete. Equation (3.6) highlights the efficiency of the method: once the modes of the system are known, it suffices to retrieve the excitation coefficients of any driving field $\mathbf{S}$ to solve the problem. In this section, we revise the properties of electromagnetic QNMs. We will describe how they are numerically computed and normalized, with some remarks on the completeness of their basis.

Poynting Theorem and quality factor

Differently from Chapter 2, where we just considered real frequencies, here the reality of time-dependent fields $\boldsymbol{\mathcal{E}}, \boldsymbol{\mathcal{H}}$ imposes $\boldsymbol{\varepsilon}(-\widetilde{\omega}^*) = \boldsymbol{\varepsilon}^*(\widetilde{\omega})$ and $\boldsymbol{\mu}(-\widetilde{\omega}^*) = \boldsymbol{\mu}^*(\widetilde{\omega})$. This means that if $[\widetilde{\mathbf{E}}_m(\boldsymbol{r}), \widetilde{\mathbf{H}}_m(\boldsymbol{r})]$ is a QNM with eigenfrequency $\widetilde{\omega}_m$, $[\widetilde{\mathbf{E}}^*_m(\boldsymbol{r}), \widetilde{\mathbf{H}}^*_m(\boldsymbol{r})]$ is a solution of source-free Maxwell equation too, with eigenfrequency $-\widetilde{\omega}^*_m$ and the same Poynting vector, indeed $\widetilde{\mathbf{E}}_m \times \widetilde{\mathbf{H}}^*_m + \widetilde{\mathbf{E}}^*_m \times \widetilde{\mathbf{H}}_m = 2\mathrm{Re}(\widetilde{\mathbf{E}}_m \times \widetilde{\mathbf{H}}^*_m)$. Let us consider for the sake of simplicity an isotropic material:

$$\nabla \times \widetilde{\mathbf{E}}_m = i\mu(\widetilde{\omega}_m)\widetilde{\omega}_m\widetilde{\mathbf{H}}_m \quad \text{and} \quad \nabla \times \widetilde{\mathbf{H}}_m = -i\varepsilon(\widetilde{\omega}_m)\widetilde{\omega}_m\widetilde{\mathbf{H}}_m \tag{3.7}$$

$$\nabla \times \widetilde{\mathbf{E}}^*_m = -i\mu(-\widetilde{\omega}^*_m)\widetilde{\omega}^*_m\widetilde{\mathbf{H}}^*_m \quad \text{and} \quad \nabla \times \widetilde{\mathbf{H}}^*_m = i\varepsilon(-\widetilde{\omega}^*_m)\widetilde{\omega}^*_m\widetilde{\mathbf{H}}^*_m \tag{3.8}$$

Let us focus now on the integral of $\nabla \cdot (\widetilde{\mathbf{E}}_m \times \widetilde{\mathbf{H}}^*_m + \widetilde{\mathbf{E}}^*_m \times \widetilde{\mathbf{H}}_m)$ over a volume V surrounded by a closed surface Σ. Applying the vector identity $\nabla \cdot (\mathbf{E}_1 \times \mathbf{H}_2) = \mathbf{H}_2 \cdot (\nabla \times \mathbf{E}_1) - \mathbf{E}_1 \cdot (\nabla \times \mathbf{H}_2)$ and the divergence theorem leads to [1]:

$$\oiint_\Sigma \mathrm{Re}(\widetilde{\mathbf{E}}_m \times \widetilde{\mathbf{H}}^*_m) \cdot \hat{\mathbf{n}} d\sigma = -\iiint_V \left[\mathrm{Im}\left[\widetilde{\omega}_m\varepsilon(\widetilde{\omega}_m)\right]\widetilde{\mathbf{E}}_m \cdot \widetilde{\mathbf{E}}^*_m + \mathrm{Im}\left[\widetilde{\omega}_m\mu(\widetilde{\omega}_m)\right]\widetilde{\mathbf{H}}_m \cdot \widetilde{\mathbf{H}}^*_m\right] d^3\boldsymbol{r} \tag{3.9}$$

where $\varepsilon - \varepsilon^* = 2i\mathrm{Im}(\varepsilon)$ was used. Expanding $\widetilde{\omega}_m = \Omega_m + i\Gamma_m/2$, Poynting theorem can be derived:

$$\frac{1}{2}\oiint_{\Sigma} \mathrm{Re}(\widetilde{\mathbf{E}}_m \times \widetilde{\mathbf{H}}_m^*) \cdot \hat{\mathbf{n}} d\sigma + \frac{\Omega_m}{2} \iiint_V \left[\mathrm{Im}\left[\varepsilon(\widetilde{\omega}_m)\right] |\widetilde{\mathbf{E}}_m|^2 + \mathrm{Im}\left[\mu(\widetilde{\omega}_m)\right] |\widetilde{\mathbf{H}}_m|^2 \right] d^3\boldsymbol{r} = \\ = \frac{\Gamma_m}{4} \iiint_V \left[\mathrm{Re}\left[\varepsilon(\widetilde{\omega}_m)\right] |\widetilde{\mathbf{E}}_m|^2 + \mathrm{Re}\left[\mu(\widetilde{\omega}_m)\right] |\widetilde{\mathbf{H}}_m|^2 \right] d^3\boldsymbol{r} \tag{3.10}$$

In case of a non-dispersive resonator, the two terms on the left-hand side of equation (3.10) describe energy losses by radiation and absorption, respectively, while the right-hand side term represents the electromagnetic energy stored in the volume V.

These quantities define in turn the resonator quality factor expressing the energy loss per cycle [6]:

$$Q_m = 2\pi \frac{\text{Energy stored}}{\text{Energy dissipated per cycle}} = \Omega_m \frac{W_e}{P_{abs} + P_{rad}} = \frac{\Omega_m}{\Gamma_m} \tag{3.11}$$

The mode Q-factor can be decomposed in two intrinsic contributions, $1/Q = 1/Q_{abs} + 1/Q_{rad}$ with $Q_{abs} = \Omega_m W_e / P_{abs}$ and $Q_{rad} = \Omega_m W_e / P_{rad}$.

Mode normalization

In order to take advantage of QNM formalism, two central questions have to be clarified.

1) How are QNMs computed and normalized? 2) Do these modes form a complete orthonormal basis susceptible to describe all the properties of the system? For time-harmonic solutions of source-free Maxwell equations satisfing outgoing-wave boundary conditions, the term $\exp[i(\boldsymbol{k} \cdot \boldsymbol{r} - i\omega t)]$ diverges at infinity, and it was already pointed out that energy is dissipated by the system. Thus standard normalizations based on energy considerations are no longer valid. The literature of lossy systems copes with the normalization problem substituting the conjugated product $\widetilde{\mathbf{E}}_m \cdot \widetilde{\mathbf{E}}_m^*$ with $\widetilde{\mathbf{E}}_m \cdot \widetilde{\mathbf{E}}_m$. Indeed the normalization based on $\widetilde{\mathbf{E}}_m \cdot \widetilde{\mathbf{E}}_m^*$ ignores the phase of the resonant mode, and it is a good approximation for slightly absorbing media or high-Q resonators [7]. Please note that the suppression of conjugated product is also detailed in textbooks [8] for the case of absorbing waveguides. However, this substitution doesn't solve the problem of diverging fields when trying to define the normalization integral over a finite volume. There have been several attempts in literature to solve this problem [2, 9–11]. The numerical solution adopted in the following takes inspiration from the literature on perfectly matched layers (PMLs) [10]. The physical domain containing the resonator and its background is enclosed by an (ideally) infinetely thick absorbing material, which damps the exponentially growing QNM field.

Within this approach, mode normalization is defined by [10]:

$$\langle \widetilde{\mathbf{E}}_m | \widetilde{\mathbf{E}}_n \rangle = \iiint_{\Omega} \left[\widetilde{\mathbf{E}}_m \cdot \left(\frac{\partial \omega \varepsilon}{\partial \omega} \right) \widetilde{\mathbf{E}}_n + \widetilde{\mathbf{H}}_m \cdot \left(\frac{\partial \omega \mu}{\partial \omega} \right) \widetilde{\mathbf{H}}_n \right] d^3\boldsymbol{r} = \delta_{mn} \tag{3.12}$$

Derivatives in equation (3.12) are taken at QNM frequencies $\widetilde{\omega}_m$ and Ω includes the physical (V) and PML-mapped volumes.

3.2 Modal analysis of linear dispersive nanoresonators

For frequency-dependent permittivities and permeabilities, the eigenvalue problem (3.3) is generally nonlinear with respect to ω. Commercially available software packages are not well-suited to directly solve numerically this problem and extract the eigenfrequencies. To this end, different approaches have been adopted in literature: pole-search approach, perturbation theory, auxiliary-fields method, Keldysh theorem, Riesz-projection method [4, 6, 11–15]. The following treatment focuses on the auxiliary-field formalism, which was presented in [6] to solve the eigenvalue problem (3.3). For the sake of completeness, we report here its main keypoints, while for a deeper analysis the interested reader can refer to [6].

Auxiliary-field formalism

In this section we restrict our analysis to isotropic and non-magnetic materials, for which $\boldsymbol{\mu}(\omega) = \mu_0$. The nonlinearity of eigenproblem (3.3) arises from the dispersive permittivity $\varepsilon(\omega)$, which for most materials can be modeled at optical frequencies with an N-pole Lorentz-Drude model:

$$\varepsilon(\omega) = \varepsilon_\infty - \varepsilon_\infty \sum_{i=1}^{N} \frac{\omega_{p,i}^2}{\omega^2 - \omega_{0,i}^2 - i\omega\gamma_i} \tag{3.13}$$

For the sake of simplicity, in the following we will use a single-pole dispersion and set $N = 1$. However, the same conclusions can be extended to the general case $N > 1$. The general idea of the method is to increase the dimension of the eigenvector in order to linearize the problem (3.3). Based on (3.13), one can introduce two auxiliary fields:

$$\mathbf{P} = -\varepsilon_0 \varepsilon_\infty \frac{\omega_p^2}{\omega^2 - \omega_0^2 + i\omega\gamma} \mathbf{E}, \; \mathbf{J} = -i\omega\mathbf{P}. \tag{3.14}$$

One can therefore expand the problem (2.13) as it follows:

$$\begin{aligned}
\nabla \times \mathbf{E}(\boldsymbol{r},\omega) =& i\omega\mu_0\mathbf{H}(\boldsymbol{r},\omega)\\
\nabla \times \mathbf{H}(\boldsymbol{r},\omega) =& -i\omega\varepsilon_0\varepsilon_\infty\mathbf{E}(\boldsymbol{r},\omega)+\mathbf{J}(\boldsymbol{r},\omega)+\mathbf{J}_0(\boldsymbol{r},\omega)\\
\mathbf{J}(\boldsymbol{r},\omega) =& -i\omega\mathbf{P}(\boldsymbol{r},\omega)\\
\varepsilon_0\varepsilon_\infty\omega_p^2\mathbf{E}(\boldsymbol{r},\omega) =& (\gamma-i\omega)\mathbf{J}(\boldsymbol{r},\omega)+\omega_0^2\mathbf{P}(\boldsymbol{r},\omega)
\end{aligned} \tag{3.15}$$

and consequently write the linearized source-free ($\mathbf{J}_0 = 0$) Maxwell eigenproblem

$$\begin{bmatrix} 0 & -i\mu_0^{-1}\nabla\times & 0 & 0\\ i\varepsilon_0^{-1}\varepsilon_\infty^{-1}\nabla\times & 0 & 0 & -i\varepsilon_0^{-1}\varepsilon_\infty^{-1}\\ 0 & 0 & 0 & i\\ 0 & i\omega_p^2\varepsilon_0\varepsilon_\infty & -i\omega_0^2 & -i\gamma \end{bmatrix} \begin{bmatrix} \widetilde{\mathbf{H}}_m\\ \widetilde{\mathbf{E}}_m\\ \widetilde{\mathbf{P}}_m\\ \widetilde{\mathbf{J}}_m \end{bmatrix} = \widetilde{\omega}_m \begin{bmatrix} \widetilde{\mathbf{H}}_m\\ \widetilde{\mathbf{E}}_m\\ \widetilde{\mathbf{P}}_m\\ \widetilde{\mathbf{J}}_m \end{bmatrix} \tag{3.16}$$

Therefore, this formulation simplifies the numerical calculation of eigenvectors $\widetilde{\boldsymbol{\psi}}_m = [\widetilde{\mathbf{H}}_m, \widetilde{\mathbf{E}}_m, \widetilde{\mathbf{P}}_m, \widetilde{\mathbf{J}}_m]$ by formally removing the dispersion.

It can be shown [6] that the following relation of quasi orthonormality holds between any couple of eigenmodes $\widetilde{\boldsymbol{\psi}}_m, \widetilde{\boldsymbol{\psi}}_n$ with eigenfrequencies $\widetilde{\omega}_m, \widetilde{\omega}_n$:

$$(\widetilde{\omega}_m - \widetilde{\omega}_n)\int_V \widetilde{\boldsymbol{\psi}}_m^T\hat{\mathbf{D}}\widetilde{\boldsymbol{\psi}}_n d^3r = i\oint_\Sigma (\widetilde{\mathbf{E}}_m\times\widetilde{\mathbf{H}}_n - \widetilde{\mathbf{E}}_n\times\widetilde{\mathbf{H}}_m)\cdot\mathbf{n}d\sigma \tag{3.17}$$

where V and Σ represents the volume and outer surface of the space under study, and the operator $\hat{\mathbf{D}} = \mathrm{diag}\left[-\mu_0, \varepsilon_0\varepsilon_\infty, \omega_0^2/(\varepsilon_\infty\omega_p^2), -1/(\varepsilon_\infty\omega_p^2)\right]$. When working in a PML-mapped space, the field tangential components on the outer surface Σ vanishes, and (3.17) reduces to the orthonormality relation

$$\int_V \widetilde{\boldsymbol{\psi}}_m^T\hat{\mathbf{D}}\widetilde{\boldsymbol{\psi}}_n d^3r = \delta_{mn} \tag{3.18}$$

which enables modal expansion and the determination of excitation coefficients α_m in (3.6).

Modal excitation coefficients of scattered field

Let us consider the scattering problem illustrated in Fig. 2.1, which is reported in Fig. 3.1a, and a similar one (b) where the nanostructure has been removed and the same source $\mathbf{J}_0$ is

applied (for example an ideal current distribution at infinity originating an incident plane wave as in figure). Two different problems can be solved, one for the total field $[\mathbf{E}_t, \mathbf{H}_t]$

$$\nabla \times \mathbf{H}_t = -i\omega\varepsilon_0\varepsilon\mathbf{E}_t + \mathbf{J}_0, \ \nabla \times \mathbf{E}_t = i\omega\mu_0\mathbf{H}_t \tag{3.19}$$

and the other for the background field $[\mathbf{E}_b, \mathbf{H}_b]$

$$\nabla \times \mathbf{H}_b = -i\omega\varepsilon_0\varepsilon_b\mathbf{E}_b + \mathbf{J}_0, \ \nabla \times \mathbf{E}_b = i\omega\mu_0\mathbf{H}_b \tag{3.20}$$

Please notice that $[\mathbf{E}_b, \mathbf{H}_b]$ is identical to the incident field $[\mathbf{E}_{inc}, \mathbf{H}_{inc}]$ just in the particular case of a resonator suspended in a uniform medium. Generally (resonators on substrates, thin films, etc...) these two fields are different, and we label with $\varepsilon_b(\boldsymbol{r})$ the permittivity distribution of background media. Subtracting term by term (3.20) from (3.19) we obtain the scattered field formulation

$$\nabla \times \mathbf{H}_S = -i\omega\varepsilon_0\varepsilon\mathbf{E}_S - i\omega\varepsilon_0\Delta\varepsilon\mathbf{E}_b, \ \nabla \times \mathbf{E}_S = i\omega\mu_0\mathbf{H}_S \tag{3.21}$$

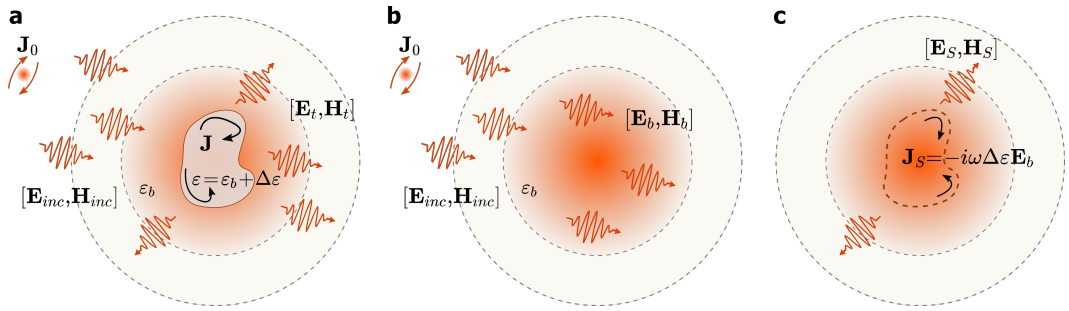

Figure 3.1: Scattered field formulation of light interaction with matter. (a) A driving source at infinity $\mathbf{J}_0$ generates the plane wave $[\mathbf{E}_{inc}, \mathbf{H}_{inc}]$ incident on the nanoobject with refractive index $\varepsilon = \varepsilon_b + \Delta\varepsilon$. This interaction originates a current distribution $\mathbf{J}$ (conduction and displacement currents) responsible for absorption and scattering mechanisms. (b) Background field $[\mathbf{E}_b, \mathbf{H}_b]$ without the resonator. (c) The same problem as (a) seen in scattered-field formalism: the external source is removed and a localized current source $\mathbf{J}_S$ is imposed in the resonator volume. Its distribution is such to radiate the same scattered field $[\mathbf{E}_S, \mathbf{H}_S]$ as in the former case.

As depicted in Fig. 3.1c, the scattered field $[\mathbf{E}_S, \mathbf{H}_S]$ by a nanostructure can equivalently be described as the field radiated by a current source distribution $-i\omega\varepsilon_0\Delta\varepsilon\mathbf{E}_b$ localized in the resonator volume (where $\Delta\varepsilon \neq 0$) [6]. Using the auxiliary-field formulation, we can again expand $\varepsilon_0\varepsilon(\mathbf{E}_S + \mathbf{E}_b) = \varepsilon_0\varepsilon_\infty(\mathbf{E}_S + \mathbf{E}_b) + \mathbf{P}_S$, and Maxwell equations in (3.15) become:

$$\begin{aligned}
\nabla \times \mathbf{E}_S(\boldsymbol{r}, \omega) &= i\omega\mu_0\mathbf{H}_S(\boldsymbol{r}, \omega) \\
\nabla \times \mathbf{H}_S(\boldsymbol{r}, \omega) &= -i\omega\varepsilon_0\varepsilon_\infty\mathbf{E}_S(\boldsymbol{r}, \omega) + \mathbf{J}_S(\boldsymbol{r}, \omega) - i\omega\varepsilon_\infty\mathbf{E}_b(\boldsymbol{r}, \omega) \\
\mathbf{J}_S(\boldsymbol{r}, \omega) &= -i\omega\mathbf{P}_S(\boldsymbol{r}, \omega) \\
\varepsilon_0\varepsilon_\infty\omega_p^2\mathbf{E}_S(\boldsymbol{r}, \omega) &= (\gamma - i\omega)\mathbf{J}_S(\boldsymbol{r}, \omega) + \omega_0^2\mathbf{P}_S(\boldsymbol{r}, \omega) - \varepsilon_0\varepsilon_\infty\omega_p^2\mathbf{E}_b(\boldsymbol{r}, \omega)
\end{aligned} \tag{3.22}$$

which can be rewritten in the matrix formulation

$$\hat{\mathbf{H}}\boldsymbol{\Psi}_S(\boldsymbol{r},\omega) = \omega\boldsymbol{\Psi}_S(\boldsymbol{r},\omega) + \mathbf{S}_b(\boldsymbol{r},\omega) \tag{3.23}$$

as

$$\underbrace{\begin{bmatrix} 0 & -i\mu_0^{-1}\nabla\times & 0 & 0 \\ i\varepsilon_0^{-1}\varepsilon_\infty^{-1}\nabla\times & 0 & 0 & -i\varepsilon_0^{-1}\varepsilon_\infty^{-1} \\ 0 & 0 & 0 & i \\ 0 & i\omega_p^2\varepsilon_0\varepsilon_\infty & -i\omega_0^2 & -i\gamma \end{bmatrix}}_{\hat{\mathbf{H}}} \underbrace{\begin{bmatrix} \mathbf{H}_S \\ \mathbf{E}_S \\ \mathbf{P}_S \\ \mathbf{J}_S \end{bmatrix}}_{\boldsymbol{\Psi}_S} = \omega \begin{bmatrix} \mathbf{H}_S \\ \mathbf{E}_S \\ \mathbf{P}_S \\ \mathbf{J}_S \end{bmatrix} + \underbrace{\begin{bmatrix} 0 \\ \left[\omega(\varepsilon_\infty - \varepsilon_b)/\varepsilon_\infty\right]\mathbf{E}_b \\ 0 \\ -i\omega_p^2\varepsilon_0\varepsilon_\infty\mathbf{E}_b \end{bmatrix}}_{\mathbf{S}_b} \tag{3.24}$$

where all the dependence on the external driving field is included in the term $\mathbf{S}_b$. Orthonormality relation in (3.18) allows to decompose the scattered field $\boldsymbol{\Psi}_S$ on the QNM basis

$$\boldsymbol{\Psi}_S(\boldsymbol{r},\omega) = \sum_{m=1}^{\infty} \alpha_m(\omega)\widetilde{\boldsymbol{\psi}}_m(\boldsymbol{r}). \tag{3.25}$$

Indeed, plugging (3.25) in (3.23) and usign orthonormality relation (3.18), the following closed form for the excitation coefficients α_m can be derived:

$$\begin{aligned} \alpha_m(\omega) =& \frac{\int_V \widetilde{\boldsymbol{\psi}}_m^T \hat{\mathbf{D}}\mathbf{S}_b d^3r}{\widetilde{\omega}_m - \omega} \\ =& \left\{ \frac{\omega}{\widetilde{\omega}_m - \omega}\varepsilon_0\left[\varepsilon(\widetilde{\omega}_m) - \varepsilon_b\right] + \varepsilon_0\left[\varepsilon(\widetilde{\omega}_m) - \varepsilon_\infty\right] \right\} \int_{V_{res}} \widetilde{\mathbf{E}}_m(\boldsymbol{r}) \cdot \mathbf{E}_b(\boldsymbol{r},\omega) d^3r \end{aligned} \tag{3.26}$$

in which the integral is over the resonator volume V_{res}, where $\mathbf{S}_b \neq 0$.

Near-field reconstruction

Once the excitation coefficients have been computed, the scattered field $[\mathbf{E}_S, \mathbf{H}_S]$ can be reconstructed through a truncated summation in equation (3.25). Furthermore in several applications, like the computation of nonlinear currents, it is necessary to retrieve the total field $[\mathbf{E}_t, \mathbf{H}_t]$. The auxiliary-field formalism opens several reconstruction scenarios with different convergence speeds.

- **Outside the resonator**: the medium is dispersionless, the auxiliary fields are equal to

zero, and a unique reconstruction is possible:

$$\mathbf{E}_t(\boldsymbol{r},\omega) = \mathbf{E}_b(\boldsymbol{r},\omega) + \mathbf{E}_S(\boldsymbol{r},\omega) \approx \mathbf{E}_b(\boldsymbol{r},\omega) + \sum_{m=1}^{N} \alpha_m(\omega)\widetilde{\mathbf{E}}_m(\boldsymbol{r}) \tag{3.27}$$

where we truncated the summation to the first N-modes

- **Inside the resonator**: different formulas can be proposed, depending on whether $\mathbf{E}_t$ is reconstructed directly as a summation of the modal electric field distributions $\widetilde{\mathbf{E}}_m$, or the auxiliary fields $\mathbf{P}_S$ or $\mathbf{J}_S$ are first reconstructed and then $\mathbf{E}_t$ is retrieved from them. These options may seem confusing, but it is noteworthy that all the reconstructions converge to the same result for $N \to \infty$. The choice of any of them determines the convergence rapidity, and consequently the number of modes N that ensures a good accuracy. In this thesis, I adopted the reconstruction proposed in [16] which was numerically proved to converge most rapidly. Taking back the definition of polarization vector auxiliary field $\varepsilon_0\varepsilon(\mathbf{E}_S + \mathbf{E}_b) = \varepsilon_0\varepsilon_\infty(\mathbf{E}_S + \mathbf{E}_b) + \mathbf{P}_S$, we derive the total field from $\mathbf{P}_S$:

$$\begin{aligned}\mathbf{E}_t(\boldsymbol{r},\omega) =& \mathbf{E}_S(\boldsymbol{r},\omega) + \mathbf{E}_b(\boldsymbol{r},\omega) = \frac{\mathbf{P}_S(\boldsymbol{r},\omega)}{\varepsilon_0[\varepsilon(\omega)-\varepsilon_\infty]} \\ &= \sum_m \frac{\alpha_m(\omega)}{\varepsilon_0[\varepsilon(\omega)-\varepsilon_\infty]}\widetilde{\mathbf{P}}_m(\boldsymbol{r}) = \sum_m \alpha_m(\omega)\frac{\varepsilon(\widetilde{\omega}_m)-\varepsilon_\infty}{\varepsilon(\omega)-\varepsilon_\infty}\widetilde{\mathbf{E}}_m(\boldsymbol{r})\end{aligned} \tag{3.28}$$

In some cases, as we will see in Section 3.3, it is more convenient to explicit the pole $\widetilde{\omega}_m - \omega$. Thus, we introduce the equivalent notation

$$\mathbf{E}_t(\boldsymbol{r},\omega) = \sum_{m=1}^{\infty} \frac{\omega}{\widetilde{\omega}_m - \omega}\beta_m(\omega)\widetilde{\mathbf{E}}_m(\boldsymbol{r}) \tag{3.29}$$

with

$$\beta_m(\omega) = \frac{\widetilde{\omega}_m\left[\varepsilon(\widetilde{\omega}_m)-\varepsilon_\infty\right] - \omega\left[\varepsilon_b-\varepsilon_\infty\right]}{\omega}\frac{\varepsilon(\widetilde{\omega}_m)-\varepsilon_\infty}{\varepsilon(\omega)-\varepsilon_\infty}\int_{V_{res}} \widetilde{\mathbf{E}}_m(\boldsymbol{r})\cdot\mathbf{E}_b(\boldsymbol{r},\omega)d^3r. \tag{3.30}$$

Weak formulation in COMSOL and eigenfunctions numerical calculation

In most of the cases, the eigenmodes of an arbitrarily shaped resonator cannot be computed with a closed-form expression, and the eigenvalue problem (3.16) must be solved numerically. Here we resorted to finite-element-method in COMSOL Multyphysics, as explained in Chapter 2. In particular, the system (3.16) can be expressed as a quadratic eigenproblem dependent on solely $[\widetilde{\mathbf{E}}_m, \widetilde{\mathbf{P}}_m]$

$$\nabla\times\mu_0^{-1}\nabla\times\widetilde{\mathbf{E}}_m - \widetilde{\omega}_m^2\left[\varepsilon_0\varepsilon_\infty\widetilde{\mathbf{E}}_m + \widetilde{\mathbf{P}}_m\right] = 0 \tag{3.31}$$

$$\varepsilon_0 \varepsilon_\infty \omega_p^2 \widetilde{\mathbf{E}}_m - (\widetilde{\omega}_m^2 + \omega_0^2)\widetilde{\mathbf{P}}_m + i\widetilde{\omega}_m \gamma \widetilde{\mathbf{P}}_m = 0 \tag{3.32}$$

which can be efficiently solved through the so-called first companion linearization [17]. When $\widetilde{\mathbf{P}}_m = 0$ (dispersionless case), (3.31) reduces to a classic Helmoltz equation, which is easily solved by the standard eigenfrequency study in COMSOL RF module. Conversely, for dispersive materials, (3.32) has to be simultaneously solved resorting to COMSOL mathematical tools. We introduce (3.32) through the partial differential equation (PDE) module in COMSOL. It is a common practice in FEM computations to implement the weak formulation to solve PDEs with defined boundary conditions, in order to avoid numerical issues when the differentiability of variables under study may be limited. The main idea is to turn the differential equations into an integral ones to reduce the difficulty of numerical algorithm in evaluating derivatives. We can do this by multiplying equations (3.31)-(3.32) by a suitably smooth test function $\mathbf{F}(\boldsymbol{r})$ and then integrating it:

$$\begin{aligned} \int_V \nabla \times \mathbf{F}(\boldsymbol{r}) \cdot \mu_0^{-1} \nabla \times \widetilde{\mathbf{E}}_m(\boldsymbol{r}) - \widetilde{\omega}_m^2 \left[\varepsilon_0 \varepsilon_\infty \mathbf{F}(\boldsymbol{r}) \cdot \widetilde{\mathbf{E}}_m(\boldsymbol{r}) + \mathbf{F}(\boldsymbol{r}) \cdot \widetilde{\mathbf{P}}_m(\boldsymbol{r}) \right] d^3 r = 0 \\ \int_V \varepsilon_0 \varepsilon_\infty \omega_p^2 \mathbf{F}(\boldsymbol{r}) \cdot \widetilde{\mathbf{E}}_m(\boldsymbol{r}) - (\widetilde{\omega}_m^2 + \omega_0^2 + i\widetilde{\omega}_m \gamma) \mathbf{F}(\boldsymbol{r}) \cdot \widetilde{\mathbf{P}}_m(\boldsymbol{r}) d^3 r = 0 \end{aligned} \tag{3.33}$$

$\widetilde{\mathbf{P}}_m$ is plugged as a weak contribution in the Helmoltz eigenvalue problem in the RF module, to account for material dispersion. Finally, the normalization condition in (3.12) is fulfilled computing the overlap integral between the retrieved field over all the PML-mapped space as shown in equation (3.18). Importantly COMSOL solver computes a finite number of eigenmodes, which finally result in truncated approximations of the scattered field. This has not to be seen as a critical limitation of the tool, first because usually a good accuracy in a finite spectrum of energies is achieved with a small amount of modes, and secondarily because the modal picture is particularly promising for capturing the physics of the system with few modes and in turn simplify calculations.

3.3 QNM implementation in nonlinear nano-optics

In Section 3.2 we recalled how the field scattered by a nanoresonator can be expanded in the natural basis of QNMs [6]. Here, resorting back to the double-step picture of nonlinear generation in nanostructures depicted in Fig. 2.9, we show the first original contribution of my PhD thesis: how to reconstruct the total electromagnetic field inside the structure, compute the nonlinear current source and finally expand the radiated field at SH on the same QNM basis calculated for the linear scattering problem. The QNM formalism proves promising for both its computational costs and the simplicity of its physical interpretation.

Nonlinear current reconstruction

The double scattering picture in Fig. 2.9 can be more conviniently reformulated through modal analysis in the following way [18], see Fig. 3.2:

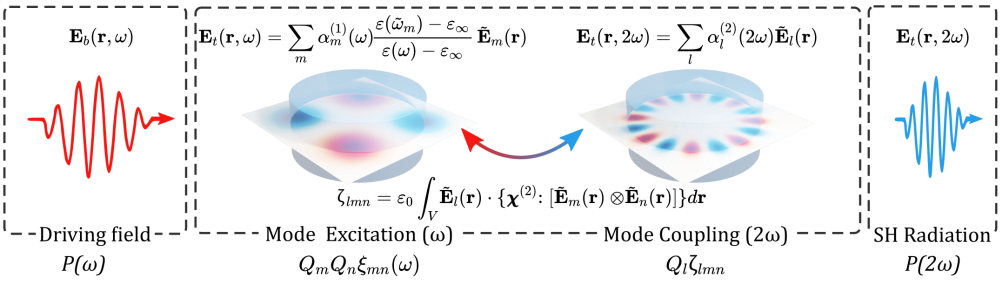

Figure 3.2: Schematic representation of nonlinear frequency generation in the QNM formalism. A driving field $\mathbf{E}_b(\omega)$ excites the modes of the nanoresonator resulting in a total field $\mathbf{E}_t(\omega)$. Such modes get coupled via the $\chi^{(2)}$ with modes that resonate near 2ω, resulting in a SH source of radiation. All the terms in the figure are clarified in the main text of this section.

- An external driving field $\mathbf{E}_b(\boldsymbol{r},\omega)$ with power $P(\omega)$ excites the QNMs of the dissipative resonator, transferring part of its energy to them. The light-matter interaction results in a total field distribution $\mathbf{E}_t(\boldsymbol{r},\omega)$ at fundamental frequency (FF). The quantity of transferred energy to the m-th mode is proportional to the excitation coefficient α_m, and the ability of this QNM to store energy is revealed by its quality factor $Q=-\mathrm{Re}(\widetilde{\omega}_m)/2\mathrm{Im}(\widetilde{\omega}_m)$.
- The quadratic nonlinearity of the material leads to the formation of a nonlinear current distribution $\mathbf{J}^{(2)}$ at 2ω, contributing to the energy transfer from the QNMs excited at ω to other modes with real eigenfrequency close to 2ω. This nonlinear mode coupling can be estimated by evaluating the spatial overlap ζ_{lmn} between the three involved modes with labels l, m and n.
- Finally these excited modes leak their energy in time, by radiating power in the far field at 2ω.

This picture encompasses several figures of merit which deserve to be addressed. Let us therefore analyse the process step by step. The nonlinear generated current $\mathbf{J}^{(2)}$ (2.76) can be written as

$$\begin{aligned}\mathbf{J}^{(2)}(\boldsymbol{r},2\omega) &= -i2\omega\mathbf{P}^{(2)}(\boldsymbol{r},2\omega) = -i2\omega\varepsilon_0\boldsymbol{\chi}^{(2)}:\left[\mathbf{E}_t(\boldsymbol{r},\omega)\otimes\mathbf{E}_t(\boldsymbol{r},\omega)\right]\\ &= -i2\omega\varepsilon_0\sum_{m,n}\alpha_m(\omega)\alpha_n(\omega)\frac{\left[\varepsilon(\widetilde{\omega}_m)-\varepsilon_\infty\right]\left[\varepsilon(\widetilde{\omega}_n)-\varepsilon_\infty\right]}{\left[\varepsilon(\omega)-\varepsilon_\infty\right]^2}\boldsymbol{\chi}^{(2)}:\left[\widetilde{\mathbf{E}}_m(\boldsymbol{r})\otimes\widetilde{\mathbf{E}}_n(\boldsymbol{r})\right]\\ &= -i2\omega\varepsilon_0\sum_{m,n}\frac{\omega^2}{(\widetilde{\omega}_m-\omega)(\widetilde{\omega}_n-\omega)}\beta_m(\omega)\beta_n(\omega)\boldsymbol{\chi}^{(2)}:\left[\widetilde{\mathbf{E}}_m(\boldsymbol{r})\otimes\widetilde{\mathbf{E}}_n(\boldsymbol{r})\right]\end{aligned} \tag{3.34}$$

where we introduced the notations ":" and "⊗" for the inner and tensorial products respectively.

Nonlinear excitation coefficients and mode overlap

The nonlinear current (3.34) provides the source term $\mathbf{S}^{(2)}$ of our radiation problem at 2ω, similarly to the term $\mathbf{S}_b$ in (3.24)

$$\begin{bmatrix} 0 & -i\mu_0^{-1}\nabla\times & 0 & 0 \\ i\varepsilon_0^{-1}\varepsilon_\infty^{-1}\nabla\times & 0 & 0 & -i\varepsilon_0^{-1}\varepsilon_\infty^{-1} \\ 0 & 0 & 0 & i \\ 0 & i\omega_p^2\varepsilon_0\varepsilon_\infty & -i\omega_0^2 & -i\gamma \end{bmatrix} \begin{bmatrix} \mathbf{H}_S \\ \mathbf{E}_S \\ \mathbf{P}_S \\ \mathbf{J}_S \end{bmatrix} = 2\omega \begin{bmatrix} \mathbf{H}_S \\ \mathbf{E}_S \\ \mathbf{P}_S \\ \mathbf{J}_S \end{bmatrix} + \begin{bmatrix} 0 \\ i\varepsilon_0^{-1}\varepsilon_\infty^{-1}\mathbf{J}^{(2)} \\ 0 \\ 0 \end{bmatrix} \tag{3.35}$$

from $\mathbf{S}^{(2)}$ we can directly derive the excitation coefficients at 2ω:

$$\begin{aligned} \alpha_l^{(2)}(2\omega) =& \frac{\int_V \widetilde{\boldsymbol{\psi}}_l^T \hat{\mathbf{D}}\mathbf{S}^{(2)}}{\widetilde{\omega}_l - 2\omega} = -\frac{2\omega}{\widetilde{\omega}_l - 2\omega}\int_V \mathbf{P}^{(2)}(\boldsymbol{r}, 2\omega)\cdot\widetilde{\mathbf{E}}_l(\boldsymbol{r})d^3r \\ =& \sum_{m,n}\frac{-2\omega^3\zeta_{lmn}\xi_{mn}(\omega)}{(\widetilde{\omega}_l - 2\omega)(\widetilde{\omega}_m - \omega)(\widetilde{\omega}_n - \omega)} \end{aligned} \tag{3.36}$$

where we defined

$$\xi_{mn}(\omega) = \beta_m(\omega)\beta_n(\omega) \tag{3.37}$$

and

$$\zeta_{lmn} = \varepsilon_0\int_{V_{res}} \widetilde{\mathbf{E}}_l(\boldsymbol{r})\cdot\left\{\boldsymbol{\chi}^{(2)} : \left[\widetilde{\mathbf{E}}_m(\boldsymbol{r})\otimes\widetilde{\mathbf{E}}_n(\boldsymbol{r})\right]\right\}d^3r \tag{3.38}$$

The main advantage of this formalism is the possibility to define with a closed-form expression the excitation coefficient of modes at harmonic frequencies. Typically just few modes capture all the physics of the system, and this enables a deep insight with extreme simplicity. Let us point out some key concepts included in (3.36):

- The l-th QNM is effectively excited at 2ω if energy is effectively transferred from an external field to two modes m and n at ω ($\xi_{mn}(\omega)$ term) and a good nonlinear spatial overlap between the three modes is ensured (ζ_{lmn} term). It is worth noticing that in the spectrally matched case, in which $\mathrm{Re}(\widetilde{\omega}_l) = 2\omega$ and $\mathrm{Re}(\widetilde{\omega}_m) = \mathrm{Re}(\widetilde{\omega}_n) = \omega$, the excitation coefficient at 2ω reduces to

$$\alpha_l^{(2)}(2\omega) = 8i\sum_{mn} Q_l Q_m Q_n \zeta_{lmn}\xi_{mn}(\omega) \tag{3.39}$$

Equation (3.39) highlights that a stronger harmonic generation occurs as light is trapped for a longer time, which allows a longer nonlinear interaction between the three modes;

- the amount of energy transferred from the pump to the resonator is quantified by the term $\xi(\omega)$. Importantly, once the modes are known for a given structure, this coefficient can be retrieved analytically for any possible pump configuration, reducing drastically the computational costs. From a design perspective, this approach provides a simple formula to optimize the pump in order to maximize SHG efficiency;

- equation (3.38) defines the spatial overlap integral between the nonlinearly interacting modes. The analyticity of this derivation is of paramount importance for nonlinear generation in non-Hermitian systems. The nonlinear overlap integral is a well-known concept in closed cavities and optical waveguides. To make a strict and useful comparison, in the case of two signals propagating along z in a waveguide with length L and transverse section S, the generation efficiency scales with

$$\begin{aligned} &\varepsilon_0 \int_V \mathbf{E}^*_{SH}(x,y) \cdot \boldsymbol{\chi}^{(2)} : \left[\mathbf{E}_{FF}(x,y) \otimes \mathbf{E}_{FF}(x,y)\right] \exp[i(k_{SH} - 2k_{FF})z] d^3r \\ &= \varepsilon_0 \int_S \mathbf{E}^*_{SH}(x,y) \cdot \boldsymbol{\chi}^{(2)} : \left[\mathbf{E}_{FF}(x,y) \otimes \mathbf{E}_{FF}(x,y)\right] dxdy \int_L \exp[i(k_{SH} - 2k_{FF})z] dz. \end{aligned} \tag{3.40}$$

  The first term denotes the modal overlap and the second the phase-matching condition, as it was presented for a bulk crystal in Chapter 2. In a nanostructure, however, the idea of propagating fields is lost, and the volume integral in (3.40) can no longer be factorized in a transverse and a propagative contribution. The concepts of phase matching and modal overlap are all included in ζ_{lmn}. Please notice that, at variance with formulations of mode coupling coefficient based on Hermitian theories [19–21], ζ_{lmn} presents no complex conjugation in the triple product $\widetilde{E}_l \widetilde{E}_m \widetilde{E}_n$. This is an inherent difference of non-Hermitian physics and results from mode normalization (3.12).
- The importance of overlap integral ζ_{lmn} is related to mode normalization. Historically this concept has always assumed a central role in Hermitian systems, the difficulty to recast it in open-cavities is mainly related to the complex problem of normalizing leaky modes. Thanks to the normalization (3.12), ζ_{lmn} acquires here a quantitative meaning: $|\zeta_{lmn}|^2$ being the SHG efficiency, now the values obtained from different resonances can be properly compared. Furthermore, being an intrinsic quantity of the system, i.e. unrelated to the excitation frequency ω, ζ_{lmn} is a good figure of merit to be optimized independently of the pump configuration.

Cross sections

Light interaction with a nanocavity is usually probed through the amount of energy that is absorbed in its volume or scattered in the far field. As shown in Chapter 2, this leads to the definition of absorption and scattering cross sections (2.30)-(2.31) which represents effective interaction surfaces.

If we apply the operation $\int_V d^3r \boldsymbol{\Psi}^\dagger \hat{\mathbf{A}}$ to both sides of $\hat{\mathbf{H}}\boldsymbol{\Psi} = \omega\boldsymbol{\Psi} + \mathbf{S}$ in (3.5), with $\boldsymbol{\Psi}^\dagger$ conjugate transpose of $\boldsymbol{\Psi}$, $\hat{\mathbf{A}} = \text{diag}[\mu_0, \varepsilon_0\varepsilon_\infty, \omega_0^2/(\varepsilon_0\varepsilon_\infty\omega_p^2), 1/(\varepsilon_0\varepsilon_\infty\omega_p^2)]$ and complex-valued ω, we get [6]:

$$-2\text{Im}(\omega)W_e = P_{abs} + P_{sca} - P_{ext} \tag{3.41}$$

where, within the auxiliary-field formulation, we have

$$W_e = \frac{1}{4}\int_V \mu_0|\mathbf{H}|^2 + \varepsilon_0\varepsilon_\infty|\mathbf{E}|^2 + \frac{1}{\varepsilon_0\varepsilon_\infty\omega_p^2}\left(|\mathbf{J}|^2 + \omega_0^2|\mathbf{P}|^2\right) d^3r \tag{3.42}$$

$$P_{ext} = -\frac{1}{2}\int_V \text{Im}\left(\boldsymbol{\Psi}^\dagger\hat{\mathbf{A}}\mathbf{S}\right) d^3r \tag{3.43}$$

$$P_{abs} = \frac{1}{2}\int_V \frac{\gamma}{\varepsilon_0\varepsilon_\infty\omega_p^2}|\mathbf{J}|^2 d^3r \tag{3.44}$$

$$P_{sca} = \frac{1}{2}\oint_\Sigma \text{Re}(\mathbf{E}\times\mathbf{H}^*)\cdot\hat{\mathbf{n}}d\sigma \tag{3.45}$$

(3.41) corresponds to the Poynting theorem: the decay of stored energy (3.42) is equal to the sum of absorbed (3.44) and scattered (3.44) power minus the total power transferred from the source to the resonator (3.43).

By replacing the source term $\mathbf{S}_b$ in scattered-field formulation, we retrieve the definition of cross-sections at real frequencies as in Section 2.2:

$$\begin{aligned}\sigma_{abs}(\omega) &= \frac{1}{2S_0}\int_V \frac{\gamma}{\varepsilon_0\varepsilon_\infty\omega_p^2}\left|\mathbf{J}_S(\boldsymbol{r},\omega)\right|^2 d^3r \\ &= \sum_m \frac{\gamma}{2S_0\varepsilon_0\varepsilon_\infty\omega_p^2}|\alpha_m(\omega)\widetilde{\omega}_m\varepsilon_0[\varepsilon(\widetilde{\omega}_m)-\varepsilon_\infty]|^2\int_V\left|\widetilde{\mathbf{E}}_m(\boldsymbol{r})\right|^2 d^3r\end{aligned} \tag{3.46}$$

$$\begin{aligned}\sigma_{ext}(\omega) &= -\frac{\omega}{2S_0}\int_V \text{Im}\left[\omega\varepsilon_0(\varepsilon_\infty-\varepsilon_b)\,\mathbf{E}_S^*(\boldsymbol{r},\omega)\cdot\mathbf{E}_b(\boldsymbol{r},\omega) - i\mathbf{J}_S^*(\boldsymbol{r},\omega)\cdot\mathbf{E}_b(\boldsymbol{r},\omega)\right] d^3r \\ &= -\sum_m \text{Im}\left\{\varepsilon_0\alpha_m(\omega)\left[\omega(\varepsilon_\infty-\varepsilon_b) - \widetilde{\omega}_m\left(\varepsilon(\widetilde{\omega}_m-\varepsilon_\infty)\right)\right]\int_V \widetilde{\mathbf{E}}_m^*(\boldsymbol{r})\cdot\mathbf{E}_b(\boldsymbol{r},\omega)d^3r\right\}\end{aligned} \tag{3.47}$$

Finally, the scattering cross section can be straightforwardly computed as the difference between extinction and absorption cross sections. This derivation is more convenient for numerical implementation, as it involves just integrals over the resonator volume which can be easily discretized at low computational costs.

With the same considerations made in Section 2.3, the concept of cross sections can be extended to SHG process, by replacing external plane-wave excitation $\mathbf{S}_b$ with the localized nonlinear current distribution $\mathbf{S}^{(2)} = [0, i\varepsilon_0^{-1}\varepsilon_\infty^{-1}\mathbf{J}^{(2)}, 0, 0]$ and normalizing to pump intensity S_0:

$$\begin{aligned}\sigma_{abs}^{(2)}(2\omega) =& \frac{P_{abs}(2\omega)}{S_0} = \frac{1}{2S_0}\int_V \frac{\gamma}{\varepsilon_0\varepsilon_\infty\omega_p^2}\left|\mathbf{J}(\boldsymbol{r},2\omega)\right|^2 d^3r \\ =& \sum_l \frac{\gamma}{2S_0\varepsilon_0\varepsilon_\infty\omega_p^2}|\alpha_l(2\omega)\widetilde{\omega}_l\varepsilon_0[\varepsilon(\widetilde{\omega}_l)-\varepsilon_\infty]|^2\int_V\left|\widetilde{\mathbf{E}}_l(\boldsymbol{r})\right|^2 d^3r\end{aligned} \tag{3.48}$$

$$\begin{aligned}\sigma_{ext}^{(2)}(2\omega) =& -\frac{\omega}{S_0}\int_V \mathrm{Im}\left[\mathbf{E}_t^{(2)*}(\boldsymbol{r},2\omega)\cdot\mathbf{P}^{(2)}(\boldsymbol{r},2\omega)\right]d^3r \\ =& \frac{\omega}{S_0}\sum_l \mathrm{Im}\left\{\alpha_l^{(2)}(2\omega)\int_V \widetilde{\mathbf{E}}_l(\boldsymbol{r})\cdot\mathbf{P}^{(2)*}(\boldsymbol{r},\omega)d^3r\right\}\end{aligned} \tag{3.49}$$

These two figures of merit linearly scale with pump intensity S_0 and enable to separately study the contribution of all modes triads $[l, m, n]$ to SHG efficiency. While all the above scattering cross sections are rigorously defined for a plane-wave excitation, for spatially non-uniform pumps they are approximated considering the average intensity $\bar{S}_0$ on the nanoresonator.

3.4 Numerical example and design guidelines

Having discussed in Section 3.3 the whole theoretical formalism and the details for numerical implementation of QNM analysis of SHG in nanoresonators, let us now show two examples of modal analysis in AlGaAs nanocylinders on a substrate. The first one is an instructive case to explain step by step how the analysis is numerically performed; the second one considers a more complex geometry and aims at demonstrating how the optimization of the overlap coefficient ζ_{lmn} can boost SHG efficiency. All the numerical examples presented here below can be reproduced through the open-access nonlinear toolbox in [22].

Nonlinear generation in AlGaAs-on-AlOx nanocavities

Let us consider for illustrative purposes the geometry in Fig. 3.3. It represents an $Al_{0.18}Ga_{0.82}As$ nanocylinder with radius $r = 220$ nm and height $h = 400$ nm lying over an AlOx substrate with constant refractive index $n_s = 1.6$. The permittivity of $Al_{.18}Ga_{.82}As$ is

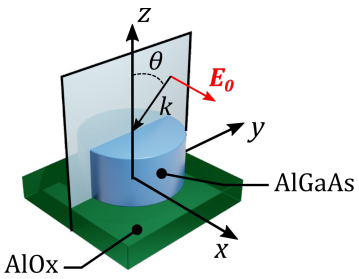

Figure 3.3: Schematic illustration of the cavity under study: an $Al_{0.18}Ga_{0.82}As$ nanocylinder over an aluminum oxide (AlOx) substrate. The external driving field is an s-polarized plane wave along x axis, with k vector aligned along $-z$.

modeled with a single-pole Lorentzian dispersion

$$\varepsilon(\omega) = \varepsilon_\infty - \varepsilon_\infty \frac{\omega_p^2}{\omega^2 - \omega_0^2 - i\omega\gamma} \qquad \begin{cases} \varepsilon_\infty = 1 \\ \omega_p = 2691 \times 2\pi \text{ THz} \\ \omega_0 = 883 \times 2\pi \text{ THz} \end{cases} \tag{3.50}$$

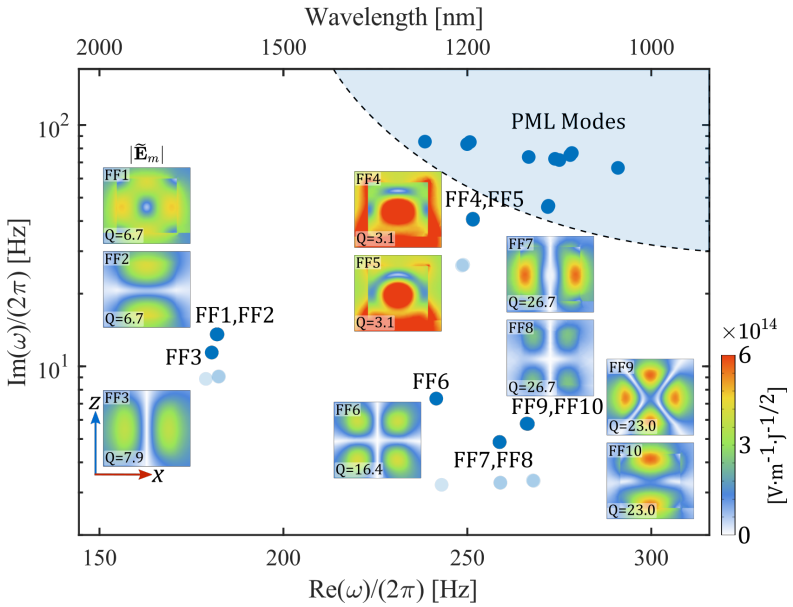

Figure 3.4: QNM distribution in the complex plane for the same AlGaAs-on-AlOx nanocylinder as in Fig. 3.3. QNM with (dark blue dots) or without (light blue dots) the substrate are reported. Two labels on the same dot indicate degenerate QNMs. Their near-field distribution $|\widetilde{E}_m|$ is shown in the xz plane at $y = 0$, i.e. in the central vertical section of the nanocylinder.

Material parameters in (3.50) are fitted from the empirical model in [23], for more detailed information on the fitting algorithm please refer to the Appendix A. Let us suppose to work below the material bangap ($\lambda > 740$ nm), thereby neglecting absorption losses ($\gamma = 0$). The model has a limited spectral validity and dispersion is introduced just in the real part of

permittivity, which is necessary to retrieve the right eigenfrequencies in the visible/near-IR. The sole numerical calculation to retrieve the optical response of such resonator for a broad spectrum and different excitation conditions is the mode calculation. The eigenfrequencies of the 10 most relevant modes in the range [1000 − 1700] nm are shown in the complex plane in Fig. 3.4 together with near electric field distribution in absolute value. They are labelled "FF"(Fundamental Frequency) as they are in the range of the pump wavelength used in the following for nonlinear generation.

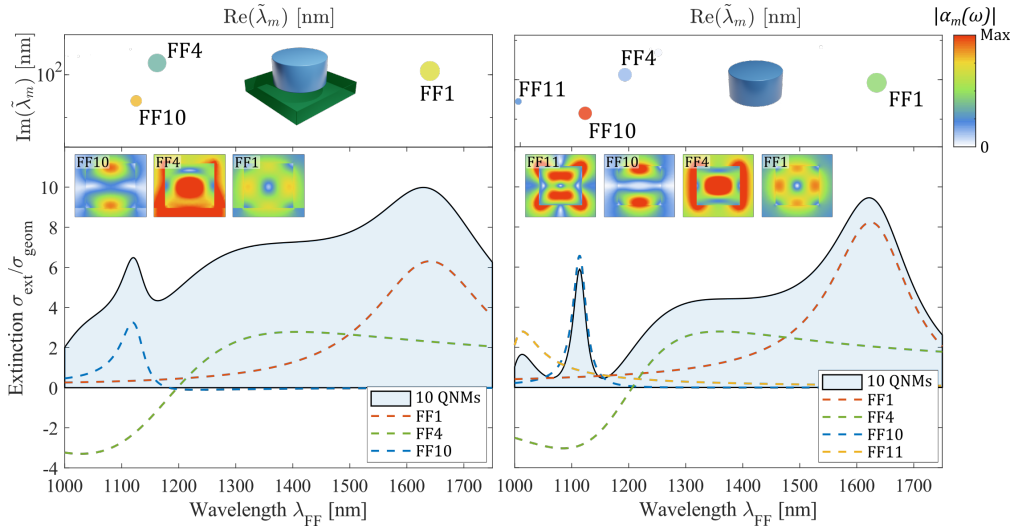

Figure 3.5: Extinction cross section of an AlGaAs nanocylinder excited by a normally impinging plane wave (linear polarization along x). The reconstruction with the 10 dominant QNMs is reported for the case of on-substrate (left) or air-suspended (right) resonator. The contribution of the most excited modes is reported as colored dashed lines. Their position in the complex plane is shown on the top: circles radius is proportional to the average of excitation coefficient in the considered spectrum, and their color corresponds to the maximum absolute value of their extinction cross section. In the inset, the near-field distribution $|\widetilde{E}_m|$ of the relevant QNMs.

Importantly, the shaded region in the complex plane reports the presence of additional modes called PML modes. These are non-physical modes which appear as soon as the infinite space that an open cavity occupies is numerically confined with the addition of perfect matching layers. Their nature and eigenfrequencies being strongly dependent on the PML mesh, they can easily be distinguished from QNMs by computing the ratio between the energy stored in the PML and in the resonator (we recall that modes are normalized before being compared and that this distinction is meaningful only if a good normalization is adopted). The contribution of PML modes has to be taken into account to boost the convergence of field reconstruction to the exact fully vectorial result (a detailed numerical comparison is reported in [6]). Finally, a first effect of placing the resonator on a substrate can be appreciated by comparing the position of QNM resonances (dark blue dots), with the light blue dots that refer to an air-suspended nanocylinder of equal size. As expected, the presence of the substrate leads to a reduction of quality factors (Im$[\widetilde{\omega}_m]$ increases) and a slight shift of the resonance Re$[\widetilde{\omega}_m]$.

It is worth considering the numerical costs for this computation: on an average performance workstation (CPU 3.70GHz - RAM 16GB) with a mesh consisting of about 35000 domain elements, the calculation of 35 modes for a fixed geometry in the spectrum [1000 − 1700] nm takes ≈ 3 minutes. On the contrary the solution of a full vectorial problem

at a fixed geometry, wavelength and pump configuration on the same machine requires around ≈ 30 seconds. However, the latter returns the full numerical result but it reveals just the resonances excited by the external pump, limiting the total physical comprehension. Therefore computing the QNMs for different geometries and following their trajectories in the complex plane still remains cost effective with respect to full numerical calculations and it enables to extract most of the physics of the system, in terms of resonant modes and their quality factors, independently of the imposed external excitation.

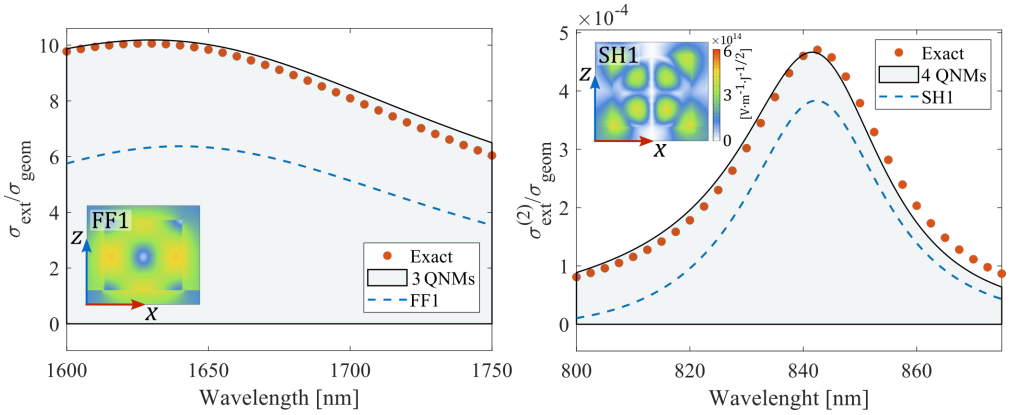

Figure 3.6: Reconstruction of FF (left) and SH (right) extinction cross sections for an AlGaAs nanocylinder excited by a normally impinging plane wave with intensity $S_0 = 1\text{GW/cm}^2$. The reconstruction with few dominant QNMs (black solid curve) is compared with the full numerical result obtained in COMSOL (orange dots) with the same Lorentzian dispersion for the permittivity. The dashed blue lines report the contribution of the most excited mode, FF1 and SH1 respectively. The insets display the near-field distributions $|\widetilde{E}_m|$ of FF1 and SH1.

Once the QNMs are known, the electric field and scattering properties for a fixed external source can be expanded on this basis (this process is referred to as "reconstruction" in the following). Let us assume to excite the nanocylinder of Fig. 3.3 with a plane wave polarized along x axis and wavevector $\boldsymbol{k}$ along $-z$ ($\theta = 0$). Working below the material bandgap where absorption is neglected ($\gamma = 0$), the extinction and scattering cross sections are equal. Using therefore equation (3.49), the scattering spectrum can be reconstructed. The result, reported in Fig. 3.5, is compared with the same geometry without the substrate, which highlights the broadening and small shift of spectral features. The air-suspended case exhibits the same qualitative behavior as shown with full numerical calculation in Fig. 2.11. The quantitative mismatch between the two is explained by the truncated reconstruction and the inaccuracy due to fitting AlGaAs permittivity with a single-pole Lorentzian. It is finally interesting to remark in Fig. 3.5 the appearence of negative extinction cross sections. According to definition in (3.17) the projection of an eigenmode m on another eigenmode n is strictly equal to zero when the integral is extended over all the PML mapped space. This means that even in the case of a driving term $\mathbf{S}_b = -i\omega\varepsilon_0\Delta\varepsilon\mathbf{E}_b$ in scattering formulation (3.21) perfectly overlapping with the m mode distribution, the overlap integral appearing in the excitation coefficient (3.26) with the mode n can be different from zero as the integration is restrained to the resonator volume V_{res}. While in a closed system this integral would be strictly equal to zero, in an open system two different QNMs can effectively interact in the resonator volume, constructively or destructively, and the negative contribution to the extinction is a footprint of this effect. When a QNM is excited alone, no negative contribution to the extinction is observed in accordance with energy conservation. Those

negative contributions have been revealed also in other QNMs toolboxes [13], and it is similar to "negative Purcell effect" reported in [10].

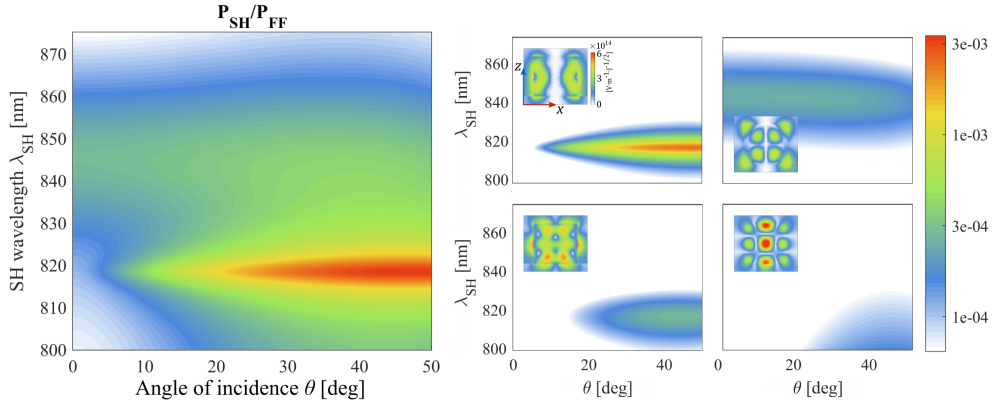

Figure 3.7: Ratio between SH $\left(P_{SH} = W_{ext}^{(2)}\right)$ and FF $\left(P_{FF} = S_0 \pi r^2\right)$ power impinging on the AlGaAs-on-AlOx cylinder of Fig. 3.3. θ is the angle of incidence between the plane-wave k-vector and the cylinder axis (z). S_0 is set at 1 GW/cm^2. The total reconstruction on the left is decomposed in its four main contribution on the right. Insets: near-field distributions $|\widetilde{E}_m|$ of the corresponding QNMs in the xz plane (the color bar is the same for the four plots).

In order to analyse SHG in the same nanocylinder, another set of 60 QNMs are computed around $\lambda = 800$ nm, and consistently with previous notation they are labelled "SH". While in principle all the modes could be computed once in one broad frequency spectrum, here the separation of FF and SH QNMs aims at boosting the calculation speed as the region of interest is spectrally limited. The total electric field is reconstructed in the pump wavelength range $\lambda_{FF} \in [1600 - 1700]$ nm, then the SH polarization vector $\mathbf{P}^{(2)}$ is retrieved and finally the nonlinear extinction cross section is computed according to (3.49). The result of such reconstruction, reported in Fig. 3.6, is compared with the fully vectorial result obtained with the same dispersion model and geometry. A small amount of QNMs (2 at FF and 4 at SH) suffices to reconstruct the extinction with good accuracy. To improve the convergence, more QNMs and PML modes should be included, but this goes beyond our scope here. For a more detailed analysis on convergence the interested reader can refer to the supplementary material of Ref.[6]. In this case we prefer to accept a tolerance of few percent but keep the number of involved QNMs low.

The advantages of modal formalism are unquestionable also when the response of the system has to be probed upon the simultaneous sweep of several pump parameters. For example, let us scan the pump wavelength as before, but also change at the same time the incident angle θ in a range $[0° - 50°]$. Fig. 3.7 reports the reconstructed ratio between SH and FF power for 7500 different pump configurations. With the same machine and mesh as before, such calculation requires $\approx$ 2 minutes (instead of $7500 \times 30'' = 62h30'$, with independent fully vectorial simulations). Obviously, as shown above, the contribution from different QNMs can be isolated, which enables to explore their near-field, study their symmetry, quality factor, cross interaction, and finally compute their radiation pattern through near-to-far field packages [24].

Phase matching in subwavelength resonators

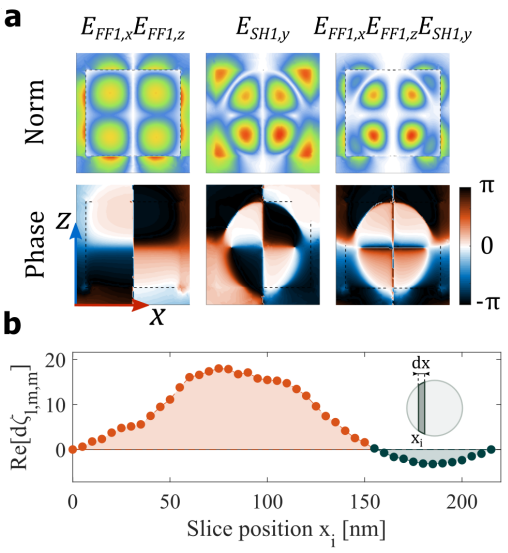

Figure 3.8: Nonlinear overlap analysis between modes FF1 and SH1. (a) Main components of the modes: norm (top) and phase (bottom). From left to right: product of x and z components of $\widetilde{\mathbf{E}}_{FF1}$; y component of $\widetilde{\mathbf{E}}_{SH1}$; main component of the nonlinear product $\widetilde{\mathbf{E}}_{SH1} \cdot [\chi^{(2)} : \widetilde{\mathbf{E}}_{FF1} \otimes \widetilde{\mathbf{E}}_{FF1}]$. (b) Discretized contribution to the overlap integral ζ_{lmn} along finite slices in the xy plane, centered at x_i with thickness $dx = 5$ nm. Only the real part is reported.

As recalled in the previous section, a key advantage of modal approach is the possibility to analyse in detail the overlap integral ζ_{lmn} between different modes. Let us just focus for example on the main excited modes FF1 and SH1. In Fig. 3.8a the electric near-field distribution of their dominant component in the xz plane at $y = 0$ is shown in norm and phase. Moreover, in the rightmost column one can find the dominant term of the overlap integral ζ_{lmn}, i.e. $E_{l,y}E_{m,x}E_{n,z}$ with l =SH1 and $m = n$ =FF1. Its phase exhibits two main regions (in black and white) which are in phase opposition. The result is similar to what happens in optical waveguides when perfect phase matching condition is not fullfilled: for a distance shorter than the coherence length L_c the SH amplitude increases, then the pump and SH waves end up in phase opposition and the amplitude decreases, producing an oscillating SH signal. Similarly, in nanoresonators, mode overlap can result in contributions to nonlinear generation with opposite signs, as shown in Fig. 3.8b where the overlap integral ζ_{lmn} has been discretized over vertical slices with thickness $dx = 5$ nm centered at different positions x_i along x axis. This effect reduces the total generated power, and its knowledge can lead to an optimization of nanocavities for nonlinear generation.

Optimizing SHG in nanocavities

In Section 3.4, I have shown how the QNM formalism can be numerically implemented and what are the advantages for the analysis of a defined nonlinear scattering problem. To make a step forward, it is reasonable to wonder if this tool can offer guidelines to optimize nonlinear generation in nanoresonators. Different routes are conceivable, but in the following we will only explore in detail the optimization of the overlap integral ζ_{lmn}. To illustrate this point, let us consider again an $Al_{0.18}Ga_{0.82}As$-on-AlOx nanodisk with a fixed

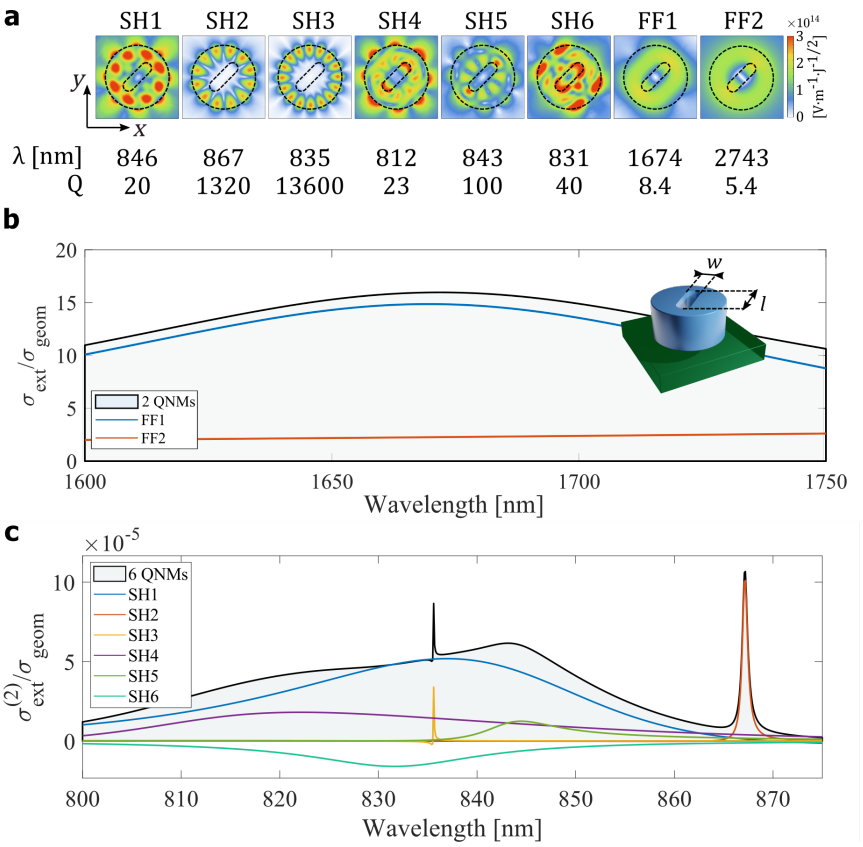

Figure 3.9: SHG in an AlGaAs-on-AlOx nanocylinder with radius $r = 440$ nm, height $h = 400$ nm and rounded-rectangular axial hole with sizes $l = 480$ nm and $w = 150$ nm (see inset). (a) Electric field distribution $|\widetilde{E}_m|$ in the xy plane (at $z = 200$ nm) of the 8 dominant QNMs around pump frequency (FF1-2) and SH (SH1-6). Their central wavelength and Q-factor are reported at the bottom. (b) Reconstructed linear extinction in the range $\lambda_{FF} \in [1600 - 1750]$ nm with 2 QNMs (black solid line), whose contribution is reported as colored lines, for normally impinging azimuthally polarized pump with total power $P = 50$ W. (c) Corresponding nonlinear extinction (i.e. SHG efficiency) decomposed in its six (SH1-6) main contributions.

height $h = 400$ nm. Varying the radius r and following how the QNMs evolve, one can single out high-Q modes either in the FF or SH range, which can boost SHG efficiency according to (3.39). Here we focus on SH modes, as the larger ratio r/λ_{SH} allows to find more easily high-Q modes at subwavelength scale. After few iterations, two high-Q modes are selected in the $[800 - 875]$ nm region for $r = 440$ nm. They resemble two low-order whispering gallery modes with quality factors of the order of 10^4 and 10^3 respectively, and are shown in Fig. 3.9a as modes SH2 and SH3. An asymmetric hole (with rounded-rectangular shape and sizes $l = 480$ nm and $w = 150$ nm) appears about the axis of the cylinder, to break the symmetry of the system (by doing so, the modes that would be symmetry-forbidden are immediately revealed before any optimization process and the degeneracy of axisymmetryc modes is lifted).

Since the main electric field component of these high-Q modes is along z, let us suppose to pump with an azimuthally polarized Gaussian beam, which maximizes the overlap integral $\widetilde{\mathbf{E}}_m \cdot \mathbf{E}_b$ with two modes polarized in the xy plane, labelled FF1 and FF2 in 3.9(a). In the paraxial approximation, the incident field can be written in cylindrical coordinates as

[25]

$$\mathbf{E}_{inc}(\rho,\theta,z) = \frac{A}{\sqrt{\pi}}\frac{2\rho}{w(z)^2}e^{-\left(\frac{\rho}{w(z)}\right)^2}e^{-2i\tan^{-1}(z/z_R)}e^{ikz}\hat{\boldsymbol{\theta}} \tag{3.51}$$

Mode	SH1	SH2	SH3	SH4	SH5	SH6
Q_l	20	1320	13600	23	100	40
$\lvert\zeta_{l11}\rvert$ [C · V]	151	12	11	42	23	106

Table 3.1: Quality factors (Q_l) and nonlinear overlap integrals ($|\zeta_{lmn}|$) of the six considered modes around SH with the dominant mode at pump frequency FF1.

with $w(z) = w_0\sqrt{1+(z/z_R)^2}$ the beam waist, $z_R = \pi w_0^2/\lambda$ the Rayleigh range, $k = 2\pi/\lambda$ the wave number, A an amplitude coefficient (in Volts) and $\hat{\boldsymbol{\theta}}$ the azimuthal unitary vector. The values of the parameters are chosen such to have 50 W of total power and a waist $w_0 = 2$ μm. The reconstructed linear σ_{ext} and nonlinear $\sigma_{ext}^{(2)}$ extinctions are shown in Fig. 3.9b-c. Even if SH3 exhibits the highest Q-factor, it just gives a minor contribution to SHG. Since, as shown in (b), most of the physics at FF is described by one dominant contribution for the adopted pump configuration, the SH modes are all mainly pumped by FF1, and the reason for this behavior stems from their spatial overlap with this QNM. Table 3.1 reports the quality factors of the six SH modes and their overlap integral $|\zeta_{l11}|$ with FF1.

Once again, since the QNMs are normalized, the different overlaps $|\zeta_{l11}|$ can be quantitatively compared. SH3 exhibits the lowest overlap, which explains its poor contribution to SHG. Similarly to the previous section, it is worth exploring the near-field distributions of FF1 and SH3 to understand the origin of such small overlap. The main field components in the xy plane are shown in Fig. 3.10a. The phase of the overlap integral in the rightmost column visually highlights angular sectors with positive (white) and negative (black) contributions. More quantitatively, Fig. 3.10b reports the overlap integral discretized over infinitesimal "slices" in the xy plane as a function of the azimuthal angle θ.

The sum of positive and negative contributions finally result in the poor SHG signal shown in Fig. 3.9. In order to boost SHG efficiency, one can think of locally reversing the sign of $\chi^{(2)}$ while keeping unaltered the cylinder permittivity ($1+\chi^{(1)}$), and thus the QNMs. Fig. 3.10b provides a quantitavive guideline toward optimization: the cylinder area is divided in 12 angular sectors with opposite $\chi^{(2)}$. Fig. 3.10c shows the nonlinear extinction of a nanodisk where contributions to ζ_{lmn} have been rephased compared with a common one. SHG power is enhanced by more than 2 orders of magnitude. This sign reversal recalls quasi-phase matching techniques commonly adopted in GaAs waveguides. Fig. 3.11a reports the summation of infinitesimal contributions to ζ_{lmn} of Fig. 3.10b as a function of θ for the optimized and unoptimized cases. These two behaviors are reminiscent of the quasi-phase matched and mismatched beams propagating in an optical waveguide, Fig. 3.11b.

This comparison is extremely instructive as it explains how the phase plays a central role also in subwavelength resonators and how QNM formalism can offer useful analogies and connections between the worlds of nonlinear optics in Hermitian and non-Hermitian systems.

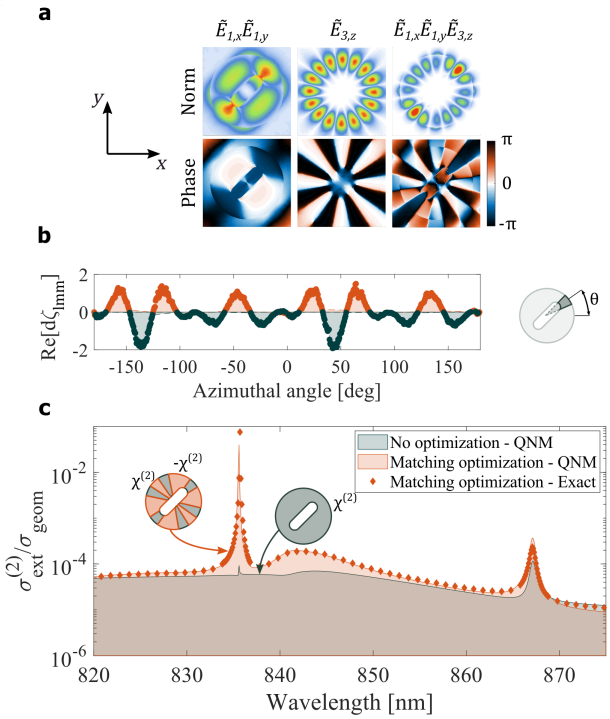

Figure 3.10: Nonlinear overlap integral optimization in nanocavities. (a) Main components of dominant mode FF1 and highest-Q mode SH3 shown in absolute value(top) and phase(bottom). From left to right: product of x and y components of $\widetilde{\mathbf{E}}_{FF1}$, z component of $\widetilde{\mathbf{E}}_{SH3}$, main component of the nonlinear product $\widetilde{\mathbf{E}}_{SH3} \cdot [\chi^{(2)} : \widetilde{\mathbf{E}}_{FF1} \otimes \widetilde{\mathbf{E}}_{FF1}]$.(b) Discretized real-part contribution to the overlap integral ζ_{lmn} along finite angular sectors in the xy plane centered at θ with width $d\theta = 0.5°$. (c) Comparison of reconstructed extinction spectrum between an homogeneous (100) AlGaAs nanocylinder (grey line) and an optimized one where half of the splices have a reversed $\chi^{(2)}$ sign. Red dots report the fully vectorial result obtained with COMSOL Multyphysics.

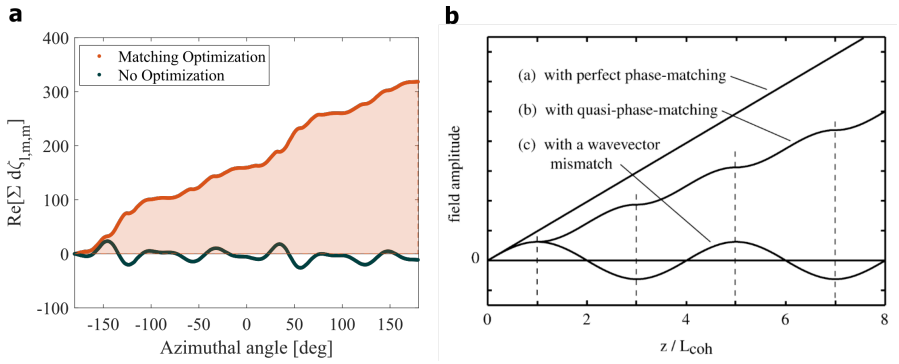

Figure 3.11: Role of the phase in nanocavities. (a) Summation of the discretized contributions to ζ_{lmn} in Fig. 3.9b for the optimized (red) and unoptimized (grey) nanocylider. (b) Spatial evolution of SHG amplitude along propagation direction in an optical waveguide in presence of wavevector mismatch, quasi phase matching and perfect phase matching. Reproduced from [26]

3.5 Conclusion

Optimization routines for nonlinear optical guided systems rely since long time on modal analysis as it offers precise guidelines to both maximize mode overlap and study phase-matching conditions and propagation of nonlinear signals. In this chapter we discussed the

extension of these concepts to unbound systems. Modal formalism in nonlinear nano-optics can provide several helpful tools: identifying high-Q modes (e.g. BIC modes) which could be symmetry forbidden or poorly excited when the resonator response is analyzed for a fixed pump configuration; reconstruct the response of the system with few dominant resonances; study the modal nonlinear overlap and predict the far-field properties of excited modes. With respect to multipolar decomposition, it offers a broader range of validity (resonators on substrates and non-uniform media, no geometry restriction, coupled nanocavities) and a deeper insight as all the modes are computed at once. In the last section of the chapter we presented an optimization algorithm based on $\chi^{(2)}$ engineering, which requires a single numerical calculation. However, many other routes are conceivable. As an example, the evolution of QNMs in the complex plane could be monitored upon the modification of the external environment, geometric parameter or again when interacting with other structures revealing strong coupling regimes. In all these studies, QNM formalism settles as a complementary numerical tool to investigate nonlinear optical properties of matter at the nanoscale and tailor the nonlinear response of nanoantennas.

References

[1] P. Lalanne, W. Yan, K. Vynck, C. Sauvan, and J. P. Hugonin, 'Light Interaction with Photonic and Plasmonic Resonances,' *Laser and Photonics Reviews*, vol. 12, pp. 1–38, 2018. DOI: 10.1002/lpor.201700113.

[2] P. T. Leung, S. Y. Liu, and K. Young, 'Completeness and orthogonahty of quasinormal modes in leaky optical cavities,' *Physical Review A*, vol. 49, pp. 3057–3067, 1994.

[3] P. T. Kristensen and S. Hughes, 'Modes and Mode Volumes of Leaky Optical Cavities and Plasmonic Nanoresonators,' *ACS Photonics*, vol. 1, pp. 2–10, 2014. DOI: 10.1021/ph400114e.

[4] B. Vial, F. Zolla, A. Nicolet, and M. Commandré, 'Quasimodal expansion of electromagnetic fields in open two-dimensional structures,' *Physical Review A - Atomic, Molecular, and Optical Physics*, vol. 89, pp. 1–15, 2014. DOI: 10.1103/PhysRevA.89.023829.

[5] M. B. Doost, W. Langbein, and E. A. Muljarov, 'Resonant-state expansion applied to three-dimensional open optical systems,' *Physical Review A - Atomic, Molecular, and Optical Physics*, vol. 90, pp. 1–14, 2014. DOI: 10.1103/PhysRevA.90.013834.

[6] W. Yan, R. Faggiani, and P. Lalanne, 'Rigorous modal analysis of plasmonic nanoresonators,' *Physical Review B*, vol. 97, pp. 1–9, 2018. DOI: 10.1103/PhysRevB.97.205422.

[7] J. Yang, H. Giessen, and P. Lalanne, 'Simple analytical expression for the peak-frequency shifts of plasmonic resonances for sensing,' *Nano Letters*, vol. 15, pp. 3439–3444, 2015. DOI: 10.1021/acs.nanolett.5b00771.

[8] A. Snyder and J. Love, *Optical Waveguide Theory*. 1979.

[9] P. T. Kristensen, C. Van Vlack, and S. Hughes, 'Generalized effective mode volume for leaky optical cavities,' *Optics Letters*, vol. 37, pp. 1649–1651, 2012. DOI: 10.1364/ol.37.001649.

[10] C. Sauvan, J. P. Hugonin, I. S. Maksymov, and P. Lalanne, 'Theory of the spontaneous optical emission of nanosize photonic and plasmon resonators,' *Physical Review Letters*, vol. 110, pp. 1–5, 2013. DOI: 10.1103/PhysRevLett.110.237401.

[11] E. A. Muljarov and W. Langbein, 'Resonant-state expansion of dispersive open optical systems: Creating gold from sand,' *Physical Review B*, vol. 93, pp. 1–6, 2016. DOI: 10.1103/PhysRevB.93.075417.

[12] Q. Bai, M. Perrin, C. Sauvan, J.-P. Hugonin, and P. Lalanne, 'Efficient and intuitive method for the analysis of light scattering by a resonant nanostructure,' *Optics Express*, vol. 21, pp. 27 371–27 382, 2013. DOI: 10.1364/oe.21.027371.

[13] D. A. Powell, 'Interference between the Modes of an All-Dielectric Meta-atom,' *Physical Review Applied*, vol. 7, pp. 1–13, 2017. DOI: 10.1103/PhysRevApplied.7.034006.

[14] F. Zolla, A. Nicolet, and G. Demésy, 'Photonics in highly dispersive media: the exact modal expansion,' *Optics Letters*, vol. 43, pp. 5813–5816, 2018. DOI: 10.1364/ol.43.005813.

[15] L. Zschiedrich, F. Binkowski, N. Nikolay, O. Benson, G. Kewes, and S. Burger, 'Riesz-projection-based theory of light-matter interaction in dispersive nanoresonators,' *Physical Review A*, vol. 98, pp. 1–5, 2018. DOI: 10.1103/PhysRevA.98.043806.

[16] T. Wu, A. Baron, P. Lalanne, and K. Vynck, 'Intrinsic multipolar contents of nanoresonators for tailored scattering,' *Physical Review A*, vol. 011803, pp. 1–5, 2020. DOI: 10.1103/PhysRevA.101.011803.

[17] F. Tisseur and K. Meerbergen, 'The Quadratic Eigenvalue Problem,' *Society for Industrial and Applied Mathematics*, vol. 43, pp. 235–286, 2001.

[18] C. Gigli, T. Wu, G. Marino, A. Borne, G. Leo, and P. Lalanne, 'Quasinormal-Mode Non-Hermitian Modeling and Design in Nonlinear Nano-Optics,' *ACS Photonics*, vol. 7, pp. 1197–1205, 2020. DOI: 10.1021/acsphotonics.0c00014.

[19] A. Rodriguez, M. Soljacic, J. D. Joannopoulos, and S. G. Johnson, 'X(2) X(3) harmonic generation at a critical power in inhomogeneous doubly resonant cavities,' *Optics Express*, vol. 15, pp. 7303–7318, 2007.

[20] Z. Lin, X. Liang, M. Lončar, S. G. Johnson, and A. W. Rodriguez, 'Cavity-enhanced second-harmonic generation via nonlinear-overlap optimization,' *Optica*, vol. 3, pp. 233–238, 2016. DOI: 10.1364/OPTICA.3.000233.

[21] M. MiInkov, D. Gerace, and S. Fan, 'Doubly resonant photonic crystal cavity based on a bound state in the continuum for efficient χ (2) nonlinear frequency conversion,' *Optica*, vol. 6, pp. 1–7, 2019. DOI: https://doi.org/10.1364/OPTICA.6.001039.

[22] P. Lalanne, W. Yan, A. Gras, C. Sauvan, J.-P. Hugonin, M. Besbes, G. Demésy, M. D. Truong, B. Gralak, F. Zolla, A. Nicolet, F. Binkowski, L. Zschiedrich, S. Burger, J. Zimmerling, R. Remis, P. Urbach, H. T. Liu, and T. Weiss, 'Quasinormal mode solvers for resonators with dispersive materials,' *Journal of the Optical Society of America A*, vol. 36, pp. 686–704, 2019. DOI: 10.1364/josaa.36.000686.

[23] S. Gehrsitz, F. K. Reinhart, C. Gourgon, N. Herres, A. Vonlanthen, and H. Sigg, 'The refractive index of AlxGa1-xAs below the band gap: Accurate determination and empirical modeling,' *Journal of Applied Physics*, vol. 87, pp. 7825–7837, 2000. DOI: 10.1063/1.373462.

[24] J. Yang, J. P. Hugonin, and P. Lalanne, 'Near-to-Far Field Transformations for Radiative and Guided Waves,' *ACS Photonics*, vol. 3, pp. 395–402, 2016. DOI: 10.1021/acsphotonics.5b00559.

[25] M. Veysi, C. Guclu, and F. Capolino, 'Focused azimuthally polarized vector beam and spatial magnetic resolution below the diffraction limit,' *Journal of the Optical Society of America B*, vol. 33, pp. 2265–2277, 2016. DOI: 10.1364/josab.33.002265.

[26] R. Boyd, *Nonlinear Optics*, 3rd. Academic Press, 2008.

SHG in AlGaAs nanoresonators 4

Contents

After having introduced the theoretical framework and all the numerical tools necessary to study the nonlinear light-matter interaction at the nanoscale, in this chapter I will focus on the fabrication of AlGaAs nanoresonators and SHG experimental characterization. At first, I will discuss the material choice, then the fabrication of isolated or arrayed nanoresonators, and finally the experimental setup to characterize their nonlinear response. Once compared the theoretical predictions and experimental measurements on the isolated resonators, I will show how they can be arranged in periodic arrays to control radiation direction and polarization states of SHG beam.

4.1 Material properties

GaAs is one of the most employed III-V alloy in optoelectronic integrated circuits as it combines several interesting properties:

- a large direct band-gap ($E_g = 1.44$ eV);
- a high refractive index in the near-IR ($n \approx 3.3$);
- the possibility to form ternary alloys with aluminum, indium and phosphorus to modify its optical properties or implement lattice-matched epitaxial semiconductor heterostructures [1];
- a zincblende crystalline structure featuring a high quadratic nonlinear response ($\chi^{(2)} \approx 200$ pm/V at $\lambda = 1550$ nm [2]) which is inhibited in centrosymmetric materials, as seen in Chapter 2.

In the following, we will aim at optimizing photonic devices operating in the C-telecom band ($\lambda \in [1530 - 1565]$ nm). This means that the SHG signal would have a higher energy than material bandgap ($E_{SH} \sim 1.6$ eV), with a consequent strong absorption (thermal losses). A well-known workaround for such limitation is shown in Fig. 4.1a: moving to the ternary $Al_xGa_{1-x}As$ alloy, the bandgap of the material increases with Al molar fraction x while the lattice constant a stays almost unvaried ($a(x) = 5.6533 + 0.0078x$) enabling the growth of epitaxial thin layers of AlGaAs on a GaAs substrate with minimal stress. Fig. 4.1b reports the bandgap variation of $Al_xGa_{1-x}As$ with an increasing aluminum molar fraction x as evidenced by empirical demonstration in [3].

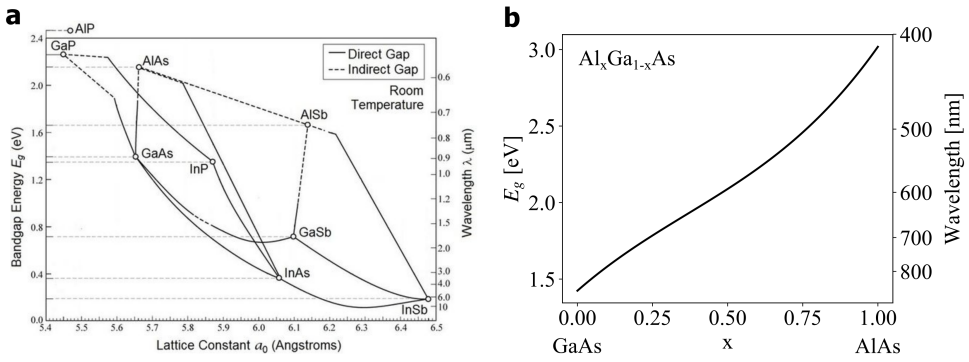

Figure 4.1: (a) III-V semiconductor alloys bandgap vs. lattice constant [4]. (b) $Al_xGa_{1-x}As$ bandgap vs. aluminum molar fraction x [3].

One would envisage the largest bandgap to operate in a transparent regime both at pump frequency and SH. In contrast, an excessive Al concentration would have two counterproductive effects, see Fig. 4.1:

(a) it reduces the refractive index of the material, leading in turn to a weaker light confinement inside the antenna's volume. In this work, the empirical model in [5] is used for the refractive index;

(b) it lowers the effective quadratic susceptibility [6].

The best trade-off was found at $x = 0.18$, for which $\chi^{(2)} \approx 200$ pm/V and the material is transparent for $\lambda > 740$ nm.

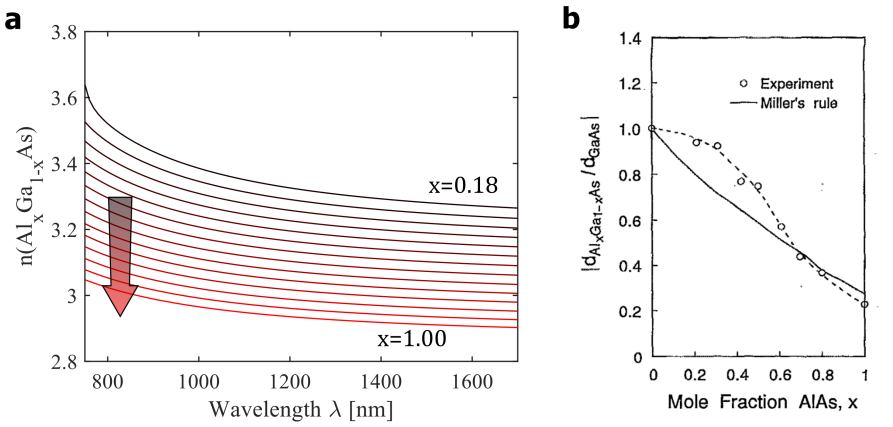

Figure 4.2: $Al_xGa_{1-x}As$ optical properties vs. aluminum molar fraction x. (a) Refractive index from [5]. (b) $Al_xGa_{1-x}As$ $\chi^{(2)}$ (normalized to GaAs) [6].

4.2 Technological platform

The way to tightly confine light at sub-λ scale is a high-index contrast between the nanoantenna and its surrounding. Two main techniques can be identified (see Fig. 4.3):

- To epitaxially grow an heterostructure of $Al_{0.18}Ga_{0.82}As/Al_{0.98}Ga_{0.02}As/GaAs$ and selectively oxidize the Al-rich layer. When the concentration of aluminum in AlGaAs is high enough, wet oxidation at high temperatures ($T = 390°$ for $x > 0.9$, typically) yields to a non-stoichiometric amorphous layer of aluminum oxide (AlOx) with refractive index ≈ 1.6. The final result is a monolithic device in which the oxide layer can be thick enough to be considered as semi-infinite.

- The epitaxially grown thin layer of $Al_{0.18}Ga_{0.82}As$ on GaAs can be reported through wafer bonding techniques on a low refractive index material, like sapphire (Al_2O_3, $n \approx 1.75$). In this way the substrate is completely transparent, enabling to collect the generated signals both in forward and backward directions.

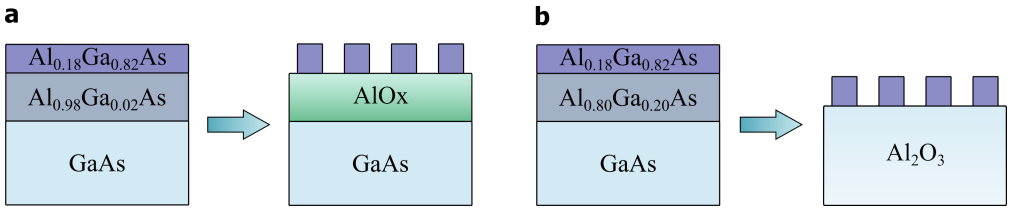

Figure 4.3: Fabrication techniques of $Al_{0.18}Ga_{0.82}As$ nanopatterned surfaces on low-index substrates. (a) Monolithic and (b) wafer bonding approaches.

Even if the two approaches offer different advantages and application solutions, they share many common points. Thus, we present first in detail the monolithic fabrication, and then we will discuss just the different aspects of wafer bonding protocol.

The fabrication process starts from an epitaxial $Al_{0.18}Ga_{0.82}As/Al_{0.98}Ga_{0.02}As/GaAs$ growth. The substrate is a non-intentionally doped (100)-oriented GaAs wafer, and the thickness t of $Al_{0.98}Ga_{0.02}As$ layer has to be large enough to minimize the effect of GaAs

substrate in the final device. A rule of thumb to consider the patterned $Al_{0.18}Ga_{0.82}As$ nanostructures optically uncoupled from the substrate is to set $t \geqslant \lambda/n_s$ where λ is the working wavelength in vacuum and n_s is the AlOx refractive index. We chose in our case $t = 1000 > 1550/1.6$ nm.

All the fabrication steps following the epitaxial growth are presented in Fig. 4.4: a negative resist is spun on the sample (b) and successively exposed to the electron beam (e-beam) lithography. Once the resist has been developed (c), the AlGaAs layer is etched (d) and finally the Al-rich layer is oxidized (e). In the following we discuss in detail these steps.

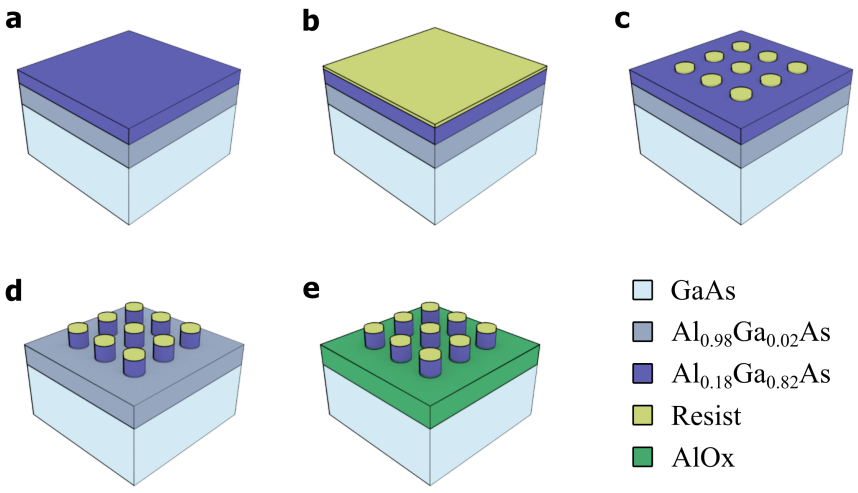

Figure 4.4: Fabrication process of AlGaAs-on-AlOx nanoresonators. (a) Starting epitaxial structure, (b) resist deposition, (c) e-beam lithography (EBL) and resist development, (d) inductively-coupled plasma reactive-ion etching, (e) wet oxidation.

Resist spinning

Regardless of the resist used, all the samples are initially treated with a standard cleaning process: 5 min of ultrasound bath at 40° in acetone to remove any organic impurity on the surface, followed by 1 min in isopropanol. The latter is suitable to dissolve non-polar contaminants, residues left by acetone, and it evaporates at a faster rate. Successively, 2 min of O_2-plasma at gas pressure of 0.6 mbar removes any possible organic residual. The cleaning is concluded by a dehydration bake at 120° for 4 min to completely dry the surface and improve resist adhesion. The fabrication protocol depicted in Fig. 4.4 suggests the use of a negative-tone resist as smaller areas have to be exposed. Two different resists have been optimized for this process, according to the specific pattern to be implemented:

- Man-2401, an industrial photoresist produced by Micro Resist Technology [7]. It offers the advantage of a good resolution with a low e-beam exposure dose (typically 120 $\mu C/cm^2$), which allows to pattern large surfaces with reasonable process times, yet it is not well suited when coping with proximity effects. We employ this solution whenever the elements to pattern are farther than 100 nm apart. Ti-prime promoter is applied on the wafer (spin rate = 4000 rpm followed by 2 min soft bake at 120°)

to improve adhesion. Then, Man-2401 is spun at 4000 rpm, ensuring a thin layer of around 100 nm, essential for a good lithographic resolution. The resist is finally soft-baked at 95° for 1 min.

- HSQ (hydrogen silsesquioxane) by Dow Corning Corporation [8]. It offers a better resolution than Man-2401, which stems both from a slightly reduced thickness and a lower sensitivity to e-beam exposure (typical used doses are around 2000 $\mu C/cm^2$), reducing the impact of secondary electrons and in turn of proximity effects. As a drawback, it requires $\sim$ 20 times the exposure time than Man-2401, which can be dramatically relevant when patterning large arrays of nanostructures. We rely on this technique to produce compact arrays or oligomers with gaps narrower than 100 nm. Being a Si-based polymer, its direct adhesion with GaAs substrate is critical and it has to be improved either with industrial promoters (e.g. Surpass3000) or by depositing a thin SiO_2 layer. We usually adopt this second solution, with a 10nm-thick SiO_2 layer deposited through PECVD at 280°. Successively, HSQ is spun at 4000 rpm followed by a double-step baking (150° for 2 min, then 200° for other 2 min).

E-beam lithography and development

All the lithographic processes are performed with a combined EBL/SEM hybrid, Pioneer Two by Raith nanofabrication. It provides an acceleration voltage up to 20 kV and a minimal beam aperture of 7 μm (10 μm is typically adopted, as it ensures almost the same resolution but a larger beam current, and in turn a faster writing speed). We commonly use nominal doses of 120 $\mu C/cm^2$ and 1800 $\mu C/cm^2$ for Man-2401 and HSQ, respectively. However, dose tests from 1 to 2 times the nominal dose are systematically performed for any different geometry. This is mostly due to the fact that changing nanoresonators size and array periodicity has a strong impact on proximity effects, leading to the impossibility of a universal dose test for any geometry. A valuable adopted alternative consists of making several replica of the same metasurface, where the designed parameters are continuously varied by few percents to ensure that at least one of the final devices is as close as possible to the desired one.

The resist is successively developed in a basic solution. Also in this case, depending on the polymer used, two different processes are implemented:

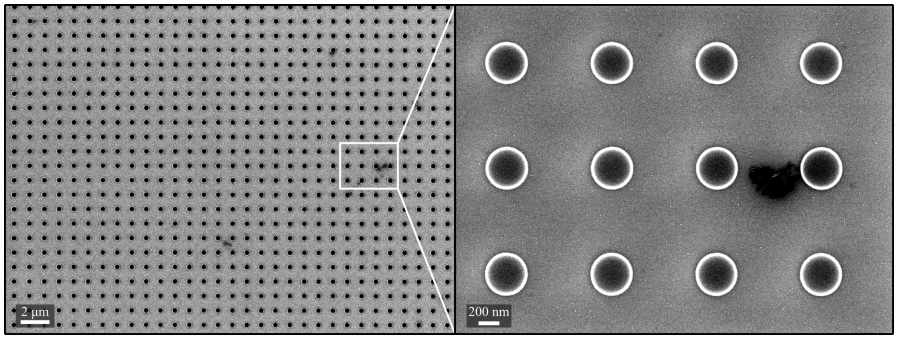

Figure 4.5: E-beam lithography result. SEM images show Man-2401 after development, corresponding to step (c) in Fig. 4.4.

- Man-2401: the sample is dipped in a solution of 2.38% tetramethyl-ammonium-hydroxide (TMAH) in water (AZ 726 MIF by Microchemicals) for 10 sec, followed by 50 sec of H_2O rinsing, and then again 40 sec in AZ 726 MIF plus 50 sec in H_2O to finely remove the unexposed resist and contaminant re-depositions. The development is followed by 18 sec of O_2-plasma, 30 sec of UV exposure, 1 min re-flow on hot-plate at 110° and 10 min hard bake at 160°. These steps aim at refining the exposed resist to smooth the edges and harden the layer for the etching process. Fig. 4.5 shows an SEM image of the lithographic mask.

- HSQ: the developer is a basic solution of buffered KOH in water (AZ 400K by Microchemicals). The sample is dipped in AZ 400K for 1 min followed by 2 min in H_2O. HSQ exhibits smoother edges than Man-2401 and, being a Si-based compound, it is more resistant to $SiCl_4$ etching, so it does not require any further re-flow or hard-bake process. An example of small gap (~ 50 nm) dimers, which can be obtained with HSQ process, is reported in Fig. 4.6.

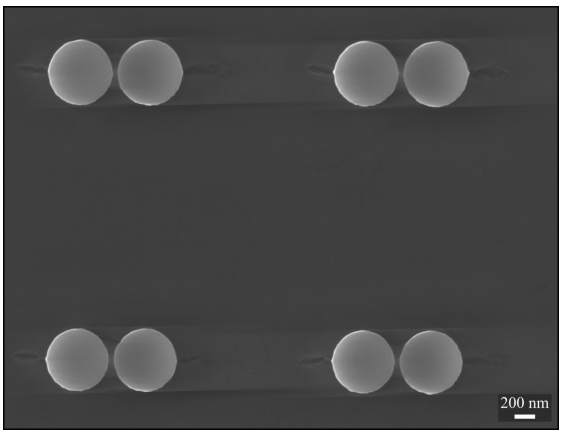

Figure 4.6: AlGaAs-on-AlOx nanodimers with 340 nm radius and 50 nm gap obtained with HSQ resist.

Reactive Ion Etching

The lithographic pattern is transferred to the AlGaAs layer through reactive ion etching (RIE). In case of HSQ resist, the 10nm-thick SiO_2 adhesion layer is removed with a preliminary CHF_3-based RIE, a standard engraving process in SOI technology. AlGaAs is etched through Inductively Coupled Plasma(ICP)-RIE commonly adopted in III-V nanofabrication. A 35 W RF source is used to create a high-density plasma through a metallic coil (the inductive component). The plasma is injected inside the sample chamber and accelerated with another 15 W RF source. The gas mixture inside the chamber is composed by Argon (30 sccm) and $SiCl_4$. Ar^+ ions provide a mechanical etching which is highly directional and poorly selective. $SiCl_x$ and $SiCl_x^+$ free radicals, produced in the plasma, chemically activate GaAs and AlGaAs surfaces, featuring high material selectivity. The combined action of free radicals and Ar^+ ions results in perfectly vertical and smooth sidewalls, see Fig. 4.7.

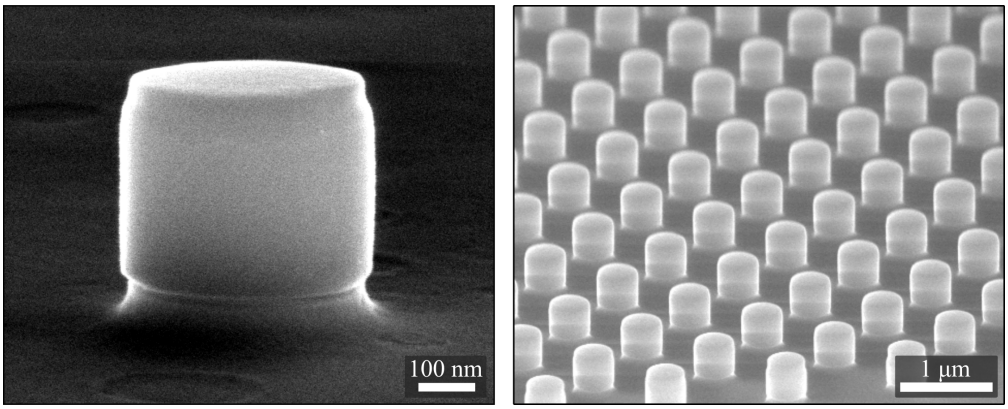

Figure 4.7: Tilted SEM images of typical fabrication results. Left: an isolated disk with radius $r = 230$ nm and height $h = 400$ nm. Right: a metasurface with period $p = 940$ nm.

Oxidation

The final step of monolithic fabrication protocol is the oxidation of aluminum-rich layer, which creates the high-index contrast necessary to tightly confine the electromagnetic field inside the resonator volume. This process is performed with an AET Technlogies wet-oxidation oven. The sample is introduced in a chamber under vacuum and slowly warmed up to 390° (20°/min) under controlled gas conditions (N_2 at 500 mbar). In the meantime, the oxidation gas (a mixture of N_2/H_2 with water vapor) is prepared in a controlled mixer. When the steady state is achieved, the gas is injected in the oven and oxidation starts. As reported in [9], when such vapor mixture interacts with AlAs it triggers a thermodynamically favorable (negative Gibbs free energies) reaction chain at high temperatures which can be written as:

$$\begin{aligned} 2\,\mathrm{AlAs} + 6\,\mathrm{H_2O_{(g)}} &= \mathrm{Al_2O_3} + \mathrm{As_2O_{3(l)}} + 6\,\mathrm{H_2} \\ \mathrm{As_2O_{3(l)}} + 3\,\mathrm{H_2} &= 2\,\mathrm{As} + 3\,\mathrm{H_2O_{(g)}} \\ \mathrm{As_2O_{3(l)}} + 6\,\mathrm{H} &= 2\,\mathrm{As} + 3\,\mathrm{H_2O_{(g)}} \end{aligned} \tag{4.1}$$

In the present case, an amorphous layer of non-stoichiometric AlOx is obtained at the end of the process. The oxidation rate and extent strongly depend on temperature and Al concentration, as shown in Fig. 4.8.

The oxidation recipe carried out in the AET oven is detailed in Table 4.1.

Wafer bonding option

An alternative solution to monolithic fabrication of high-index contrast nanostructures is provided by wafer bonding techniques. In this case the AlGaAs nanoresonator lies on a transparent sapphire substrate. The fabrication protocol differs from AlGaAs-on-AlOx platform just for few steps that we list here below.

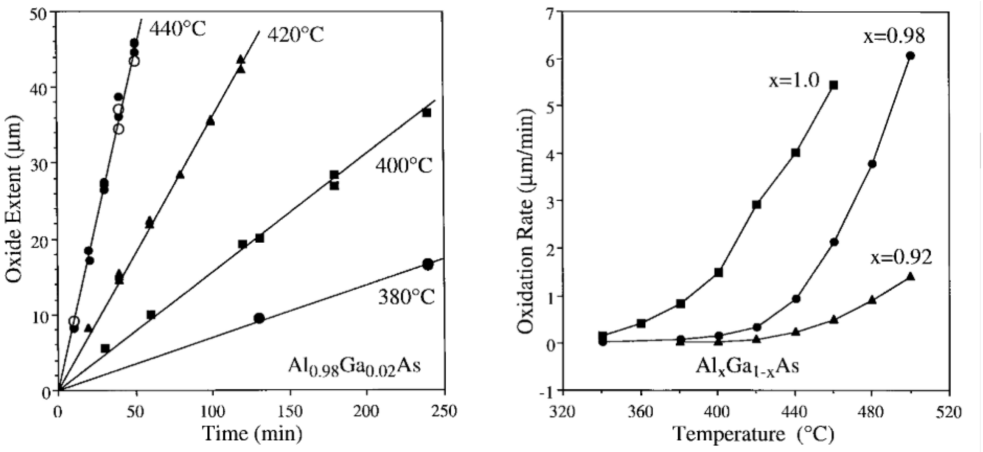

Figure 4.8: $Al_xGa_{1-x}As$ oxidation properties vs. temperature, process time, and Al molar fraction (x) [9].

Process Description		Oxidation Chamber		Humid Gas		Dry Gas	
Step	Time [min:sec]	Temp [Deg]	Pressure [mbar]	N_2H_2 [l/min]	H_2O [g/h]	N_2 [l/min]	N_2H_2 [l/min]
Initial vacuum	01:00	20°	$\sim 9 \times 10^{-2}$	0.0	0.0	0.0	0.0
N_2 injection	05:00	20°	500	0.0	0.0	0.5	0.0
N_2H_2 in evaporator	01:00	20°	500	0.6	0.0	0.5	0.0
H_2O in evaporator	01:00	20°	500	0.6	4.0	0.5	0.0
Heating (20°/min)	18:30	390°	500	0.6	4.0	0.5	0.0
N_2H_2 in chamber	00:30	390°	500	0.6	4.0	0.0	1.0
Humid gas injection	30:00	390°	500	0.6	4.0	0.0	1.0
Cooling	30:00	20°	$\sim 9 \times 10^{-2}$	0.0	0.0	0.0	0.0

Table 4.1: Oxidation program in AET Technologies oven.

Raw wafer

The sample preparation starts from a molecular beam epitaxy MBE growth of a 400-nm-thick $Al_{0.18}Ga_{0.82}As$ layer on a (100) GaAs substrate. A 500-nm-thick $Al_{0.8}Ga_{0.2}As$ sacrificial layer is inserted before the AlGaAs epitaxial growth. The sample is then glued on a sapphire host substrate with a flip-chip process. Finally GaAs substrate and sacrificial layer are removed by mechanical and selective chemical etching, leaving only the 400-nm-thick AlGaAs as a mirror-flat surface.

Spin coating and lithography

The first lithographic tests done on wafer bonded samples showed that the developed Man2401 resist was much thinner with respect to the monolithic protocol, too thin to withstand the entire etching process. Two routes can be conceived to overcome the problem: 1) using a slower spin rate to ensure a thicker Man-2401 layer, 2) moving to a different resist compound. The second strategy was adopted in the present work, using Man-2403 which preserves the same chemical properties as the previous one with about three times its thickness. The above protocols for spin coating and lithographic exposure are therefore

maintained.

Finally, being the substrate non-conductive, strong charge accumulation issues can occur during e-beam lithography. For this reason, a discharging coating (Electra 92 by AllResist) is applied after Man-2403. This conductive polymer is spun at 4000 rpm and successively baked at 90° for 2 min. It results in a thin 40 nm layer whose sole effects is to favor charge removal during lithography. It is then solved in water before Man-2403 development.

4.3 Nonlinear microscopy

In order to experimentally probe the nonlinear optical properties of nanoresonators, one must rely on two facilities: 1) an optical system to properly excite a nanostructured surface and detect its response with good spatial resolution; 2) a high-power laser source which can induce a detectable nonlinear response inside the resonator. The optical system developed by us to perform nonlinear microscopy is schematically presented in Fig. 4.9.

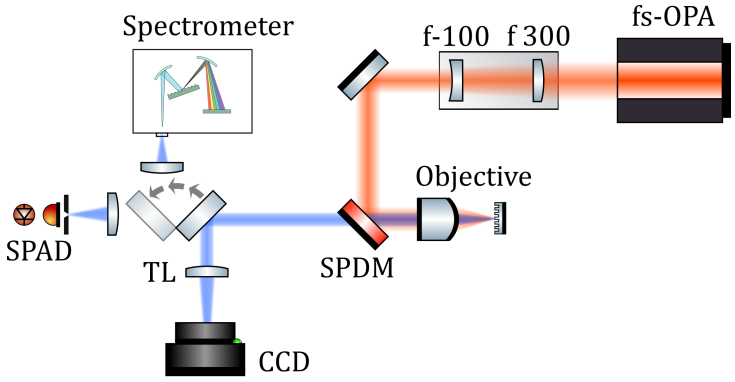

Figure 4.9: Simplified sketch of a microscope for nonlinear characterization in epi-illumination configuration. (SPDM: Short-Pass Dichroic Mirror, TL: Tube Lens, CCD: Charge Coupled Device, SPAD: Single Photon Avalanche Diode)

A broadly tunable femtosecond source in epi-illumination configuration provides the high-intensity pulsed excitation in the near-IR. A microscope objective focuses this beam to a diffraction-limited spot with Airy disk size

$$d = 1.22 \times \frac{\lambda}{n\mathrm{NA}} \tag{4.2}$$

where λ is the laser wavelength, NA the objective numerical aperture and n the medium refractive index (air in this case). This tight focusing combined with a high-power laser enables to achieve field intensities of the order of GW/cm^2, essential to generate detectable nonlinear signals in low-Q nanocavities. The harmonic response is then filtered by a short-pass dichroic mirror and imaged on a CCD camera, through a tube lens. This hybrid configuration between widefield and confocal microscopy offers the advantages of a high-intensity, diffraction-limited excitation and the possibility to image at once the nonlinear response on a high-sensitivity camera. Alternatively, the harmonic signal can be filtered by a pinhole to remove the out-of-focus components and detected with a single-photon

avalanche diode, implementing a confocal microscopy. Finally, its spectral features can be analyzed through a spectrometer. In the following, we will detail all the different parts of this setup and describe further imaging options.

Coherent source

Differently from closed cavities, where the high-Q factors enable nonlinear optics with continuous wave sources, the generation of nonlinear signals in dielectric nanoresonators imposes to work with pulsed optical beams. In my PhD thesis, the excitation beam is generated in an optical parametric amplifier (OPA - Mango by Amplitude) pumped by a mode-locked Yt-doped fiber laser (Satsuma by Amplitude). The mode-locked cavity generates a 10 W pulsed beam at 1030 nm with a temporal width $\tau \sim 200$ fs and repetition rate of 1 MHz (corresponding to 10 µJ). In the OPA, part of this signal is frequency-doubled with a nonlinear crystal, and the rest is exploited for supercontinuum generation. These two products constitute the pump and seed signals of a DFG process, respectively, which is the core of the OPA cavity. Adjusting the phase-matching conditions for the two beta barium borate (BBO) crystals where the DFG occurs, one can tune the generated beam in a broad spectrum between 600 and 2400 nm.

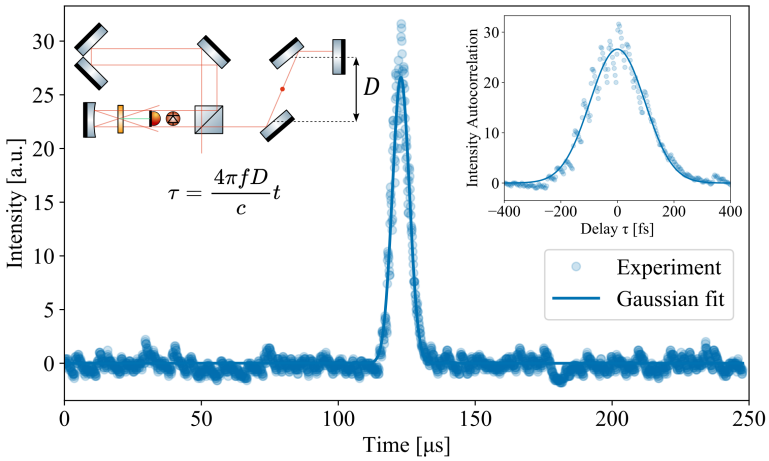

Figure 4.10: Autocorrelation measurement of optical pulses. The main plot reports the autocorrelator trace acquired through the oscilloscope. Top left: sketch of the interferometer configuration. Top right: reconstruction of laser pulse shape.

The pulse duration at $\lambda = 1550$ nm was characterized through the FR-103 autocorrelator by Femtochrome. The adopted configuration is a rotational Michelson interferometer. The time delay depends on the stage angular velocity (see Fig. 4.10), allowing to measure fs pulses in the µs domain with a common oscilloscope. The two halves of the splitted beam are recombined on a nonlinear crystal, and SHG signal returns the intensity autocorrelation

$$A(\tau) = \int_{-\infty}^{\infty} I(t)I(t-\tau)dt. \tag{4.3}$$

The measured full width half maximum (FWHM) of $A(\tau)$ is 229 fs which, assuming a

Gaussian pulse profile, corresponds to $\sqrt{2}$ times the pulse duration. We estimated therefore the FWHM of laser beam at 1550 nm ~160 fs.

Pump spectrum analysis, reported in Fig. 4.11, shows a peak centered at 1557 nm with a width of 18.4 nm (corresponding to a bandwidth of 2.75 THz). Before reaching the spectrometer, the OPA beam passes through a few more dispersive elements than for reaching the autocorrelator. We can thus reasonably assume that the Gaussian pulse is transform-limited.

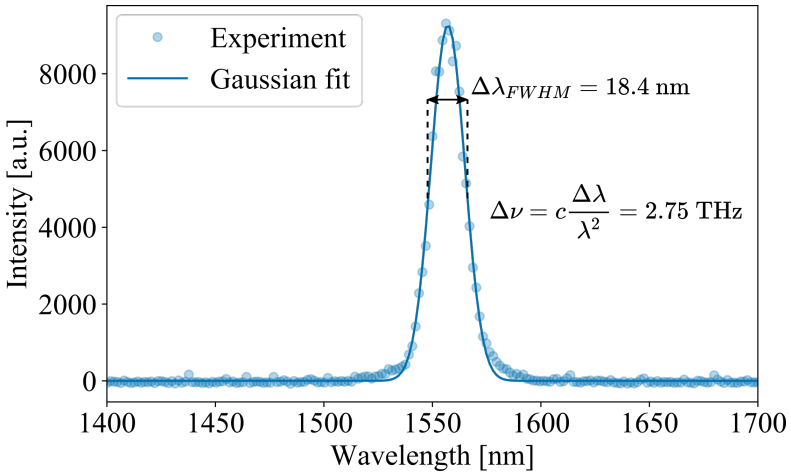

Figure 4.11: Spectral width of OPA laser beam measured through Ocean Optics NIRQuest.

Optical focusing system

The OPA beam exhibits a waist of around 6 mm, while most of the microscope objectives used during characterization (in particular high-NA ones) have a rear aperture of ~ 2 mm. Two different solutions have been adopted in time not to waste most of input power: 1) a slowly convergent lens (with focal distance $\geqslant$ 500 mm) is placed along the excitation path; 2) a collimator in beam-reducer configuration (i.e. a Galileian telescope with magnification 1/3, see Fig. 4.9). The latter can be placed in any position along excitation path and produces a collimated beam. However, it increases the divergence of input ray. The former solves this problem producing a slowly converging beam, but its position along the excitation path is critical.

In order to characterize SHG in reflection configuration, a short-wavelength-pass dichroic mirror is inserted before the objective (Thorlabs DMSP950 was used in all the experiment illustrated in the following).

The choice of microscope objective depends on the desired excitation spot size and collection angle. When probing single resonators, the choice of high-NA objective is favored. In the present work two 100X-magnification objectives are alternatively used (LCPLFLN100X or LMPLFLN100X by Olympus) with numerical apertures of 0.85 and 0.8 corresponding to maximum collection angles of 58° and 53°, respectively. Whenever a larger region has to be excited and the collection angle can be reduced, low-NA 10X-magnification objectives are preferred. A general overview of different solutions is reported in Table 4.2.

Objective	LCPLFLN100X	LMPLFLN100X	LMPLN10XIR	Leitz NPL10XDF
Magnification	100X	100X	10X	10X
NA	0.85	0.8	0.3	0.2
Collection angle	58°	53°	17°	12°
Spot size(*)	2.22 µm	2.36 µm	6.3µm	9.45µm

Table 4.2: Overview on different objectives properties. (*) Diffraction limited spot size at $\lambda = 1550$ nm.

Imaging with camera

The CCD camera in Fig. 4.9 relies on a high-sensitivity sensor (Sony ICX825AL) with quantum efficiency around 38% at 775 nm, which allows to detect low-power signals generated in dielectric resonators. For example, in the simplest configuration, the camera enables to image in the real space the SHG signal by single nanoresonators, as sketched in Fig. 4.12a. The system is coupled to a motorized stage composed by a 3-axis closed-loop piezo actuator (Nanomax300 by Thorlabs), for displacements within 20 µm with 5 nm resolution, mounted on two stepper motors (Newport UE41PP with MM4006 controller), for longer travel range in the xy-plane with 1 µm resolution. The whole system is synchronized through LabVIEW environment, which allows to align the focused beam on a single resonator, acquire the SHG signal in camera, and move to the following structure. At any acquisition just a region of interest (ROI) of 120×120 pixels of the total 1392×1040 CCD sensor is recorded. In this way a complete mapping of a SHG by individual resonators can be extracted as shown in Fig. 4.12b.

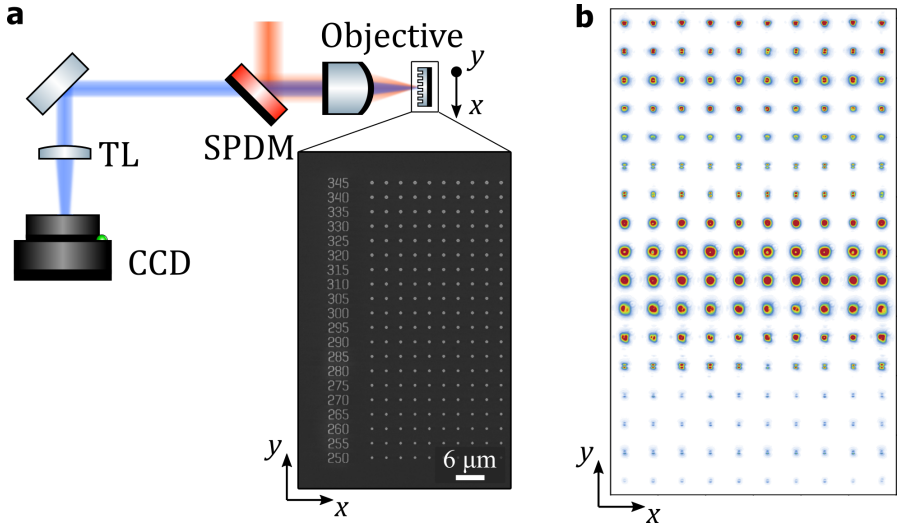

Figure 4.12: SHG characterization with a CCD camera. (a) Experimental setup: an array of nanodisks (shown in the inset) is placed on a translation stage, SHG in backward direction is collected by a CCD camera. (b) Processed result. Nanodisks radius increases along y-axis and identical structures are repeated along x-axis.

CCD camera response was calibrated with a power meter, as described in Appendix B, to extract a quantitative information on SHG efficiency.

Back-focal-plane imaging

Besides real-space analysis, it is often helpful to image the Fourier space which gives direct information on the radiation pattern of a nanoantenna. The simplest way to implement reciprocal-space microscopy is to add a lens, usually called Bertrand lens, along the detection path so as to Fourier transform the image plane. This concept is depicted in Fig. 4.13a.

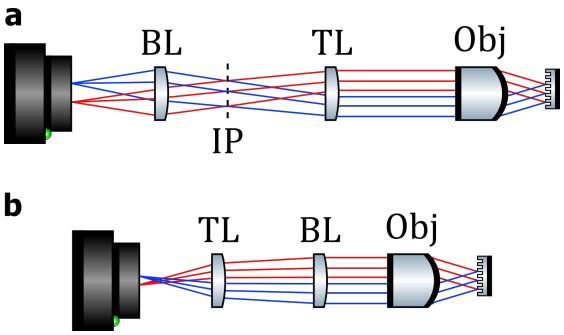

Figure 4.13: Back focal plane (BFP) imaging configurations. (a) a Bertrand lens (BL) is used to Fourier transform image plane (IP). (b) BL focus is placed in correspondence of objective back focal plane to project Fourier space at infinity.

In a simple ray-tracing picture, one can think that all the beams emitted from the sample at different positions, but with the same angle (blue and red in Fig4.13), are focused on the same spot on the camera. Thus, the resulting image describes the distribution of $k_{\parallel}$ in the object plane. The main disadvantages of this configuration is that moving from real to Fourier space imaging is not trivial, furthermore Bertrand lens (BL) and Tube lens (TL) form a finite conjugate pair, meaning that their distance is critical. A more practical solution consists in directly imaging with a Bertrand lens the back focal plane of the objective. In this case, Fourier image is projected at infinity and the tube lens is used to create the image in camera. BL and TL are now infinitely conjugated and deviations on BL position cause just defocus at camera plane. Finally, this configuration enables to move from real to Fourier plane with the simple addition of one optical element along detection path. For a more exhaustive comparative analysis the interested reader can refer to [10].

In order to extract a quantitative angular information from BFP imaging, the Fourier space was calibrated by means of a diffraction grating. For example, in case of 10X objective, a 1D groove array with 100 lines per mm, corresponding to a period $\Lambda = 10\mu m$, was imaged at 775 nm. From grating law, one expects to image a series of peaks corresponding to the in-plane wavevector component of diffracted orders:

$$k_{\parallel}^{out} = \frac{2\pi}{\lambda}\sin(\theta) = k_{\parallel}^{in} + m\frac{2\pi}{\Lambda} \tag{4.4}$$

From BFP image, shown in Fig. 4.14, one can therefore extract the relationship between camera pixels and rad/m in the Fourier space.

$$K = 314\ \text{px} \leftrightarrow \frac{2\pi}{\Lambda} = 0.628\text{rad}/\mu\text{m} \tag{4.5}$$

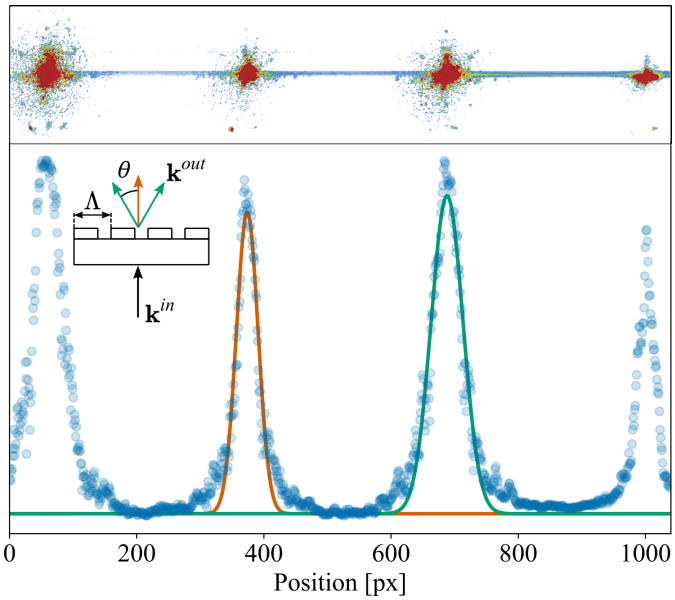

Figure 4.14: BFP calibration. Top: Fourier image of a grating with period Λ (shown in the inset) obtained with configuration in 4.13b. Bottom: Gaussian fit to extract diffraction orders distance on the camera.

The complete setup is shown in Fig. 4.15. Starting from the parametric source, it includes a motorized power control constituted by a half-wave plate (Thorlabs AHWP10M-1600) plus a Glan Taylor polarizer (Thorlabs GT10); a collimator to reduce beam waist to around 2 mm; an half-wave plate (Thorlabs AHWP10M-1600) to control the pump beam polarization; a removable lens (FL) to focus excitation beam on the rear focal plane of microscope objective allowing to control beam size or incident angle; a beam splitter (BS - Thorlabs BSN12) and an InGaAs photodiode (PD - Newport 818-IG) to continuously monitor the pump power; a short pass dichroic mirror (SPDM - Thorlabs DMSP950); two mirrored detection paths to characterize SHG in backward or forward direction. Detection paths are featured with a short pass (SP - Thorlabs FESH850) filter to remove any contribution from pump beam and substrate TPA and a removable BL (Thorlabs LA4102-A-ML) to image Fourier space. Other detection possibilities are offered by a fibered spectrometer (Broadcom QminiVIS/NIR), a SPAD (IDQ ID120) and a Silicon power meter (PD - Newport 818-SL).

Stokes parameters polarimetry

The polarization state of SH light is evaluated through the experimental measurement of Stokes parameters. Polarization of a generic beam, with intensity I and degree of polarization p, can be described by two parameters, see Fig. 4.16a: ψ, called *inclination*, denoting the orientation of polarization ellipse with respect to x-axis; and χ, called *ellipticity*, expressing the ratio between the two semi-axes.

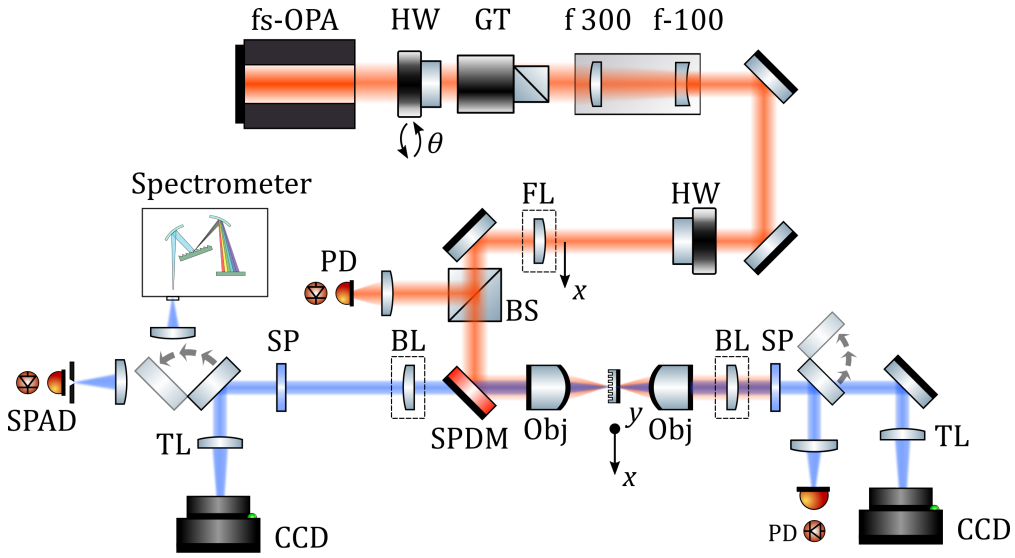

Figure 4.15: Illustration of the complete experimental setup for nonlinear microscopy both in backward and forward direction.

One can therefore define the Stokes vector as:

$$\mathbf{S} = \begin{bmatrix} I \\ Q \\ U \\ V \end{bmatrix} = \begin{bmatrix} I \\ Ip\cos(2\psi)\cos(2\chi) \\ Ip\sin(2\psi)\cos(2\chi) \\ Ip\sin(2\chi) \end{bmatrix} \tag{4.6}$$

Based on these parameters, one can completely describe the polarization state of light as a point on the Poincaré sphere, see Fig. 4.16a: an horizontal/vertical linear polarization corresponds to $Q = \pm 1$,U=0,V=0; a diagonal one to $Q = 0$,U=$\pm$1,V=0; and a right/left circular one to $Q = 0$,U=0,V=$\pm$1. Projecting definition (4.6) on different coordinate systems it can be straightforwardly demonstrated that

$$\mathbf{S} = \begin{bmatrix} I \\ Q \\ U \\ V \end{bmatrix} = \begin{bmatrix} |E_x|^2 + |E_y|^2 \\ |E_x|^2 - |E_y|^2 \\ |E_a|^2 - |E_b|^2 \\ |E_r|^2 + |E_l|^2 \end{bmatrix} \tag{4.7}$$

where $E_{x,y}$ are electric-field components on x/y axis respectively, $E_{a,b}$ on the two diagonals, and $E_{r,l}$ on a circular basis. This directly provides an experimental pathway to evaluate Stokes vector. Changing the orientation ϕ of a wire-grid polarizer, see Fig. 4.16b, one can extract the four field components $|E_{x,y,a,b}|^2$. Adding a quarter-wave plate oriented at $\theta = \pm 45°$ and setting $\phi = 0°$ with respect to horizontal axis, $|E_{r,l}|^2$ can be consequently measured.

Inverting (4.6), one can finally plot the inclination ψ and ellipticity χ in the Fourier space.

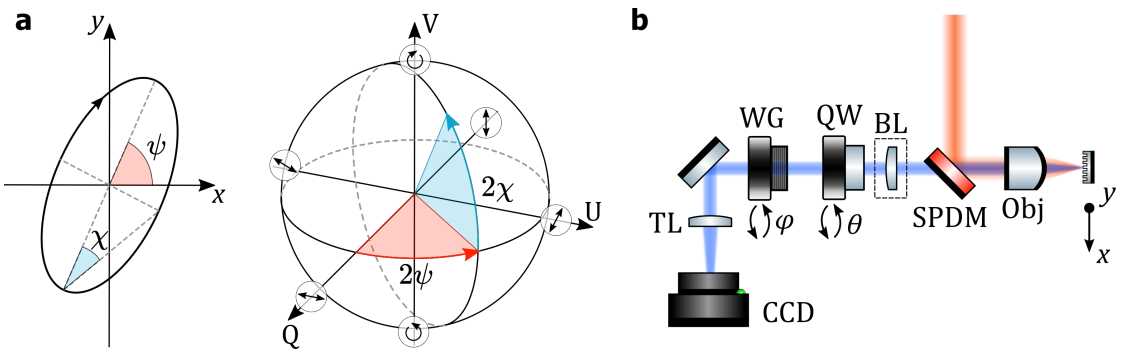

Figure 4.16: Measurement of Stokes parameters. (a) Elliptical polarization representation on Poincaré sphere. (b) Experimental setup. WG: Wire-Grid polarizer, QW: Quarter-Wave plate.

4.4 SHG from isolated particles

The first experimental investigations were carried out on isolated AlGaAs-on-AlOx nanodisks. Being these the first measurements performed with aforementioned nonlinear microscope, the choice of a well-studied geometry allowed direct comparison with existing works in literature, so as to probe our optical setup, validate theoretical predictions, and test our fabrication process.

Compared to two paradigmatic examples of SHG in AlGaAs nanodisk, Gili et al. [11] and Camacho-Morales et al. [12], our first epitaxial structures were based on a metalorganic chemical vapor deposition (MOCVD) as in [12] instead of molecular beam epitaxy (MBE) as in [11]. The thickness of AlGaAs layer was set to 350 nm, i.e. thicker than 300 nm in [12] and thinner than 400 nm in [11]. We adopted the $Al_{0.18}Ga_{0.82}As$-on-AlOx monolithic configuration as in [11], with the only difference that MOCVD growth enables an abrupt transition between GaAs substrate and $Al_{0.98}Ga_{0.02}As$ layer, while in [11] two 90 nm transition layers with varying Al concentration were implemented to reduce oxidation-induced interface strain.

MOCVD was performed at C2N in a Veeco Turbodisc D180 reactor using a hydrogen carrier gas, trimethylgallium and trimethylaluminum as organometallic precursors to elementary gallium and aluminum, and arsine as a gas precursor to arsenic. The structure was grown at 705°C reactor temperature and 70 Torr pressure. A thin GaAs interlayer was added between the Al-rich and Al-poor AlGaAs layers as a barrier against oxidation, ensuring a smoother interface between the oxide and the nanoantenna.

Full numerical calculations, described in Chapter 2 and [13], were used to study linear and nonlinear response of AlGaAs nanodisks with varying radii. Setting the pump at telecom wavelength (λ_{FF} = 1550 nm), the decomposed linear scattering and internal energy of air-suspended nanodisks are shown in Fig. 4.17a. Within the radii range between 200 and 250 nm, nanoantennas exhibit a magnetic dipole resonance, more efficient than electric dipole in confining energy inside the nanodisk volume.

Following the protocol of Section 4.2, we fabricated matrices of nanodisks with nominal radii varying from 180 to 260 nm with 5 nm step along $[1\bar{1}0]$ crystallographic direction, separated by 6 µm distance, see Fig. 4.17b. The structures were repeated along [110] axis to

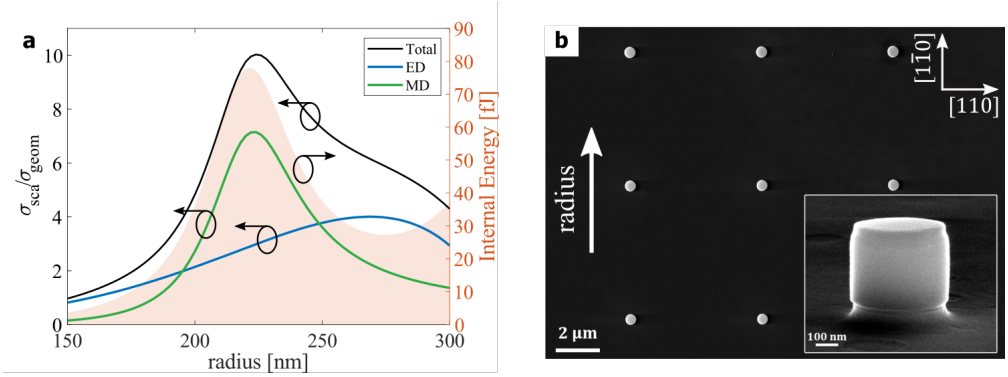

Figure 4.17: Isolated AlGaAs nanodisks. (a) Scattering cross section (left) and internal energy (right) of an air-suspended nanodisk with fixed height $h = 350$ nm, excited by a plane wave at normal incidence and $\lambda = 1550$ nm. Green (blue) solid curve reports magnetic (electric) dipole contribution to the scattering. (b) SEM image of a nanodisk array with 6 µm interaxial distance.

enable a statistical analysis on SHG.

The quality of technological process was investigated through TEM microscopy. The sample surface was spin-coated with benzo-cyclobutene (BCB) for planarization and surface protection, and a platinum layer was deposited for charge removal. Then, a TEM lamella was realized through Focused Ion Beam (FIB) etching. High angle annular dark-field scanning transmission electron microscopy (HAADF-STEM) and energy-dispersive X-ray (EDX) spectroscopy measurements were carried out in a FEI Titan TEM operating at 200 keV. A low-magnification HAADF-STEM micrograph is reported in Fig. 4.18a. Four antennas are visible on top of the AlOx layer. The main interest of this analysis is the evaluation of interfaces between AlOx layer and both the antennas and the wafer, which appear smooth and free of air voids. The TEM micrograph of the antennas, see Fig. 4.18b, reveals fringes only in crystalline portions of the sample, i.e. the wafer and the antennas, while AlOx appears completely amorphous. The interface between the antennas and the AlOx layer was investigated more precisely using HAADF STEM and EDX. Figs. 4.18c and 4.18d show the atomically resolved HAADF-STEM micrographs of the base (c) and the whole volume (d) of nanoantenna. AlOx is separated from the $Al_{0.18}Ga_{0.82}As$ by a 20 nm thick layer of mixed AlOx/GaAsOx. The profile of HAADF contrast in Fig. 4.18e shows a 5 nm thick plateau before the atomic columns of the crystalline $Al_{0.18}Ga_{0.82}As$, which corresponds to the oxidation of the initial GaAs interlayer. The plot in Fig. 4.18f shows the results of EDX measurements along the middle of HAADF STEM micrograph in Fig. 4.18e. EDX results corroborate the HAADF-STEM observation and confirm that the AlOx layer is separated from the $Al_{0.18}Ga_{0.82}As$ by only a 20 nm layer of mixed oxide. AlGaAs composition is also shown to be homogeneous throughout the nanoantenna body. In addition to recalling that the quality of the oxidation process should not depend on the growth technique [14], we also note that this MOCVD AlGaAs-on-AlOx sample behaves comparably to similar MBE samples in terms of mechanical stability [15].

Using the experimental setup of Fig. 4.15, we characterized the SHG from isolated pillars in backward direction with Olympus LMPLFLN100X objective (NA=0.8). OPA signal wavelength was set at $\lambda_{FF} = 1550$ nm, average power $P_{FF} = 0.5$ mW (corresponding to $I_{FF} \sim 3$ GW/cm^2 peak intensity) and input linear polarization along [110]-crystallographic

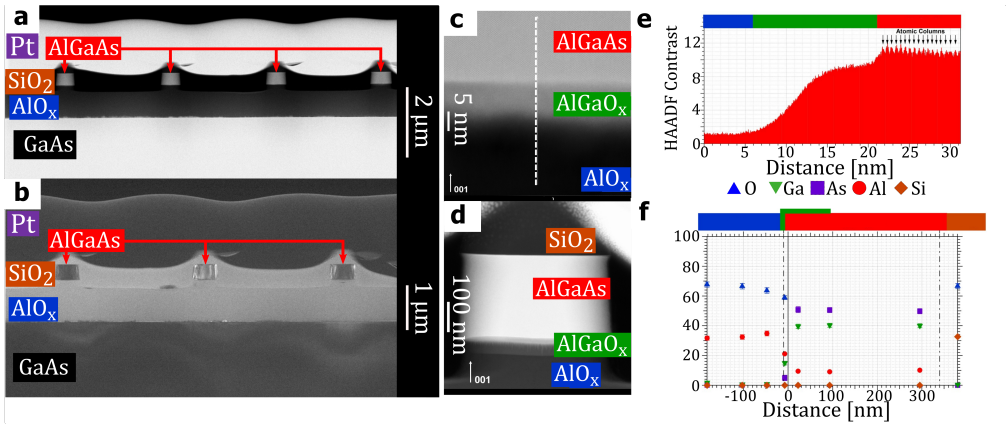

Figure 4.18: TEM images of AlGaAs-on-AlOx nanoantennas. (a) HAADF-STEM micrograph of four nanorods. (b) TEM side-view of the sample. (c) and (d) HAADF-STEM resolving the AlGaAs-AlOx interface (c) and the whole antenna (d). (e) Contrast profile along the white dashed line in (c). (f) EDX measurements performed on the same antenna as in (d).

axis. Measured SHG from nanodisks with different radii was compared with numerical calculations in COMSOL Multiphysics. In order to retrieve a good matching with experimental results, the presence of the substrate and the limited collection angle due to NA were considered, see Fig. 4.19. SHG efficiency was normalized by the incident power on nanoantennas:

$$\eta_{SHG} = \frac{P_{SH}}{(I_{FF}\pi r^2)^2} \tag{4.8}$$

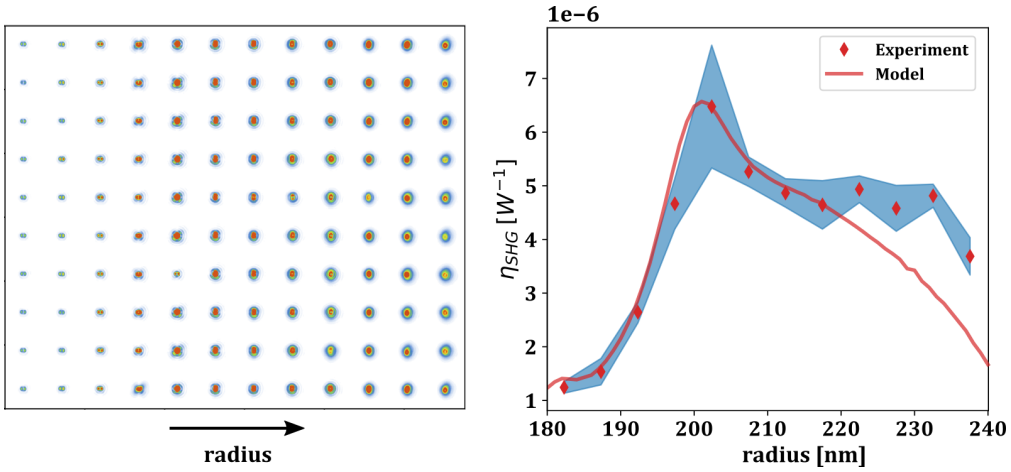

Figure 4.19: SHG measurement from the nanoantennas of Fig. 4.17b. Left: post-processed CCD acquisitions for increasing radii. Right: numerical (solid line) and experimental (dots) SHG efficiency. Blue shaded area denotes the standard deviation over 10 resonators with the same nominal geometry.

Our measured peak efficiency $\eta_{SHG} \sim 6.2 \times 10^{-6}$ W^{-1} in Fig. 4.19 is very close to the maximum value that we can infer from the results reported in [12] report a maximum dimensionless conversion efficiency of 8.5×10^{-5} for an optimized disk with r =245 nm and h = 300 nm ($\eta_{SHG} \sim 6.4 \times 10^{-6}$ W^{-1}).

We finally performed Fourier-space imaging (setup of Fig. 4.13) and Stokes parameters analysis (setup of Fig. 4.16b) to retrieve the radiation diagram and linear polarization state for different disks radii. Our experimental results and theoretical predictions are compared in Fig. 4.20. As reported by several theoretical and experimental works in literature [12, 16–19], all the studied geometries exhibit a null SHG along normal direction upon normal incidence of the pump beam. This behavior can be explained by the selection rules imposed via the $\chi^{(2)}$ tensor of (100)-AlGaAs and the symmetry of both resonator and the excitation [20].

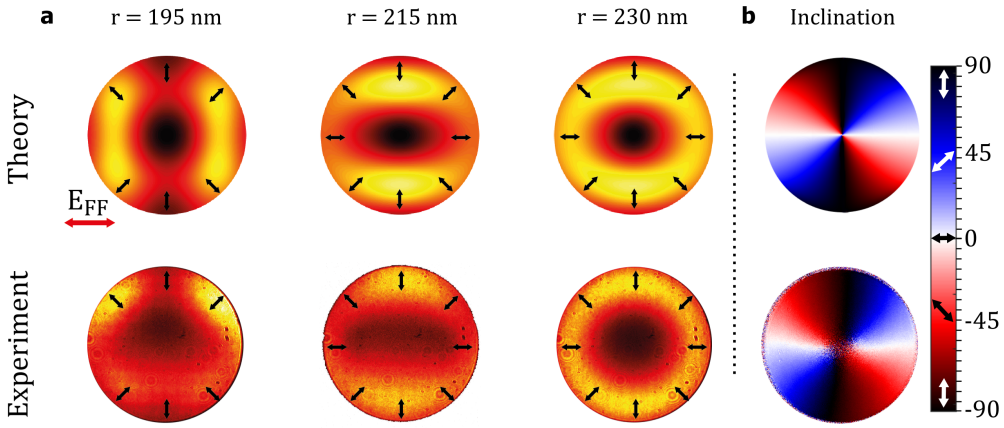

Figure 4.20: BFP analysis of SHG from isolated nanoantennas with varying radii reporting intensity (a) and inclination (b) restricted to a NA=0.8

In Ref. [17], the authors show that for a pump with a linear polarization at 45° from [100] crystalline axis, SHG is dominated by electric quadrupole and octupole, resulting in a radially polarized SH in backward direction. Here, we retrieve a similar outcome by analyzing the inclination pattern of Fig. 4.20b.

Although this polarization control mechanism and the high SHG efficiency seem promising for practical implementations, the null on-axis emission is usually undesirable. Possible workarounds have been demonstrated exciting the nanodisk with a tilted pump [19], or integrating a grating to redirect SH emission [21]. Yet, they require particular configurations which are not always easy to implement. In the following we will focus on nanoantenna arrays, to explore how the properties of isolated resonators are affected by a periodic arrangement, and question if this configuration can provide a control mechanism for on-axis operation.

4.5 From isolated to periodic structures

The first concepts evoked with reference to periodic dielectric structures are diffraction gratings and photonic crystals. Therefore, before showing the nonlinear properties of our AlGaAs metasurfaces, let us provide a more general context for the gratings that we will treat in the following. As a pedagogic example, let us consider an array of GaAs nanodisks with dispersionless permittivity $\varepsilon_r = 12$, radius $r = 200$ nm, period $a = 1000$

nm and thickness $h = 400$ nm. These geometrical parameters are close to the nonlinear metasurfaces studied afterwards. Let us report in Fig. 4.21 the dispersion diagram for the first 8 bands of this photonic crystal slab. Numerical calculations were performed with the open-source software package MIT photonic bands (MPB) [22]. For simplicity, we focus only on TE-like modes, for which the electric field is parallel to the slab (xy-plane) and exhibit even-symmetry with respect to z-axis [23]. Differently from a 2D photonic crystal, in this case the in-plane wavevector $k_{||}$ is conserved while the out-of-plane component k_z is not. Indeed, the yellow shaded region in Fig. 4.21 corresponds to the continuum of radiation modes in air.

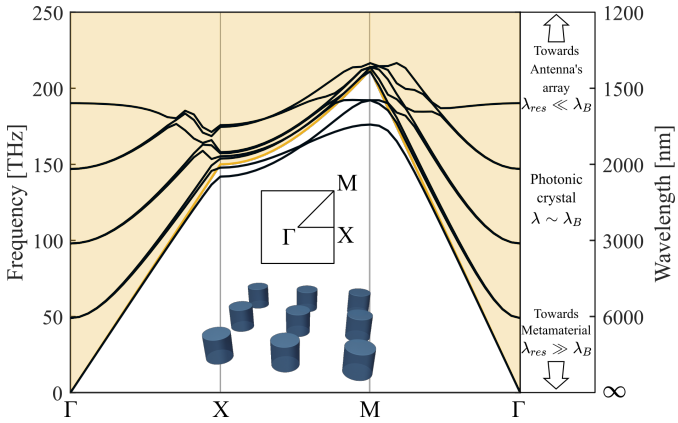

Figure 4.21: Photonic crystal slab made of air-suspended GaAs nanorods with radius $r = 200$ nm, thickness $h = 400$ nm and period $a = 1000$ nm. First 8 band with even symmetry (TE-like modes) are reported. The yellow region denotes the light cone.

The eigenmodes in the irreducible Brillouin zone below the light cone ($\omega < c|k_{||}|$) are guided modes infinitely confined within the slab, while above the light cone they have finite lifetime and they can couple to radiation modes. For this reason, in literature they are referred to as *guided resonances* [24]. Some of these eigenstates can be completely decoupled from radiation modes for symmetry reasons, e.g. when electric and magnetic field are even under 180° rotation around z-axis (C_2 symmetry) at Γ-point, resulting in bound states in the continuum (BIC) with diverging quality factors [25].

In this work we are mostly interested in the region around Γ-point, where almost all the modes are above the light cone. Furthermore, at variance with most photonic crystals, the constitutive elements in this case (i.e. dielectric nanorods) are themselves resonant. We therefore distinguish three regions in the frequency spectrum depending on the relationship between the wavelength λ_{res} of the first resonant mode of isolated element and Bragg wavelength $\lambda_B/n_{\text{eff}} = 2a$:

- for very compact structures (a small) or high refractive index, one can achieve the condition $\lambda_{res} \gg \lambda_B$. The incident wave with $\lambda \sim \lambda_{res}$ perceives the material as uniform as it is the case for metamaterials [26].

- when $\lambda_{res} \ll \lambda_B$ the properties of isolated resonators dominate the scattering. The structure can be treated as an antenna array and for $\lambda < a$ diffraction orders appear.

- between these two regions, incoming light couples with Bloch modes of the structure

which oscillate between the two interfaces, eventually interfering. The properties of isolated resonators are modulated by the periodic array, and guided resonances of the photonic crystal can be excited.

Let us therefore analyze the diffraction properties of the grating in the near-IR frequency range (150-250 THz) of interest. Fig. 4.22a reports the zero-order reflection efficiency for a varying s-polarized wave with incident angle θ from the normal. Calculations are performed with open-source RETICOLO package [27], implementing rigorous coupled wave analysis (RCWA). The yellow shaded region denotes the appearance of first diffraction order and the analysis is restricted to TE-polarization. There are four propagative Bloch modes within the structure, three symmetric and one antisymmetric*. The real part of their electric field computed at normal incidence and $\lambda = 1200$ nm is shown in Fig. 4.22b. At $\theta = 0$ just symmetric modes contribute to the scattering. Increasing θ, the symmetry of the system is broken and quasi-antisymmetric modes can give a contribution. The black solid line in Fig. 4.22a reports the reflectivity for $\theta = 20°$, highlighting a sharp Fano resonance around 195 THz. These anomalies were already addressed in literature and explained with Fabry-Perot resonances of nearly-antisymmetric modes [28]. They gained a renewed interest more recently for the possibility to excite high Q-factor resonances, e.g. to boost nonlinear generation [29]. For θ approaching zero, this Fano resonance collapses to a symmetry protected BIC [25] with diverging Q. Similarly, also at larger angles these guided resonances can diverge to a BIC, or embedded state, with no leakages due to destructive interference of several radiation channels [30].

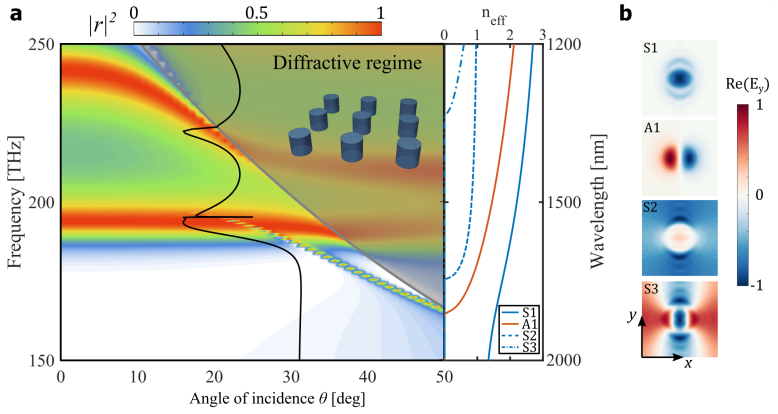

Figure 4.22: RCWA analysis of a 2D grating made from GaAs nanorods as in 4.21. (a) TE-reflectivity increasing incidence angle θ from the normal. Yellow shaded region displays the emergence of first diffraction order and Rayleigh anomalies†. Black solid line reports a cut view for $\theta = 20°$. On the right: dispersion of the four propagating Bloch modes at normal incidence. (b) Electric near-field of the same four modes computed at $\lambda = 1200$ nm.

Out of these critical points, which are due to collective effects, optical coupling between neighboring structures only moderately affects the resonant behavior of isolated elements. Following the literature on plasmonic crystals, we can distinguish two coupling regimes [31]:

* The symmetric-antisymmetric distinction is strictly valid just at Γ-point. Out of this condition we speak of quasi-symmetric/antisymmetric.

† At about 230 THz the 0^{th}-transmission order coefficient exhibits a singular point with discontinuous derivative that indicates the appearance of a diffracted order.

- *Near-field coupling*. In densely packed arrays, nanoantennas strongly interact in the near-field, leading to a complete modification of their resonances due to mode hybridization.

- *Far-field coupling*. When the wavelength of the scattered light is comparable with the array periodicity, the electromagnetic field perceived by every nanoantenna is the sum of external excitation and diffraction from neighboring structures. In this thesis, I focus on this mechanism. As we will see in the following, this regime can be studied through coupled-dipole approximation. It can finally lead to new collective modes or to Q-factor increase of single-particle resonances [32–34].

The upper panel of Fig. 4.23a reports the scattering multipolar decomposition for a GaAs nanodisk, with the same radius r and height h as before, for $\theta = 0$. Numerical calculations, performed as described in Chapter 2, reveal the electric/magnetic nature of different resonances. By replacing PMLs with Floquet-Bloch boundary conditions, we can compute the near-field distribution inside the array with the same constituents and period $a = 1000$ nm. Then, we can project it onto spherical wave functions and extract the multipolar electric/magnetic coefficients $a_{E,M}$, so as to evaluate the scattering contribution from a unit cell. The result, reported on the bottom panel of Fig. 4.23a, suggests that the array partially shifts some resonances and enhances the quality factors (and in turn electromagnetic field confinement), while keeping the major features unaltered. This conclusion is confirmed by inspecting the near-field enhancement inside the structure for the magnetic dipole resonance at $\lambda = 1615$ nm, see Fig. 4.23b. Please note that such a behavior is much more pronounced for wavelengths close to array periodicity. In the following section we will evaluate quantitatively the effect of the array on SHG efficiency and radiation properties.

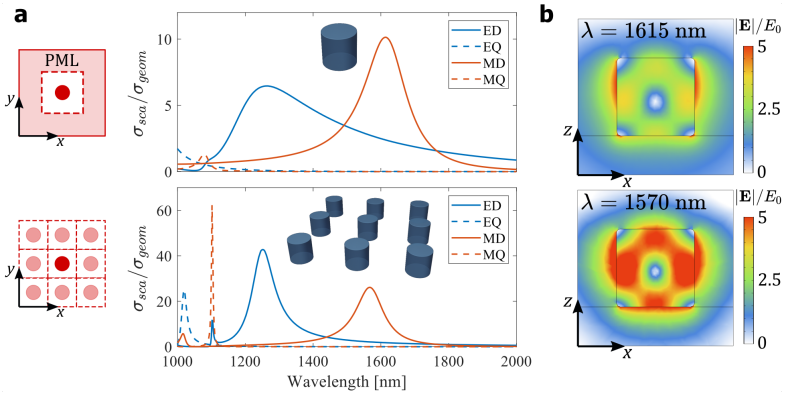

Figure 4.23: Comparison between isolated (top) and arrayed (bottom) nanoantennas. (a) Electric (blue) and magnetic (red) multipolar contribution to the scattering efficiency‡. An x-polarized normally impinging plane wave was considered. (b) Electric near-field enhancement in correspondence of magnetic-dipole resonance peak at $\lambda = 1615$ and 1570 nm, respectively.

‡ Please note that this definition of scattering cross section is rigorous just in the case of an isolated resonator. The contributions to σ_{sca} in Fig. 4.23 are computed as $\pi/k^2(2l+1)|a_{E,M}(l)|^2$.

Nonlinear antenna arrays

We numerically and experimentally verified the effect of resonators coupling in AlGaAs-on AlOx metasurfaces made of nanorods with fixed height $h = 400$ nm [35]. Array period a, and nanodisks radius r can be varied to analyze the impact of different geometrical configurations. As a first step, we fixed the external plane-wave excitation at $\lambda_{FF} = 1550$ nm normally impinging on the metasurface, and we scanned over r and a to maximize SHG into the zero-diffracted order. In Fig. 4.24 we report a SEM image of a metasurface with $r = 200$ nm and $a = 1025$ nm, corresponding to the optimized case. With the optical setup in Fig. 4.15, we experimentally investigated the SHG in backward direction for different values of r, a and λ_{FF} (see Fig. 4.25). An objective with numerical aperture NA=0.1 was used for two reasons: 1) ensure a Gaussian beam excitation with waist $w_0 \sim 25$ μm and peak intensity $I_0 = 0.5$ GW/cm^2, and 2) filter out first-diffraction orders in collection.

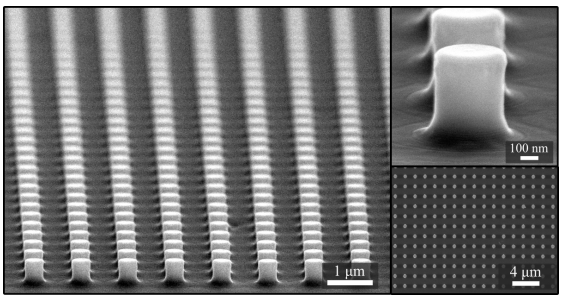

Figure 4.24: Tilted and top-view SEM images of AlGaAs-on-AlOx metasurface.

Based on these numerical and experimental evidences, we can make some important observations:

- Fig. 4.25a demonstrates a resonant condition relying on meta-atom size: SHG is enhanced for radii between 200 and 210 nm. These parameters correspond to magnetic-dipole excitation in isolated nanodisks [11, 13], we therefore expect the resonant behavior of the isolated constituents to be a key feature for boosting SHG.

- Pump wavelength scan, see Fig. 4.25b, exhibits a peaked response around 1550 nm with a quality factor $Q \sim 50$, much larger than Mie-resonances in isolated all-dielectric particles.

- Finally, varying the metasurface period, see Fig. 4.25c, we observe an optimum value at $a = 1025$ nm with a significant SHG drop far from this point.

Total collected SH power, P_{SH}, is normalized by the number of excited nanostructures M and pump power on nanodisks surface $P_{FF} = I_0 \pi r^2$

The so-computed SHG efficiency

$$\eta_{SHG} = \frac{P_{SH}}{M(I_0 \pi r^2)^2} = \frac{P_{SH} a^2}{\pi^3 w_0^2 (I_0 r^2)^2} \tag{4.9}$$

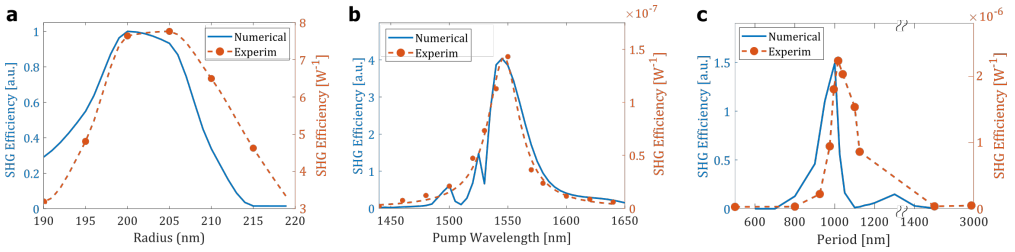

Figure 4.25: Numerical (blue) and experimental (red) SHG from AlGaAs-on-AlOx metasurfaces with fixed thickness $h = 400$ nm. (a) SHG efficiency varying nanorods radii at fixed periodicity $a = 1025$ nm and wavelength $\lambda_{FF} = 1550$ nm. (b) Sweep over pump wavelength for fixed radius $r = 200$ nm and periodicity $a = 1025$ nm. (c) SHG from metasurfaces made from identical building blocks ($r = 200$ nm) but different periods.

from a meta-atom inside the array can be fairly compared with isolated nanostructure performances. The maximum recorded value, $\eta_{SHG} \sim 2 \times 10^{-6}$ W^{-1} is 50 times larger than the isolated counterpart within the same NA [21]. Therefore, the role of the array is not limited to sum up the contribution from isolated resonators and it deserves further investigations.

We used for this purpose the coupled-dipole model [33, 36, 37]. Within this approximation, every particle is modeled as a dipole with electric and magnetic polarizabilities $\alpha_{e,m}$ related to Mie coefficients as $\alpha_{e,m} = i(6\pi/k^3)a_{E,M}$, with k the wavevector in the surrounding medium. The analysis is restricted to electric/magnetic dipolar response, higher multipolar contributions being negligible in our case (large wavelengths). When excited by the external pump, every particle scatters the electromagnetic field proportionally to its dipole moment. The total field perceived by each meta-atom is therefore the sum of external driving field and the radiation from all other dipoles. According to the formalism proposed in [36], the metasurface effective polarizability can be written as

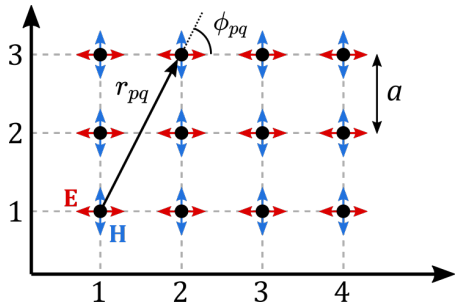

Figure 4.26: Square lattice of electric- and magnetic-dipoles with period a.

$$\alpha_{e,m}^{meta} = \frac{1}{\alpha_{e,m}^{-1} - S} \tag{4.10}$$

where S is the retarded-dipole sum

$$S = \sum_{p \neq q} e^{ikr_{pq}} \left[\frac{(1 - ikr_{pq})(3\cos^2\phi_{pq} - 1)}{r_{pq}^3} + \frac{k^2 \sin^2\phi_{pq}}{r_{pq}} \right] \tag{4.11}$$

with r_{pq} the distance between dipoles and ϕ_{pq} the angle between $\boldsymbol{r}_{pq}$ and polarization vector of other particles (see Fig. 4.26). Metasurface resonances correspond to the poles of $\alpha_{e,m}^{meta}$, i.e. Re$[1/\alpha_{e,m} - S] = 0$, and they result from the interplay of isolated particles ($\alpha_{e,m}$) and array properties (S). Here, we restrict the analysis just to nearest neighbors. Real parts of $1/\alpha_{e,m}$ and S for a metasurface with period $a = 1025$ nm and nanodisks radius $r = 200$ nm, see Fig. 4.27a, cross at $\lambda = 1540$ and 760 nm for the electric dipole as well as at 1570 and 770 nm for the magnetic one.

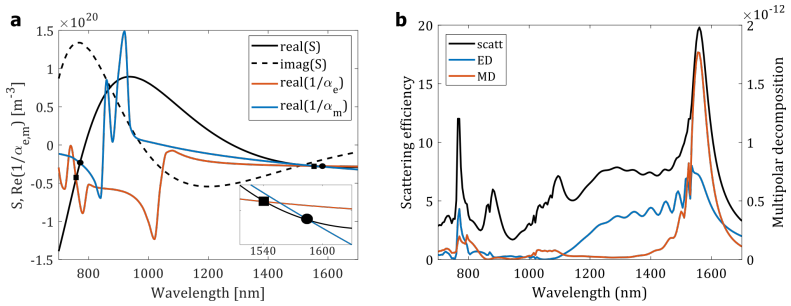

Figure 4.27: (a) Coupled-dipole model for AlGaAs nanoantennas array with period $a = 1025$ nm. Black curves report real (solid) and imaginary (dashed) part of retarded dipole sum. In red (blue) the real part of inverse electric (magnetic) polarizability for an isolated antenna. (b) Multipolar decomposition of scattering cross section of an AlGaAs nanoantenna inside the same array.

In order to probe this semi-analytical result, we numerically computed the electromagnetic field inside the resonator volume with FEM simulation in COMSOL and extracted electric- and magnetic-dipole contributions, as shown in Chapter 2. The role of neighboring structures is automatically taken into account imposing periodic boundary conditions at the unit-cell borders. Multipolar decomposition of the scattering from a unit cell in Fig. 4.27b highlights a clear correspondence between electric/magnetic dipole resonances and the effective polarizability poles, validating the semi-analytical model. Compared to the response of isolated nanodisks, one can conclude that the impact of the array is twofold: 1) a partial shift of some resonance positions; 2) an enhancement of resonance quality factors. In particular the latter occurs when Im$(S) < 0$ corresponding to a reduction of radiative damping due to dipolar interactions, as well documented in literature [38]. This explains the high Q-factor observed in Fig. 4.25b. Meanwhile, the position of magnetic-dipole resonance is almost unaltered, explaining why in Fig. 4.25a the maximum SHG is found for radii close to the isolated counterparts [11].

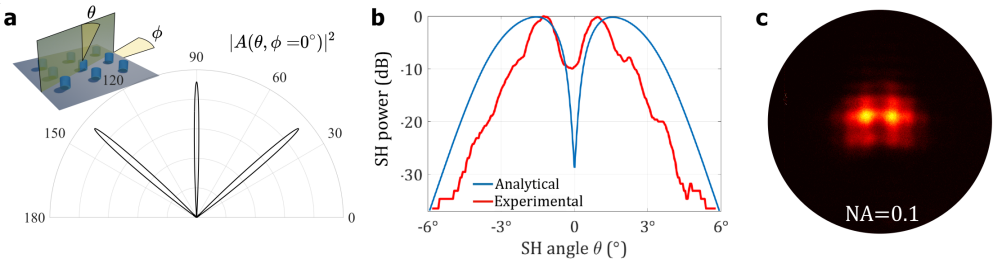

Figure 4.28: SH far-field analysis. (a) Polar plot of the array factor for a metasurface with period $a = 1025$ nm, computed at wavelength $\lambda = 775$ nm and azimuthal angle $\phi = 0°$. (b) Semi-analytical (blue) and experimental (red) far field at plane $\phi = 0$. (c) Experimental Fourier imaging in the whole numerical aperture NA=0.1.

Moreover at SH frequency, where the modes are even more confined and the role of the

array less important, similar resonances are excited in both cases. Based on this observation, the SH far-field pattern can be predicted through the independent emitters approximation. In this framework, the total radiation intensity can be written as

$$I_{\text{far}}^{\text{tot}}(\theta,\phi) = |A(\theta,\phi)|^2 I_{\text{far}}(\theta,\phi) \tag{4.12}$$

where $I_{\text{far}}(\theta,\phi)$ is the radiation pattern of the isolated element and $A(\theta,\phi)$ the array factor of the metasurface with θ (ϕ) the polar (azimuthal) direction of radiated plane wave $\boldsymbol{k}$-vector in the far field. For a 2D array of $N \times N$ independent emitters with period a, this can be written as [39]

$$A(\theta,\phi) = \sum_{p,q}^{N} c_{pq} e^{i\boldsymbol{k}\cdot\boldsymbol{r}_{pq}} = \sum_{p,q}^{N} c_{pq} e^{ika(p\sin\theta\cos\phi + q\sin\theta\sin\phi)} \tag{4.13}$$

with $\boldsymbol{r}_{pq}$, c_{pq} the position and amplitude of (p,q)-th emitter, respectively. For an array of uniform antennas with equal coefficients c_{pq}, (4.13) can be further simplified. Here, in order to take into account the experimental Gaussian beam excitation at FF, $A(\theta,\phi)$ is computed imposing

$$c_{pq} = e^{-\frac{2(\boldsymbol{r}_{pq}-\boldsymbol{r}_0)^2}{w_0^2}} \tag{4.14}$$

with $\boldsymbol{r}_0$ and w_0 the central position and waist of the Gaussian beam. The factor 2 reflects the quadratic dependence of SHG power on pump power. Fig. 4.28a reports $|A(\theta,\phi)|^2$ on the xz-plane (ϕ=0) and Fig. 4.28b compares the semi-analytical result obtained with equation (4.13) and the experimental back-focal plane of the metasurface with r = 200 nm and a = 1025 nm. In view of these observations, we can extract an important conclusion from the behavior shown in Fig4.25c: for short periods non-local interactions prevail and the resonant properties of isolated nanostructures are lost; on the opposite limit, for long periods, most of the power from isolated structures is coupled to the first diffraction orders, and SH signal collected within a NA=0.1 decreases. Between these two regimes, there is a region where Mie-resonances are preserved and the role of the array is to enhance the field confinement and partially redirect SHG into the zero-diffracted order. Clearly, we still expect a null at exactly normal direction $\theta = 0$. Nevertheless, a 50-fold SHG enhancement for $\theta < 6°$ enables, within some extents, on-axis applications. Furthermore, even with the heavy approximation of the coupled-dipole model limited to first neighbors, we can accurately explain the observed experimental features. Long-range non-local interactions give therefore a minor contribution in this regime, and SHG can be engineered based on Mie-resonances of single structures, as we will see in the next section.

Polarization control in periodic arrays

Control of SH polarization can be achieved through two different mechanisms: either keeping the metasurface unaltered and switch FF polarization with the aim of switching

the excited modes at pump frequency and in turn at SH; or, conversely, fixing the pump polarization and modifying the metasurface morphology, so as to reshape the excited resonances. Accordingly, in order to implement these functionalities, let us focus on two geometries, see Fig. 4.29:

- the former, Fig. 4.29a-b, is achieved through nanorods with fixed radius r. By changing pump linear polarization from [100] to [110] the same magnetic dipole resonance is excited at FF. Yet, the different orientation with respect to crystalline axis results in a different nonlinear coupling to SH modes mediated by $\chi^{(2)}$-tensor. As a consequence, SHG exhibits different polarization properties;

- the latter relies on nanocylinders with elliptical bases which induce a slight asymmetry in the system such to favor the emission with a defined polarization state. As sketched in Fig. 4.29c, pump polarization is fixed along [100] crystalline axis, and the ellipse semiaxes a and b are along [110] and [1$\bar{1}$0], respectively. By swapping a and b, see Fig. 4.29d, the symmetry is reversed and the orthogonal SH polarization is favored.

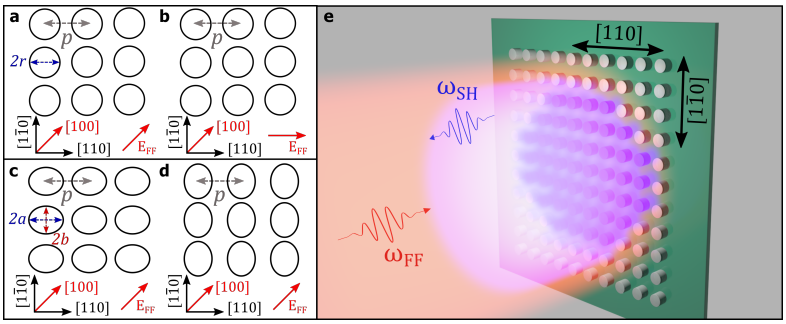

Figure 4.29: SH polarization control in AlGaAs metasurfaces. (a-b) First option: an array of nanodisks with radius r and period p is excited with pump polarization along [100] (a) or [110] (b). (c-d) Second option: elliptical basis meta-atoms with different semi-axes a and b excited by the same pump polarized along [100]. (e) Artist's view of SHG from a metasurface, with the scattered signal collected in backward direction.

The design of such circular- and elliptical-basis nanocylinders, which constitute the building blocks of our metasurfaces, entirely roots on FEM modeling in COMSOL Multiphysics. We decomposed the SH poynting vector $\mathbf{S}^{(2)}$ in order to separate the contributions with orthogonal electric-field orientations and consequently extract the generated power (integral of $\mathbf{S}^{(2)}$ over 2π steradians in backward direction) with different polarizations. In the following, we refer to horizontal (H) or vertical (V) polarization for an electric field aligned along array axis [110] or [1$\bar{1}$0], respectively; whereas we call principal (D_1) or secondary (D_2) diagonal for an electric field aligned along [100] or [010], respectively.

We first probed experimentally isolated structure properties, as shown in Section 4.4. Then we moved to periodic arrays with the the configuration sketched in Fig. 4.29e: a 2D square array aligned along [110] and [1$\bar{1}$0] axes is excited by a Gaussian beam at fixed wavelength $\lambda_{FF} = 1550$ nm and waist $w_0 \sim 9$ µm. SHG is collected in backward direction with the same microscope objective (NA=0.2). AlGaAs-on-AlOx nanorods have a fixed height $h = 350$ nm.

Fixed geometry, switching pump

For the design of circular basis nanocylinders we used as figures of merit the normalized difference between H- and V-polarized SHG when pump is aligned along [110], and between D_1 and D_2 for a pump along [100] (see Fig. 4.30a). For $r \in [205 - 215]$ nm we predict to simultaneously maximize H-V and D_1-D_2 contrast. Experimentally, we find the best results for $r = 215$ nm. As depicted in Fig. 4.30b, when pump polarization is rotated by 45° the near-field distribution at SH is completely modified, proving that nonlinear coupling with different modes is favored in the two cases. Fourier-space imaging restricted to a NA=0.8 (see Fig. 4.30c) highlights that in the isolated structure SHG direction and polarization are two strongly correlated properties. However, this polarization control is rather unpractical due to the large angular separation of the two SH lobes. This limitation motivates the transition to periodic arrays so as to decouple these two properties and engineer SH polarization in the zero-diffraction order. The choice of unit-cell dimensions relied again on FEM simulations: we scanned over different periods (see Fig. 4.30c) finding a maximized SHG for $p = 940$ nm.

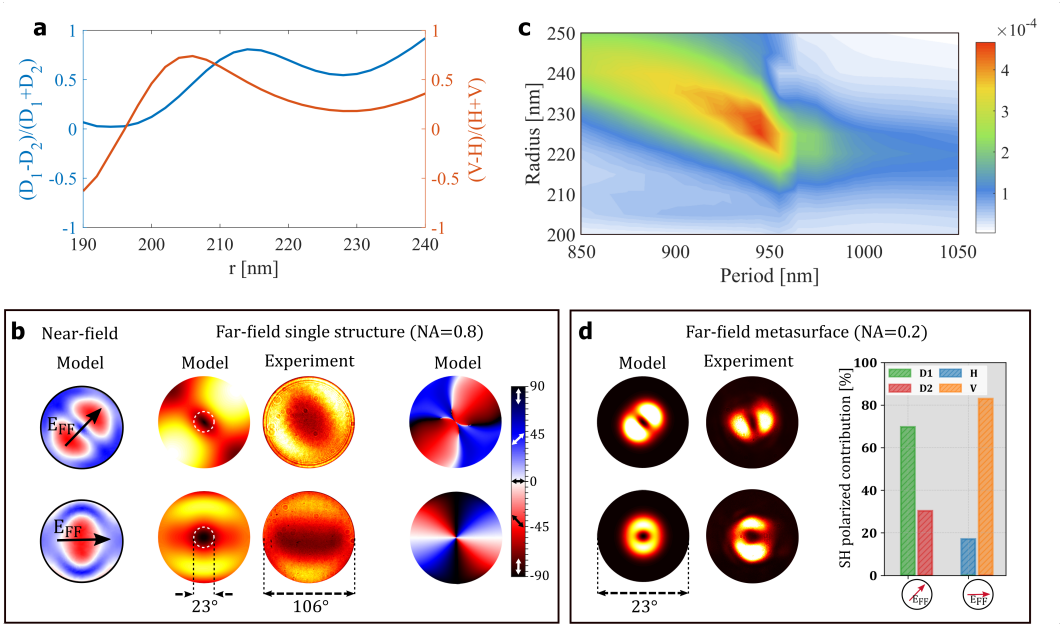

Figure 4.30: Metasurfaces of AlGaAs circular nanocylinders. (a) Normalized difference between two orthogonal polarizations $D_1 - D_2$ (blue) and $V - H$ (red) vs. r for fixed height $h = 350$ nm, corresponding to Fig. 4.29a and 4.29b, respectively. (b) Near- and far-field properties of an isolated AlGaAs nanodisk with radius $r = 215$ nm. (c) SHG efficiency in backward direction for a metasurface vs. r and p. (d) Far-field properties of a metasurface with period $p = 940$ nm and same meta-atoms as in (b).

Metasurfaces radiation pattern was predicted with independent emitters approximation in (4.12) and validated by experimental characterization, see Fig. 4.30d. For an input polarization aligned along [100], we recorded a ratio of about 7:3 between the two diagonal polarizations, while for input polarization along [110] we measured a ratio 1:4 between horizontally and vertically polarized SHG.

Fixed pump, rotating meta-atoms

In case of elliptical bases (Fig. 4.29c-d) we fixed the optimized period $p = 940$ nm and modified the two semiaxes a and b to maximize the contrast between H and V polarizations. Based on numerical model, see Fig. 4.31, we set $a = 240$ and $b = 200$ nm.

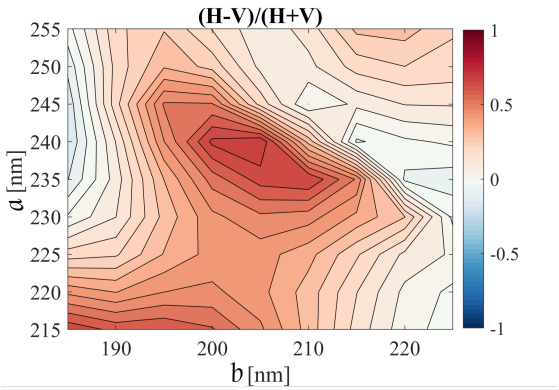

Figure 4.31: Normalized contrast between H- and V-polarized SHG from a metasurface made of nanocylinders with elliptical basis as in Fig. 4.29c,d. Period $p = 940$ nm is kept fixed and the scan is over the two basis semiaxes a and b.

As in the previous case, let us study first the properties of isolated structures, see Fig. 4.32a-c. At variance with circular bases, now the near-field distribution at SH is identical under $\pi/2$-rotation, meaning that the same mode is excited at FF as expected from system symmetry. Once again SH polarization properties are strictly related with emission directions, implying that the two orthogonal states are obtained for different azimuthal angles in the two geometries. Moving to metasurfaces, Fig. 4.32d, the control mechanism is maintained with a ratio between principal and secondary polarizations of about 4:1. Experimental results for the two cases are not perfectly symmetric due to astigmatism effects during e-beam lithography and slight misalignment introduced in characterization process.

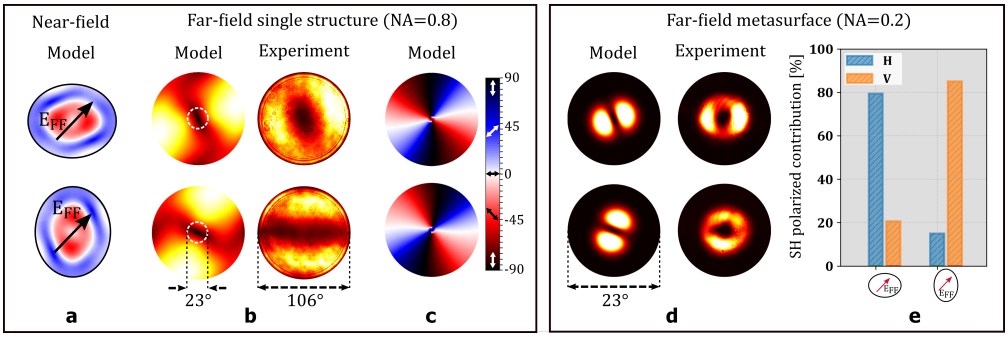

Figure 4.32: Elliptical-nanodisks metasurfaces. (a) Near-field distribution of the mainly excited SH mode, with the indication of FF polarization. (b) SH radiation pattern of an isolated element within a solid angle set by a NA=0.8 (corresponding to 106° field of view) of the microscope objective. White dashes delimit a region with NA=0.2 (corresponding to 23° field of view). (c) Inclination of SH linear polarization direction for the single element. (d) BFP imaging of SH generated by a metasurface with the same constitutive elements as in (c), period $p = 940$ nm, and collection restricted to NA=0.2 (e) Polarization components of SHG from the two metasurfaces.

The role of the array can be better appreciated comparing SH intensity within white

dashed line in Fig. 4.32b and radiation pattern in Fig. 4.32d. This result is even more explicit using a high-NA objective (NA=0.8) for metasurface Fourier imaging. In order to ensure a large excitation spot, pump beam was focused in the back focal plane of the objective. Comparison between isolated and arrayed elements is reported in Fig. 4.33: 20% of total emitted power is conveyed within 8° from the normal in case of a metasurface enabling quasi on-axis polarization control.

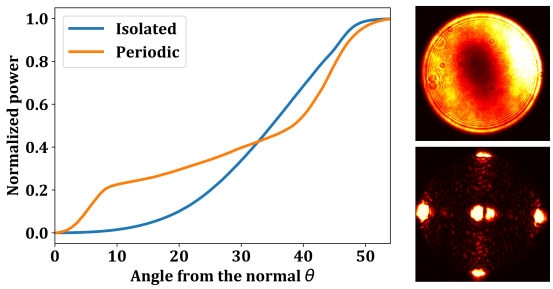

Figure 4.33: Integral of SH measured power for an increasing angle θ from the normal direction. Inset: back focal plane images of SHG from isolated (top) and arrayed (bottom) nanodisks with elliptical basis as in Fig. 4.32 within a $NA = 0.8$.

4.6 Conclusion

In this chapter we demonstrated the fabrication and experimental characterization of AlGaAs-on-AlOx metasurfaces. Differently from works in literature proving SHG into first-diffraction order [18], here we showed that 20% of SHG from metasurfaces is directed into the zero-diffraction order in backward direction. Exploiting the far-field coupling between nanoantennas in the array, we recorded a 50-fold SHG enhancement compared to isolated resonators. At variance with experimental works based on collective modes (e.g. Fano resonances) [40] to boost SHG, our optimization protocol roots on isolated resonator properties. This idea is particularly convenient for engineering SH radiation pattern, polarization and also SH phase, that is a key point to design metasurfaces for nonlinear beam shaping, as it will be discussed in the following chapter.

References

[1] E. Rosencher and B. Vinter, *Optoelectronics*. Cambridge University Prss, 2002.

[2] I. Shoji, T. Kondo, A. Kitamoto, M. Shirane, and R. Ito, 'Absolute scale of second-order nonlinear-optical coefficients,' *Journal of the Optical Society of America B*, vol. 14, pp. 2268–2294, 1997. DOI: 10.1364/josab.14.002268.

[3] D. Aspnes, S. Kelso, R. Logan, and R. Bhat, 'Optical properties of AlxGa1-xAs,' vol. 60, pp. 754–767, 1986.

[4] E. F. Schubert, *Light-Emitting Diodes*. Cambridge University Press, 2006.

[5] S. Gehrsitz, F. K. Reinhart, C. Gourgon, N. Herres, A. Vonlanthen, and H. Sigg, 'The refractive index of AlxGa1-xAs below the band gap: Accurate determination and empirical modeling,' *Journal of Applied Physics*, vol. 87, pp. 7825–7837, 2000. DOI: 10.1063/1.373462.

[6] M. Ohashi, T. Kondo, R. Ito, S. Fukatsu, Y. Shiraki, K. Kumata, and S. S. Kano, 'Determination of quadratic nonlinear optical coefficient of AlxGa1-xAs system by the method of reflected second harmonics,' *Journal of Applied Physics*, vol. 74, pp. 596–601, 1993. DOI: 10.1063/1.355272.

[7] Micro Resist Technology, *Negative Tone Photoresist Series ma-N 2400 - Processing Guidelines*.

[8] Dow Corning Corporation, *HSQ XR-1541 Electron-Beam resist - Product information*.

[9] K. D. Choquette, K. M. Geib, C. I. Ashby, R. D. Twesten, O. Blum, H. Q. Hou, D. M. Follstaedt, B. E. Hammons, D. Mathes, and R. Hull, 'Advances in selective wet oxidation of AlGaAs alloys,' *IEEE Journal on Selected Topics in Quantum Electronics*, vol. 3, pp. 916–925, 1997. DOI: 10.1109/2944.640645.

[10] J. Kurvits, M. Jiang, and R. Zia, 'Comparative analysis of imaging configurations and objectives for Fourier microscopy,' *JOSAA*, vol. 32, pp. 2082–2092, 2012. DOI: 10.1364/JOSAA.32.002082.

[11] V. F. Gili, L. Carletti, A. Locatelli, D. Rocco, M. Finazzi, L. Ghirardini, I. Favero, C. Gomez, A. Lemaître, M. Celebrano, C. De Angelis, and G. Leo, 'Monolithic AlGaAs second-harmonic nanoantennas,' *Optics Express*, vol. 24, pp. 15 965–15 971, 2016. DOI: 10.1364/OE.24.015965.

[12] R. Camacho-Morales, M. Rahmani, S. Kruk, L. Wang, L. Xu, D. A. Smirnova, A. S. Solntsev, A. Miroshnichenko, H. H. Tan, F. Karouta, S. Naureen, K. Vora, L. Carletti, C. De Angelis, C. Jagadish, Y. S. Kivshar, and D. N. Neshev, 'Nonlinear Generation of Vector Beams from AlGaAs Nanoantennas,' *Nano Letters*, vol. 16, pp. 7191–7197, 2016. DOI: 10.1021/acs.nanolett.6b03525.

[13] L. Carletti, A. Locatelli, O. Stepanenko, G. Leo, and C. De Angelis, 'Enhanced second-harmonic generation from magnetic resonance in AlGaAs nanoantennas,' *Optics Express*, vol. 23, pp. 26 544–26 550, 2015. DOI: 10.1364/OE.23.026544.

[14] Y. Chen, A. Roshko, and K. A. Bertness, 'Comparison of AlGaAs Oxidation in MBE and MOCVD Grown Samples,' *Materials Research Society*, vol. 692, pp. 1–6, 2002.

[15] V. F. Gili, L. Carletti, F. Chouchane, G. Wang, C. Ricolleau, D. Rocco, A. Lemaître, I. Favero, L. Ghirardini, M. Finazzi, M. Celebrano, C. D. Angelis, and G. Leo, 'Role of the substrate in monolithic AlGaAs nonlinear nanoantennas,' *Nanophotonics*, vol. 7, pp. 517–521, 2017. DOI: 10.1515/nanoph-2017-0026.

[16] L. Carletti, A. Locatelli, D. Neshev, and C. De Angelis, 'Shaping the Radiation Pattern of Second-Harmonic Generation from AlGaAs Dielectric Nanoantennas,' *ACS Photonics*, vol. 3, pp. 1500–1507, 2016. DOI: 10.1021/acsphotonics.6b00050.

[17] S. S. Kruk, R. Camacho-Morales, L. Xu, M. Rahmani, D. A. Smirnova, L. Wang, H. H. Tan, C. Jagadish, D. N. Neshev, and Y. S. Kivshar, 'Nonlinear optical magnetism revealed by second-harmonic generation in nanoantennas,' *Nano Letters*, vol. 17, pp. 3914–3918, 2017. DOI: 10.1021/acs.nanolett.7b01488.

[18] F. J. Löchner, A. N. Fedotova, S. Liu, G. A. Keeler, G. M. Peake, S. Saravi, M. R. Shcherbakov, S. Burger, A. A. Fedyanin, I. Brener, T. Pertsch, F. Setzpfandt, and I. Staude, 'Polarization-Dependent Second Harmonic Diffraction from Resonant GaAs Metasurfaces,' *ACS Photonics*, vol. 5, pp. 1786–1793, 2018. DOI: 10.1021/acsphotonics.7b01533.

[19] L. Carletti, G. Marino, L. Ghirardini, V. F. Gili, D. Rocco, I. Favero, A. Locatelli, A. V. Zayats, M. Celebrano, M. Finazzi, L. Giuseppe, C. de Angelis, and D. N. Neshev, 'Nonlinear goniometry by second harmonic generation in AlGaAs nanoantennas,' *ACS Photonics*, vol. 5, pp. 4386–4392, 2018. DOI: 10.1021/acsphotonics.8b00810.

[20] K. Frizyuk, I. Volkovskaya, D. Smirnova, A. Poddubny, and M. Petrov, 'Second-harmonic generation in Mie-resonant dielectric nanoparticles made of noncentrosymmetric materials,' *Physical Review B*, vol. 99, pp. 1–17, 2019. DOI: 10.1103/PhysRevB.99.075425.

[21] L. Ghirardini, G. Marino, V. F. Gili, I. Favero, D. Rocco, L. Carletti, A. Locatelli, C. de Angelis, M. Finazzi, M. Celebrano, D. N. Neshev, and L. Giuseppe, 'Shaping the nonlinear emission pattern of a dielectric nanoantenna by integrated holographic gratings,' *Nano Letters*, vol. 18, pp. 6750–6755, 2018. DOI: 10.1021/acs.nanolett.8b02432.

[22] S. G. Johnson and J. D. Joannopoulos, 'Block-iterative frequency-domain methods,' *Optics Express*, vol. 8, pp. 173–190, 2001.

[23] J. D. Joannopoulos, S. G. Johnson, J. N. Winn, and R. D. Meade, *Photonic Crystals. Molding the flow of light*. Princeton University Press, 2008.

[24] S. Fan and J. D. Joannopoulos, 'Analysis of guided resonances in photonic crystal slabs,' *Physical Review B - Condensed Matter and Materials Physics*, vol. 65, pp. 1–8, 2002. DOI: 10.1103/PhysRevB.65.235112.

[25] C. W. Hsu, B. Zhen, A. D. Stone, J. D. Joannopoulos, and M. Soljacic, 'Bound states in the continuum,' *Nature Reviews Materials*, vol. 1, pp. 1–13, 2016. DOI: 10.1038/natrevmats.2016.48.

[26] M. V. Rybin, D. S. Filonov, K. B. Samusev, P. A. Belov, Y. S. Kivshar, and M. F. Limonov, 'Phase diagram for the transition from photonic crystals to dielectric metamaterials,' *Nature Communications*, vol. 6, pp. 6–11, 2015. DOI: 10.1038/ncomms10102.

[27] J. P. Hugonin and P. Lalanne, *Reticolo Software for Grating Analysis*, 2021. [Online]. Available: https://www.lp2n.institutoptique.fr/light-complex-nanostructures.

[28] P. Lalanne, J. P. Hugonin, and P. Chavel, 'Optical properties of deep lamellar gratings: A coupled bloch-mode insight,' *Journal of Lightwave Technology*, vol. 24, pp. 2442–2449, 2006. DOI: 10.1109/JLT.2006.874555.

[29] M. MiInkov, D. Gerace, and S. Fan, 'Doubly resonant photonic crystal cavity based on a bound state in the continuum for efficient χ (2) nonlinear frequency conversion,' *Optica*, vol. 6, pp. 1–7, 2019. DOI: https://doi.org/10.1364/OPTICA.6.001039.

[30] C. W. Hsu, B. Zhen, J. Lee, S. L. Chua, S. G. Johnson, J. D. Joannopoulos, and M. Soljačić, 'Observation of trapped light within the radiation continuum,' *Nature*, vol. 499, pp. 188–191, 2013. DOI: 10.1038/nature12289.

[31] V. G. Kravets, A. V. Kabashin, W. L. Barnes, and A. N. Grigorenko, 'Plasmonic Surface Lattice Resonances: A Review of Properties and Applications,' *Chemical Reviews*, vol. 118, pp. 5912–5951, 2018. DOI: 10.1021/acs.chemrev.8b00243.

[32] G. Vecchi, V. Giannini, and J. Gómez Rivas, 'Shaping the fluorescent emission by lattice resonances in plasmonic crystals of nanoantennas,' *Physical Review Letters*, vol. 102, pp. 2–5, 2009. DOI: 10.1103/PhysRevLett.102.146807.

[33] A. B. Evlyukhin, C. Reinhardt, A. Seidel, B. S. Luk'Yanchuk, and B. N. Chichkov, 'Optical response features of Si-nanoparticle arrays,' *Physical Review B - Condensed Matter and Materials Physics*, vol. 82, pp. 1–12, 2010. DOI: 10.1103/PhysRevB.82.045404.

[34] C. Cherqui, M. R. Bourgeois, D. Wang, and G. C. Schatz, 'Plasmonic Surface Lattice Resonances: Theory and Computation,' *Accounts of Chemical Research*, vol. 52, pp. 2548–2558, 2019. DOI: 10.1021/acs.accounts.9b00312.

[35] G. Marino, C. Gigli, D. Rocco, A. Lemaître, I. Favero, C. De Angelis, G. Leo, C. D. Angelis, and G. Leo, 'Zero-order second harmonic generation from AlGaAs-on-insulator metasurfaces,' *ACS Photonics*, vol. 6, pp. 1226–1231, 2019. DOI: 10.1021/acsphotonics.9b00110.

[36] L. L. Zhao, K. Lance Kelly, and G. C. Schatz, 'The extinction spectra of silver nanoparticle arrays: Influence of array structure on plasmon resonance wavelength and width,' *Journal of Physical Chemistry B*, vol. 107, pp. 7343–7350, 2003. DOI: 10.1021/jp034235j.

[37] V. A. Markel and A. K. Sarychev, 'Propagation of surface plasmons in ordered and disordered chains of metal nanospheres,' *Physical Review B - Condensed Matter and Materials Physics*, vol. 75, pp. 1–11, 2007. DOI: 10.1103/PhysRevB.75.085426.

[38] S. Zou and G. C. Schatz, 'Theoretical studies of plasmon resonances in one-dimensional nanoparticle chains: Narrow lineshapes with tunable widths,' *Nanotechnology*, vol. 17, pp. 2813–2820, 2006. DOI: 10.1088/0957-4484/17/11/014.

[39] S. Orfanidis, *Electromagnetic Waves and Antennas*. 2016, pp. 1088–1118.

[40] P. P. Vabishchevich, S. Liu, M. B. Sinclair, G. A. Keeler, G. M. Peake, and I. Brener, 'Enhanced Second-Harmonic Generation Using Broken Symmetry III-V Semiconductor Fano Metasurfaces,' *ACS Photonics*, vol. 5, pp. 1685–1690, 2018. DOI: 10.1021/acsphotonics.7b01478.

Phase encoding in nonlinear metasurfaces 5

Contents

The very essence of many optical devices, e.g. lenses, spatial light modulators and waveplates, lies in the control of EM field phase to implement some functionality. Phase delay is acquired through the propagation in refractive components, and wavefront shaping is regulated by the laws of refraction, reflection and diffraction. The domain of flat optics aims at achieving the same results within a shorter distance than vacuum wavelength. The first example we can think of is the Fresnel lens: the same phase profile provided by a conventional lens can be reproduced dividing it into an ideally infinite set of concentric annular sections imprinting a phase jump between 0 and 2π. Nevertheless, the first implementations of this concept, at the beginning of XIX century, were still based on Snell law, essentially resulting in more compact, yet bulky, devices. The idea that the functionality of a prism could be reproduced through a grating with thickness equal to λ was concretely formulated by Lord Rayleigh in 1888 [1]:

> "If it were possible to introduce at every part of the aperture of the grating an arbitrary retardation, all the light might be concentrated in any desired spectrum. By supposing the retardation to vary uniformly and continuously we fall upon the case of ordinary prism; but there is then no diffraction spectrum in the usual sense. To obtain such it would be necessary that the retardation should gradually alter by a wavelength in passing over any element of the grating, and then fall back to its previous value, thus springing suddenly over a wavelength."

That concept led in 1910 to the achievement of the first blazed (or echelette) grating in the near-IR by Wood [2]. At first, practical implementations evolved much faster in the RF

range, mainly due to technological reasons, leading to the experimental demonstration of phase-delay engineering already in the 40s [3], which showed for the first time the possibility to reproduce the phase profile of a plano-convex lens through conducting plates acting as waveguides. The first diffractive optical elements (DOEs) approximated continuous phase profiles with multilevel photolithography [4, 5]; then, in the 80s, the development of e-beam lithography enabled the creation of blazed grating and Fresnel lenses with high efficiencies (70% and 50%, respectively) at 633 nm [6]. The optical phase delay $\Delta\phi$ acquired by the wave propagating in these dielectric components with respect to vacuum (see Fig.5.1) depends on the thickness h and refractive index n of the material at each transverse position x

$$\Delta\phi(x) = \frac{2\pi}{\lambda}(n-1)h(x) \tag{5.1}$$

successfully implementing the intuition of Lord Rayleigh a century before. Nevertheless, blazed gratings and DOEs in general are subjected to two strong limitations:

- the phase discontinuities introduce a shadow effect represented in the inset of Fig. 5.1. Part of the light bounces towards undesired directions due to total internal reflection at sidewalls. This region of the grating will not behave as expected, and the steeper the phase profile (i.e. the deflection angle), the more severe will be this undesired effect;

- the computed phase delay is valid for the design wavelength in (5.1), and the efficiency consequently decreases as one get farther from this value.

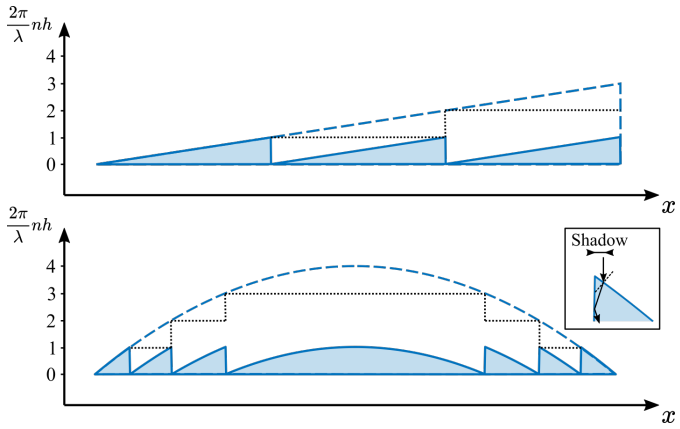

Figure 5.1: Examples of blazed grating to scale down a prism (top) and a lens (bottom). Inset: sketch of shadow effect.

The wish to overcome those limitations motivated several works in the last 30 years. In the following, we will first discuss the main approaches proposed in literature. Understanding the mechanisms for linear beam shaping will let us derive some general criteria for the design of metasurfaces to control the wavefront of nonlinear generation. Finally, I will demonstrate numerically and experimentally how to develop $\chi^{(2)}$-metasurfaces for SH beam steering, focusing and holography.

5.1 Linear metasurfaces design

The central problem of metasurface design for beam shaping is sketched in Fig. 5.2a: how can we find a set of nanostructures which enforce a defined phase jump to the incoming wave, such to finely reproduce any arbitrary and continuous phase profile? Fig. 5.2b depicts the particular case that we will study in the following, i.e. a metasurface fabricated by selectively etching a uniformly thick layer, called binary blazed grating, as the refractive index distribution in space can assume two values: n_h (completely etched material) or n_m (no etching). In general the adopted nanostructures could have different heights, yet Fig. 5.2b represents the most convenient condition for fabrication.

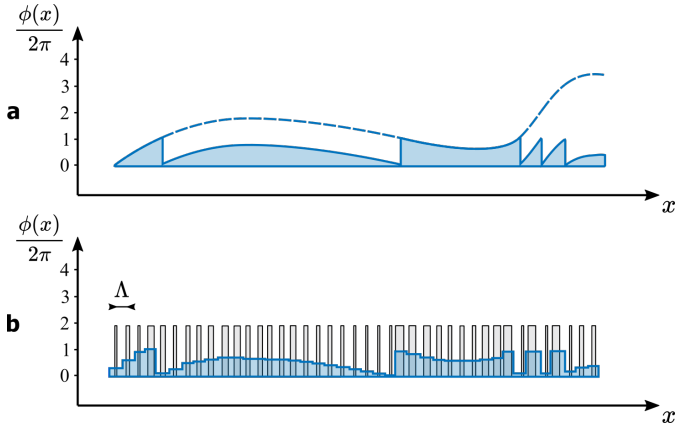

Figure 5.2: Design of a binary blazed grating. An arbitrary phase profile (a) is sampled through a discrete set of nanostructures (in gray) placed at a distance Λ (b).

The ultimate goal of flat optics is accomplished by respecting two requirements:

1) the set of nanostructures should allow to cover the whole $[0 - 2\pi]$ range, and their properties should not be modified by the presence of neighboring structures, i.e. close nanostructures should be optically uncoupled;

2) Nyquist sampling criterion must be satisfied, i.e. phase should be sampled with a sub-wavelength resolution ($\Lambda < \lambda$) in order to funnel all incoming light into the desired diffraction order.

The second requirement already implies that the metasurface is composed by a periodic arrangement of nanostructures. In a general picture this is not mandatory, but, as it will be clear in the following, this is more convenient from the calculation point of view. These two conditions are somehow in conflict: one would prefer to finely sample the phase, as illustrated by the right part of Fig. 5.2b, where the discrepancy between the desired and the sampled profile is more striking; however the smaller Λ, the stronger the optical coupling between neighboring structures. Finding the best compromise between these two constraints is a core task of metasurface design.

Regardless of the adopted physical mechanism, most of the approaches in literature start from the same optimization step, that is the determination of a one-to-one mapping between the imprinted phase and the shape of the elementary units (termed in the following

as meta-atoms), with the aim to create a library of building blocks to reproduce any desired phase profile. This process is often termed as *lookup-table* (LUT) generation. The related calculations are usually performed on periodic arrays of identical meta-atoms, by extracting the amplitude and phase of transmission coefficient as a function of some tuning parameter, usually the meta-atom size. LUT properties accurately approximate the behavior of the metasurface when the encoded phase variation between two close meta-atoms is significantly smaller than $2\pi/\lambda$. However, for rapidly varying phases, LUT predictions become the less accurate as the optical coupling between nearest neighbors gets stronger.

Depending on the nature of the meta-atoms, we can identify two categories of metasurfaces for beam shaping:

- guiding nanostructures, in which a phase delay is acquired through wave propagation along nanoscale pillars;

- resonant nanostructures, in which the scattered field exhibits a phase lag with respect to incident field as expected from a driven harmonic oscillator.

Here below we will comparatively present the two cases. Both of them can be adopted to implement geometric phase control, which we will briefly introduce without discussing it in detail.

Non-resonant approach

In the early 90s, thanks to the development of robust Fourier-expansion numerical methods, several research groups started to investigate binary gratings with sub-λ periods to model artificial materials with graded index [7, 8], see Fig. 5.3a. The original problem, sketched in Fig. 5.3b, was to realize under which conditions a binary grating with period Λ and thickness h could be approximated to a thin film with effective index n_{eff}.

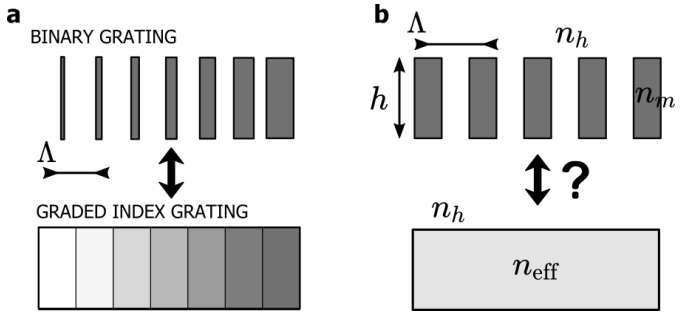

Figure 5.3: (a) Binary grating realized by etching a uniformly thick dielectric layer (top) modeling a graded index grating (bottom). (b) Top: homogeneous binary grating made from dielectric nanopillars with index n_m, height h and period Λ in a surrounding medium with index n_h. Bottom: artificial thin film with effective index n_{eff} that should reproduce the same functionality.

This equivalence is legitimate if three conditions are fulfilled [9]:

- only zero-diffraction orders propagate in the host medium, all higher orders being evanescent. This condition defines a diffraction cutoff which depends only on the

period Λ, working wavelength λ and host medium index n_h, while being uncorrelated to the thickness, size and index of the nanopillars.

- Only one propagating mode is supported by the structure. If we denote with z the propagation axis through the grating, this mode travels between the two boundaries with a phase term $\exp(i2\pi n_{\text{eff}} z/\lambda)$, where $n_h < n_{\text{eff}} < n_m$, as it would occur in a thin film. At variance with the previous one, this condition depends mainly on the refractive index and geometry of the nanopillars forming the grating, and it is called for this reason *structural cutoff* [10]. In this regime one gets somehow closer to what happens in the long-wavelength (or static) limit, where effective medium theories exist and periodic structures support only one propagating mode.

- The grating thickness h is large enough to ensure that evanescent modes are attenuated and do not tunnel through the grating, giving an extra contribution to transmission.

We further remark that a full 2π modulation in a binary grating is ensured for a minimum value $h = \lambda/(n_m - n_h)$, n_m corresponding to n_{eff} of sites where the dielectric material is not etched at all, and n_h where the latter is completely removed. Based on this point, one would conclude that a high-index material is preferable. However, this would result in: 1) a smaller Λ which is convenient for a fine phase sampling but can be challenging from a fabrication point of view, and 2) larger Fresnel losses at the grating interface.

Let us consider the binary blazed grating in Ref. [11], as it will provide a pedagogic example of LUT calculation and a benchmark for the resonant approach. Its meta-atom is sketched in the inset of Fig. 5.4a: a square TiO_2 ($n_m = 2.3$) nanopillar lying on an SiO_2 substrate ($n_s = 1.46$), with air ($n_h = 1$) cladding and excitation provided by a He-Ne laser ($\lambda = 633$ nm). Since homogenization cannot be used in this space of parameters and no analytical approximations exist, the structural cutoff has to be determined numerically by increasing Λ. We consider a 2D square lattice with $\Lambda = 272$ nm and $h = \lambda/(n_m - 1) \approx 817$ nm as in [11], and we compute amplitude and phase of transmission coefficient ($t = E_t/|E_i|$) of uniform gratings made of identical meta-atoms. In the following we consider TE polarization, but similar results can be shown for the TM case. Repeating the computation for increasing values of nanopillar size one can get the LUT in Fig. 5.4a. Various numerical tools can be adopted for these calculations, from RCWA to FDTD and FEM. In the present case, we resort to RCWA [12] setting periodic boundary conditions along x and y (retaining 17×17 Fourier components), for its fast convergence.

The nanowaveguide being single-mode, Fig. 5.4b shows the effective index of its propagative Bloch mode in the structure and its near-field distribution for a pillar edge $L = 180$ nm. The phase acquired during propagation is $\phi = 2\pi n_{\text{eff}} z/\lambda$.

Let us now use the LUT in Fig. 5.4a to design a sawtooth phase profile $\phi(x) = 2\pi/(N\Lambda)x$ along x and being constant along y, with a number N of meta-atoms per super-cell. This corresponds to a blazed grating with steering angle

$$\theta_B = \sin^{-1}\left(\frac{\lambda}{n_s a}\right) \tag{5.2}$$

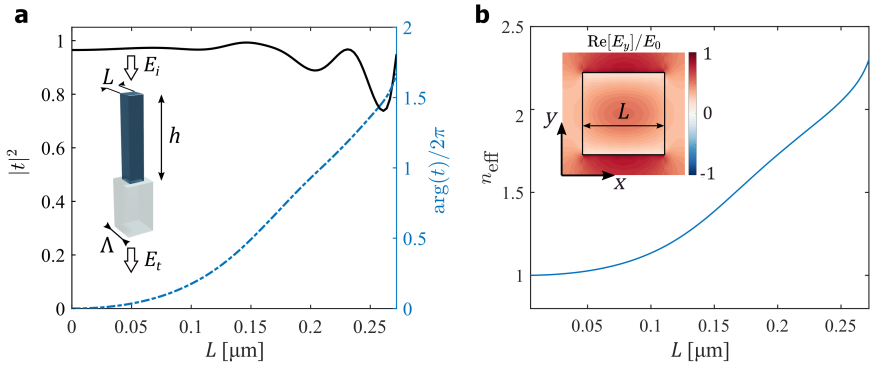

Figure 5.4: LUT calculation for non-resonant metasurfaces based on TiO_2 nanoposts on SiO_2 [11]. (a) Square modulus (black solid curve - left axis) and phase (blue dashed curve - right axis) of transmission coefficient $t = E_t/|E_i|$ at $\lambda = 633$ nm, for increasing pillar size L. Inset: sketch of the considered geometry, $h = 817$ nm and $\Lambda = 272$ nm. (b) Effective index of the sole propagative Bloch mode vs. pillar size. Inset: Corresponding real part of y-component of electric field distribution (obtained by imposing periodic conditions along x and y).

with $a = N\Lambda$ the size of the super-cell along x. The blazing efficiency of this grating into the first diffracted order is shown in Fig 5.5a as a function of N. As expected, by increasing the number of meta-atoms per super-cell, corresponding to less steep phase profiles, the efficiency increases. Remarkably, with $N = 5$ ($a/\lambda \approx 2.15$), the diffraction efficiency already exceeds 80% and the device remains reliable also for TM polarization and excitation from the substrate.

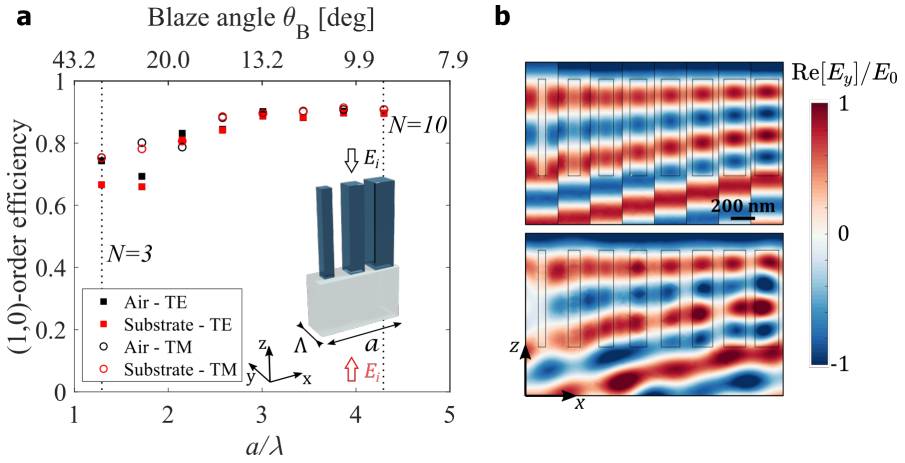

Figure 5.5: (a) Blazed binary grating diffraction efficiency vs. super-cell size $a = N\Lambda$ with $N = 3, 4, ...10$ at $\lambda = 633$ nm for TE (full squares) and TM (empty circles) polarizations. Red (black) marks denote an excitation from the air (substrate), see inset. The two dashed lines denote the cases for $N = 3$ and $N = 10$. (b) y-component of electric near field for the case $N = 8$ and excitation from air in the xz-plane at $y = 0$. Top: juxtaposed field distributions for the 8 elements as computed in the LUT. Bottom: near-field distribution in the real super-cell [13].

Fig 5.5b compares the near-field of 8 separate meta-atoms, as expected from the LUT calculation, and the near-field inside the final super-cell. Placing nanopillars with different dimensions one close to the other clearly introduces some deviations from LUT expectations. However, since for most of the structures the wave is guided inside the dielectric pillar, the binary blazed grating can be seen as a phased array of nearly independent coherent emitters, and optical coupling between neighboring structures introduces just a minor deviation [14]. Thus, the ability of waveguiding mechanism to outperform conventional

echelette gratings has to be attributed to a reduction of the shadowing zone and small coupling between adjacent pillars [15, 16].

Recently, it was predicted and demonstrated that moving to higher refractive index (i.e. Si instead of TiO_2), the single-mode condition could be moderately relaxed, ensuring that nearest-neighbor coupling remains small, even above structural cutoff [17]. Several successive works adopted this approach to reduce the aspect ratio of TiO_2 metasurfaces [18–23]. In this regime the meta-atoms are weakly resonant and the presence of multiple propagating modes results in a steeper phase dependence on nanopillar size [19] than in Fig. 5.4a. The strong field confinement in the high-index material is the key feature responsible for the reliability of LUT calculation and high efficiency of the final device. High-contrast arrays have been reported to enable simultaneous control of polarization and phase of transmitted wave [18], sub-wavelength focusing [19] and tunable metasurfaces with varying focal distance [23].

Resonant approach

As announced in Section 1.1, due to their finite effective mass, free electrons in metallic nanoantennas react with increasing phase lag to the driving EM field close to a LSPR. The equation of motion of electrons under a forced excitation at frequency ω can be approximated with a damped harmonic oscillator:

$$\ddot{x} + \gamma\dot{x} + \omega_0^2 x = \frac{eE_0}{m}\exp(i\omega t) \tag{5.3}$$

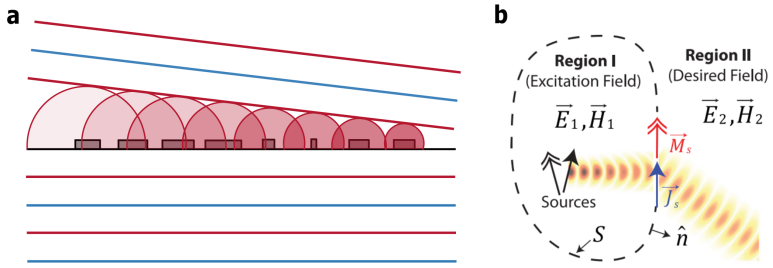

Figure 5.6: (a) Resonant metasurfaces working principle. Every resonator acts as a secondary source inducing an arbitrary phase jump. (b) Huygens' metasurfaces concept. Arbitrary fields in two regions separated by a closed surface S which provides electric and magnetic current sources. The surface equivalence principle returns the fictitious electric and magnetic surface currents that satisfy the boundary conditions [24].

with m the effective mass, γ the damping factor, ω_0 the plasmon resonance frequency and E_0 the driving field amplitude. A more complete picture includes the Abraham-Lorentz force term accounting for radiation losses, which we neglect in this general introduction.

The solution at steady-state has the harmonic form $x(t) = A\exp(i\omega t + \phi)$, with

$$\begin{aligned} A &= \frac{A_0}{\sqrt{\omega^2\gamma^2 + \left(\omega_0^2 - \omega^2\right)^2}} \\ \phi &= \tan^{-1}\left(\frac{\gamma\omega}{\omega_0^2 - \omega^2}\right) + n\pi \end{aligned} \tag{5.4}$$

At low frequencies $\omega \ll \omega_0$, the electron motion and consequently the scattered field are in phase with driving field, while $\phi = \pi$ for $\omega \gg \omega_0$. At exactly resonance frequency $\phi = \pi/2$. Thus, instead of impressing a phase delay through propagation inside a dielectric nanoguide, one could think to impose a phase jump to the scattered field based on the phase lag in (5.4), see Fig. 5.6a. This idea holds promises for the possibility of creating ultra-thin devices [25, 26]. However, experimental demonstrations show efficiencies of about 1% for ultra-flat lenses [27], well below the expected performances for practical application. The main limitations of plasmonic metasurfaces using only resonant scattering rely on few factors: 1) the inability to achieve a full 2π phase control with a single plasmon resonance, 2) impedance matching issues and poor forward directivity of the scattering, 3) high thermal losses of metals [28] but for mid- or far-IR operation.

Nevertheless, tailoring meta-atoms resonances remains attractive to design metasurfaces with arbitrary electric and magnetic polarizabilities. This idea was developed in 2013 by Pfeiffer and Grbic [24] who proposed a new paradigm to generate arbitrary field patterns for a given illumination. We can summarize it in the following terms: let us consider two spatial regions (I and II in Fig. 5.6b) separated by a surface S. In region I we impose the illumination field $[\mathbf{E}_1, \mathbf{H}_1]$, while in region II the desired one $[\mathbf{E}_2, \mathbf{H}_2]$. In general, the EM field is discontinuous on S. According to surface equivalence principle, the boundary conditions are satisfied introducing the electric and magnetic surface currents

$$\begin{aligned} \mathbf{J}_s &= \hat{\mathbf{n}} \times (\mathbf{H}_2 - \mathbf{H}_1) \\ \mathbf{M}_s &= -\hat{\mathbf{n}} \times (\mathbf{E}_2 - \mathbf{E}_1) \end{aligned} \tag{5.5}$$

Thus, it is expected that one could shape the wavefront of scattered field by arranging a set of meta-atoms with arbitrary electric (α_e^{eff}) and magnetic (α_m^{eff}) polarizabilities so as to satisfy

$$\begin{aligned} j\omega\alpha_e^{\text{eff}}\mathbf{E}_t|_S &= \hat{\mathbf{n}} \times (\mathbf{H}_2 - \mathbf{H}_1) \\ j\omega\alpha_m^{\text{eff}}\mathbf{H}_t|_S &= -\hat{\mathbf{n}} \times (\mathbf{E}_2 - \mathbf{E}_1) \end{aligned} \tag{5.6}$$

The unit-cells forming the final metasurface can be seen as secondary Huygens sources

of outgoing waves with engineered phase. They are termed for this reason Huygens metasurfaces (HMS).

In this context, dielectric resonators exhibiting both electric and magnetic resonances gained a strong interest for two reasons: 1) in the aforementioned harmonic oscillator picture, the combination of two resonances, each providing a π phase delay, ensure a full 2π phase control; 2) according to first Kerker condition [29], the far-field interference of two resonating modes in phase opposition can lead to purely forward scattering, which in turn may provide Huygens sources of forward-propagating waves. The latter feature was experimentally demonstrated by several groups in 2013 for Si [30, 31] and GaAs [32] NPs. Let us consider in the following the same geometry as in the pioneering work in Ref. [33], proposing Si nanodisks for controlling the phase of transmitted wave at optical frequencies. Fig. 5.7a shows the amplitude and phase of transmission coefficient t at $\lambda = 1340$ nm, for Si nanodisk arrays suspended in a homogeneous medium ($n_h = 1.66$), with fixed period $\Lambda = 666$ nm, thickness $h = 220$ nm and varying diameters. The interference of electric- and magnetic-dipole resonances centered at the same frequency results in an almost flat unitary transmission with a phase spanning over the whole $[0 - 2\pi]$ range.

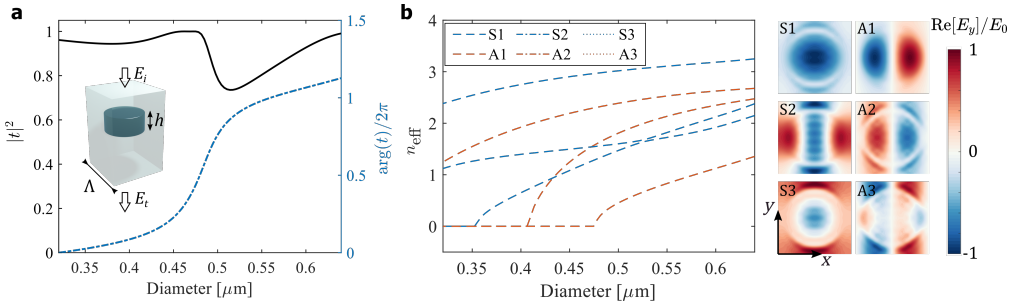

Figure 5.7: LUT calculation for resonant metasurfaces based on Si nanodisks ($n_m = 3.5$) in an homogeneous medium ($n_h = 1.66$). (a) modulus square (black solid curve - left axis) and phase (blue dashed curve - right axis) of transmission coefficient $t = E_t/|E_i|$ at $\lambda = 1340$ nm for increasing nanodisks diameter. In the inset a sketch of the considered geometry, $h = 220$ nm and $\Lambda = 666$ nm. (b) Effective index of the six propagative Bloch modes vs. nanodisk diameter. Inset: Corresponding real part of electric field distribution (y-component) for the three symmetric (S1-3) and three antisymmetric (A1-3) modes [13].

Bloch mode analysis, shown in Fig. 5.7b, highlights another central difference with respect to the non-resonant case: six modes, divided into symmetric (S1-3) and antisymmetric (A1-3) propagate in the structure [13]. Importantly, since the LUT is computed at normal incidence, just symmetric modes contribute to its properties. Such symmetry constraint is broken when implementing a spatially-varying phase profile and antisymmetric modes could provide an additional contribution.

In analogy with the non-resonant case, we use as a benchmark a sawtooth phase profile to steer the transmitted beam at various blazing angles. Remarkably, Fig. 5.8a reveals that first-order diffraction efficiency is lower than 50% for all the considered gratings.

It is therefore questionable whether LUT predictions and Kerker condition are preserved when one designs a non-constant phase profile. To this end, let us consider an adiabatic phase variation implementing a sawtooth profile over $N = 16$ unit cells. We expand the polarization vector inside each meta-atom in multipole moments contributions in Cartesian coordinates as done in [34]. First Kerker condition is satisfied when the contribution to

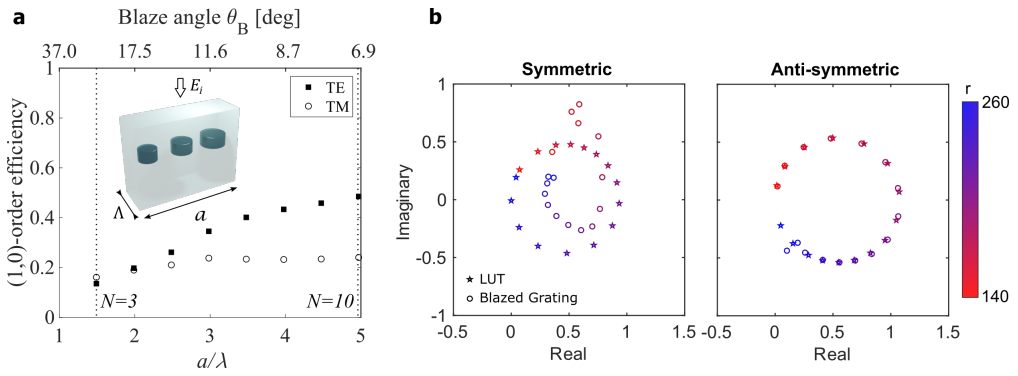

Figure 5.8: Huygens metasurface performances (a) Diffraction efficiency into the 1^{st} order vs. super-cell size $a = N\Lambda$ with $N = 3, 4, ...10$ at $\lambda = 1340$ nm for TE (full squares) and TM (empty circles) polarizations. The two dashed lines denote the cases for $N = 3$ and $N = 10$. (b) Multipolar decomposition of EM near-field in silicon nanodisks metasurfaces. The scattered electric fields from symmetric (left) and anti-symmetric (right) multipoles for meta-atoms in a meta-grating (circle marks) and in a uniform array (star marks) under TE polarization. Color bar denotes the increasing nanodisk radius, from $r = 143$ nm (red) to $r = 261$ nm (blue) [13].

back-scattering from symmetric multipoles (electric and toroidal dipoles and magnetic quadrupoles) cancels out the antisymmetric (magnetic dipole and electric quadrupole) one. Fig. 5.8b confirms that, when we consider uniform arrays of identical meta-atoms as in LUT calculations, the contribution from symmetric and antisymmetric multipoles form similar trajectories in the complex plane and Kerker condition is satisfied for all the considered nanodisk radii. Conversely, this requirement does no longer hold in the real device limiting its diffraction efficiency.

We can gain a deeper physical insight by exploring the electric near-field with the aim of evaluating the impact of meta-atoms optical coupling. Let us consider the same 16 meta-atoms as before, to design a blazed grating with total period $a = N\Lambda \approx 10.66$ μm corresponding to a deviation angle $\theta_B \approx 4.3°$. Fig. 5.9a-b reports the electric near-field enhancement in case of isolated and arrayed nanodisks, respectively. Their comparison reveals that HMS properties stem from the collective resonances, not from isolated nanodisk modes, and LUT predictions in Fig. 5.7a strictly depend on the presence of the array. However, the argument that the nanodisks behave collectively as a resonator does not entirely explain the performances in Fig. 5.8a.

When comparing the LUT predictions (Fig. 5.9b) with the steering meta-grating (Fig. 5.9c), one immediately remarks that the field in the 8 pillars closest to the abrupt phase transition (4 on the left-most and 4 on the right-most region of Fig. 5.9b-c) strongly differs. This $\approx 4\lambda$-wide region acts as the shadow zone in conventional DOEs, representing the main limitation of HMS performances. Furthermore, considering the adiabatic variation in diameter (≈ 3 nm between adjacent nanostructures in the middle region), also the minor differences in the central 8 nanodisks seem difficult to explain.

Fig. 5.9d shows the LUT calculation imposing an external field with a small incident angle $\theta_i = -\theta_B = -4.3°$. Such a small variation suffices to induce considerable modifications in all the nanodisks: the reason for this behavior has to be attributed to the presence of antisymmetric modes revealed in Fig. 5.8b, whose contribution is no longer negligible at $\theta_i \neq 0$. Besides, they always play a role when constructing a spatially varying phase

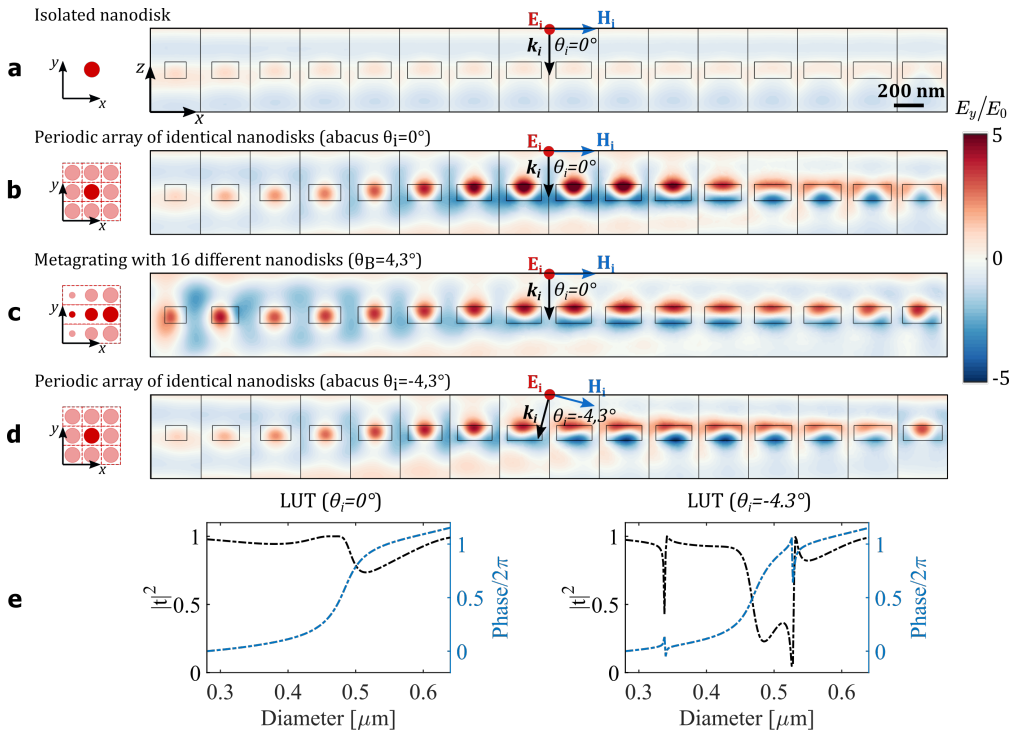

Figure 5.9: y-component of electric near-field in the xz plane of Huygens' meta-gratings at $y = 0$. All the maps are obtained for the same polarization (TE) and wavelength (λ=1340 nm). Incident electric/magnetic field orientations are reported with red/blue arrows. Field amplitudes are normalized to the incident field. (a) Isolated nanodisks. (b) Arrayed nanodisks as in LUT of Fig. 5.7a. The diameters are chosen to uniformly sample the $[0, 2\pi]$ phase interval. (c) Meta-grating obtained by placing in a super-cell the 16 meta-atoms of (b): it corresponds to a design deviation angle $\theta_B = 4.3°$. (d) Same as in (b), for an incident angle $\theta_i = -4.3°$. The same color scale is applied in all plots, allowing for a direct comparison. (e) Transmission coefficient comparison, in square modulus (black) and phase (blue), between an incident angle $\theta_i = 0°$ (left) and $\theta_i = -4.3°$ (right) on a uniform metasurface of identical nanodisks [13].

profile. This assumption is better understood with a reciprocity argument: a metasurface designed to blaze at an angle θ_B, upon normal excitation from the top, should diffract light at normal direction when excited by a plane wave incident with an angle $\theta_i = \theta_B$ from the bottom. The LUT calculation at an angle $\theta_i = \theta_B$ in Fig. 5.9e exhibits several dips in transmission amplitude where the phase varies the most attributed to the presence of antisymmetric modes. A design based on this LUT will result in poor performances. Consequently, reciprocity imposes that the design of metasurfaces with spatially varying phase profiles cannot restrict to the properties of symmetric modes not even for normal incidence operation [13].

Even if these considerations are based on a specific geometry, similar performances have been reported for other HMS designs: in [35], HMS based on polycrystalline silicon meta-atoms exhibit 36% measured efficiency in steering at 14° a laser beam at 1550 nm; 45% diffraction efficiency was reported for HMS deflecting a beam at 705 nm by 10° [36]; and 36% efficiency for a meta-grating operating at 650 nm [37]. Experimental demonstrations of HMS sensitivity to incidence angle have been reported in [38]. Better performances were achieved through a second optimization step aimed at compensating the effect of optical coupling by slightly modifying nanodisks geometries. This approach enabled an experimental 57% diffraction efficiency at 1340 nm, being, however, highly polarization sensitive. Optimization

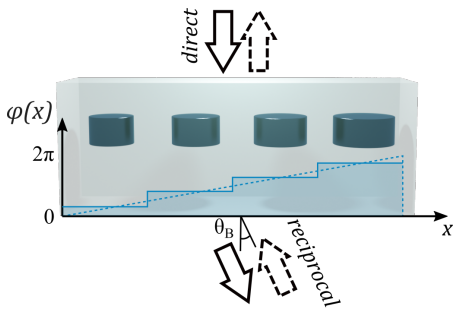

Figure 5.10: Huygens' blazed grating steering a beam at an angle θ_B when excited at normal incidence (solid arrow). By reciprocity, the same grating deflects at normal direction a beam from the bottom with an incident angle equal to θ_B (dashed arrow). The blue solid (dashed) curve denotes the approximated (targeted) phase profile.

processes based on genetic algorithms led to flat-lenses with designed NA=0.51 and focusing efficiency equals to 60% [39]. On the other hand, such significant improvements come at a price: global optimization often favors non-local interactions making the metasurface more sensitive to wavelength and incident angle variations, and the advantages of a one-to-one mapping provided by the LUT are lost.

Ideally, a Huygens' component is formed by resonant meta-atoms which purely scatter in forward direction and independently sample the phase at a subwavelength distance. It represents an optical phased array made of resonant constituents (i.e. optical nanoantennas). In this perspective, it is worth making some considerations[13]:

- The effective interaction surface of an optical nanoantenna with an external plane wave is represented by its scattering cross-section, which, at resonance, is much larger than its geometrical cross-section. Independent resonators operation imposes the meta-atoms distance to be larger than this value, which constitutes a severe constrain on subwavelength sampling condition.

- Fulfillment of first Kerker condition requires the resonators to be multimodal, i.e. to work far from static electric-dipole (long wavelength) approximation. As already seen introducing coupled-dipole approach in Chapter 4, the field perceived by each particle is the sum of external field and scattered field by all other particles in the array. Close to resonances, the latter contribution can be comparable or stronger than the former one. Long range coupling promoted by dipole-dipole interaction [40] leads to much larger cross-talk than evanescent coupling in nanoguiding approach.

In conclusion, the resonant approach does not come without a price, yet the high sensitivity to geometrical and dielectric parameters can be attractive to modulate metasurface response, as well as the lower aspect ratio with respect to nanoguiding approach. In the limit where high efficiency and fine phase sampling are not required, instead large tunability and thin devices are preferred, HMS offer a potential alternative. Nevertheless, I believe that aforementioned observations should be carefully considered whenever designing HMS.

5.2 Nonlinear wavefront control

Optical metasurfaces for nonlinear wavefront shaping integrate in the same device two functionalities: harmonic field generation and phase encoding. Thus, it is worth adding two observations with respect to Section 5.1:

- as announced in Chapter 2, nonlinear optical response of materials is typically very weak, therefore a detectable nonlinear generation must rely on the presence of strong local field enhancement: a resonant approach seems the only viable solution;

- as seen in Chapter 3, an efficient SHG depends on a double resonant condition at pump and harmonic frequencies.

The necessity of resorting to nanoresonators determined also the late development of nonlinear metasurfaces at optical frequencies, which set up on the technological progress triggered by resonant plasmonic metasurfaces. In 2015, based on LSPR of metallic nanorods, Li et al. [41] extended the concept of Pancharatnam-Berry phase to the nonlinear regime. By applying the principle of spin-rotation coupling of light [42], they demonstrated for the first time the control of TH polarization vector phase upon the orientation of meta-atoms with four-fold rotational symmetry (C4). Accordingly, SH beam steering was also demonstrated by moving from C4 to C3 symmetry. Although the EM field enhancement is provided by the plasmonic resonators, the nonlinear generation properties stem from a 100-nm-thick polydioctylfluorene (PFO) coating on the Au-nanostructures. In the same year, Segal and coworkers [43] developed the concept of nonlinear photonic crystals, proposed by Berger [44] at the end of the 90s, to demonstrate discrete SHG phase sampling in plasmonic metasurfaces. Despite the restriction of phase modulation to just two values (0 and π), this idea enabled the realization of ultra-thin nonlinear Fresnel zone plates (FZP) with $\eta_{SHG} \sim 4 \times 10^{-14}$ W^{-1}. The year after, the same group extended this principle by adding the spatial modulation of SHG amplitude achieved by changing the geometry of metallic SRR [45]. A continuous phase control of THG, not restricted to circular polarization, was demonstrated for the first time by Almeida et al. [46]. Based on the near-field properties of V-shaped antennas [25], the authors demonstrated a direct relationship between the phase of EM field at FF and the third-order polarization vector, with 10^{-8} conversion efficiency for a peak pump power of 6 MW ($\eta_{THG} \sim 2.5 \times 10^{-22}$ W^{-2}). All these works explored different design techniques, demonstrating nonlinear holography with flat metasurfaces [46], and they envisaged the possibility to image through nonlinear meta-lenses [47], opening the way to new optical functionalities and fundamental physics studies.

However, the reported conversion efficiencies were too low for practical applications. For this reason, several research groups started considering all-dielectric metasurfaces as a more attractive solution [48, 49]. The mature SOI technology favored the development of $\chi^{(3)}$ metasurfaces. It is worth underlining two main differences between Si and plasmonic metasurfaces: 1) the nonlinear polarization currents originate from volume resonances, enabling to exploit the bulk nonlinearity of the material, and 2) the thermal-losses are drastically reduced, allowing to increase pump power without sample damaging. In 2018, Wang et al. [50] demonstrated TH beam shaping, extending Huygens condition to the case of nonlinear harmonic generation, with an experimental diffraction efficiency of

92%. Importantly, this impressive result suggests that the above-discussed limitations for linear HMS may not apply in the context of nonlinear nanophotonics where the current sources are localized. Furthermore, the reported conversion efficiency $\eta_{THG} \sim 9 \times 10^{-16}$ W^{-2} is one-million-times larger than the record value with plasmonic counterparts. Such performances were confirmed by later works which demonstrated nonlinear holography [51] and nonlinear imaging with 48% diffraction efficiency [52].

When approaching the problem of metasurface design for nonlinear beam shaping, the starting question which comes to the mind is: which material could offer the best performances for practical applications? Non-centrosymmetric materials with strong $\chi^{(2)}$ susceptibilities would appear as the most appealing choice to realize metasurfaces with high conversion efficiencies. In contrast, no works on all-dielectric $\chi^{(2)}$ meta-gratings working in the VIS/near-IR have been reported in the literature. The prevalence of SOI over $\chi^{(2)}$-materials cannot be explained by purely technological reasons, instead it requires two further considerations:

- all the above-mentioned works are based on isotropic nonlinear susceptibilities. As a consequence, the nonlinear polarization vector can always be related to FF electric field through a dependence of the type

$$P^{(n)} \propto \chi^{(n)} \left[|E_{FF}| \, e^{il\phi} \right]^n . \tag{5.7}$$

  Conversely, $\chi^{(2)}$ nonlinearities exhibit a full-tensorial character adding a further technical difficulty. One can deal with this issue resorting to fully vectorial simulations, but a general and intuitive relationship between FF and harmonic phases is no longer available;

- the most promising III-V materials to work in the VIS/near-IR regime, (100)-GaAs and AlGaAs, exhibit a $\chi^{(2)}$ tensor structure with dominating off-diagonal terms, which are unfavorable for on-axis applications in the case of axially symmetric geometries. Specifically, it is well known in literature that, upon a normally impinging excitation, (100)-AlGaAs nanodisks exhibit a SH radiation pattern with two radiation lobes at large angles and a null on the optical axis [53–56].

In the following I will demonstrate a possible strategy to overcome these issues. The above-discussed general considerations provide us three preliminary criteria that will constitute the cornerstone of our numerical design for SH beam shaping in AlGaAs metasurfaces:

(*i*) **On-axis SHG**. As previously announced, axially symmetric resonators made of (100)-AlGaAs are inconvenient from this point of view. Consequently, two different strategies have been suggested in literature to provide on-axis SHG. The first one proposes to move from (100)-AlGaAs epitaxial growth to other crystallographic orientations as (110) or (111) [57, 58] , see Fig. 5.11a, in order to excite modes at SH with odd azimuthal orders that favor on-axis emission. The second one employs symmetry breaking to redirect SHG towards normal direction [59], see Fig. 5.11b. Both have their pros and cons, but we adopt the latter for the more robust technological processes developed with (100)-AlGaAs.

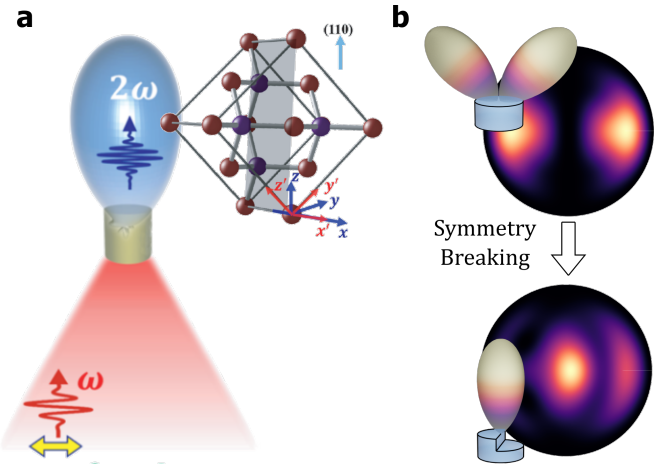

Figure 5.11: Techniques to provide on-axis SHG from AlGaAs nanoresonators. (a) A normally impinging beam on a (110)-AlGaAs nanodisk excites SH multipoles with odd azimuthal orders and in turn normal emission [57]. (b) Numerically calculated cross-polarized SH radiation in the Fourier plane from a (100)-AlGaAs nanodisk (top) and nanochair (bottom). Inducing a symmetry breaking in an axially symmetric nanodisk favors normal emission.

(ii) **Low-Q uncoupled resonators**. In Chapter 3, we saw that at resonance the excitation coefficient of the l-th mode at SH is $\alpha_l^{(2)} \propto Q_l Q_m Q_n \zeta_{lmn}$, with m, n two modes at FF and ζ_{lmn} the overlap integral. This would suggest to exploit high-Q resonances to boost SHG efficiency. However, in dielectrics, high-Q modes stem from either collective effects [60, 61] or large size-to-wavelength ratio in isolated structures [62], and both these conditions are unfavorable for sub-λ phase sampling. Moreover, sharp spectral features and sensitivity to surrounding environment of high-Q resonances make them ideal for sensing, ultra-fast switching or all-optical modulation, but less appealing for broad-band operations. Thus, we consider low-Q resonances as a better-suited compromise between generation efficiency and locally adjustable EM response.

(iii) **Continuous $[0-2\pi]$ SH phase sampling at constant amplitude**. Due to the difficulty to establish a direct relationship as (5.7) in presence of an anisotropic nonlinearity, we resort to FEM simulations. This enable to extract the SH radiation properties for different geometries and identify a set of nanoresonators with equal SHG efficiency and varying phases in the whole $[0-2\pi]$ interval.

We take inspiration from asymmetric diffraction gratings used to reveal symmetry protected modes and achieve normal-incidence response for spectral filtering [63]. The meta-atom considered in the following is sketched in Fig. 5.12: it stems from an AlGaAs cylinder with elliptical basis, where one fourth of the volume has been etched away. The difference in the two halves heights, h and $h/2$, induces a retardation between the two radiation lobes at large angles that put them back in phase and favors SHG along the normal to the substrate (see Fig. 5.11b). This "nanochair"-shaped resonator lies on a transparent sapphire substrate that allows to work in a transmission configuration. There are two main reasons to engineer SHG in air rather than in the substrate: 1) it allows larger unit-cell size Λ, as the first diffraction orders become evanescent for $\Lambda < \lambda_{SH}/n$, with n the refractive

index of propagation medium; and 2) SHG wave does not cross any interface before being collected by the objective, reducing measurement errors. We fix $h = 400$ nm, as for the metasurfaces explored in Chapter 4, and we study the SHG properties for varying semiaxes a and b, as well as unit-cell size Λ.

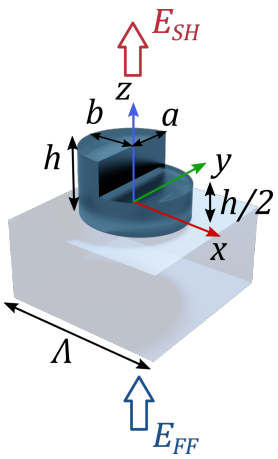

Figure 5.12: AlGaAs-on-sapphire nanochair meta-atom.

The fulfillment of conditions *(i)*-*(iii)* can result in a library of building blocks to be arranged in any desired configuration to reproduce an on-demand phase profile.

With the aim of minimizing optical coupling between neighboring structures and construct a robust LUT, it is interesting to start from the study of isolated particles ($\Lambda \to \infty$). Let us set pump wavelength $\lambda_{FF} = 1550$ nm, intensity $I_0 = 1$ GW/cm^2, and linear polarization along x direction aligned with [100] crystallographic axis of AlGaAs (this choice turns out to be the most favorable for phase sampling). EM near-fields were computed with FEM simulations in COMSOL Multiphysics as described in Chapter 2, and radiation patterns were extracted through near-to-far-field transformation package RETOP [64]. A resonant mode with main x and z electric field components dominates the scattering at FF as sketched in Fig. 5.13a for two semiaxes $a = 280$ nm and $b = 260$ nm. In turn, this results in a mostly y-polarized SH field, whose radiation diagram is sketched in Fig. 5.13b. Modifying nanochair geometry, resonances at FF and SH get reshaped and their overlap changes.

Fig. 5.13c reports the phase and amplitude of y-polarized SH field at normal direction, while Fig. 5.13d shows the orientation angle of the main radiation lobe with respect to z. Among the several ways to evaluate the radiation pattern in Fig. 5.13b, we consider the orientation of the SHG maximum as it allows to select the geometries with a dominating central lobe close to the normal. This last result highlights that it exists a space of parameters in which nanochairs satisfy conditions *(i)*, even though for the moment it is still not clear if *(iii)* can be fulfilled. Importantly, besides the emission redirection mechanism, nanochair symmetry offers also the opportunity to extend the phase properties in Fig. 5.13c: upon an in-plane rotation of 180°, x-component of the electric field at FF is unaltered while z-component is π-shifted. Consequently the y-component of SH polarization vector $P_y^{(2)} = 2\varepsilon_0\chi^{(2)}E_xE_z$ is π-shifted too, see Fig. 5.14.

In the following I will first discuss how to construct a LUT preserving the properties of

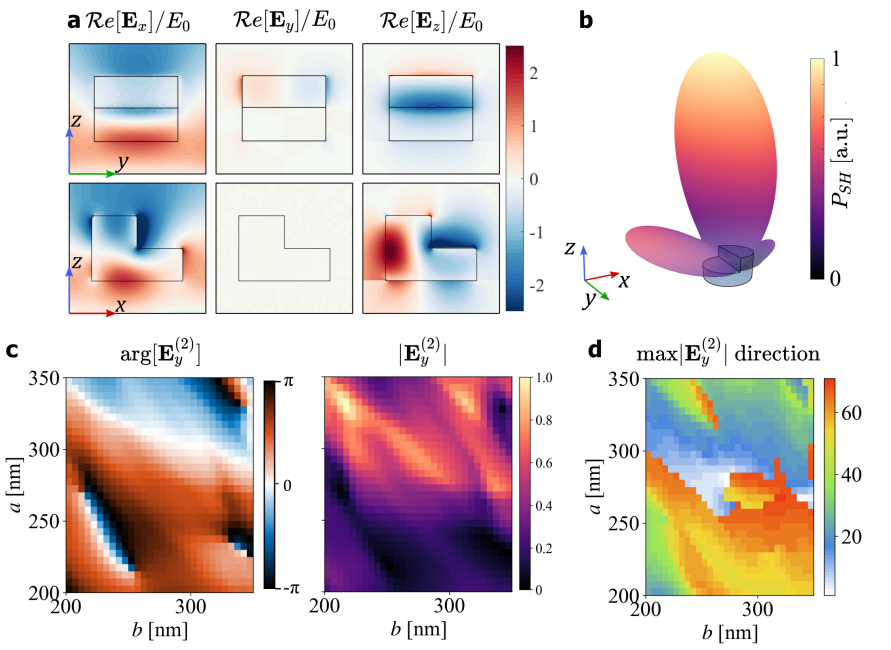

Figure 5.13: Near- and far-field properties of an isolated nanochair. (a) Side views in the yz-plane at $x = 0$ (top) and xz-plane at $y = 0$ (bottom) of the three electric field components (real part) at $\lambda_{FF} = 1550$ nm. (b) y-polarized SH radiation pattern, colorbar is in arbitrary units. (c) Phase (left) and normalized amplitude (right) of SH y electric field component valued at normal direction (z) vs. nanochair semiaxes a and b. (d) Orientation (in degrees) of the maximum SH radiation lobe with respect to z-axis.

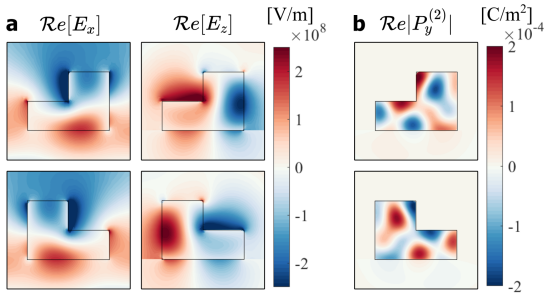

Figure 5.14: (a) x- (left) and z- (right) electric near-field components at $\lambda_{FF} = 1550$ nm for the same nanochair upon an in-plane rotation of 180°. An input pump intensity $I_0 = 1$ GW/cm^2 is considered. (b) y-component of the second order polarization vector at $\lambda_{SH} = 775$ nm for the two cases.

isolated resonators and minimizing sampling distance. Then, I will provide the fabrication protocol and the experimental demonstration of three different devices: $\chi^{(2)}$ beam steerer, $\chi^{(2)}$ meta-lens and $\chi^{(2)}$ meta-hologram.

Lookup table computation

Fig. 5.13c-d suggest that, if ideally resonators were not perturbed by the presence of neighboring structures, it should be possible to extract a one-to-one mapping between a geometrical parameter (let us label it with a for simplicity) and the phase of SHG at normal direction, see Fig. 5.15.

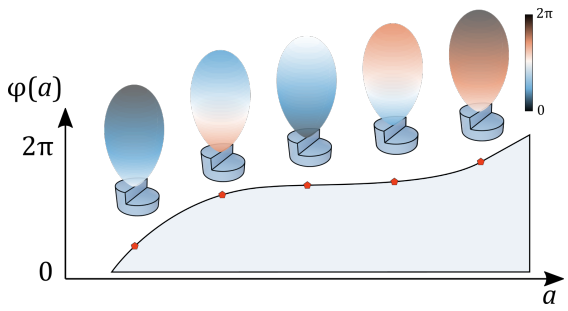

Figure 5.15: Nonlinear phased array concept. An ideal LUT provides a set of nanoresonators exhibiting on-axis SHG with constant amplitude and a phase which varies with a geometrical parameter a.

This concept evokes the idea of a nonlinear optical phased array in which every resonator independently generates an harmonic field with an on-demand phase on a sub-λ scale. In order to verify the domain of validity of this statement, we performed periodic simulations with finite unit-cell sizes Λ by replacing PML at the borders of the modeled domain with Floquet-Bloch boundary conditions. We maintained the same pump field with identical phase to ensure a meaningful comparison with isolated resonators.

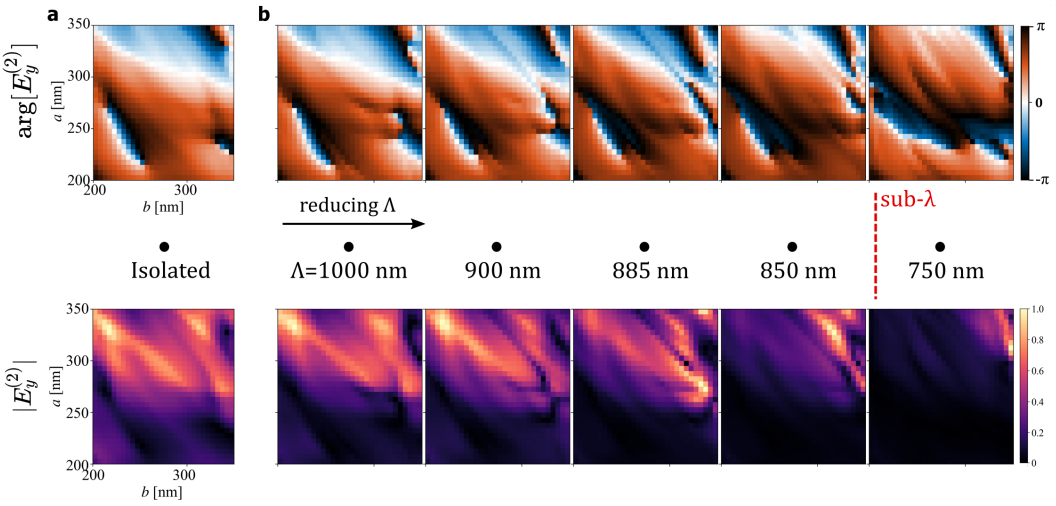

Figure 5.16: (a) Phase (top) and normalized amplitude (bottom) of SH electric field (y-component) vs. nanochair semiaxes a and b for an isolated structure ($\Lambda \to \infty$). (b) Same as (a) for a decreasing meta-atom size from $\Lambda = 1000$ nm (left) to 750 nm (right). The red dashed line denotes the sub-λ threshold.

Fig. 5.16 proves that for $\Lambda < 900$ nm collective effects become less and less negligible. $\Lambda < \lambda_{SH}$ would be preferable for a fine phase sampling, however in this case the LUT predictions would be lost when nanochairs with different geometries are placed close to each other. Conversely, for $\Lambda \geqslant 900$ nm, LUT results stem from isolated resonator properties providing a more robust set of meta-atoms. The best trade-off appears to be at $\Lambda = 900$ nm, although in this case SHG power is partially funneled into the first diffraction order. Such compromise can be fairly acceptable if the radiation pattern at SH is highly directional. Blue dots in Fig. 5.17 report the far-field calculation of a meta-atom with $a = 280$ nm and $b = 260$ nm.

Inter-particle interaction in the near-field is taken into account through periodic boundary conditions, while far-field interference is included via the multiplication of this result by the

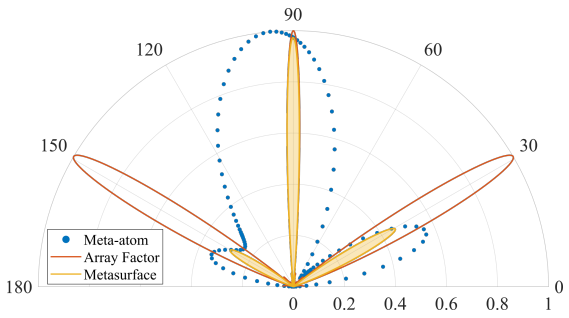

Figure 5.17: SH radiation diagram of nanochair metasurfaces in the xz-plane. Blue dots: y-polarized SH far-field from an isolated nanochair with $a = 280$ and $b = 260$ nm. Red solid line: array factor computed for $\Lambda = 900$ nm and $N = 8$ structures. Yellow shaded area: product between the two previous curves.

array factor of the metasurface (red curve). If the meta-atom features an emission lobe with a maximum close to the normal and decreasing at large angles, most of the generated power from the metasurface is funneled into the zero-diffracted order (yellow shaded area). The calculation of cross-polarized SH field amplitude and phase along the normal in Fig. 5.16 for the two nanochair orientations (see Fig. 5.18a) are thus complemented by the evaluation of the main lobe direction in Fig. 5.18b.

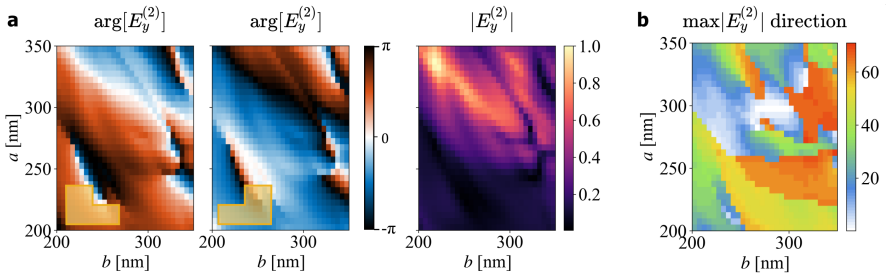

Figure 5.18: LUT calculations for nanochairs-on-sapphire metasurfaces with $\Lambda = 900$ nm. (a) Phase (left) and normalized amplitude (right) of SH y electric field component valued at normal direction (z) vs. nanochair semiaxes a and b. Insets: nanochair orientation. (b) Direction (in degrees) of the maximum SH radiation lobe from the single meta-atom with respect to z-axis.

The algorithm to identify the elementary building blocks for wavefront shaping implements the following workflow:

1) from LUT in Fig. 5.18a, single-out the resonators with a radiation lobe at $\theta < \theta_{Max}$, with θ_{Max} the maximum accepted deviation from the normal

2) iteratively impose an amplitude mask to filter out just the resonators exhibiting an SHG amplitude in the range $[A_i - \varepsilon, A_i + \varepsilon]$, with A_i the target amplitude for i-th iteration and ε a tolerance factor

3) define an error function e between the target phase profile to implement ϕ_T and the real phase profile ϕ_R provided by the subset of selected resonators

$$e_i = \sum_n \left[\phi_T(n) - \phi_R(n)\right]^2 . \tag{5.8}$$

4) repeat the procedure until the maximum SHG amplitude A_i is found, which ensures an acceptable error e.

The two free parameters, θ_{Max} and ε, can be set by the user to find the best compromise between a large SHG amplitude and the quality of phase sampling: for large values of θ_{Max} and ε it will be easier to find a set of resonators with high SHG satisfying the required criteria, but probably they will not provide the same constant amplitude and they will radiate at large angles from the normal. We found the best trade-off for $\theta_{Max} = 15°$ and $\varepsilon = A_i/10$.

We started by implementing a sawtooth phase profile, which constitutes the ideal initial benchmark to probe the reliability of the design, due to the moderate computational costs required to evaluate the diffraction efficiency of the final device.

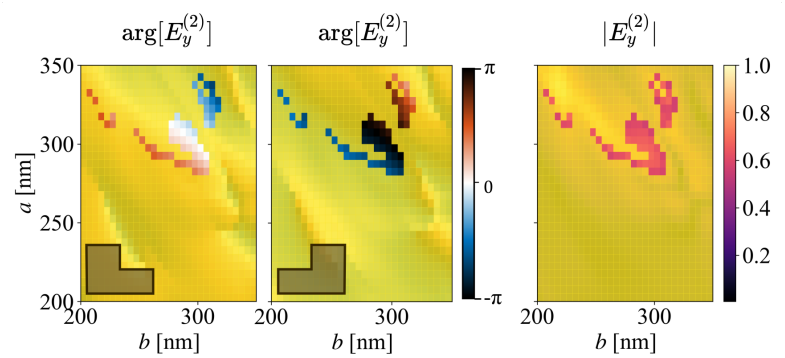

Figure 5.19: Filtered LUT in Fig. 5.18a showing the selected building blocks that span the whole $[0, 2\pi]$ range with almost constant amplitude.

Imposing as a target phase function $\phi_T(n) = 2\pi(n - 1/2)/N$ in $[0, 2\pi]$ with $N = 8$ elements, we found an optimized value for the amplitude filter at 63% of maximum $|\mathbf{E}_y^{(2)}|$ in Fig. 5.18a. The filtered LUT with the subset of available structures for nonlinear phase shaping is reported in Fig. 5.19.

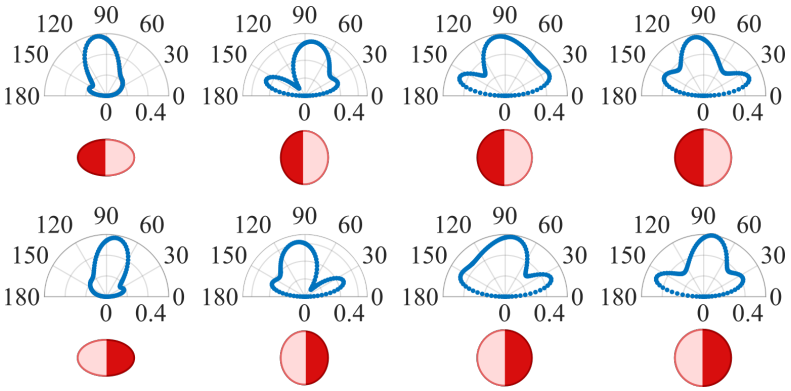

Figure 5.20: SH radiation patterns in the xz plane for 8 selected nanochairs that uniformly sample the $[0, 2\pi]$ phase interval.

Fig. 5.20 reports the radiation diagrams of the 8 nanochairs which better reproduce the target phase profile. They all provide an emission lobe with a maximum close to the normal

and similar amplitude, but some of them feature also an intense emission at large angles. In order to evaluate the diffraction performances, we model a super-cell made from these 8 elements placed close to each other. It corresponds to a meta-grating steering the SHG beam at an angle $\theta_B = \sin^{-1}(\lambda_{SH}/N\Lambda) \sim 6.2°$. We first compare the near-field distributions as predicted by LUT calculation (i.e. arrays made of identical resonators) and the full vectorial simulation of the whole super-cell (made of 8 different nanochairs), see Fig. 5.21. As seen in Section 5.1, this inspection reveals if the predictions of LUT are preserved in the final device. Optical coupling should be more critical at larger wavelengths (i.e. at FF), however Fig. 5.21a proves that the main features of LUT are unchanged in the real meta-grating. While the large unit-cell size ($\Lambda > \lambda_{SH}$) prevents to observe the steering behavior in Fig. 5.21b, a tilted continuous wavefront with an angle $\theta_B \sim 6.2°$ from the normal is retrieved in Fig. 5.21c, at a distance of about $13\lambda_{SH}$.

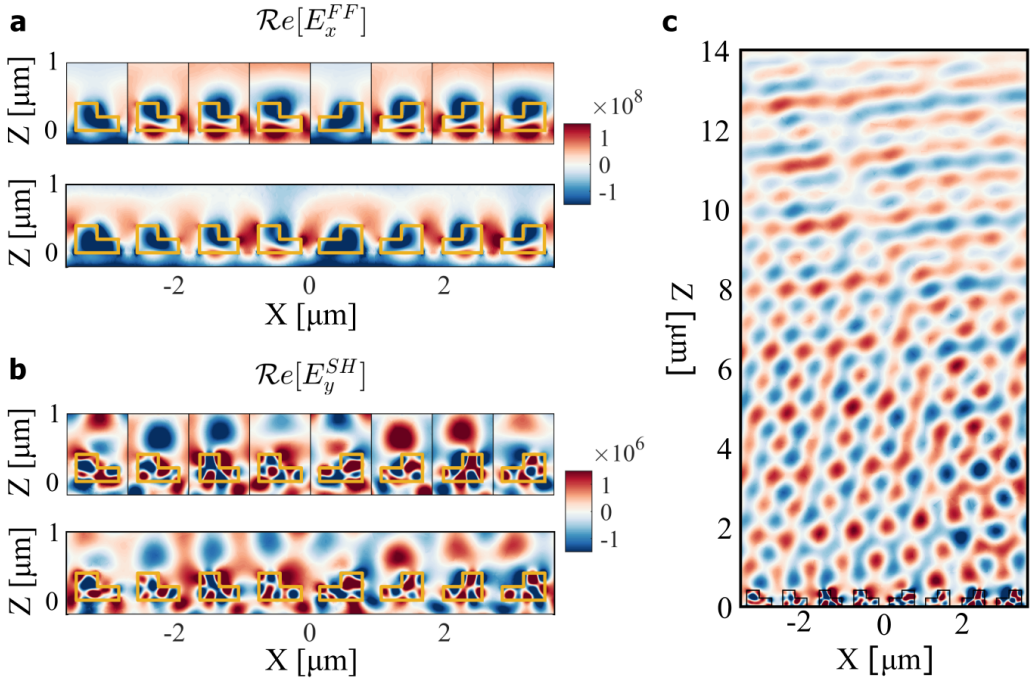

Figure 5.21: Near-field maps of a $\chi^{(2)}$ meta-grating. The super-cell is composed by $N = 8$ resonators providing a sawtooth phase profile that steers SHG at an angle $\theta_B = 6.2°$ from the normal. (a) x-component of FF electric field predicted by LUT (top) and in the real super-cell (bottom). (b) Same as (a) for the y-component of SH electric field. (c) Same as (b) extended to a larger simulation domain.

Projecting the near-field of Fig. 5.21b into the far-field, we find a diffraction efficiency of $\sim 52\%$, see Fig. 5.22. The rest of SHG in forward direction is lost into higher diffraction orders due to the relatively large unit-cell size.

Now that all the design elements have been introduced, I will first provide the fabrication protocol of nanochair metasurfaces and then discuss the experimental verification of the real devices.

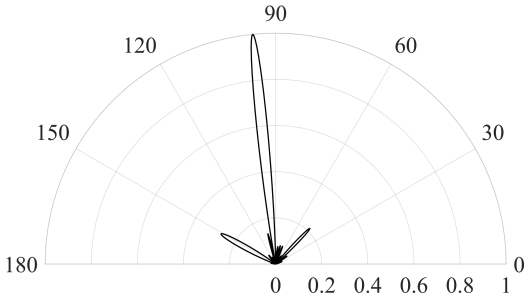

Figure 5.22: Near-to-far field transformation of electric field distribution in Fig. 5.21b.

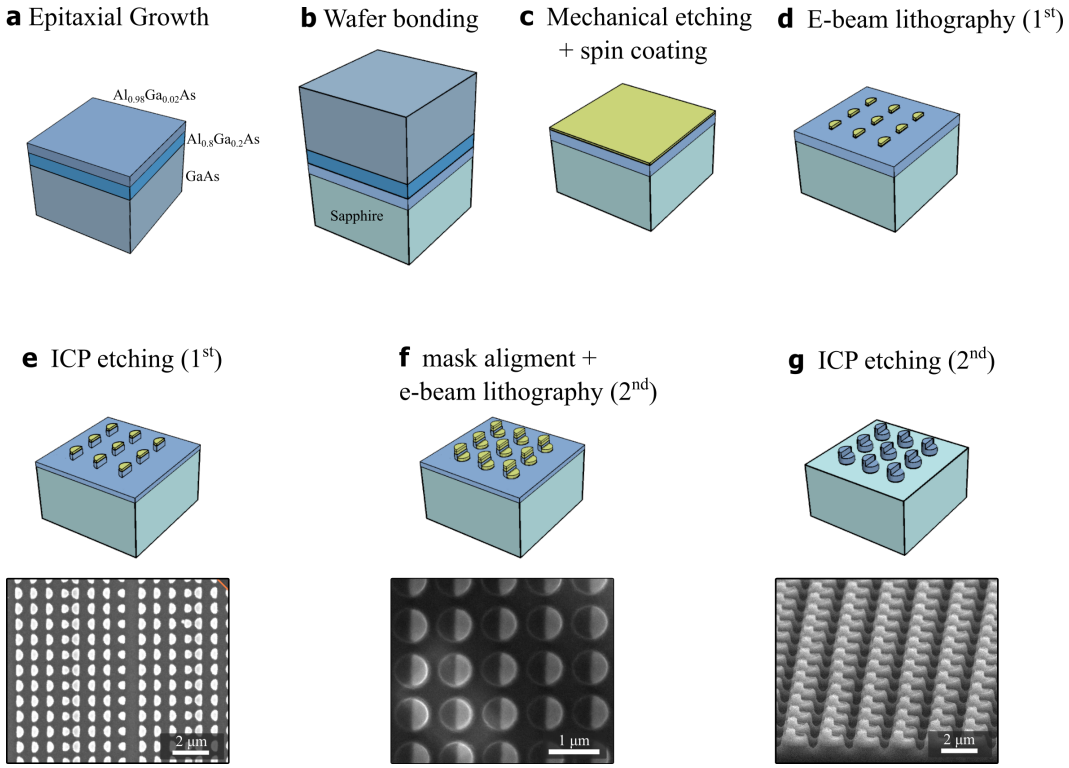

Figure 5.23: Nanochairs-on-sapphire fabrication. SEM images refer to steps e to g, respectively.

Sample fabrication

The fabrication process of nanochair resonators is summarized in Fig. 5.23. The technological protocol starts with a bonding process to report a 400-nm-thick $Al_{0.18}Ga_{0.82}As$ layer on a sapphire substrate, as detailed in Chapter 4.

Nanochairs patterning relies on a two-step lithography. HSQ resist would be the best choice for highest fabrication reliability, yet it requires long exposure times and a 10-nm thick SiO_2 adhesion layer (see Chapter 4) which reduces the clarity of alignment marks in the second lithography. We therefore opted for Man2403 negative resist.

The first half of the chair structure, as well as the alignment marks at the borders of

every writing field, were patterned by e-beam lithography with an accelerating voltage of 20 kV and exposure dose of 120 $\mu C/cm^2$. A first ICP-RIE dry etching with $SiCl_4$ transferred the first half of cylinder pattern to the AlGaAs layer. During this process, in-situ interferometry enabled to accurately control the etching depth, ensuring to stop once 200 nm of $Al_{0.18}Ga_{0.82}As$ were removed. The SEM image of Fig. 5.23e shows the result after this step.

The second e-beam lithography, which aims at defining the basis of the nanochairs, follows the same recipe as the first one. An accurate alignment is ensured by the automatic procedure of Raith Pioneer Two EBL system, proven by the SEM imageof Fig. 5.23f. The fabrication was completed with a second ICP etching, with the same characteristics as the former one, and plasma oxygen to remove Man resist.

Proximity effects and unoptimized e-beam lithography resulted in systematic deviations of real geometrical parameters from designed ones, and some inaccuracy in the chair profile. However, we want to stress that fabrication tolerances required by LUT in Fig. 5.18 are perfectly achievable with the state-of-the-art e-beam instrumentation. As an example, let us provide, in Fig. 5.24, an SEM image of an isolated nanochair. Optical performances of nanochair metasurfaces are partly limited by fabrication inaccuracies, whose optimization is yet beyond the scope of this PhD thesis.

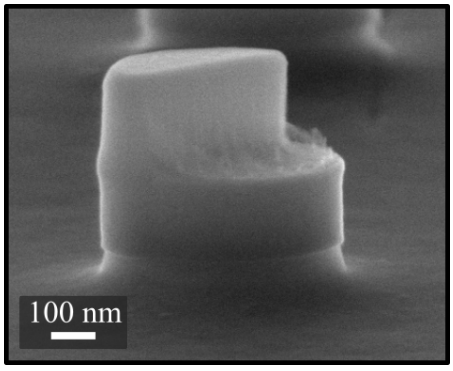

Figure 5.24: SEM image of an isolated nanochair resonator.

Nonlinear beam steering

As a first test device we fabricated the nonlinear beam steerer analyzed in Fig. 5.21 along with a benchmark uniform metasurface made of identical nanochairs. Fig. 5.25 shows a top and side view of the fabricated device, with 70 μm×70 μm size.

For its optical characterization, we used the horizontal microscope described in Chapter 4 with a few modifications (see Fig. 5.26). Pump and SH power are monitored by Newport 818-IG and 818-SL detectors, respectively. Pump wavelength is fixed at $\lambda_{FF} = 1550$ nm and input polarization is set by an achromatic half-waveplate (Thorlabs AHWP10M-1600) and calibrated in the object plane through a wire grid polarizer (Thorlabs WP25M-UB).

In order to ensure an almost uniform excitation on the whole metasurface, we used a plano-convex lens with focal distance $f = 400$ mm, focusing pump beam on the rear focal

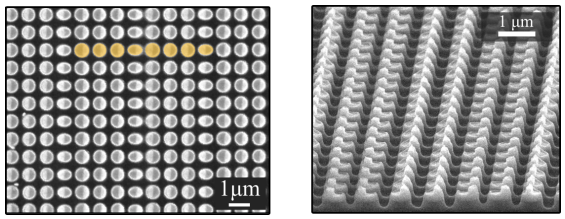

Figure 5.25: Top (left) and tilted (right) SEM views of the AlGaAs-on-sapphire meta-grating designed in Fig. 5.21.

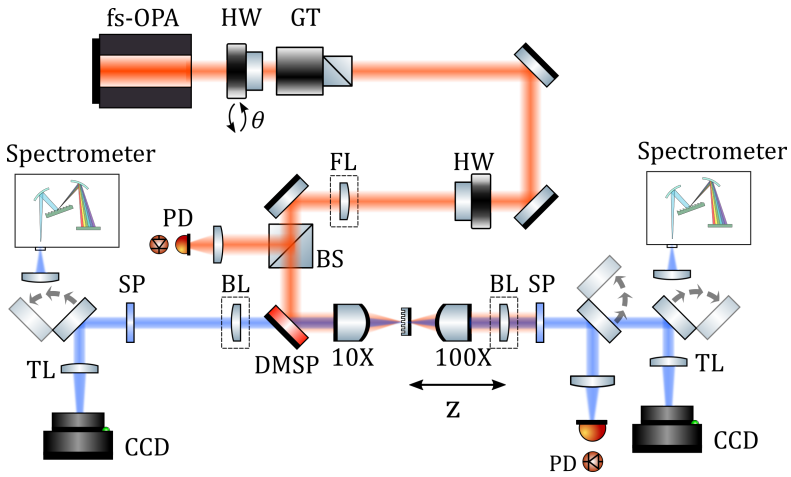

Figure 5.26: Horizontal microscope for nonlinear characterization of $\chi^{(2)}$ meta-gratings. HW: half-wave plate; GT: Glan-Taylor polarizer; FL: focusing lens (f = 400 mm); BS: beam splitter; PD: photodiode; DMSP: dichroic mirror; 10X-100X: microscope objectives with NA = 0.2 and 0.8, respectively; BL: Bertrand lens; SP: short-pass filter; TL: lens tube

plane of a 10X (NA=0.2) microscope objective. Knife-edge measurement in the object plane, see Fig. 5.27, demonstrates that with this configuration [65] we obtain a collimated beam with $w_0 \sim 100$ µm waist.

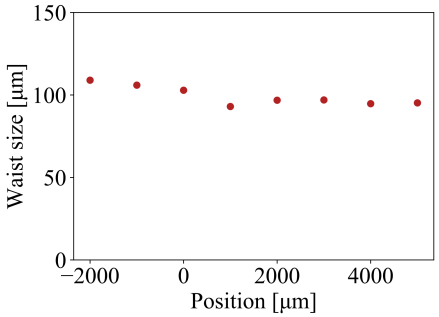

Figure 5.27: Knife-edge measurement of pump beam at λ_{FF} = 1550 nm in the space between two microscope objectives. z = 0 corresponds to the focal distance of 10X objective.

The SH beam in the forward direction was collected by a 100X (NA=0.8) objective, and the Fourier plane was imaged on a CCD camera by placing a Bertrand lens on the collection path (see Section 4.3). Such setup was first adopted to compare the far-field emission of nanochairs- and nanocylinders-on-sapphire, which can be found in Appendix C. Thus, we imaged the SH Poynting vectors in the k-space of the reference sample and the beam steerer

(see Fig. 5.28). To obtain the numerical predictions, we multiplied the radiation pattern of Fig. 5.22 by the array factor that accounts for the total $L_x \cdot L_y$ =70 µm × 70 µm metasurface size.

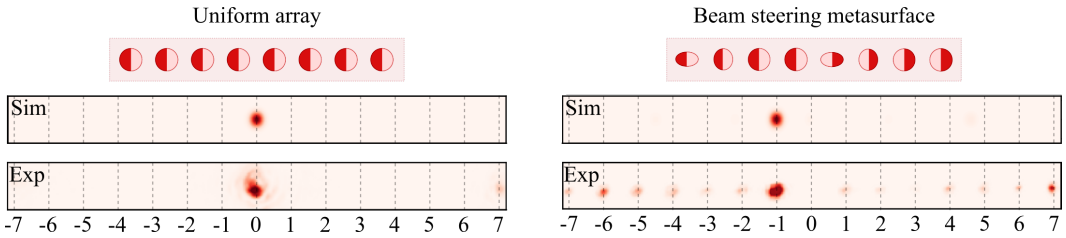

Figure 5.28: Comparison between SH Fourier imaging of a uniform array composed by identical nanochairs with a = 320 nm and b = 310 nm (left) and the meta-grating in Fig. 5.21 (right). Insets: sketch of the super-cell Numerically simulated far-fields (Sim) and experimental BFP (Exp). Pump wavelength is λ_{FF} = 1550 nm and Fourier-space is restricted to the objective NA=0.8 (corresponding to a maximum collection angle of ≈ 53° from the normal).

The NA of the microscope objective enables to visualize up to 8 diffraction orders (from -7 to +7), and Fig. 5.28 demonstrates that most of the collected SHG power from the beam steerer is funneled into the first diffraction order. Fig. 5.29 provides a closer comparison between numerical model and experiment in polar coordinates: diffraction efficiency at design wavelength is 47% which fairly validates numerical predictions.

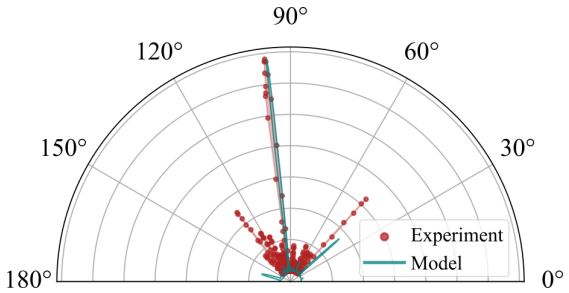

Figure 5.29: Polar plot of SH radiation pattern from Fig. 5.28 in the xz-plane. Red dots: experimental data. Blue solid curve: numerical predictions extended to the whole space in forward direction.

We further studied the spectral response of this device to investigate the operation bandwidth. At first, we swept the pump wavelength and measured the SHG power from the reference metasurface with the photodiode. Fig. 5.30 highlights a resonant peak at λ_{FF}=1570 nm with FWHM≈65 nm, revealing a Q-factor around 23, which we mainly ascribe to SH resonances.

Then, we measured the spectral behavior of the meta-grating. Fig. 5.31a displays the power funneled into the 15 diffraction orders within the objective NA for $\lambda_{FF} \in [1450 - 1650]$ nm. The maximum diffraction efficiency (47%) is achieved for the design wavelength λ_{FF}=1550 nm and it remains larger than 40% in the range $\lambda_{FF} \in [1540 - 1600]$ nm, as shown in Fig. 5.31b. Although at larger wavelengths diffraction efficiency increases over 70%, we do not consider this spectral region as a useful working range as SHG efficiency drops, consistently with Fig. 5.30.

In order to evaluate the nonlinear conversion efficiency, we measured the SHG power with the Newport 818-SL photodiode. The obtained relationship $\bar{P}_{SH}$ vs. $\bar{P}_{FF}$, shown in

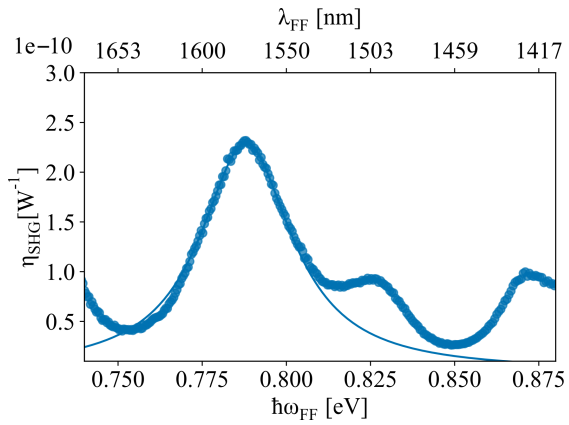

Figure 5.30: Spectral SHG efficiency for the uniform array of Fig. 5.28. The Lorentzian fit reveals a resonant peak at 0.788 eV (1574 nm) with a full-width-half-maximum of 0.033 eV (65 nm).

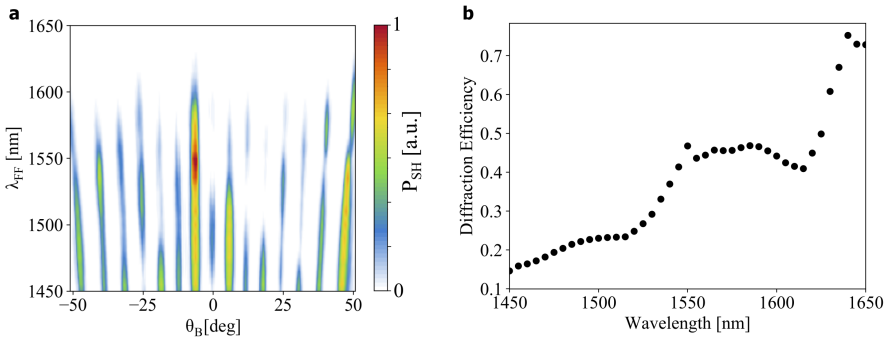

Figure 5.31: $\chi^{(2)}$ meta-grating dispersion. (a) SHG power spectrum vs. emission angle, obtained by repeating experimental measurement in Fig. 5.28 for different pump wavelengths and normalizing with respect to the input power. (b) diffraction efficiency into the 1^{st} order as a function of the incident wavelength. This is a slice of (a) around the steering angle $\theta_B = 6.2°$

Fig. 5.32, exhibits a logarithmic dependence with fit slope 1.96 ± 0.04, as expected from a $\chi^{(2)}$ process. Please note that Fig. 5.32 reports the time-average power measured by photodiodes of Fig. 5.26. Pump power has been renormalized by beam splitter (Thorlabs BSN12) and dichroic mirror (Thorlabs DMSP950) reflectivity, R_{BS} and R_{DM} respectively, as well as the metasurface fill factor FF

$$\bar{P}_{FF} = P_{PD} \frac{1 - R_{BS}}{R_{BS}} R_{DM} \frac{L_x L_y \, \mathrm{FF}}{\pi w_0^2} \tag{5.9}$$

where P_{PD} is the power measured by the photodetector.

The maximum recorded conversion ratio $\bar{P}_{SH}/\bar{P}_{FF}$ was 1.3×10^{-5} for an average pump power $P_{FF} = 7.4$ mW, being four-order-of-magnitude higher than SHG record in plasmonic metasurfaces [43]. Please note also that the measurement for increasing and decreasing power in Fig. 5.32 returns the same result proving that the sample is not damaged in the range of FF power. Working in TPA-free regime, we indeed expect that it should be possible to further increase the pump power, at variance with SOI devices operating in the same band. Actually for very high FF power we remark a slight deviation from the quadratic fit,

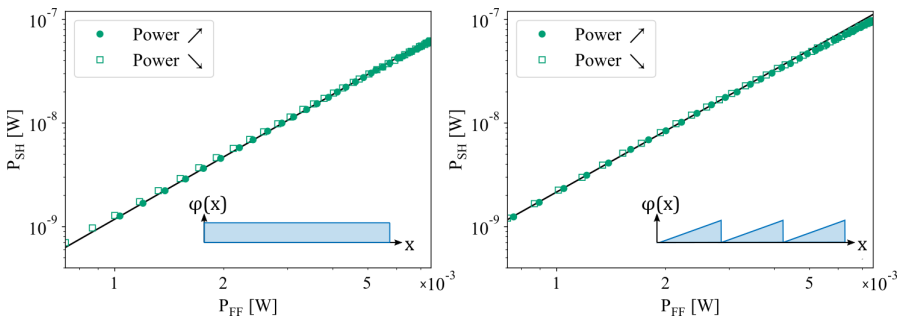

Figure 5.32: Experimental SH vs. FF time-averaged power for the two metasurfaces of Fig. 5.28. Full dots and empty squares refer to increasing or decreasing FF power, respectively, proving that the sample does not undergo irreversible processes when illuminated at high power.

which could herald a saturation possibly due to either three-photon absorption or surface defects. Considering our pulse duration $\tau_p \sim 160$ fs and repetition rate $RR = 1$ MHz, we estimate a SHG efficiency $\eta_{SHG} = 2.8 \times 10^{-10}$ W^{-1}. Since this value depends on the size of the metasurface, we computed also the intrinsic SHG efficiency in the single resonator as

$$\eta_{SHG}^{res} = \frac{\bar{P}_{SH}}{N\left[\bar{P}_{FF}^{res}\right]^2}\frac{1}{\tau_p RR} \tag{5.10}$$

with

$$\bar{P}_{FF}^{res} = P_{PD}\frac{1-R_{BS}}{R_{BS}}R_{DM}\frac{ab}{w_0^2} \tag{5.11}$$

resulting in an intrinsic conversion efficiency $\eta_{SHG}^{res} = 9.3 \times 10^{-7}$ W^{-1} which is comparable with reported performances in literature on single AlGaAs resonators [53, 66].

Nonlinear meta-lenses

The second class of devices that we studied includes $\chi^{(2)}$ flat lenses. The possibility to generate and focus nonlinear beams to a diffraction-limited spot size with a single meta-lens envisages new perspectives for nonlinear imaging with unconventional features that are not predicted by classical lens theory [47, 52]. I designed a metasurface focusing the SHG signal at a distance f by imposing a hyperboloidal phase profile to SHG

$$\phi_T(x,y) = \frac{2\pi}{\lambda_{SH}}\left(\sqrt{f^2+x^2+y^2} - |f|\right). \tag{5.12}$$

I designed two different lenses with dimensions $L_x \cdot L_y = 70\ \mu\text{m} \times 70\ \mu\text{m}$, which focus SHG beam at $f = 175$ and $70\ \mu$m from the metasurface. They roughly corresponds to numerical aperture NA=0.2 and 0.5, respectively. Please note that these values are estimated using NA=$\sin\theta = \sin[\arctan(D/2f)] \approx (D/2f)$ with $D = L_x = L_y$ being the diameter of

the inscribed circle, and they are therefore slightly underestimated. Fig. 5.33 reports an example of the obtained phase profile with the LUT in Fig. 5.18.

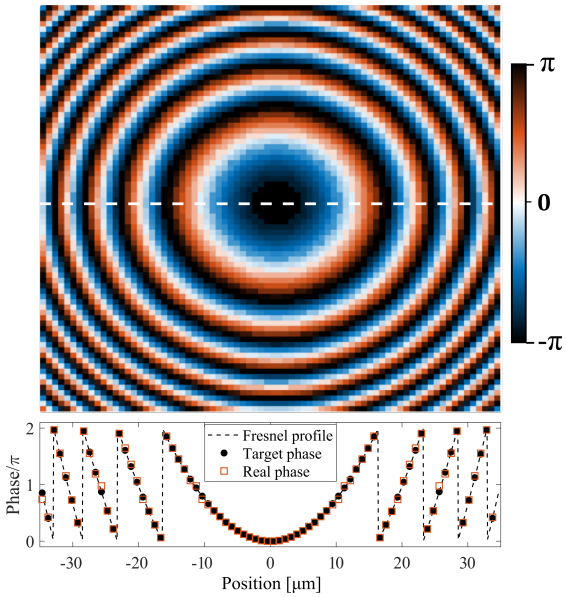

Figure 5.33: Calculated Fresnel phase profile (5.12) with the LUT of Fig. 5.18. Inset: cut view along the white dashed line, showing the target phase at sampling points (black dots) and the one obtained with nanochairs (red squares).

We used the *Raith GDSII MATLAB toolbox* [67] to automatically extract the lithographic mask from the target phase profile and LUT calculations. Fig. 5.34 shows two SEM images of the fabricated devices.

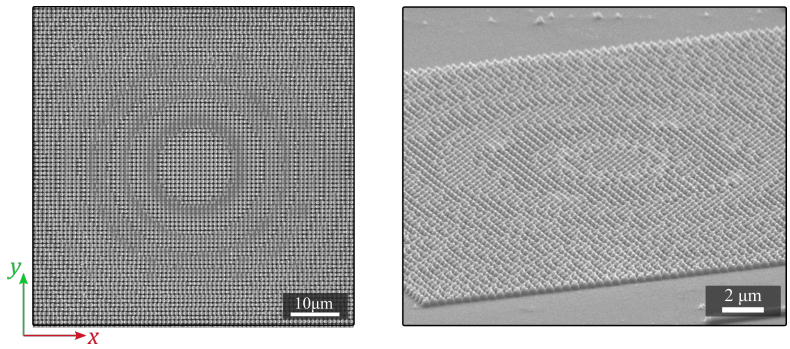

Figure 5.34: Top (left) and tilted (right) SEM images of fabricated $\chi^{(2)}$ meta-lenses.

To characterize their focusing properties, the collection objective of Fig. 5.26 was mounted on a motorized stage (Thorlabs Z812B) which provides a minimum displacement of 0.2 μm. In order to reconstruct the 3D profile of the SH beam, we acquired an image every $\Delta z = 1$ μm and we fix $z = 0$ at object plane (where the lens is perfectly imaged by the CCD camera). In order to extract a spatial information, the images acquired by CCD camera were calibrated through a 20 μm-long reference mark fabricated close to the metasurfaces (see Fig. 5.35) which corresponds to 300 pixels. We can therefore considered an uncertainty of 0.07μm on the following beam measurements.

The 3D reconstruction of SH beam for the two meta-lenses is reported in Fig. 5.36. The

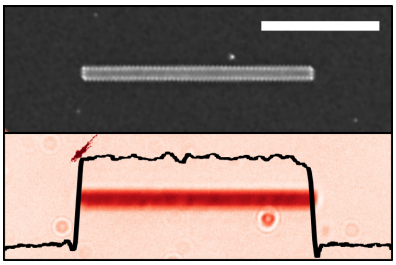

Figure 5.35: Reference mark for spatial calibration. Top: SEM image, the white scale bar equals to 10 µm. Bottom: image acquired by CCD camera with 100X objective. The black curve represents the sum of pixels along vertical direction.

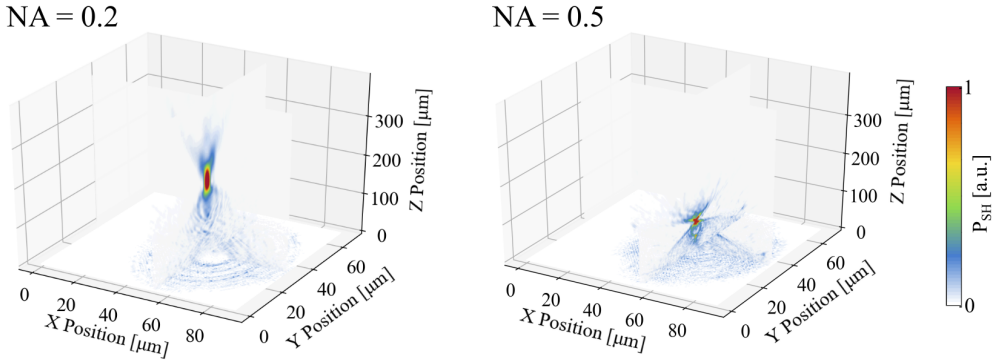

Figure 5.36: Experimental 3D reconstruction of SHG beam from two $\chi^{(2)}$ meta-lenses designed to focus SH at $f = 175$ µm (left) and 70 µm (right).

acquired data enable to perform a numerical knife edge by integrating over one of the two in-plane axes (x or y) at each z position. As an example, Fig. 5.37 shows the experimental intensity profile together with the fit result, assuming a Gaussian beam with $M^2 = 1$, at z positions 40 and 140 µm.

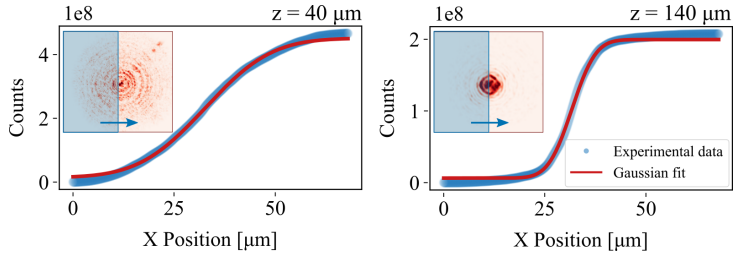

Figure 5.37: Numerical knife-edge analysis. Insets: SHG acquired by CCD camera at positions $z = 40$ µm (left) and 140 µm (right). Integrated counts along the blue arrow (blue dots) are fitted with an erf function assuming a Gaussian beam (green line).

We can therefore reconstruct the waist profile $w(z)$ and fit it with

$$w(z) = w_0\sqrt{1 + \left(\frac{z - f}{z_R}\right)^2} \tag{5.13}$$

with $z_R = \pi w_0^2/\lambda_{SH}$ the Rayleigh distance and w_0 the waist at focal plane. Fig. 5.38 reports

the fit results for the two meta-lenses At $z = f$ the acquired images exhibit the characteristic Airy pattern of diffraction limited spots with an intensity profile of the type:

$$I(x) = I_0 \left[\frac{2J_1\left(\frac{2\pi}{\lambda_{SH} x \mathrm{NA}}\right)}{\frac{2\pi}{\lambda_{SH} x \mathrm{NA}}} \right]^2 \tag{5.14}$$

with J_1 the Bessel function of the first kind. The first minimum of Airy function is at $x = 1.22\lambda_{SH}/(2\mathrm{NA})$. Approximating the Airy pattern with a Gaussian distribution $I(x) = I_0' \exp(-2x^2/w_0^2)$, one finds $w_0 \sim 0.42\lambda_{SH}/\mathrm{NA}$. Thus, for the two designed lenses with NA=0.2 and 0.5, we would expect $w_0 \sim 1.63$ and 0.66 µm, respectively. From fit process in Fig. 5.38, we found experimental spot sizes $w_0 = 1.75$ and 0.65 µm at focal distances $f = 185$ and 75 µm respectively, which are in fair agreement with theoretical predictions if one considers the experimental uncertainty and the aforementioned slight underestimation of meta-lens NA.

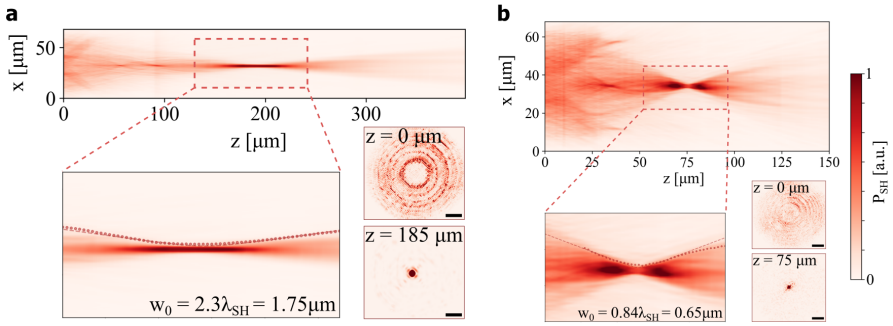

Figure 5.38: Side view reconstruction of SHG beam from the two $\chi^{(2)}$ meta-lenses, with measured focal distances $f = 185$ µm (a) and $f = 70$ µm (b), respectively. The zoomed regions around the focal point report the knife-edge measurement (dots) and the Gaussian beam waist fit (dashed line) used to retrieve the focal spot dimensions of 1.75 µm (a) and 0.65 µm (b), respectively. Insets: SHG acquired at the metasurface plane $z = 0$ and at focal plane $z = f$. The black scale bars in all the four insets correspond to 10 µm.

In order to assess the meta-lens performances, we formed an intermediate image plane along the collection path through two plano-convex lenses (see Fig. 5.39a) and we spatially filtered the focused power with a movable iris. Fig. 5.39b reports the SHG vs. FF power at object ($z = 0$) and focal ($z = f$) planes. Total SHG is identical to previously reported results for beam steerer, while diffraction efficiency is about 20% and 18% in the two cases. Although the diffraction efficiency of the present devices is upper-bounded by phase sampling distance and we are just considering SHG in forward direction, these experimental evidences are, to the best of our knowledge, the highest reported performances for SH beam shaping with flat metasurfaces.

Nonlinear holography

The identification of a reliable set of building blocks for nonlinear phase encoding is extremely attractive to design any transfer function. In view of future perspectives, we harness this point using the same LUT of Fig. 5.18 to probe the proposed method on a more

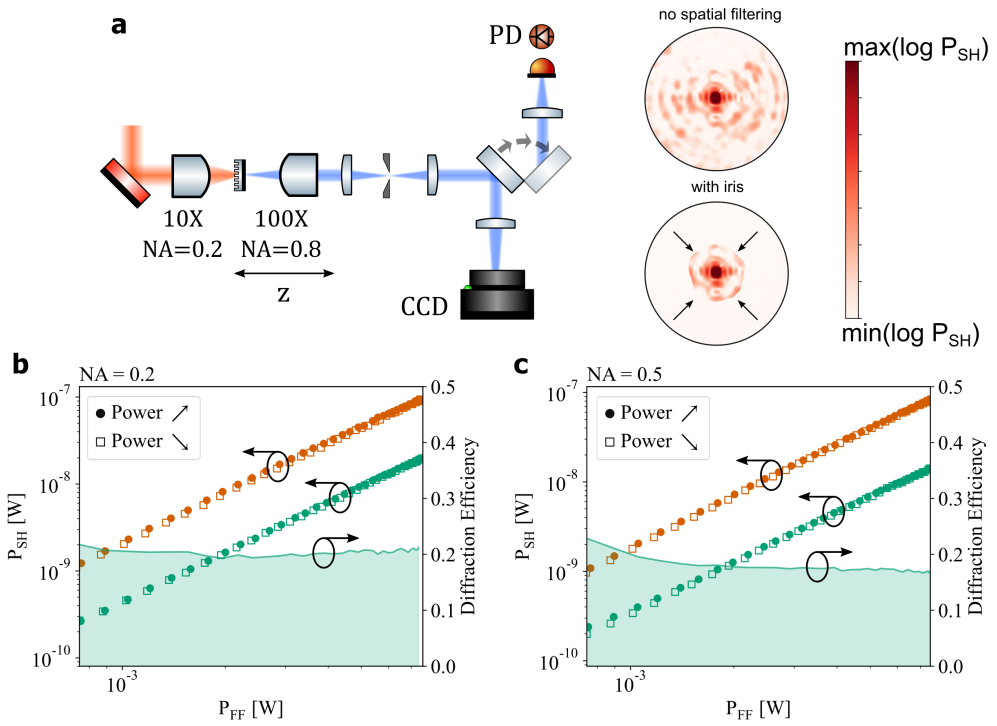

Figure 5.39: Experimental nonlinear meta-lenses efficiency. (a) Schematics of the used spatial filtering along the collection path, adopted to remove out-of-focus contributions: an intermediate image plane is created with two plano-convex lenses (Thorlabs LA4725-B-ML) and the interesting region is selected with a variable size aperture. (b-c) Total (orange) and focused (green) SH vs. FF power for designed NA=0.2 (b) and 0.5 (c). Right axes display the ratio between the two, providing the diffraction efficiencies of the devices.

complex phase profile: a 2D hologram showing the logo of the University of Paris, which involves higher spatial frequencies and requires a better resolution. The phase mask was computed starting from a set of $N = 16$ resonators uniformly sampling the $[0, 2\pi]$ phase range. A Gerchberg-Saxton (GS) algorithm was implemented to iteratively optimize the phase mask, as reported in Fig. 5.40.

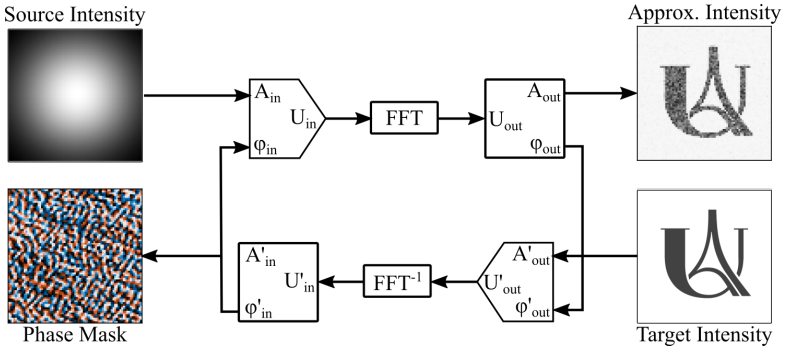

Figure 5.40: Gerchberg-Saxton algorithm for the calculation of holographic phase mask. A source amplitude profile A_{in} with initial random phase φ_{in} is Fourier transformed to retrieve its distribution at infinity U_{out}. The amplitude is therefore replaced by the desired target distribution and thus back propagated to object plane through inverse Fourier transform. The process is iterated up to convergence, obtaining the desired phase mask.

The amplitude and phase profile at object plane were projected at infinity through Fourier transform and compared with the desired intensity profile, and the error was corrected back, up to convergence. Please notice that in this case we designed the hologram

at infinity, but an analogue result can be obtained in the near-field by replacing FFT with numerical Fresnel integral transform [68, 69]. As a source intensity at object plane we set a Gaussian beam $I(\rho) = I_0 \exp(-4\rho^2/w_0^2)$, with $\rho^2 = x^2 + y^2$. The factor 4 arises from the second-order nature of $\chi^{(2)}$ process and w_0 is set at 100 μm. Fig. 5.41 comparatively shows theoretical predictions and experimental results. As for the meta-grating and meta-lenses, we ascribe the discrepancy between GS prediction and the experimental meta-hologram to an unoptimized lithography. The latter results in non-nominal values of nanochair semiaxes a and b, and it has large margins for improvement. However, beyond the technological optimization, we believe that this first proof-of-concept clearly validates the proposed design protocol and unveils an attractive scenario for future applications.

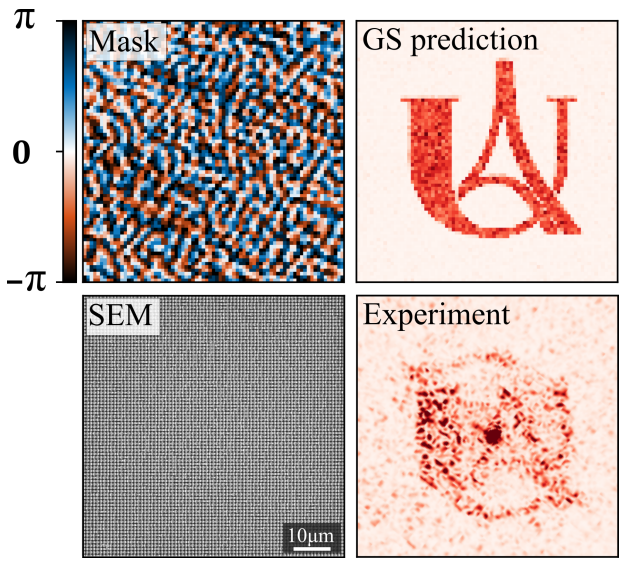

Figure 5.41: All-dielectric $\chi^{(2)}$ holography. (Top) designed phase mask (left) and intensity profile obtained with a GS algorithm (right), based on 16 elements which uniformly sample the $[0, 2\pi]$ interval. (Bottom) SEM image of the final metasurface (left) and the experimental characterization at SH (right).

5.3 Conclusion and perspectives

In this chapter we discussed how to implement SHG with imprinted spatially varying phase in all-dielectric metasurfaces. With a view to this ambitious goal, we started with the analysis of phase shaping in linear metasurfaces, to understand the pros and cons of resonant approach with respect to the well-established binary blazed gratings. This was crucial as resonators appear to be the sole possible solution to provide interesting efficiencies for practical applications in the nonlinear regime. We discussed general criteria to design meta-atoms that enable the construction of a reliable LUT for obtaining an on-demand phase transfer function. LUT is not the only possible way; for example, in the last decade inverse design proved to be more and more attractive as it enables to include and take advantage from non-local interactions, optimizing the metasurface as a whole. However, these calculations are often much more demanding in terms of computational costs, they offer a poorer physical insight, and they are less versatile when new phase profiles have to be designed.

In the present version, the computed LUT has two limitations: 1) part of SHG is emitted in the backward direction and consequently lost, and 2) the unit-cell size does not allow sub-λ phase sampling at SH. The former is not a severe one in a first demonstration, as the large $\chi^{(2)}$ nonlinearity of AlGaAs already ensures high performances. However, the latter one constitutes a more serious constraint for diffraction efficiency. We expect that this issue might be overcome by exploring a larger space of parameters for the geometry of the meta-atom. As an example for future perspectives, Fig. 5.42a reports the SH amplitude along z for taller nanochairs, and Fig. 5.42b-c proves that, setting $h = 580$ nm, a continuous phase control can be achieved with smaller basis semiaxes a and b, in turn enabling to eventually reduce meta-atom size.

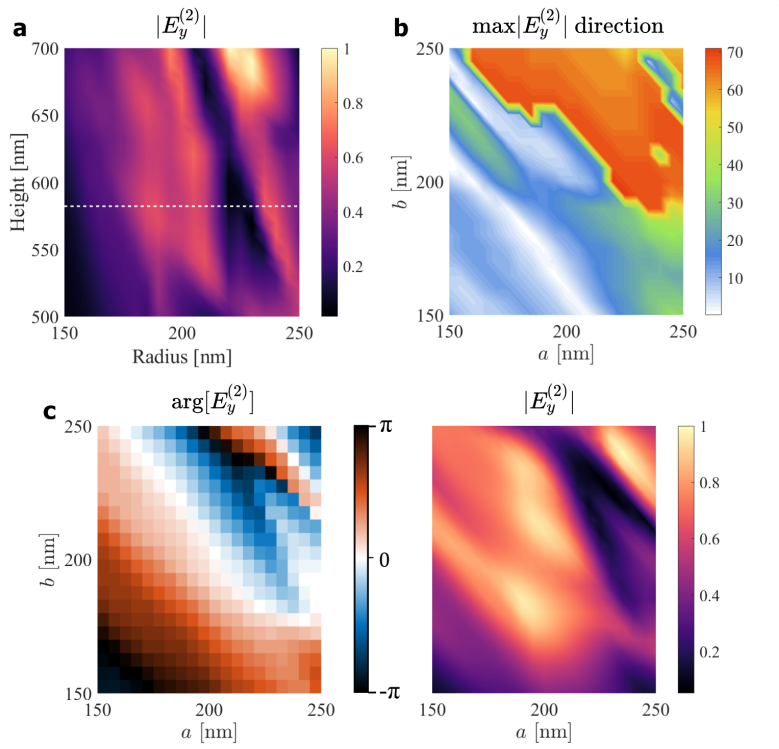

Figure 5.42: (a) SH amplitude in forward normal direction vs. nanochair total height h and radius r of its circular basis. (b) Direction (in degrees) of the maximum SH radiation lobe with respect to z-axis from an isolated nanochair with height $h = 580$ nm. (c) Phase (left) and normalized amplitude (right) of SH y electric field component valued at normal direction (z) vs. nanochair semiaxes a and b.

Fig. 5.42 illustrates just one example of the various possible paths towards future improvements. Anyhow, the numerical investigations provided in this chapter, all corroborated by experimental evidences, already endorse low-Q AlGaAs-on-sapphire resonators for nonlinear beam shaping. The measured SHG efficiency of 1.3×10^{-5} is six-order-of-magnitude higher than SHG record in plasmonic metasurfaces [45], three-order-of-magnitude higher than THG in plasmonic metasurfaces [46], and one-order-of-magnitude higher the record value for THG in silicon metasurfaces [51, 52, 70]. Beyond the demonstration of three SH beam-shaping devices, we have shown the first implementation of nonlinear meta-optics providing $0 - 2\pi$ phase control and conversion efficiency compatible with real-world applications. We believe that the combination of these two aspects can pave the way to an ambitious evolution like a flat-optics camera for night vision. Of course, this should not be seen as an alternative to InGaAs camera or Ge-Sn photodetectors which exhibit incompara-

ble performances up to 2.6 μm [71]. Contrarily, we believe that our proof-of-concept can spur further work on nonlinear metasurfaces based on SFG, enabling to convert mid-IR signals (where compact cameras are either lacking or very expensive) up to near-IR or visible range, and image them with cMOS-compatible semiconductor focal planes.

References

[1] L. Rayleigh, 'Wave theory of light,' in *Scientific Papers - Vol III*, Cambridge University Press, 1888, p. 108.

[2] R. Wood, ' LXXXV. The echelette grating for the infra-red,' *The London, Edinburgh, and Dublin Philosophical Magazine and Journal of Science*, vol. 20, pp. 770–778, 1910. DOI: 10.1080/14786441008636964.

[3] Winston E. Kock, 'Metallic Delay Lenses,' *Bell System Technical Journal*, vol. 27, pp. 58–82, 1948.

[4] L. D'Auria, J. P. Huignard, A. M. Roy, and E. Spitz, 'Photolithographic fabrication of thin film lenses,' *Optics Communications*, vol. 5, pp. 232–235, 1972. DOI: 10.1016/0030-4018(72)90086-7.

[5] G. J. Swanson, 'Binary Optics Technology : The Theory and Design of Multi-level Diffractive Optical Elements,' Tech. Rep., 1989, pp. 1–53.

[6] T. Fujita, H. Nishihara, and J. Koyama, 'Blazed gratings and Fresnel lenses fabricated by electron-beam lithography,' *Optics Letters*, vol. 7, pp. 578–580, 1982. DOI: 10.1364/ol.7.000578.

[7] W. Stork, N. Streibl, H. Haidner, and P. Kipfer, 'Artificial distributed-index media fabricated by zero-order gratings,' *Optics Letters*, vol. 16, pp. 1921–1923, 1991. DOI: 10.1364/ol.16.001921.

[8] M. W. Farn, 'Binary gratings with increased efficiency,' *Applied Optics*, vol. 31, pp. 4453–4458, 1992. DOI: 10.1364/ao.31.004453.

[9] P. Lalanne and M. Hutley, 'Artificial Media Optical Properties—Subwavelength Scale,' in *Encyclopedia of Optical Engineering*, 2011, pp. 62–71. DOI: 10.1081/e-eoe.

[10] P. Lalanne, S. Astilean, P. Chavel, E. Cambril, and H. Launois, 'Blazed binary subwavelength gratings with efficiencies larger than those of conventional échelette gratings,' *Optics Letters*, vol. 23, pp. 1081–1083, 1998. DOI: 10.1364/ol.23.001081.

[11] P. Lalanne, S. Astilean, P. Chavel, E. Cambril, and H. Launois, 'Design and fabrication of blazed binary diffractive elements with sampling periods smaller than the structural cutoff,' *Journal of the Optical Society of America A*, vol. 16, pp. 1143–1156, 1999. DOI: 10.1364/josaa.16.001143.

[12] J. P. Hugonin and P. Lalanne, *Reticolo Software for Grating Analysis*, 2021. [Online]. Available: https://www.lp2n.institutoptique.fr/light-complex-nanostructures.

[13] C. Gigli, Q. Li, P. Chavel, G. Leo, M. Brongersma, and P. Lalanne, 'Fundamental limitations of Huygens metasurfaces for optical beam shaping,' *arXiv*, pp. 1–18, 2020.

[14] M. S. L. Lee, P. Lalanne, J. C. Rodier, P. Chavel, E. Cambril, and Y. Chen, 'Imaging with blazed-binary diffractive,' *Journal of Optics A: Pure and Applied Optics*, vol. 4, S119–S124, 2002.

[15] P. Lalanne, 'Waveguiding in blazed-binary diffractive elements,' *Journal of the Optical Society of America A*, vol. 16, pp. 2517–2520, 1999. DOI: 10.1364/josaa.16.002517.

[16] S. M. Kamali, E. Arbabi, A. Arbabi, and A. Faraon, 'A review of dielectric optical metasurfaces for wavefront control,' *Nanophotonics*, vol. 7, pp. 1041–1068, 2018. DOI: 10.1515/nanoph-2017-0129.

[17] S. Vo, D. Fattal, W. V. Sorin, Z. Peng, T. Tran, M. Fiorentino, and R. G. Beausoleil, 'Sub-wavelength grating lenses with a twist,' *IEEE Photonics Technology Letters*, vol. 26, pp. 1375–1378, 2014. DOI: 10.1109/LPT.2014.2325947.

[18] A. Arbabi, Y. Horie, M. Bagheri, and A. Faraon, 'Dielectric metasurfaces for complete control of phase and polarization with subwavelength spatial resolution and high transmission,' *Nature Nanotechnology*, vol. 10, pp. 937–943, 2015. DOI: 10.1038/nnano.2015.186.

[19] A. Arbabi, Y. Horie, A. J. Ball, M. Bagheri, and A. Faraon, 'Subwavelength-thick lenses with high numerical apertures and large efficiency based on high-contrast transmitarrays,' *Nature Communications*, vol. 6, pp. 1–6, 2015. DOI: 10.1038/ncomms8069.

[20] A. Arbabi, E. Arbabi, S. M. Kamali, Y. Horie, S. Han, and A. Faraon, 'Miniature optical planar camera based on a wide-angle metasurface doublet corrected for monochromatic aberrations,' *Nature Communications*, vol. 7, pp. 1–9, 2016. DOI: 10.1038/ncomms13682.

[21] S. Kruk, B. Hopkins, I. I. Kravchenko, A. Miroshnichenko, D. N. Neshev, and Y. S. Kivshar, 'Invited Article: Broadband highly efficient dielectric metadevices for polarization control,' *APL Photonics*, vol. 1, 2016. DOI: 10.1063/1.4949007.

[22] Z. Zhou, J. Li, R. Su, B. Yao, H. Fang, K. Li, L. Zhou, J. Liu, D. Stellinga, C. P. Reardon, T. F. Krauss, and X. Wang, 'Efficient Silicon Metasurfaces for Visible Light,' *ACS Photonics*, vol. 4, pp. 544–551, 2017. DOI: 10.1021/acsphotonics.6b00740.

[23] E. Arbabi, A. Arbabi, S. M. Kamali, Y. Horie, M. S. Faraji-Dana, and A. Faraon, 'MEMS-tunable dielectric metasurface lens,' *Nature Communications*, vol. 9, pp. 1–9, 2018. DOI: 10.1038/s41467-018-03155-6.

[24] C. Pfeiffer and A. Grbic, 'Metamaterial Huygens' surfaces: Tailoring wave fronts with reflectionless sheets,' *Physical Review Letters*, vol. 110, pp. 1–5, 2013. DOI: 10.1103/PhysRevLett.110.197401.

[25] N. Yu, P. Genevet, M. a. Kats, F. Aieta, J.-P. Tetienne, F. Capasso, and Z. Gaburro, 'Light Propagation with Phase Discontinuities: Generalized Laws of Reflection and Refraction,' *Science*, vol. 334, pp. 333–337, 2011. DOI: 10.1126/science.1210713.

[26] N. Yu and F. Capasso, 'Flat optics with designer metasurfaces,' *Nature Materials*, vol. 13, pp. 139–150, 2014. DOI: 10.1038/nmat3839.

[27] F. Aieta, G. Patrice, M. Kats, N. Yu, R. Blanchard, Z. Gaburro, and F. Capasso, 'Aberration-Free Ultrathin Flat Lenses and Axicons at Telecom Wavelengths Based on Plasmonic Metasurfaces,' *Nano Letters*, vol. 12, pp. 4932–4936, 2012. DOI: https://doi.org/10.1021/nl302516v.

[28] P. Genevet, F. Capasso, F. Aieta, M. Khorasaninejad, and R. Devlin, 'Recent advances in planar optics: from plasmonic to dielectric metasurfaces,' *Optica*, vol. 4, pp. 139–152, 2017. DOI: 10.1364/optica.4.000139.

[29] M. Kerker, D. S. Wang, and C. L. Giles, 'Electromagnetic Scattering By Magnetic Spheres.,' *Journal of the Optical Society of America*, vol. 73, pp. 765–767, 1983. DOI: 10.1364/JOSA.73.000765.

[30] Y. H. Fu, A. I. Kuznetsov, A. E. Miroshnichenko, Y. F. Yu, and B. Luk'yanchuk, 'Directional visible light scattering by silicon nanoparticles,' *Nature Communications*, vol. 4, pp. 1–6, 2013. DOI: 10.1038/ncomms2538.

[31] I. Staude, A. E. Miroshnichenko, M. Decker, N. T. Fofang, S. Liu, E. Gonzales, J. Dominguez, T. S. Luk, D. N. Neshev, I. Brener, and Y. Kivshar, 'Tailoring directional scattering through magnetic and electric resonances in subwavelength silicon nanodisks,' *ACS Nano*, vol. 7, pp. 7824–7832, 2013. DOI: 10.1021/nn402736f.

[32] S. Person, M. Jain, Z. Lapin, J. J. Sáenz, G. Wicks, and L. Novotny, 'Demonstration of zero optical backscattering from single nanoparticles,' *Nano Letters*, vol. 13, pp. 1806–1809, 2013. DOI: 10.1021/nl4005018.

[33] M. Decker, I. Staude, M. Falkner, J. Dominguez, D. N. Neshev, I. Brener, T. Pertsch, and Y. S. Kivshar, 'High-Efficiency Dielectric Huygens' Surfaces,' *Advanced Optical Materials*, vol. 3, pp. 813–820, 2015. DOI: 10.1002/adom.201400584.

[34] A. B. Evlyukhin, T. Fischer, C. Reinhardt, and B. N. Chichkov, 'Optical theorem and multipole scattering of light by arbitrarily shaped nanoparticles,' *Physical Review B*, vol. 94, pp. 1–7, 2016. DOI: 10.1103/PhysRevB.94.205434.

[35] M. I. Shalaev, J. Sun, A. Tsukernik, A. Pandey, K. Nikolskiy, and N. M. Litchinitser, 'High-Efficiency All-Dielectric Metasurfaces for Ultracompact Beam Manipulation in Transmission Mode,' *Nano Letters*, vol. 15, pp. 6261–6266, 2015. DOI: 10.1021/acs.nanolett.5b02926.

[36] Y. F. Yu, A. Y. Zhu, R. Paniagua-Domínguez, Y. H. Fu, B. Luk'yanchuk, and A. I. Kuznetsov, 'High-transmission dielectric metasurface with 2π phase control at visible wavelengths,' *Laser and Photonics Reviews*, vol. 9, pp. 412–418, 2015. DOI: 10.1002/lpor.201500041.

[37] S.-q. Li, X. Xu, R. M. Veetil, V. Valuckas, and A. I. Kuznetsov, 'Phase-only transmissive spatial light modulator based on tunable dielectric metasurface,' *Science*, vol. 364, pp. 1087–1090, 2019. DOI: 10.1126/science.aaw6747.

[38] D. Arslan, K. E. Chong, A. E. Miroshnichenko, D.-y. Choi, D. N. Neshev, T. Pertsch, Y. S. Kivshar, and I. Staude, 'Angle-selective all-dielectric Huygens ' metasurfaces,' *Journal of Physics D: Applied Physics*, vol. 50, pp. 1–8, 2017.

[39] H. Cai, S. Srinivasan, D. A. Czaplewski, A. B. Martinson, D. J. Gosztola, L. Stan, T. Loeffler, S. K. Sankaranarayanan, and D. López, 'Inverse design of metasurfaces with non-local interactions,' *npj Computational Materials*, vol. 6, pp. 1–8, 2020. DOI: 10.1038/s41524-020-00369-5.

[40] L. L. Zhao, K. Lance Kelly, and G. C. Schatz, 'The extinction spectra of silver nanoparticle arrays: Influence of array structure on plasmon resonance wavelength and width,' *Journal of Physical Chemistry B*, vol. 107, pp. 7343–7350, 2003. DOI: 10.1021/jp034235j.

[41] G. Li, S. Chen, N. Pholchai, B. Reineke, P. W. H. Wong, E. Y. B. Pun, K. W. Cheah, T. Zentgraf, and S. Zhang, 'Continuous control of the nonlinearity phase for harmonic generations,' *Nature Materials*, vol. 14, pp. 607–612, 2015. DOI: 10.1038/nmat4267.

[42] M. Berry, 'Quantal phase factors accompanying adiabatic changes,' *Proc. R. Soc. Lond. A*, vol. 392, pp. 45–57, 1984. DOI: 10.1142/9789813221215_0006.

[43] N. Segal, S. Keren-Zur, N. Hendler, and T. Ellenbogen, 'Controlling light with metamaterial-based nonlinear photonic crystals,' *Nature Photonics*, vol. 9, pp. 180–184, 2015. DOI: 10.1038/nphoton.2015.17.

[44] V. Berger, 'Second-harmonic generation in monolithic cavities,' *JOSA B*, vol. 14, pp. 1351–1360, 1997.

[45] S. Keren-Zur, O. Avayu, L. Michaeli, and T. Ellenbogen, 'Nonlinear Beam Shaping with Plasmonic Metasurfaces,' *ACS Photonics*, vol. 3, pp. 117–123, 2016. DOI: 10.1021/acsphotonics.5b00528.

[46] E. Almeida, O. Bitton, and Y. Prior, 'Nonlinear metamaterials for holography,' *Nature Communications*, vol. 7, pp. 1–7, 2016. DOI: 10.1038/ncomms12533.

[47] C. Schlickriede, N. Waterman, B. Reineke, P. Georgi, G. Li, S. Zhang, and T. Zentgraf, 'Imaging through Nonlinear Metalens Using Second Harmonic Generation,' *Advanced Materials*, vol. 30, pp. 1–7, 2018. DOI: 10.1002/adma.201703843.

[48] T. Pertsch and Y. Kivshar, 'Nonlinear optics with resonant metasurfaces,' *MRS Bulletin*, vol. 45, pp. 210–220, 2020. DOI: 10.1557/mrs.2020.65.

[49] K. Koshelev and Y. Kivshar, 'Dielectric Resonant Metaphotonics,' *ACS Photonics*, vol. 7, A–K, 2020. DOI: 10.1021/acsphotonics.0c01315.

[50] L. Wang, S. Kruk, K. Koshelev, I. Kravchenko, B. Luther-Davies, and Y. Kivshar, 'Nonlinear Wavefront Control with All-Dielectric Metasurfaces,' *Nano Letters*, vol. 18, pp. 3978–3984, 2018. DOI: 10.1021/acs.nanolett.8b01460.

[51] Y. Gao, Y. Fan, Y. Wang, W. Yang, Q. Song, and S. Xiao, 'Nonlinear Holographic All-Dielectric Metasurfaces,' *Nano Letters*, vol. 18, pp. 8054–8061, 2018. DOI: 10.1021/acs.nanolett.8b04311.

[52] C. Schlickriede, S. S. Kruk, S. S. Kruk, L. Wang, B. Sain, Y. Kivshar, and T. Zentgraf, 'Nonlinear Imaging with All-Dielectric Metasurfaces,' *Nano Letters*, vol. 20, pp. 4370–4376, 2020. DOI: 10.1021/acs.nanolett.0c01105.

[53] R. Camacho-Morales, M. Rahmani, S. Kruk, L. Wang, L. Xu, D. A. Smirnova, A. S. Solntsev, A. Miroshnichenko, H. H. Tan, F. Karouta, S. Naureen, K. Vora, L. Carletti, C. De Angelis, C. Jagadish, Y. S. Kivshar, and D. N. Neshev, 'Nonlinear Generation of Vector Beams from AlGaAs Nanoantennas,' *Nano Letters*, vol. 16, pp. 7191–7197, 2016. DOI: 10.1021/acs.nanolett.6b03525.

[54] L. Carletti, A. Locatelli, D. Neshev, and C. De Angelis, 'Shaping the Radiation Pattern of Second-Harmonic Generation from AlGaAs Dielectric Nanoantennas,' *ACS Photonics*, vol. 3, pp. 1500–1507, 2016. DOI: 10.1021/acsphotonics.6b00050.

[55] L. Carletti, G. Marino, L. Ghirardini, V. F. Gili, D. Rocco, I. Favero, A. Locatelli, A. V. Zayats, M. Celebrano, M. Finazzi, L. Giuseppe, C. de Angelis, and D. N. Neshev, 'Nonlinear goniometry by second harmonic generation in AlGaAs nanoantennas,' *ACS Photonics*, vol. 5, pp. 4386–4392, 2018. DOI: 10.1021/acsphotonics.8b00810.

[56] K. Frizyuk, I. Volkovskaya, D. Smirnova, A. Poddubny, and M. Petrov, 'Second-harmonic generation in Mie-resonant dielectric nanoparticles made of noncentrosymmetric materials,' *Physical Review B*, vol. 99, pp. 1–17, 2019. DOI: 10.1103/PhysRevB.99.075425.

[57] L. Xu, G. Saerens, M. Timofeeva, D. A. Smirnova, I. Volkovskaya, M. Lysevych, R. Camacho-morales, M. Cai, K. Z. Kamali, L. Huang, F. Karouta, H. H. Tan, C. Jagadish, A. E. Miroshnichenko, R. Grange, D. N. Neshev, and M. Rahmani, 'Forward and Backward Switching of Nonlinear Unidirectional Emission from GaAs Nanoantennas,' *ACS Nano*, vol. 14, pp. 1379–1389, 2020. DOI: 10.1021/acsnano.9b07117.

[58] J. D. Sautter, L. Xu, A. E. Miroshnichenko, M. Lysevych, I. Volkovskaya, D. A. Smirnova, R. Camacho-Morales, K. Zangeneh Kamali, F. Karouta, K. Vora, H. H. Tan, M. Kauranen, I. Staude, C. Jagadish, D. N. Neshev, and M. Rahmani, 'Tailoring Second-Harmonic Emission from (111)-GaAs Nanoantennas,' *Nano Letters*, vol. 19, pp. 3905–3911, 2019. DOI: 10.1021/acs.nanolett.9b01112.

[59] D. Rocco, C. Gigli, L. Carletti, G. Marino, M. A. Vincenti, G. Leo, and C. D. Angelis, 'Vertical Second Harmonic Generation in asymmetric dielectric nanoantennas,' *IEEE Photonics Journal*, vol. 12, pp. 1–7, 2020. DOI: 10.1109/JPHOT.2020.2988502.

[60] N. Bernhardt, K. Koshelev, S. J. White, K. W. C. Meng, J. E. Fröch, S. Kim, T. T. Tran, D. Y. Choi, Y. Kivshar, and A. S. Solntsev, 'Quasi-BIC Resonant Enhancement of Second-Harmonic Generation in WS2Monolayers,' *Nano Letters*, vol. 20, pp. 5309–5314, 2020. DOI: 10.1021/acs.nanolett.0c01603.

[61] L. Xu, K. Zangeneh Kamali, L. Huang, M. Rahmani, A. Smirnov, R. Camacho-Morales, Y. Ma, G. Zhang, M. Woolley, D. Neshev, and A. E. Miroshnichenko, 'Dynamic Nonlinear Image Tuning through Magnetic Dipole Quasi-BIC Ultrathin Resonators,' *Advanced Science*, vol. 1802119, pp. 1–7, 2019. DOI: 10.1002/advs.201802119.

[62] K. Koshelev, S. Kruk, E. Melik-Gaykazyan, J.-H. Choi, A. Bogdanov, H.-G. Park, and Y. Kivshar, 'Subwavelength dielectric resonators for nonlinear nanophotonics.,' *Science (New York, N.Y.)*, vol. 367, pp. 288–292, 2020. DOI: 10.1126/science.aaz3985.

[63] M. Scherr, M. Barrow, and J. Phillips, 'Long-wavelength infrared transmission filters via two-step subwavelength dielectric gratings,' *Optics Letters*, vol. 42, pp. 518–521, 2017. DOI: 10.1364/ol.42.000518.

[64] J. Yang, J. P. Hugonin, and P. Lalanne, 'Near-to-Far Field Transformations for Radiative and Guided Waves,' *ACS Photonics*, vol. 3, pp. 395–402, 2016. DOI: 10.1021/acsphotonics.5b00559.

[65] P. Hauer, J. Grand, A. Djorovic, G. R. Willmott, and E. C. Le Ru, 'Spot Size Engineering in Microscope-Based Laser Spectroscopy,' *Journal of Physical Chemistry C*, vol. 120, pp. 21 104–21 113, 2016. DOI: 10.1021/acs.jpcc.6b04574.

[66] V. F. Gili, L. Carletti, A. Locatelli, D. Rocco, M. Finazzi, L. Ghirardini, I. Favero, C. Gomez, A. Lemaître, M. Celebrano, C. De Angelis, and G. Leo, 'Monolithic AlGaAs second-harmonic nanoantennas,' *Optics Express*, vol. 24, pp. 15 965–15 971, 2016. DOI: 10.1364/OE.24.015965.

[67] N. I. for Nanotechnology, *Raith_GDSII MATLAB toolbox*. [Online]. Available: https://github.com/nrc-cnrc/Raith%7B%5C_%7DGDSII.

[68] D. Mas, J. Garcia, C. Ferreira, L. M. Bernardo, and F. Marinho, 'Fast algorithms for free-space diffraction patterns calculation,' *Optics Communications*, vol. 164, pp. 233–245, 1999. DOI: 10.1016/S0030-4018(99)00201-1.

[69] L. Junchang and W. Yanmei, 'An indirect algorithm of Fresnel diffraction,' *Optics Communications*, vol. 282, pp. 455–458, 2009. DOI: 10.1016/j.optcom.2008.10.060.

[70] K. Wang, J. G. Titchener, S. S. Kruk, L. Xu, H.-p. Chung, M. Parry, I. I. Kravchenko, Y.-h. Chen, A. S. Solntsev, Y. S. Kivshar, D. N. Neshev, and A. A. Sukhorukov, 'Quantum metasurface for multiphoton interference and state reconstruction,' *Science*, vol. 1108, pp. 1104–1108, 2018.

[71] T. Pham, W. Du, H. Tran, J. Margetis, J. Tolle, G. Sun, R. A. Soref, H. A. Naseem, B. Li, and S.-Q. Yu, 'Systematic study of Si-based GeSn photodiodes with 26 µm detector cutoff for short-wave infrared detection,' *Optics Express*, vol. 24, p. 4519, 2016. DOI: 10.1364/oe.24.004519.

Conclusion and outlook 6

For the last years, the rapidly evolving domain of nonlinear nanophotonics has witnessed the possibility to strongly enhance harmonic response in sub-λ resonators and harness their radiation properties. As a means to feed such progress, it is pivotal to develop robust design and experimental tools that ease the physical comprehension and offer clear guidelines for optimization. Such resources, combined with the recent technological progress, promote the demonstration of unprecedented flat devices providing new perspectives to the 60-years-old domain of nonlinear optics.

In this PhD thesis we have investigated SHG in AlGaAs nanoresonators, producing three original results which might contribute to such progress:

Modal formalism of nonlinear generation in open-cavities

We implemented QNM formalism to study harmonic generation in non-Hermitian systems, which provides fundamental parallelisms and highlights substantial differences with respect to nonlinear phenomena in guided systems. Although we specifically focused on SHG, the formalism can be straightforwardly extended to all nonlinear processes. Its strength relies on the appropriate normalization of numerically computed modes. This facilitates the definition of clear figures of merit to evaluate generation efficiency in terms of modes quality factors and overlap integrals. This, in turn, provide useful guidelines for the design of open-cavities. We limited ourselves to the investigation of up-conversion process, but it seems likely that the rapid exploration of cavity modes and the low computation costs required by a semi-analytical approach will constitute a cornerstone for the study of down-conversion processes, with an impact in the domain of quantum optics in open cavities.

Diffraction and polarization control in AlGaAs-on-AlOx metasurfaces

The performances of isolated nanoresonators, even in the best optimized case, are still far from those of guided systems. Nanocavities offer a precious advantage when their properties can be modulated on a fast timescale, when they can be combined with local emitters or, finally, when they are arranged in large arrays to control either the polarization or the phase of nonlinearly generated beams. This idea pushed us towards the study of all-dielectric $\chi^{(2)}$ metasurfaces. We tried to understand and define the similarities and differences of these devices with respect to photonic crystals and plasmonic metamaterials. Relying on the established technological knowledge of the DON group, we developed AlGaAs-on-AlOx metasurfaces to promote far-field interference of resonator arrays and manipulate SH radiation patterns. Finally, we showed that the emission properties of resonant modes in isolated nanoresonators can be preserved in periodic arrays with a view to control SHG polarization state.

SH wavefront shaping in AlGaAs-on-sapphire metasurfaces

Periodic arrays of identical particles provide a limited control over nonlinear radiation properties. We therefore investigated and demonstrated a design tool to spatially manipulate SHG amplitude and phase. Compared with existing work on THG in Si nanodisks, the additional difficulty represented by the fully tensorial $\chi^{(2)}$ susceptibility was tackled numerically, identifying a robust set of building blocks regardless of the targeted phase profile. In order to work in transmission configuration, we moved from the well-established monolithic AlGaAs-on-AlOx technology to a wafer-bonded AlGaAs-on-sapphire platform and we improved the fabrication protocol to realize axially asymmetric nanoresonators. Thus, we demonstrated three devices that concurrently up-convert a pump at telecom wavelength to 775 nm and define its wavefront so as to steer it, focus it or implement an holographic image, respectively. We reported an experimental diffraction efficiency of 47% to deflect a SH beam at 6.2° with $\approx 1.3 \times 10^{-5}$ conversion efficiency for an average pump power of 7.4 mW. To our knowledge this constitutes the largest reported generation efficiency in nonlinear beam shaping devices to date.

What's next?

The results discussed in this thesis open the way to several developments.

Nonlinear generation in coupled resonators

QNM formalism offers a suitable framework to study nonlinear generation in systems where several resonators are coupled in the near-field, e.g. dimers, trimers and oligomers. Mode hybridization is deeply studied in the linear regime, and it may offer interesting possibilities to tune nonlinear properties, induce a fast-switching response or promote topological effects.

Modal formalism of down-conversion processes in open-cavities

Nowadays SPDC processes in open cavities are predicted with fully vectorial simulations which model the corresponding up-conversion phenomena of SHG and SFG. However, due to the large number of degrees of freedom in open systems, it is hard to achieve a one-to-one correspondence between up- and down-conversion processes. In turn, this requires to perform a huge amount of numerical simulations for a complete analysis. This burden is heavier than for closed cavities, where the presence of further constraints (e.g. phase matching conditions) largely reduces the parameter space. In non-Hermitian systems, conversely, one often resorts to severe approximations to make calculations less painful. In this context, the development of a quantum-classical correspondence within QNM framework seems promising to extrapolate general criteria for the design of efficient quantum sources at the nanoscale. Moreover, the semi-analytic character of QNM formalism will enable to rapidly scan a large amount of parameters making predictions more accurate.

Optimization of nonlinear beam shaping devices

Although the results discussed in Chapter 5 provide a proof-of-concept to assess the feasibility of AlGaAs metasurfaces for SH beam shaping, plenty of room remains for

improvement both from the design and fabrication points of view. The optimization of nanochair meta-atom may yield to a spatially finer phase sampling. In parallel, the development of more stable fabrication protocols, combined with state-of-the-art e-beam lithography, might reduce proximity effects and improve the quality of nanochairs, reducing the distance between nominal and actual device properties.

Improved meta-atom design approaches

In the first proof-of-concept of this thesis, the design of nanochair meta-atoms relied on an initial qualitative intuition followed by extensive FEM simulations, scanning over some geometrical parameters to retrieve the desired radiation properties. The general criteria proposed in Chapter 5 for $\chi^{(2)}$ metasurfaces design might be combined with modal analysis in Chapter 3. This might open more convenient paths to $[0-2\pi]$ phase control. Alternatively, the full numerical design could be improved with machine learning techniques, partially loosing the physical comprehension but eventually gaining in performances.

Quantum metasurfaces

Finally, all the optimization techniques and numerical tools developed in this thesis might be exploited for the design of quantum $\chi^{(2)}$ metasurfaces. In this case the control of SPDC processes in sub-λ resonator arrays might be adopted to shape the amplitude, phase and polarization state of generated entangled photons.

Appendices

Lorentz model for AlGaAs permittivity

A

Auxiliary-field formulation in Chapter 3 requires an analytical model for material refractive index. As a reference for $Al_xGa_{1-x}As$ ternary alloy, we adopt Gehrsitz empirical model [1] which accurately describes the real part of the permittivity below the material bandgap. In the following we fit empirical data with a single-pole Lorentzian model

$$\varepsilon(\omega) = \varepsilon_\infty - \varepsilon_\infty \frac{\omega_p^2}{\omega^2 - \omega_0^2 - i\omega\gamma}. \tag{A.1}$$

Since in the case of $Al_{0.18}Ga_{0.82}As$ we work in a regime where material absorption is negligible for $\lambda < 740$ nm, we can set $\gamma = 0$. Consequently we use nonlinear least-squares method, see Fig. A.1 to find best-fit parameters $\omega_0 = 5.55 \times 10^{15}$ rad/s, $\omega_p = 1.69 \times 10^{15}$ rad/s and $\varepsilon_\infty = 1$.

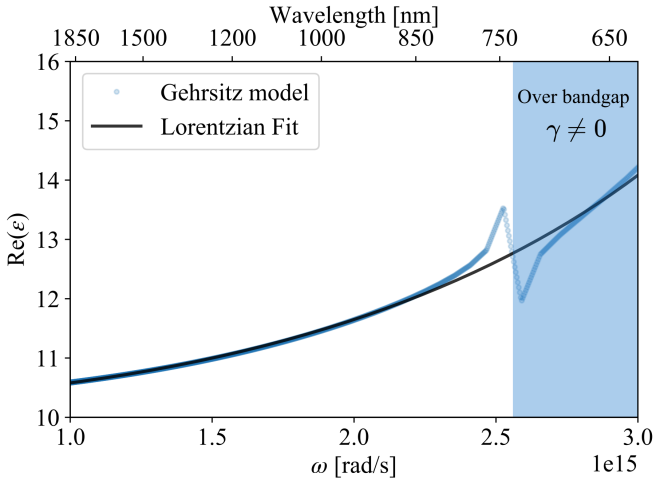

Figure A.1: Real part of $Al_{0.18}Ga_{0.82}As$ permittivity form empirical Gehrsitz model (blue dots) fitted with a single pole Lorentzian (black solid line).

Importantly, this result holds whenever resonances close to or above the material bandgap give a negligible contribution. Due to the absence of empirical or analytical models on the complex permittivity for such specific alloy composition, the extension of this fit to a broader working range was not pursued in this thesis.

References

[1] S. Gehrsitz, F. K. Reinhart, C. Gourgon, N. Herres, A. Vonlanthen, and H. Sigg, 'The refractive index of AlxGa1-xAs below the band gap: Accurate determination and empirical modeling,' *Journal of Applied Physics*, vol. 87, pp. 7825–7837, 2000. DOI: 10.1063/1.373462.

Camera calibration

B

Real-space imaging (see Chapter 4) is helpful to study the resonant behavior of nanoantennas by changing their size or excitation wavelength, but it doesn't give any quantitative information on the generation efficiency. For this purpose, the CCD sensor was calibrated with a reference power meter. The adopted configuration is shown in Fig. B.1a.

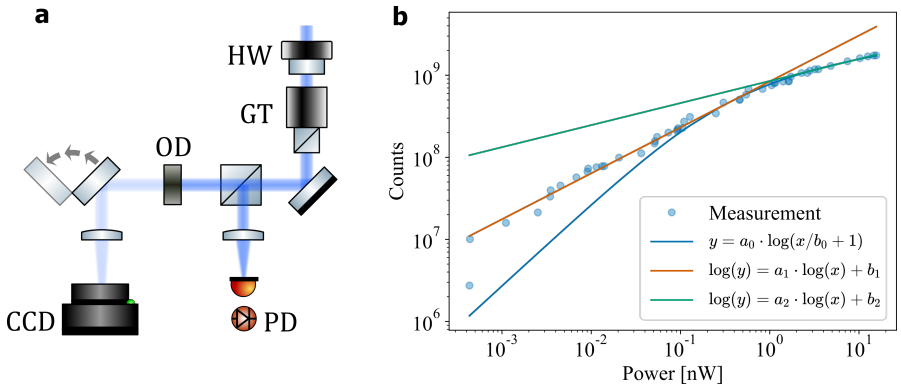

Figure B.1: CCD camera power calibration. (a) Experimental setup: HW - Half Waveplate, GT - Glan Taylor polarizer, OD: Optical Density. (b) Extracted fit.

A 775 nm pulsed beam from the OPA cavity is controlled in intensity by a motorized half-wave plate and a Glan-Taylor polarizer. It is then split by a 90:10 (R:T) beamsplitter (BSX11 by Thorlabs). One half is directed on a power meter (Newport 2835-c with 818-IR sensor), the other half is attenuated by a neutral optical-density filter (measured transmittivity $2.85{\times}10^{-5}$) and imaged on the camera. Consistently with previous measurements, a region of interest of 120×120 pixels is imposed. The extracted relationship between total counts and measured power is reported in Fig. B.1(b), where the x-axis refers to time-average power measured by the power meter. Since the total CCD counts do not scale linearly with laser power, two alternative fit functions can be used to approximate this dependence:

- a logarithmic function

$$y = a_0 \cdot \log\left(\frac{x}{b_0} + 1\right) \tag{B.1}$$

  with $a_0 = 3.63 \times 10^8$ and $b_0 = 0.13$, which is valid for a measured power >50 pW.

- a double step log-log function

$$\log(y) = a_{1,2} \cdot \log(x) + b_{1,2} \tag{B.2}$$

  with a saturation threshold separating the two slopes at 1 nW.

Such calibration curves are used in parallel with Newport 818-SL photodiode to estimate the generation efficiency of dielectric nanoantennas.

C On-axis SHG emission

As a proof of concept on the on-axis emission provided by symmetry breaking, we compared two uniform metasurfaces: one based on the nanochair meta-atoms with semiaxes $a = 320$ and $b = 310$ nm, as shown in Chapter 5, while the other one composed of their cylindrical counterparts with radius $r = 210$ nm (this radius enables a maximum SHG efficiency for common nanocylinders). We studied their SHG radiation pattern through Fourier space imaging, performed as illustrated in Chapter 4. Fig. C.1a shows that, at variance with the nanocylinders, the nanochairs exhibit a main lobe along z. The integration over the azimuthal angle φ vs. the emission angle θ (Fig. C.1b), proves that in the latter case 60% of the SHG power is emitted for $\theta < 8°$. This percentage decreases to less than 10% in the case of nanocylinders.

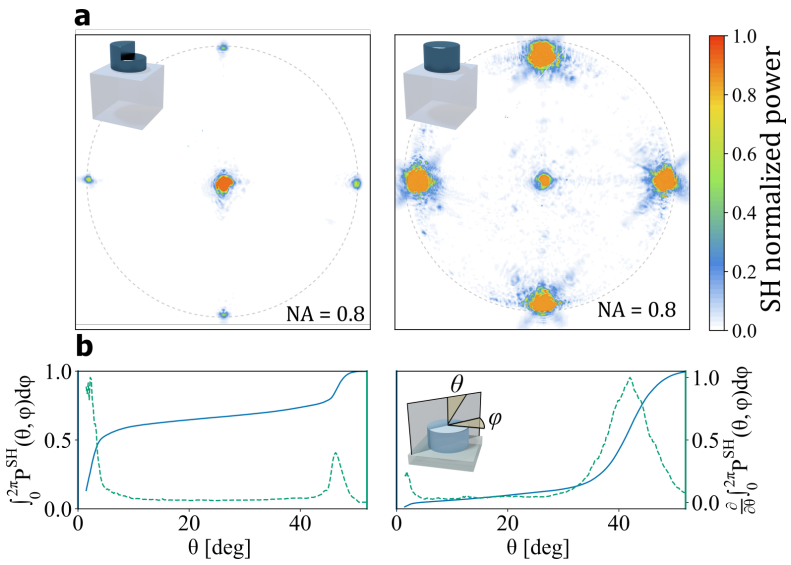

Figure C.1: (a)Experimental Fourier-plane imaging of the SHG in forward direction from uniform arrays of nanochairs (left) and nanocylinders (right). SHG power has been normalized for better visualization of all the emission lobes. (b) Normalized SHG power, integrated over the azimuthal angle φ in the range $[0 - 2\pi]$, vs. θ (solid blue line, left axis) and its derivative (dashed green line, right axis)

Acknowledgements

After three years and half of navigation in the waters of a PhD thesis, I find my self looking back at this intense journey and I see my bag filled of many experiences, competences, proving steps and awesome moments. I see the initial steps, when I understood that the game was harder than expected; I see a lot of effort and determination to get to the final result; I see hard situations, getting to complain that science is too often driven by a feeling of vanity; but especially I see the great satisfaction and ambition in learning new concepts, develop projects and sharing competences with great people. This bag is for sure much heavier than it was at the beginning of this journey, but the thing I'm mostly grateful for is the fantastic crew I met on board.

I would start thanking the captain of the boat, my thesis director, Giuseppe, for helping me to clarify in many moments my too chaotic thoughts and putting the right words behind too intricate investigations, but also for working hard to provide us the best conditions to carry out a cutting-edge research activity. After you brought me and Giuseppe to the Cnano conference in Dijon with your car, I understood you were willing to resort to any means to make us achieve the best results. You never missed to make me know your point of view, and I've always been jealous of your transparency and determination. I think that in time we got to very open and direct conversations, that I've always appreciated, and this has been extremely helpful in this pathway.

I want to thank Philippe and all the guys in LP2N at Institut d'Optique for hosting me greatly during the two weeks I spent there and making me feel as part of the group. I owe you a lot Philippe for all the things I learned during our collaboration and the competences I acquired. You passed me a vision of what making good science means, sometimes a bit extreme, sometimes questionable, but for sure authentic and passionate. I believe that those discussions in your office in front of the blackboard have been key moments for my scientific growth, and I will be always grateful for that. I want to thank also all the researchers I had the chance to collaborate with during these three years, Costa and all the guys in Brescia, Jean-Michel, Julien and Alberto in Grenoble, Isabelle at C2N, Michele and all the group in Milan, Mark and Qitong in Stanford and Pierre in Saint Etienne. You have been of great support and a fundamental source of inspiration.

Having the right guides who show you the way in this journey is for sure a large fortune, but if you row alone, the trip can soon get painful. I strongly believe that this is the main driving force of the MPQ laboratory where I had the chance to work in the last 3 years. When you enter an office with ten young PhDs from different countries united by both scientific and personal interests you might think that this 3-year travel can just go on in an amazing way and you realize how all the context is promising, but this is by no means so trivial. The atmosphere we built up all together was possible as we wanted to share a lot of things together, more curious of what the person close to you could offer than jealous of your personal knowledge. I saw a group growing up, I saw young researchers working one close to the other, and then stop everything in the evening when a voice was raising up saying: "Aperò populaire ce soir?". I saw complicity in solving technical issue, in fighting to make sure that every student could work in the best conditions feeling the minimum stress and pressure, I saw complicity in the public demonstrations as well as at Caminito Cabaret, on the Seine's docks or all around a raclette. I thank you all (without naming everybody because in time the list became so long) for all the scientific discussion we had together, the help you gave

me, and also for all the time we spent together. And I'm including in this very long list, also the former members of the group who somehow kept on being part of the team (Pierre, Mehdi, Evelio and Lucien). Thanks for the time spent together and the funny discussions. Thanks to Lucien for the support in finishing this manuscript, and for sharing the love for wine (and also Uniqlo socks apparently), I know that one day you will manage to switch to italian wine. I'm proud of calling all of you friends rather than colleagues, I'm proud of having been part of this crew, and I thank you all for having played this game together.

Une bande de thésards bien motivés mais souvent maladroits en salle blanche et presque analphabètes quand ils doivent faire de la paperasserie serait perdu sans ceux qui jouent la partie des responsables dans le labo. Merci Pascal, Stephan, Christophe et Rémi pour avoir surveillé sur tous mes fabrications et pour toutes les discussions sur la magie noire de la nanofabrication. Pascal, la première fois que je suis rentré en salle blanche, ça m'a pris 5 minutes pour me faire engueuler, avec la tête de Stéphan qui rigolait arrière. Faire le flic est contre ta nature, mais je te prie de continuer, c'est une étape tellement nécessaire pour les nouveaux doctorants et tellement rigolo pour les autres, que la salle blanche pourrait difficilement s'en passer. Stéphan, plus que l'ingénieur de salle blanche t'as toujours été le collègue qui savait tout faire et la réponse à mille problèmes. Je t'ai vu une seul fois vraiment en difficulté, t'avais mon t-shirt de Neil Young que j'ai revu après six mois. Depuis, ce t-shirt ne me rappelle plus le concert de Neil Young mais l'anniv de Dom. Deuxième énorme merci à Sandrine, Jocelyne, Nathalie et Anne. Votre explosion de rire entendue de place d'it jusqu'à Bercy est l'arme secrète de conquête d'MPQ, elle te fait énerver les premières 5 millisecondes quand t'arrive pas à terminer une simulation, mais après je me retrouvais à rigoler sans savoir pourquoi. Je suis tellement jalouse des murs de votre bureau, ils doivent en avoir entendu beaucoup dans le temps. Merci vraiment pour votre disponibilité et patience et pour avoir résisté à me crier au-dessus à chaque fois que je vous redemandais comment remplir la fiche de liaison ou un ordre de mission trois jours avant le départ.

I have never been good in keeping the different aspects of my life disconnected, and very often the funny and the bad moments of the thesis followed me from the lab back home. I have to thank "la ferme des animaux", my flat mates, Sam Juju and Ed, for the long discussions (and laugh) during our dinners, central moments to analyze and debate the highlights of the day. And since this was not enough to give you a key role during my PhD, a pandemic chose to make us colleagues 24h per day, when the living room turned in our favorite co-working space. Thank guys, you have been of vital importance to remain human and not completely alienate. I take this opportunity to thank also all the big family of CitéU, the wonderland that gave me so many friends and great moments. And since we speak about great moments, I cannot forget to acknowledge the other seven Frontons: Sam, Adonis, Pablo, Josemi, Jonny, Guille and Charlie for degenerating all together in the dream of a rock revolucionario. I don't know how it happened that we gathered all together and all the alchemy was generated, but I'm happy that it happened somehow and it will remain in a magic world where you can get rid of all preoccupations and problems. Among the extra supporters during this PhD a central position was occupied by the Italian group of climbers, and especially my jolly illuminated guide, Albe. We shared together this untouchable moment during the week when you realize that no matter how unsuccessful you could be in physics, you are much worse in climbing! Hopefully we discovered the jollypower too late, otherwise we would be working the hardest 8a wall now instead of doing physics.

E poi, come ogni viaggio in mare, non ci si ferma mai in nuovo porto senza partire con la mente verso la propria Itaca. Un grazie particolare alla famiglia "sur place", Leo e Zoe, perché avete sempre

fatto in modo che, sebbene stando a Parigi, con soli 20 minuti di bici era come tornare a casa in Italia. E un immenso grazie alla famiglia fisicamente più a distanza, ma sempre collegata, Benji Alba Andri e Laura. Grazie per aver supportato ed aver sempre creduto in questa avventura sebbene sappia quanto è faticosa questa distanza che ci separa. Grazie anche a tutte quelle zecche maledette degli amici montecassianesi, "che pozzate non staccavve mai da questa pellaccia!" Grazie a tutti voi per essere le radici di cui vado fiero.

Infine, un grazie speciale va a chi è stato lì al mio fianco a remare ogni giorno insieme a me. Forse ho un pò imbrogliato Sam dicendo che c'è voluta una pandemia per renderci colleghi 24 ore al giorno? Se penso all'esitazione iniziale di trovarci a fare un dottorato nello stesso laboratorio mi viene da ridere ora. Direi che ce la siamo cavata piuttosto bene, e che aver condiviso tanto di questa avventura alla fine ci ha aiutato un bel pò. Grazie per esserti sorbettata più di tutti le polemiche di un marinaio un pò brontolone. Grazie per essere una motivatrice determinata ma sempre lucida e razionale, che in più di un'occasione mi ha dato quella botta in testa che ti riporta nel mondo vero. Grazie per essere l'altra metà della mela!

List of publications

[1] G. Marino, **C. Gigli**, D. Rocco, A. Lemaître, I. Favero, C. De Angelis, G. Leo. *Zero-order second harmonic generation from AlGaAs-on-insulator metasurfaces*. ACS Photonics 6, 1226-1231 (2019).

[2] **C. Gigli**, G. Marino, S. Suffit, G. Patriarche, G. Beaudoin, K. Pantzas, I. Sagnes, I. Favero, G. Leo. *Polarization-and diffraction-controlled second-harmonic generation from semiconductor metasurfaces*. JOSA B 36, E55-E64 (2019).

[3] **C. Gigli**, G. Marino, A. Borne, P. Lalanne, G. Leo. *All-dielectric nanoresonators for $\chi^{(2)}$ nonlinear optics*. Frontiers in Physics 7, 1-7 (2019).

[4] **C. Gigli**, T. Wu, G. Marino, A. Borne, G. Leo, P. Lalanne. *Quasinormal-mode non-Hermitian modeling and design in nonlinear nano-optics*. ACS Photonics 7, 1197-1205 (2020).

[5] D. Rocco, **C. Gigli**, L. Carletti, G. Marino, M.A. Vincenti, G. Leo, C. De Angelis. *Vertical Second Harmonic Generation in Asymmetric Dielectric Nanoantennas*. IEEE Photonics Journal 12, 1-7 (2020).

[6] **C. Gigli**, Q. Li, P. Chavel, G. Leo, M. Brongersma, P. Lalanne. *Fundamental limitations of Huygens' metasurfaces for optical beam shaping*. *In preparation*.

[7] **C. Gigli**, G. Marino, A. Artioli, D. Rocco, C. De Angelis, J. Claudon, J.M. Gérard, G. Leo. *Tensorial phase control in nonlinear meta-optics*. Optica 8, 269-276 (2021).

List of abbreviations

AlGaAs	Aluminum-Gallium-Arsenide.
AlOx	Aluminum Oxide.
BFP	Back Focal Plane.
CGH	Computer Generated Hologram.
DFG	Difference-Frequency Generation.
DOE	Diffractive Optical Element.
EM	Electro-Magnetic.
FDTD	Finite Difference Time Domain.
FEM	Finite Element Modeling.
FF	Fundamental Frequency.
FWM	Four-Wave Mixing.
HMS	Huygens' Metasurface.
LSPR	Localized Surface Plasmon Resonance.
LUT	Look-Up Table.
MBE	Molecular Beam Epitaxy.
MOCVD	Metalorganic Chemical Vapor Deposition.
NP	Nanoparticle.
PML	Perfectly Matched Layer.
QNM	Quasi Normal Mode.
RCWA	Rigorous Coupled Wave Analysis.
RF	Radio Frequency.
SFG	Sum Frequency Generation.
SH	Second Harmonic.
SHG	Second-Harmonic Generation.
SPP	Surface Plasmon Polariton.
TH	Third Harmonic.
THG	Third-Harmonic Generation.
TPA	Two-Photon Absorption.

VSWF Vector Spherical Wave Function.